

Title	Development of a novel probe integrated with a micro-structured impedance sensor for the detection of breast cancer
Authors	Savage, Niall Thomas Patrick
Publication date	2016
Original Citation	Savage, N. T. P. 2016. Development of a novel probe integrated with a micro-structured impedance sensor for the detection of breast cancer. PhD Thesis, University College Cork.
Type of publication	Doctoral thesis
Rights	© 2016, Niall Thomas Patrick Savage. - http://creativecommons.org/licenses/by-nc-nd/3.0/
Download date	2025-07-03 23:01:06
Item downloaded from	https://hdl.handle.net/10468/3022

*Development of a novel probe integrated with a
micro-structured impedance sensor for the
detection of breast cancer*

By

Niall Thomas Patrick Savage B.Sc. M.Sc.

A thesis presented to the National University of Ireland, Cork for the degree
of Doctor of Philosophy



**Tyndall National Institute and Graduate School of Medicine and Health,
National University Of Ireland, Cork,
Éire**

Supervisors:

Dr Eric Moore, Dr Brian O'Donnell, Mr Martin O'Sullivan

Head of Programme:

Dr Liam Fanning

July 2016

This thesis is dedicated to the memory of

Dr Wesley E.P.A. van Oeffelen

Gifted Scientist, Amazing Friend, Wonderful Person

Requiescant In Pace

i. Acknowledgements

I would like to extend my sincere thanks to all those people who helped me the course of this thesis. In particular I would like to thank my supervisors Dr Eric Moore, Dr Brian O'Donnell and Mr Martin O'Sullivan for their guidance and encouragement throughout the entire project.

I would like to thank Molecular Medicine Ireland for funding this project as part of the Clinical and Translational Research Scholarship Programme which gave me the opportunity to undertake this PhD project.

I would like to sincerely thank all of my colleagues in the Tyndall National Institute and the Life Science Interface Group whose help and advice was both welcome and necessary for the completion of this thesis. I would like to say thanks to Eileen, Karen, Gerard, Lisa, Shauna and Una for putting up with me over many years. Special thanks are required for Michelle Fitzgerald who was incredibly helpfully with during the cell culture experiments among other things throughout and who helped get me through my first year. Special thanks are also necessary for Dr Walter Messina whose advice and experience was invaluable throughout the entire project.

I would like to thank all of the research staff in Tyndall National Institute and University College Cork who contributed significantly to this research including Dan O'Connell, Lynette Keeney, Vince Lodge, Suzanne Crotty, Finbarr Waldron, Paul Tassie, Ken Rodgers, Donal O'Sullivan, Dermot Heuston, Richard Murphy and Cathal Doherty.

I would like to thank all of the staff of CUH in the departments of surgery and histopathology for their amazing help and support during the breast cancer clinical study. Without their input it would not have been possible to test even one sample. Thanks to the nursing and surgical staff including Marie, Christine and Ms Abeeda Butt. I cannot possibly thank the staff of the histopathology department enough because without their incredible assistance and patience I would not have recorded or analysed even one sample. I would like to thank all of the staff of the department especially Leonne, Ciarán, Yvonne, Elaine, Paula and Dr Michael (Bill) Bennett for their

help and support. Extra special thanks has to go to Sinéad Carey who went above and beyond the call of duty to help me throughout this project.

I am forever indebted to the all the brave and courageous women who gave me permission to use their tissue samples in the breast cancer study. This project would have been for nothing without their incredible generosity.

I would like to offer the most sincere thanks of all to my amazing family and friends who got me through this incredibly difficult process. To my parents Michael and Fionnuala, I will never be able to fully describe how much your love and support has meant to me every day of my life. To my brothers Kevin and Paul; you are the best brothers I could ask for. I would like to sincerely thank my aunt, Aíne Ní Fhiannusa, for all her help and support. To “The future brains of Ireland”, my MMI friends Niamh, Ciara, Mike, Eanna, Steph, Edel, Marie and all the rest, you were a great bunch of guys and girls to go through this with. Thanks to Michelle Kenny for very kindly proofreading my thesis. Finally to my amazing girlfriend Louise, I definitely would not have finished this thesis without your incredible love and support. Thank you for always Bearing with me.

Thank you all from the bottom of my heart.

ii. Abstract

The work described in this thesis focuses on the development of an innovative bioimpedance device for the detection of breast cancer using electrical impedance as the detection method. The ability for clinicians to detect and treat cancerous lesions as early as possible results in improved patient outcomes and can reduce the severity of the treatment the patient has to undergo. Therefore, new technology and devices are continually required to improve the specificity and sensitivity of the accepted detection methods. The gold standard for breast cancer detection is digital x-ray mammography but it has some significant downsides associated with it. The development of an adjunct technology to aid in the detection of breast cancers could represent a significant patient and economic benefit. In this project silicon substrates were patterned with two gold microelectrodes that allowed electrical impedance measurements to be recorded from intact tissue structures. These probes were tested and characterised using a range of *in vitro* and *ex vivo* experiments. The end application of this novel sensor device was in a first-in-human clinical trial. The initial results of this study showed that the silicon impedance device was capable of differentiating between normal and abnormal (benign and cancerous) breast tissue. The mean separation between the two tissue types was 4,340 Ω with $p < 0.001$. The cancer type and grade at the site of the probe recordings was confirmed histologically and correlated with the electrical impedance measurements to determine if the different subtypes of cancer could each be differentiated. The results presented in this thesis showed that the novel impedance device demonstrated excellent electrochemical recording potential; was biocompatible with the growth of cultured cell lines and was capable of differentiating between intact biological tissues. The results outlined in this thesis demonstrate the potential feasibility of using electrical impedance for the differentiation of biological tissue samples. The novelty of this thesis is in the development of a new method of tissue determination with an application in breast cancer detection.

iii. Declaration

I hereby declare that this thesis is my own work, in partial fulfilment of the requirements of the Doctor of Philosophy degree. It is based on research carried out in the Tyndall National Institute and Cork University Hospital, University College Cork, Ireland between October 2012 and March 2016.

Niall Thomas Patrick Savage BSc. MSc.

iv. Table of Contents

i. Acknowledgements	i
ii. Abstract	iii
iii. Declaration	iv
iv. Table of Contents	v
v. Table of Figures	xi
vi. Table of Tables	xvii
vii. Table of Equations	xix
viii. List of Abbreviations	xx
1. General Introduction	2
1.1 Thesis Objectives	2
1.2 Thesis Overview	2
1.3 Microsystems	3
1.4 Biosensors	4
1.5 Cancer	7
1.6 Breast Cancer	8
1.6.1 Ductal Carcinoma in situ	12
1.6.2 Breast Cancer Detection	13
1.6.2.1 X-ray Mammography	14
1.6.2.2 Limitations of Mammography	14
1.7 Prostate Cancer Detection	16
1.8 Unmet user needs	17
1.9 Electrical Impedance	18
1.10 Electrical Impedance Tomography	21
1.10.1 TransScan TS 2000	21
1.10.2 Mammography Electrical Impedance Device	22
1.10.3 Dartmouth Ag/AgCl Device	23
1.11 Invasive Breast Cancer Detection	25
1.12 Prostate Cancer Detection	28
1.12.1 Dual-needle	28
1.12.2 Tip-exposure	29
1.13 Impedance in the Brain	30
1.14 Device Solutions	32
1.15 References	34
2. Impedance Probe Fabrication, Characterisation and Validation	42

2.1 Objectives	42
2.2 Introduction	42
2.2.1 Impedance Probe Design	43
2.3 Instrumentation and Techniques	47
2.3.1 Scanning Electron Microscope	47
2.3.2 Energy-dispersive X-ray Analysis	47
2.3.3 Focused-ion Beam	48
2.3.4 Atomic Force Microscopy	49
2.3.5 Cyclic Voltammetry.....	50
2.4 Experimental Details	54
2.4.1 Reagents and Materials.....	54
2.4.2 Instrumentation.....	54
2.5 Procedures.....	55
2.5.1 Fabrication	55
2.5.1.1 Silicon Probes	55
2.5.1.2 Stainless Steel.....	56
2.5.1.3 Probe Packaging	57
2.5.2 Probe Cleaning.....	58
2.5.3 Continuity Testing.....	60
2.5.4 Material Characterisation.....	61
2.5.4.1 Scanning Electron Microscope	61
2.5.4.2 Energy-dispersive X-ray Analysis	61
2.5.4.3 Focused-ion Beam	62
2.5.4.4 Atomic Force Microscopy	62
2.5.4.5 Break Strength Testing.....	63
2.5.4.6 Optical Profilometry	63
2.5.5 Electrochemical Characterisation	63
2.5.5.1 Potassium Ferri/Ferrocyanide Solution.....	63
2.5.5.2 Cyclic Voltammetry Setup.....	64
2.5.5.3 Electrical Impedance Testing.....	66
2.6 Results and Discussion	67
2.6.1 Silicon Probes	67
2.6.1.1 Wafer Fabrication	67
2.6.1.2 Silicon Probe Packaging.....	68
2.6.1.3 Scanning Electron Microscope	68
2.6.1.4 Energy-dispersive X-ray Analysis	70

2.6.1.5 Focused-ion Beam	72
2.6.1.6 Atomic Force Microscopy	73
2.6.1.7 Breakage Tests	75
2.6.1.8 Cyclic Voltammetry	77
2.6.1.9 Electrical Impedance Testing	85
2.6.2 Stainless Steel Probes	87
2.6.2.1 Scanning Electron Microscope	88
2.6.2.2 Energy-dispersive X-ray Analysis	90
2.6.2.3 Continuity Testing	91
2.6.2.4 Optical Profilometry	92
2.6.2.5 Breakage Testing	94
2.7 Conclusions	94
2.7.1 Future Work	96
2.8 References	98
3. Validation of Biocompatibility and Impedance in Biological Samples	102
3.1 Objectives	102
3.2 Introduction	102
3.2.1 Cell Culture	103
3.2.2 Resazurin Assay	104
3.2.3 Cell Culture Holders	105
3.2.4 Pressure Testing	106
3.2.5 Depth Testing	107
3.3 Experimental Details	108
3.3.1 Reagents and Materials	108
3.3.2 Instrumentation	108
3.4 Procedures	109
3.4.1 Cell Culture	109
3.4.1.1 MCF-7 Cell Culture Preparation	109
3.4.1.2 A549 Cell Culture Preparation	112
3.4.1.3 HT-29 Cell Culture Preparation	113
3.4.1.4 Silicon Biocompatibility	114
3.4.1.5 Resazurin Assay	114
3.4.1.6 Scanning Electron Microscope	115
3.4.1.7 O-ring Biocompatibility	117
3.4.1.8 Impedance Modulus Measurements	117
3.4.1.9 Stainless Steel Biocompatibility	118

3.4.2 Meat Tissue Recordings.....	119
3.4.2.1 Beef Recordings.....	119
3.4.2.2 Pressure Testing	119
3.4.2.3 Depth Testing	120
3.4.2.4 Parasitic Capacitance Testing	121
3.4.2.5 Lamb Recordings	122
3.4.2.6 Pork Recordings.....	122
3.4.3 Statistical Analysis.....	123
3.5 Results	124
3.5.1 Cell Culture	124
3.5.1.1 Silicon Biocompatibility	124
3.5.1.2 Resazurin Cell Viability Assay	125
3.5.1.3 Scanning Electron Microscopy	127
3.5.1.4 O-ring Biocompatibility.....	128
3.5.1.5 Culture of Cells on Silicon Probes	129
3.5.1.6 Stainless Steel Biocompatibility	131
3.5.2 Meat Tissue Results.....	133
3.5.2.1 Beef Impedance Recordings	133
3.5.2.2 Pressure Testing	136
3.5.2.3 Depth Testing	139
3.5.2.4 Parasitic Capacitance Testing	141
3.5.2.5 Lamb Impedance Recordings.....	142
3.5.2.6 Pork Impedance Recordings	145
3.5.2.7 All Tissues Combined.....	150
3.6 Conclusions.....	152
3.6.1 Future Work	153
3.7 References.....	154
4. Human Breast Tissue Clinical Trial.....	158
4.1 Objectives	158
4.2 Introduction	158
4.2.1 Ethical Approval	158
4.2.2 Clinical Trial Protocol.....	159
4.2.2.1 Clinical Trial Protocol Sample.....	161
4.3 Experimental	168
4.3.1 Materials.....	168
4.3.2 Instrumentation.....	168

4.4 Procedures.....	168
4.4.1 Device Cleaning	168
4.4.2 Before Surgery	168
4.4.3 During Surgery	169
4.4.4 Histopathology Laboratory.....	169
4.4.5 After Recording	171
4.4.6 Statistical Analysis.....	172
4.5 Results and Discussion	174
4.5.1 Consented Patients	174
4.5.2 Impedance Modulus Recordings	176
4.5.3 Pathology Findings.....	178
4.5.4 Inter-rater Reliability Analysis	180
4.5.5 Paired-samples T Test Analysis	183
4.5.5.1 Optimum Frequency Selection	183
4.5.5.2 All Study Participants.....	183
4.5.5.3 All Cancers.....	185
4.5.5.4 All Primary Breast Cancers.....	186
4.5.5.5 All Invasive Ductal Cancers	187
4.5.5.6 Differentiation by Cancer Type	188
4.5.5.6.1 Invasive Ductal Carcinoma Grade 3	189
4.5.5.6.2 Invasive Ductal Carcinoma Grade 2	191
4.5.5.6.3 Mixed Invasive Ductal and Lobular Carcinoma Grade 2	192
4.5.5.6.4 Invasive Lobular Carcinoma Grade 2.....	193
4.5.5.6.5 Invasive Mucinous Carcinoma Grade 2	195
4.5.5.6.6 Metastatic Squamous Cell Carcinoma	196
4.5.5.6.7 Fibroadenoma	198
4.6 Discussion.....	199
4.7 Conclusions.....	203
4.7.1 Future Work	204
4.8 References.....	207
5. Summary and Future Work	210
5.1 Chapter 1 Summary	210
5.2 Chapter 2 Summary	210
5.2.1 Chapter 2 Future Work.....	211
5.3 Chapter 3 Summary	211
5.3.1 Chapter 3 Future Work.....	212

5.4 Chapter 4 Summary	212
5.4.1 Chapter 4 Future Work	213
5.5 Thesis Conclusion	213
6. Appendices	216
6.1 Patient Information Leaflet.....	216
6.2 Patient Consent Form	219
6.3 Summary of C.V. for Chief Investigator	221
6.4 Ethical Approval Application	222
6.5 List of Oral and Poster Presentations	223
6.5.1 Conference Proceedings	223
6.5.2 Oral Presentations.....	223
6.5.3 Poster Presentations	223
6.5.4 Demonstrations	225
6.6 Clinical Trial Images	226
6.6.1 Macroscopic Images	226
6.6.2 Microscopic Images.....	229
6.7 Dimensions of Cell Culture Holders.....	238
6.8 Paired-samples T test Outputs	239
6.8.1 Beef, Lamb and Pork.....	239
6.8.2 Clinical Trial Samples.....	239

v. Table of Figures

Figure 1.1: Schematic layout of a biosensor. Figure is Author's own.....	5
Figure 1.2: The histological classification of breast cancer subtypes. HPF – High Powered Field. Reference [33].....	9
Figure 1.3: Left: The anatomical structure of the breast and chest wall. Right: The steps along the way towards the development of invasive ductal carcinoma. Reference [34].	10
Figure 1.4: The molecular classification of breast cancers based on the intrinsic molecular subtypes of breast cancer identified by micro-array analysis. Reference [33].	12
Figure 1.5: A simple equivalent circuit model of biological tissues. R_i – intracellular resistance, C_m – cell membrane capacitance, R_e – extracellular resistance. Figure is Author's own.....	20
Figure 1.6: An equivalent circuit model of biological cell behaviour. R_i – intracellular resistance, R_e – extracellular resistance, R_m – cell membrane resistance, C_i – intracellular capacitance, C_e – extracellular capacitance, C_m – cell membrane capacitance. Figure is Author's own.....	20
Figure 1.7: The electrical impedance mammography device with the 256-electrode design. Reference [93].....	22
Figure 1.8: The two geometries used by Mäki <i>et al.</i> to design an electrical impedance biopsy needle. Reference [101].	26
Figure 1.9: Images of the IDE electrodes on the curved surface of the needle; (A) IDE electrodes on the needle assembled with syringe (B) microscopic image for detailed view, and (C) SEM image showing the projected boundaries of the needle. Reference [102].	27
Figure 1.10: A bio-impedance needle probe constructed from two stainless steel needles, each 1 mm in diameter and tapered to a point. Reference [17].....	28
Figure 1.11: The EIS-Biopsy probe design (a), with polyimide insulation and the exposed tips (b). Reference [103].	29
Figure 1.12: The probe design in which the platinum electrodes are placed at non-constant inter-electrode separation distances. Reference [23].	30
Figure 1.13: The design and dimensions of the micro-electrode tip and a scanning electron micrograph image of a SU-8 micro-needle tip. Reference [25].	31
Figure 1.14: A schematic overview of the breast cancer detection pathway and the area in which the novel probe device fits within the pathway. Figure is Author's own.	33
Figure 2.1: The design pattern for the masks used in the production of the stainless steel and silicon probes. The total length of the patterned probes is 39 mm and the pitch between probes is 3.7 mm.	45
Figure 2.2: A close-up of the design pattern for the recording electrodes for the stainless steel and silicon probes. The dimensions of the electrode pads and the gold tracks are shown.	45
Figure 2.3: A close-up of the design pattern for the connection pads for the stainless steel and silicon probes. The dimensions of the output pads are shown.	46
Figure 2.4: The outline (light blue) of the mask used during the passivation process for both the recording and output electrode pads. This area is etched to remove the Si ₃ N ₄ to expose the electrodes and allow electrical signals to be conducted.	46

Figure 2.5: An example of an FEI Quanta 650 FEG SEM. Reference [12].	47
Figure 2.6: An example of an FEI Quanta 3D Dual Beam FIB. Reference [20].	49
Figure 2.7: An example of an AFM cantilever and tip. Reference [23].	49
Figure 2.8: The forward and reverse potentials versus time of a typical cyclic voltammogram. Redrawn from reference [28].	51
Figure 2.9: The effect of increasing scan rate on the peak current response of reversible electrochemical reaction. Reference [28].	52
Figure 2.10: A simple schematic of a three-electrode electrochemical cell, showing the working electrode, reference electrode and counter electrode immersed in solution. The electrodes are all connected to a potentiostat so that the potential differences between the electrodes can be measured. Figure is Author's own.	53
Figure 2.11: An expanded view conceptualised drawing of the individual layers deposited during the fabrication of the silicon probes. Black – 525µm Silicon Substrate; Green – 300nm SiO ₂ ; Yellow – 20 nm/220 nm Titanium/Gold; White – 250 nm Si ₃ N ₄ . Figure was produced by Dr Walter Messina.	55
Figure 2.12: A packaged probe showing the plastic tubing filled with hardened 2-part epoxy covering the electrical connects.	58
Figure 2.13: The Heraeus VT5042EK vacuum oven used in the probe packaging process.	58
Figure 2.14: The Ultrawave QS3 ultrasonic water-bath used during the probe cleaning protocol.	59
Figure 2.15: The Harrick Plasma oxygen-plasma cleaner and vacuum pump used during the silicon probe cleaning protocol.	60
Figure 2.16: A Fluke 16 multimeter which was used to determine if a short-circuit existed in the stainless steel and silicon probes.	61
Figure 2.17: The equipment setup for the CV measurements using a PalmSens potentiostat and a three electrode circuit.	64
Figure 2.18: The Ag/AgCl and platinum wire electrodes and a silicon probe in a solution of potassium ferri/ferrocyanide and KCl during CV measurement.	65
Figure 2.19: A silicon wafer after the entire deposition process had been completed.	67
Figure 2.20: The stages of the device packaging process including diced, shaped and electrically packaged.	68
Figure 2.21: A) A 140x magnification SEM image of the gold electrode surface and underlying silicon substrate. B) A 250x magnification SEM image of the gold electrode surface and underlying silicon substrate. C) A 25,000x magnification SEM image of the gold electrode surface. D) A 50,000x magnification SEM image of the gold electrode surface. E) A 100,000x magnification SEM image of the gold electrode surface.	70
Figure 2.22: A) The EDX spectrum of the surface of a gold electrode from a silicon probe. B) The EDX spectrum from the surface of a gold electrode on a different silicon probe from the one analysed in A).	71
Figure 2.23: A) A 20,000x magnification SEM image of the focused-ion beam milling site on the gold electrode. B) A 150,000x magnification SEM image of the hole milled using the FIB instrument. The approximate layer thickness of the gold (A), titanium (B) and SiO ₂ (C) layers are also shown.	72
Figure 2.24: The position of the AFM cantilever during one of the measurement recordings.	74

Figure 2.25: A representative image from one of the AFM scans performed on the gold surface of the silicon probe.	74
Figure 2.27: A silicon probe held in position between the two plates of the Instron force testing instrument.....	76
Figure 2.28: A cyclic voltammogram of the left and right electrodes of a gold probe prior to cleaning and directly after cleaning. The cleaning protocol resulted in an increase in both the anodic and cathodic peak currents.....	78
Figure 2.29: The overlaid CV graphs from the left electrode of 5 silicon probes from the same batch.	79
Figure 2.30: A) Cyclic voltammograms of a left working electrode displaying an increase in peak current with increasing scan rate from 10 mV/s to 100 mV/s. B) A graph of the redox peak currents -v- the square root of the scan rate from 10 mV/s to 100 mVs.	82
Figure 2.31: A) Cyclic voltammograms of a right working electrode, from the same probe as in Figure 2.34, which shows the increase in peak current with increasing scan rate from 10 mV/s to 100 mV/s. B) A graph of the redox peak currents -v- the square root of the scan rate from 10 mV/s to 100 mVs.	83
Figure 2.32: A silicon probe inserted in to the gelatine (orange) and lard (white) model during the electrical impedance testing.	85
Figure 2.33: The average of the fixed frequency (4,500 Hz) recordings obtained as one of the silicon probes was moved between layers of gelatine and lard at 30 second intervals.....	86
Figure 2.34: A close-up view of a patterned stainless steel wafer with 12 electrode pairs.....	88
Figure 2.35: A) A 288x magnification SEM image of the recording electrode pads of a stainless steel prototype device. B) A 1,500x magnification SEM image of a surface defect identified in the left electrode of the stainless steel probe imaged in A). An approximate measurement of the width of defect is displayed on the image.	89
Figure 2.36: A 305x magnification SEM image of the insulated gold tracks of a stainless steel probe.	90
Figure 2.37: An EDX spectrum of a gold electrode on a stainless steel substrate. .	91
Figure 2.38: A representative image from one of the optical profilometry scans performed on the surface of the bare stainless steel wafer.	93
Figure 2.39: A graph of topographical profile of the surface of the bare stainless steel wafer.	93
Figure 2.40: The mean RMS roughness of the surface of the stainless steel wafer obtained using optical profilometry. N=1; Mean \pm S.D.....	94
Figure 3.1: A) The expanded view of the cell culture probe holder including an O-ring which forms a water-tight seal. B) The design drawing of the constructed cell culture holder and probe. C) The side-profile view of the cell culture probe holder.	106
Figure 3.2: The Class II biological safety cabinet in the Tissue Culture Facility in Tyndall National Institute.....	110
Figure 3.3: The haemocytometer used during the cell culture counts.....	111
Figure 3.4: The layout of a haemocytometer with the 5 large boxes highlighted which are counted during a cell count. Modified by Author from Reference [16]. .	111

Figure 3.5: The individual components of the cell culture probe holder. A) Bottom of holder, B) O-ring, C) Top of holder, D) Plastic film cover and screws, E) An unpackaged silicon prototype.....	117
Figure 3.6: The assembled cell culture probe holder from the top A) and bottom B).	118
Figure 3.7: An example of a Weitlaner tissue retractor that was used in the pressure testing of the beef rib samples. Reference [19].	120
Figure 3.8: The total length of the silicon probe prior to insertion in the gelatine gel.	121
Figure 3.9: Micrographic images of the tip of the silicon probe seeded with control (no cells; A) and HT-29 cells (400,000 cells per device) for 24 hr (B) and 48 hr (C).	124
Figure 3.10: Micrographic images of the tip of the silicon probe seeded with control (no cells; A) and MCF-7 cells (400,000 cells per device) for 24 hr (B).	125
Figure 3.11: The result of the resazurin assay which shows the cell viability of MCF-7 cells grown on the silicon devices compared to both positive and negative controls. N=4 and each sample was tested in triplicate. Data shown is the average of the % viability value \pm S.D.	126
Figure 3.12: 35x magnification SEM images of a silicon probe seeded with MCF-7 cells at increasing voltage from a) 5, b) 10, c) 20 and d) 30 kV.	128
Figure 3.13: The images taken of the O-ring biocompatibility study. A) The outer edge of the O-ring in black with cells grown to confluence adjacent to it. B) An image taken from the same well as A) which shows growth across the entire well. C) An image of one of the control wells used in the experiment in which a confluent cell layer was present.	129
Figure 3.14: A) 10x magnification image of a silicon probe seeded with 100,000 A549 cells. B) 2.5x magnification image of a silicon probe seeded with 200,000 A549 cells. C) 10x magnification image of a silicon probe seeded with no cells as a control.	130
Figure 3.15: A549 cells seeded at 80,000 (A) and 120,000 (B) cells per well for a period of 24 hours on the stainless steel wafer with plastic cell culture wells attached. The cells are stained with propidium iodide (500nM) nuclear stain.	132
Figure 3.16: A) A silicon probe in the fat of a beef rib sample. B) A close up image of a silicon probe in a section of fat in a beef rib sample.	133
Figure 3.17: The triplicate impedance modulus values for beef fat and muscle obtained using 3 applied voltages (10, 30 and 50 mV peak voltage) across a frequency sweep from 100,000-1,000 Hz.	134
Figure 3.18: The Bode plot of the averaged values for beef rib fat and muscle frequency sweep recordings at 10 mV peak voltage. N=9.	134
Figure 3.19: The result of the paired-samples T test to compare the means of the beef rib fat and muscle impedance modulus recordings at 3 kHz. Mean \pm S.D., N=9, $p < 0.001$	136
Figure 3.20: The average values for the test of pressure on the modulus of the electrical recordings obtained in a beef rib muscle sample. The averages of the triplicate recordings for each variable are shown.	137
Figure 3.21: The average values for the test of pressure on the modulus of the electrical recordings obtained in a beef rib fat sample. Average of triplicate recordings for each variable.	138

Figure 3.22: The probe and ruler used to measure the depth of penetration during experimentation at 10 mm (A), 15 mm (B) and 20 mm (C).....	140
Figure 3.23: The results of the depth of penetration experiments at three depths 10, 15 and 20 mm. Values shown are averages of triplicate recordings at each depth.	140
Figure 3.24: The average plot of the capacitive reactance response of a silicon probe in HBSS buffer. N=1.	141
Figure 3.25: A) A silicon probe placed in an area of fat in a lamb centre loin sample. B) A close up of the probe in the fat tissue (right).....	142
Figure 3.26: The triplicate electrical impedance modulus values for lamb fat and muscle obtained using 3 applied peak voltages (10, 30 and 50 mV) across a frequency sweep from 100,000-1,000 Hz.....	142
Figure 3.27: The Bode plot of the averaged values for lamb centre loin fat and muscle frequency sweep recordings at 10 mV peak amplitude. N=9.	143
Figure 3.28: The result of the paired-samples T test to compare the means of the lamb centre loin fat and muscle impedance recordings at 3 kHz. Mean \pm S.D., N=9, $p < 0.001$	144
Figure 3.29: A) A silicon probe in a region of fat in a pork centre loin sample. B) A close up of the probe in the fat tissue (right).	145
Figure 3.30: The triplicate electrical impedance values for pork fat and muscle obtained using 3 applied voltages (10, 30 and 50 mV peak voltage) across a frequency sweep from 100,000-1,000 Hz.....	146
Figure 3.31: The Bode plot of the averaged values for pork centre loin fat and muscle frequency sweep recordings at 10 mV peak voltage. N=9.	147
Figure 3.32: The result of the paired-samples T test to compare the means of the pork centre loin fat and muscle impedance recordings at 3 kHz. Mean \pm S.D., N=9, $p = 0.001$	148
Figure 3.33: A modified Bland-Altman plot of the phase angle for each of the pork fat recordings. The mean \pm 1.96 S.D have been plotted on the graph.....	149
Figure 3.34: A modified Bland-Altman plot of the phase angle for each of the pork muscle recordings. The mean \pm 1.96 S.D have been plotted on the graph.	149
Figure 3.35: The result of the paired-samples T test to compare the combined beef, lamb and pork fat and muscle impedance recordings at 3 kHz. Mean \pm S.D., N=27, $p < 0.001$	151
Figure 4.1: The placement of a packaged probe in a cancerous lesion in a wide-local excision sample obtained from Study Participant 05.....	171
Figure 4.2: A wide-local excision sample obtained from Study Participant 05 which contained a tumour of approximately 3 cm diameter. The orientation sutures can clearly be seen at two locations on the sample.	175
Figure 4.3: The areas of interest in the wide-local excision sample of study participant 11. The areas are the cancerous lesion (Red), fat necrosis (Green) and normal tissue (Blue).....	177
Figure 4.4: A partially inked ultrasound wire-guided diagnostic excisional biopsy specimen with an incision made in to an area of fibroadenoma shown in white from study participant 08.....	178
Figure 4.5: The microscopic images obtained from the healthy tissue margin (A) and the cancerous lesion (B) of study participant 02 as confirmed by a consultant pathologist.	179

Figure 4.6: The Bode plot of the average impedance values for the tissue margin and lesion. N=23.....	184
Figure 4.7: The Bode plot of the average impedance values for the tissue margin and cancer tumours. N=21.....	186
Figure 4.8: The average impedance values for the tissue margin and tumour for primary breast cancers. N=20.....	187
Figure 4.9: The average impedance values for the tissue margin and tumour for primary breast cancers. N=15.....	188
Figure 4.10: The Bode plot of the averaged electrical impedance results of the invasive ductal carcinoma grade 3 samples recorded during the clinical trial. N=11.	190
Figure 4.11: The Bode plots of the averaged electrical impedance results of the invasive ductal carcinoma grade 2 patients consented to the clinical trial. N=4....	192
Figure 4.12: The electrical impedance results from the mixed invasive ductal and lobular carcinoma grade 2 sample. N=3.....	193
Figure 4.13: The averaged electrical impedance result of the invasive lobular carcinoma (ILC) grade 2 patient consented to the clinical trial. N=1.....	194
Figure 4.14: The mean values of the tissue margin and lesion recordings obtained at a frequency of 20 kHz from the tissue margins and cancer from the ILC Grade 2 specimen. N=1.....	195
Figure 4.15: The electrical impedance results of the invasive mucinous carcinoma (IMC) grade 2 patients consented to the clinical trial. N=1.	195
Figure 4.16: The mean values of the tissue margin and lesion recordings obtained at a frequency of 20 kHz from the tissue margins and cancer from the IMC Grade 2 sample. N=1.	196
Figure 4.17: The Bode plot of the electrical impedance recordings taken from the metastatic squamous cell carcinoma (MSCC) specimen. N=1.	197
Figure 4.18: The mean values of the tissue margin and lesion recordings obtained at a frequency of 20 kHz from the tissue margins and cancer from the metastatic squamous cell carcinoma patient. N=1.	197
Figure 4.19: The Bode plot of the averaged electrical impedance results of the fibroadenoma patients consented to the clinical trial. N=2.....	198
Figure 4.20: The mean \pm S.D. of the tissue margin and fibroadenoma recordings obtained at a frequency of 20 kHz from the tissue margins and benign lesions from the fibroadenoma patients. N=2; mean \pm S.D.; p = 0.029.....	199

vi. Table of Tables

Table 1.1: Selection of the most common cancer biomarkers for 8 common cancer types. AFP – Alpha-fetoprotein; BRCA – Breast Cancer; CA – Cancer Antigen; CASA – Cancer-associated Serum Antigen; CEA – Carcinoembryonic Antigen; EGF – Epidermal Growth Factor; ER/PR – Oestrogen/Progesterone Receptor; HCG – Human Chorionic Gonadotrophin; HCG – Human Chorionic Gonadotropin; HER2 – Human Epidermal Growth Factor Receptor 2; ING-1 – Inhibitor of Growth Family, Member 1; NSE – Neuron Specific Enolase, NY-BR-1 – New York Breast 1; NY-ESO-1 – New York Oesophageal Squamous Cell Carcinoma 1; p53 – Tumour Protein 53; PSA – Prostate Specific Antigen; TAG – Tumour-associated glycoprotein 72. Table was redrawn from reference [7].	6
Table 1.2: The top 5 most common cancers in men and women diagnosed in the USA in 2014. Reference [12].	7
Table 1.3: The size of each aspect of the micro-needle probe. Reference [25].	31
Table 2.1: The experimental methods that will be used in Chapter 2 and the purpose of each of them.	42
Table 2.2: The probe specifications and dimensions used in the design of the photolithography masks.	44
Table 2.3: The total calculated recording surface area of each of the gold electrodes.	46
Table 2.4: The SEM imaging parameters used after the FIB milling procedure	62
Table 2.5: The AFM imaging parameters used in the analysis of the gold electrode surface.	62
Table 2.6: The parameters used for the cyclic voltammetry measurements performed using a three-electrode set-up with the silicon probes, a Ag/AgCl reference and a platinum counter electrode.	65
Table 2.7: The theoretical and approximate values of the deposition layers observed on the silicon probes using SEM imaging.	73
Table 2.8: The values of the applied force in Newton obtained during the silicon probe breaking force tests.	77
Table 2.9: The anodic and cathodic peak voltages and peak differences of the clean and unclean electrodes measured using cyclic voltammetry.	79
Table 2.10: The peak anodic and cathodic potentials and differences for the five silicon probes from the same batch scanned at a rate of 0.1 V/s.	80
Table 2.11: The linear regression equations for the anodic (I _{pa}) and cathodic (I _{pc}) peak current -v- square root of the scan rate for the left and right working electrodes for a gold probe. The test solution used was 5mM [Fe(CN) ₆] ^{3-/4-} in 1 M potassium chloride (KCl).	84
Table 2.12: The corrected time values for each of the gelatine and lard layers tested.	87
Table 3.1: MEME complete media composition.	110
Table 3.2: DMEM/F12 complete media composition.	112
Table 3.3: McCoy's 5A complete media composition.	113
Table 3.4: The layout used for the resazurin assay experiments.	115
Table 3.5: The cell fixation process required for SEM imaging.	116
Table 3.6: The acetone dehydration process required for SEM imaging	116

Table 3.7: The different methods of applying pressure to the beef rib muscle and fat samples.	120
Table 3.8: The averaged results of each replication of the resazurin assay and the standard deviation.	126
Table 3.9: The data output for the normality testing performed on average beef fat and muscle recordings at a frequency of 3 kHz. N=9.	135
Table 3.10: The data output for the normality testing performed on average lamb fat and muscle recordings at a frequency of 3 kHz. N=9.	144
Table 3.11: The data output for the normality testing performed on average pork fat and muscle recordings at a frequency of 3 kHz. N=9.	147
Table 4.2: The patient age, type and grade of the tumour samples analysed during the study.	179
Table 4.3: The IRR analysis of the cancerous recordings obtained from study participant 05 including 3 healthy recordings including the outlying values.	180
Table 4.4: The IRR analysis of the cancerous recordings obtained from study participant 03 including 2 cancerous recordings excluding the outlying values. ...	180
Table 4.5: The average measures output from the IRR analysis of study participant 07 before and after data set 01 was removed.	181
Table 4.6: The average measures output from the IRR analysis of study participant 09 before and after data set 01 was removed.	181
Table 4.7: The IRR analysis for the entire tissue margin recordings obtained from the total patient cohort.	182
Table 4.8: The IRR analysis for all of the cancer recordings obtained during the clinical study.	182
Table 4.9: The IRR analysis for all of the fibroadenoma recordings obtained from two patients.	183
Table 4.10: The data output for the normality testing performed on average tissue margin and lesion recordings for each patient. N=17.	184
Table 4.11: The data output for the normality testing performed on average tissue margin and cancer recordings for each patient. N=21.	185
Table 4.12: The data output for the normality testing performed on average tissue margin and cancer recordings for each patient. N=20.	186
Table 4.13: The data output for the normality testing performed on average tissue margin and cancer recordings for each patient. N=15.	187
Table 4.14: The data output for the normality testing performed on average tissue margin and cancer recordings for each patient. N=11.	189
Table 4.15: The IRR analysis for all of the IDC Grade 3 tissue margin and cancer recordings obtained during the clinical study.	190
Table 4.16: The data output for the normality testing performed on average tissue margin and cancer recordings for each patient. N=4.	191

vii. Table of Equations

Equation 1.1: Equation for the determination of electrical impedance (Z). R – resistance, j – square root of -1, ω – angular frequency, L – inductance and C – capacitance.	18
Equation 1.2: Formula for the calculation of value of a two plate capacitor. C – capacitance, ϵ – permittivity, A – area of each plate, d – distance between plates. Reference [77].	18
Equation 2.1: The relationship between the anodic and cathodic peak currents. n = number of electrons transferred.	51
Equation 2.2: The ratio of the peak anodic and cathodic peak current which equals 1 for reversible chemical reactions.	51
Equation 2.3: The Randles-Sevcik equation for the calculation of peak current in a reversible system.	52
Equation 3.1: Calculation of number of cells per millilitre of cell suspension.	112
Equation 3.2: The calculation of the concentration of resazurin in solution.	114
Equation 3.3: The calculation for capacitance using reactance. f – Applied Frequency, X_c – Reactance, C – Capacitance.	122

viii. List of Abbreviations

A – Area of plate
AC – Peak Alternating Current
ACR – American College of Radiology
AFM – Atomic Force Microscopy
AFP – Alpha-fetoprotein
Ag/AgCl – Silver/Silver Chloride
AJCC – American Joint Committee on Cancer
ATP – Adenosine Triphosphate
BIRADS – Breast Imaging-Reporting and Data System
BRCA – Breast Cancer
C – Capacitance
CA – Cancer Antigen
CA3 – Cornu Ammonis 3
CASA – Cancer-associated Serum Antigen
 C_e – Extracellular Capacitance
CEA – Carcinoembryonic Antigen
 CF_4 – Tetrafluoromethane
 C_i – Intracellular Capacitance
 C_m – Cell Membrane Capacitance
CNB – Core-Needle Biopsy
CNM-IMB – *Centro Nacional de Microelectrónica*
 CO_2 – Carbon Dioxide
CREC – Clinical Research Ethics Committee of the Cork Teaching Hospitals
CT – Computed Tomography
CUH – Cork University Hospital
CV – Cyclic Voltammetry
D – Distance between Plates
DCIS – Ductal Carcinoma in situ
DMEM/F12 - Dulbecco's Modified Eagle Medium: Nutrient Mixture F-12
DNA – Deoxyribonucleic acid
DRE – Digital Rectal Exam
 ΔE – Peak Voltage Separation
 ϵ – Permittivity
ECIS – Electric Cell-substrate Impedance Sensing

EDTA – Ethylenediaminetetraacetic Acid
 EDX - Energy-dispersive X-ray
 EGF – Epidermal Growth Factor
 EIS – Electrical Impedance Spectroscopy
 EIT – Electrical Impedance Tomography
 EMAF – Electron Microscopy and Analysis Facility
 E_{pa} – Anodic Peak Potential
 E_{pc} – Cathodic Peak Potential
 ER – Oestrogen Receptor
 FIB – Focused-Ion Beam
 Ga^{+} – Gallium ion
 GdDTPA – Gadolinium Diethylene Tri-amine Penta-Acetic Acid
 HBSS – Hank’s Balanced Salt Solution
 HCG – Human Chorionic Gonadotrophin
 HER2 – Human Epidermal Growth Factor Receptor 2
 HPF – High-Powered Field
 Hz - Hertz
 IBC – Invasive Breast Carcinoma
 IDC – Invasive Ductal Carcinoma
 ILC – Invasive Lobular Carcinoma
 IMC – Invasive Mucinous Carcinoma
 ING-1 – Inhibitor of Growth Family Member 1
 I_{pa} – Anodic Peak Current
 IPA – Isopropyl Alcohol
 I_{pc} – Cathodic Peak Current
 IRR – Inter-rater Reliability
 j – Square Root of -1
 KCl – Potassium Chloride
 $K_3[Fe(CN)_6]$ – Potassium Ferricyanide Salt
 $K_4[Fe(CN)_6]$ – Potassium Ferrocyanide Salt
 L – Inductance
 M – Metastasis
 MCF-7 – Michigan Cancer Foundation 7
 MEIK – Mammography Electrical Impedance
 MEME – Minimum Essential Media Eagle

MEMS – Micro-electromechanical System
 MRI – Magnetic Resonance Imaging
 MSCC – Metastatic Squamous Cell Carcinoma
 n – Electron Stoichiometry
 N – Lymph Nodes
 NAP – National Access Programme
 NEAA – Non-essential Amino Acid
 NPV – Negative Predictive Value
 NSE – Neuron Specific Enolase
 NY-BR-1 – New York Breast 1
 NY-ESO-1 – New York Oesophageal Squamous Cell Carcinoma 1
 OsO₄ – Osmium Tetroxide
 P53 – Tumour Protein 53
 PBS – Phosphate-buffered Saline
 PECVD – Plasma-Enhanced Chemical Vapour Deposition
 PET – Positron Emission Topography
 PI – Propidium Iodide
 PR – Progesterone
 PSA – Prostate-Specific Antigen
 R – Resistance
 R_i – Intracellular Resistance
 R_e – Extracellular Resistance
 R_m – Cell Membrane Resistance
 SEM – Scanning Electron Microscope
 S.D. – Standard Deviation
 SFI – Science Foundation Ireland
 SiO₂ – Silicon Dioxide
 Si₃N₄ – Silicon Nitride
 SPSS – IBM Statistical Analysis Package 20
 T – Primary Tumour
 TAG – Tumour-associated Glycoprotein 72
 TIDA – Technology Innovation Development Award
 TMS – Tetramethylsilane
 TNI – Tyndall National Institute
 US – Ultrasound

USA – United States of America

v – Scan Rate

V_1 – Initial Voltage

V_2 – Final Voltage

ω – Angular Frequency

X_c – Reactance

Z – Electrical Impedance

Chapter 1

General Introduction

1. General Introduction

1.1 Thesis Objectives

The work described in this thesis focuses on the development of an innovative bioimpedance device for the detection of breast cancer using electrical impedance as the detection method. The ability for clinicians to detect and treat cancerous lesions as early as possible results in improved patient outcomes and can reduce the severity of the treatment the patient has to undergo. Therefore, new technology and devices are continually required to improve the specificity and sensitivity of the accepted detection methods. The four main objectives of this thesis were:

- 1) Design and fabrication of a novel impedance probe
- 2) Packaging, characterisation and testing of the fabricated devices
- 3) Biocompatibility and tissue differentiation testing using the impedance sensors
- 4) A first-in-human clinical trial to differentiate between normal and abnormal tissues in *ex vivo* breast tissue specimens.

The novelty of this thesis is in the development of a new method of tissue determination with an application in breast cancer detection.

1.2 Thesis Overview

Chapter 1 provides an introduction to breast cancer as a disease and how it is currently detected using x-ray mammography. The chapter also provides an overview of previous work undertaken using electrical impedance as a cancer detection method in a number of different body tissues. During the course of the Ph.D. project there was a key research question which needed to be answered:

- Can we use electrical impedance to differentiate between healthy and cancerous tissues of the breast?

In an attempt to answer this question it was hoped that a significant body of new research in the area of breast cancer detection would be produced as

well as a number of new research questions that would require future investigation.

Chapter 2 investigates the design, fabrication and characterisation of both stainless steel and silicon prototype devices patterned with gold microelectrodes. The fabrication of the stainless steel prototypes was unsuccessful at producing probes that were suitable for electrochemical recording. However, the silicon probes proved to be effective and reliable prototypes and were fully characterised using a suite of techniques including imaging and electrochemical measurements.

Chapter 3 involves the determination of the biocompatibility and tissue differentiation ability of the prototype devices. A number of biocompatibility tests were performed involving light, fluorescent and electron microscopy as well as a resazurin cell viability assay. The silicon probes were then tested, using animal samples, to determine their ability to differentiate between fat and muscle tissues. A number of secondary experiments were conducted to determine the effect of applied voltage, depth and pressure on the electrical impedance detection capability of the silicon devices.

Chapter 4 describes the first in-human clinical trial that was undertaken to demonstrate the ability of the silicon prototypes to differentiate between tissue margins and cancerous lesions in *ex vivo* samples obtained during breast surgeries.

1.3 Microsystems

Microsystems or a micro-electromechanical system (MEMS) is a term used to describe sub-millimetre integrated electro-mechanical systems that contain both electrical and mechanical components. Typically, these miniaturised devices perform non-electronic functions such as sensing or actuation. The integrated components generally range from 1 μm to 1 mm in size and are fabricated in a parallel manner through photolithography [1]. The use of photolithographic tools for the fabrication of microsystem devices results in the ability to produce large quantities of identical devices with an extremely low per unit cost. This provides an extremely reliable and

repeatable manufacturing process which can be readily optimised for the production of novel prototype devices. Silicon substrates are the most widely used in the production of microsystem devices because it is a chemically inert material compatible with existing semi-conductor fabrication processes [1]. The fabrication process for devices in microsystems usually involves the deposition of multiple photolithographic layers such as material deposition, patterning and pattern transfer which will be further discussed in greater detail in Chapter 2 of this thesis. The flexibility of the fabrication processes involved with creating new MEMS devices has expanded the capability and scope of microsystems and has resulted in many different application areas. These can include healthcare, energy management and environmental monitoring. In the area of healthcare, MEMS devices are becoming increasingly common. These can be used in monitoring patient wellbeing and recovery, assessing infection development and diagnosing diseases. This requires technological advancements which can be addressed by microsystem devices. Within the larger definition of microsystems there exists a smaller subsection of the research community involved in the area of life science interfaces. This research is focused on exploiting design, fabrication and characterisation tools to enable the manipulation, detection and characterisation of a wide range of small molecules, nucleic acids, proteins and cells. The focus of healthcare and life science interface research in the area of microsystem technology has resulted in the development of novel devices and hardware platforms to address key societal challenges, particularly in the area of new diagnostic and screening techniques for the increased sensitivity and specificity of disease detection. A significant amount of the research conducted within the life science interface community is involved with the development or improvement of biosensor devices.

1.4 Biosensors

A biosensor is defined as a self-contained integrated device which is capable of providing specific quantitative or semi—quantitative analytical information using a biological recognition element which is in direct spatial contact with a transducer element. This produces a signal which is sent to a processing unit

which presents the data in a useable format for the user (Figure 1.1). Biosensors have a range of applications covering diverse fields including: medicine, pharmaceuticals, food and process control, environmental monitoring, defence and security. The primary market for biosensors is in medical diagnostics. Self-monitoring of blood glucose is one of the largest users of biosensors and this is evident from the market size which was estimated be worth \$11.1 billion worldwide in 2014 [2]. This is an increasing market due to the increasing incidence of diabetes worldwide which is estimated to be 366 million people by 2030 [3].

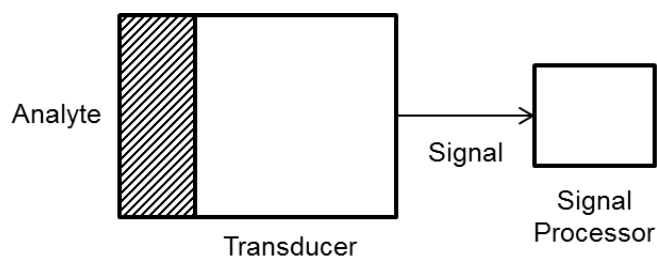


Figure 1.1: Schematic layout of a biosensor. Figure is Author's own.

The current trend towards personalised medicine worldwide will lead to significant increases in the utilisation of biosensors for the monitoring of routine physiological measurements such as blood pressure, heart rate, blood glucose, blood alcohol, activity and exercise tracking [4]. Biosensors can also be utilised in the monitoring of chronic conditions, infection control and rehabilitation [5]. There are applications for biosensors outside of healthcare monitoring which include: detection of bacteria and pesticides in air, water, food and detection of chemical and biological weapons. The incorporation of multiple biosensors in an integrated device has led to a dramatic increase in the usability and functionality of biomedical devices across all areas of healthcare and patient monitoring. Biosensors can be broadly classified in three distinct types:

- 1) Electrical
- 2) Mechanical
- 3) Electrochemical

The biosensors of interest to this particular research are electrical impedance sensors. This type of sensor measures the change of electrical properties in a system due to the proximity or contact with an analyte or biomarker. The use of these biosensors has become widespread and they use a raw electrical signal such as current or impedance that can be directly processed and analysed by the user. In the area of cancer diagnostics a significant number of tests have been developed that incorporate biosensors for the rapid detection of cancer cells or biomarkers [6]. Biomarkers are defined as a biological molecule found in blood, other body fluids, or tissues that are a sign of a normal or abnormal process or of a condition or disease. They are a potentially valuable tool in a number of areas including the early detection of cancer, pre-treatment staging, determining response to chemotherapy treatment and monitoring disease progression. The most commonly assessed biomarkers in cancer are outlined in Table 1.1:

Table 1.1: Selection of the most common cancer biomarkers for 8 common cancer types. AFP – Alpha-fetoprotein; BRCA – Breast Cancer; CA – Cancer Antigen; CASA – Cancer-associated Serum Antigen; CEA – Carcinoembryonic Antigen; EGF – Epidermal Growth Factor; ER/PR – Oestrogen/Progesterone Receptor; HCG – Human Chorionic Gonadotrophin; HCG – Human Chorionic Gonadotropin; HER2 – Human Epidermal Growth Factor Receptor 2; ING-1 – Inhibitor of Growth Family, Member 1; NSE – Neuron Specific Enolase, NY-BR-1 – New York Breast 1; NY-ESO-1 – New York Oesophageal Squamous Cell Carcinoma 1; p53 – Tumour Protein 53; PSA – Prostate Specific Antigen; TAG – Tumour-associated glycoprotein 72. Table was redrawn from reference [7].

Type of Cancer	Biomarker
Breast	BRCA1, BRCA2, CA 15-3, CA 125, CA 27.29, CEA, NY-BR-1, ING-1, HER2, ER/PR
Colon	CEA, EGF, p53
Liver	AFP, CEA
Lung	CEA, CA 19-9, NSE, NY-ESO-1
Melanoma	Tyrosinase, NY-ESO-1
Ovarian	CA 125, HCG, p53, CEA, CA 549, CASA, CA 19-9, CA 15-3, TAG72
Prostate	PSA

Impedance based biosensors can be used to monitor cell morphology, detect antibodies, deoxyribonucleic acid (DNA) analysis and growth and motility in tissue culture environments which is known as electric cell-substrate impedance sensing (ECIS) [8]. In this technique, cells are cultured on

electrodes immersed in the tissue culture medium. The cells attach to and spread across the electrode surface. An alternating current (AC) at a specified frequency is applied between the working and reference electrodes and the change impedance measured. Since the current is constant, the measured magnitude and phase responses are assumed to be proportional to the impedance [8]. At relatively low frequencies (<100 Hz), resistive behaviour is predominant, while at higher frequencies (>100 KHz) capacitive effects are more dominant. The impedance of the circuit is substantially increased by the presence of cells at moderate frequencies [9].

1.5 Cancer

Cancer is defined as abnormal and uncontrolled cell growth due to an accumulation of specific genetic and epigenetic defects which are environmental in origin. Unregulated cell growth leads to the formation of a tumour mass that over time becomes independent of normal homeostatic checks and balances. Tumour cells, in essence, become resistant to programmed cell death, which is known as apoptosis, and other antigrowth defences within the body. As the cancer progresses, the tumour begins to spread beyond the site of origin and metastasize to other body organs and systems [7]. Cancer is a leading cause of death worldwide, accounting for 8.2 million deaths annually, representing 14% of all deaths [10, 11]. There are over 200 distinct forms of cancer including lung, prostate, breast, ovarian, hematologic, skin, colon, and leukaemia. The most common cancer subtypes diagnosed in men and women in the United States of America (USA) each year are outlined in Table 1.2 [12].

Table 1.2: The top 5 most common cancers in men and women diagnosed in the USA in 2014. Reference [12].

Rank	Cancer in Men	Cancer in Women
1	Prostate	Breast
2	Lung and Bronchus	Lung and Bronchus
3	Colon and Rectum	Colon and Rectum
4	Urinary Bladder	Uterine Corpus
5	Melanoma of the Skin	Thyroid

In 2000, Ireland introduced a national breast cancer screening service, BreastCheck. The National Breast Screening Programme, aimed to reduce the number of deaths from breast cancer in Ireland amongst women aged 50-64. By providing an effective screening service of the highest possible quality, a significant number of breast cancers can be detected at an earlier stage. Following a phased roll-out of mammography-centred screening, the numbers of women screened grew from 45,000 in 2000 to over 140,000 in 2014 [13, 14]. Mammography-based breast cancer detection has a number of limitations which provide an imperative to improve both the technology and the screening process.

In the past two decades a significant amount of clinical research has been conducted in which electrical impedance was used to differentiate between healthy and cancerous tissues including cancers of the breast [15, 16], prostate [17, 18], bladder [19-21], kidney [22, 23], brain [24-26], lung [27, 28], liver [29], stomach [30], and tongue [31, 32]. The next four sections of this chapter will focus on the detection of breast and prostate cancer which are the two most commonly occurring malignancies in women and men respectively [11].

1.6 Breast Cancer

Breast cancer is the most common carcinoma diagnosed in women worldwide [12]. It is a genetically and histologically heterogeneous disease that can be categorised into many different subtypes. The most broad distinction is between in situ and invasive carcinomas with both containing many more subtypes. In situ cancer refers to a cancerous growth or tumour which is still confined to the site from which it started, and has not spread to surrounding tissue or other organs in the body. The classification contains both ductal (DCIS) and lobular subgroups [33]. The term invasive is described as any cancerous growth which has infiltrated beyond its site of origin to the surrounding healthy tissue. The major invasive breast tumour types include invasive ductal carcinoma (IDC) and invasive lobular carcinoma (ILC) along with other less common subtypes including mucinous and tubular [33] (Figure 1.2).

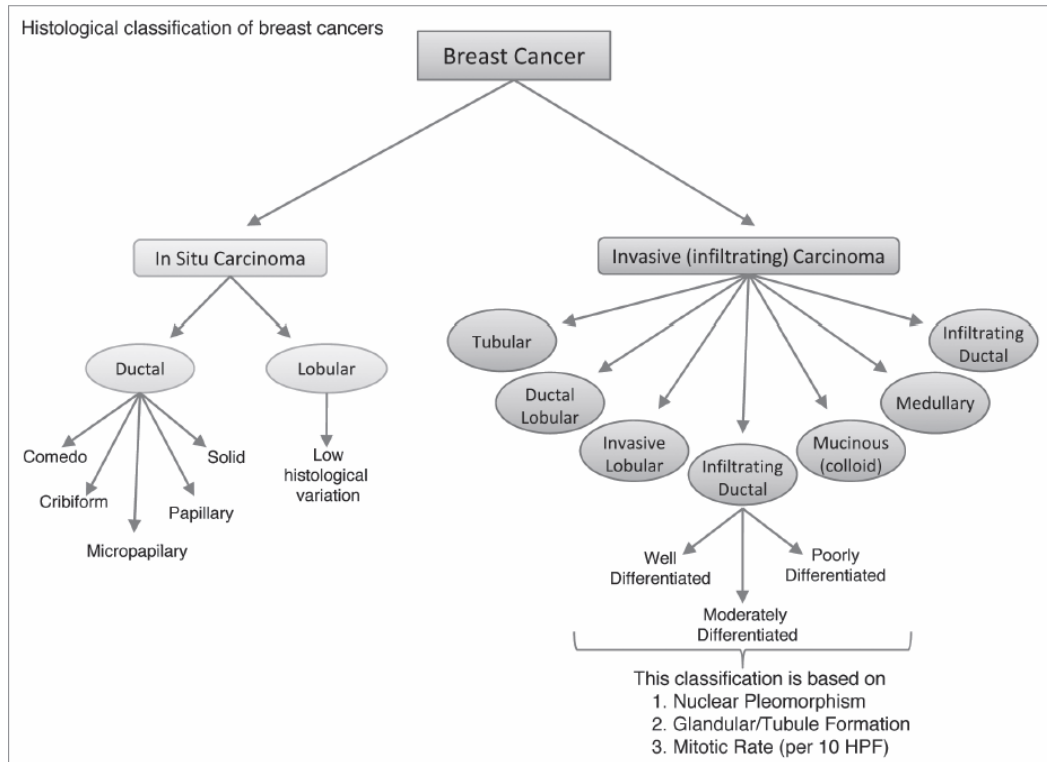


Figure 1.2: The histological classification of breast cancer subtypes. HPF – High Powered Field. Reference [33].

The most common form of breast cancer is IDC accounting for almost 80% of all breast cancers [34]. This type of cancer develops initially as an abnormal replication of cells which make up the single cell layer of the milk ducts. These structures are responsible for transporting milk from the milk-producing lobules to the nipple during lactation (Figure 1.3).

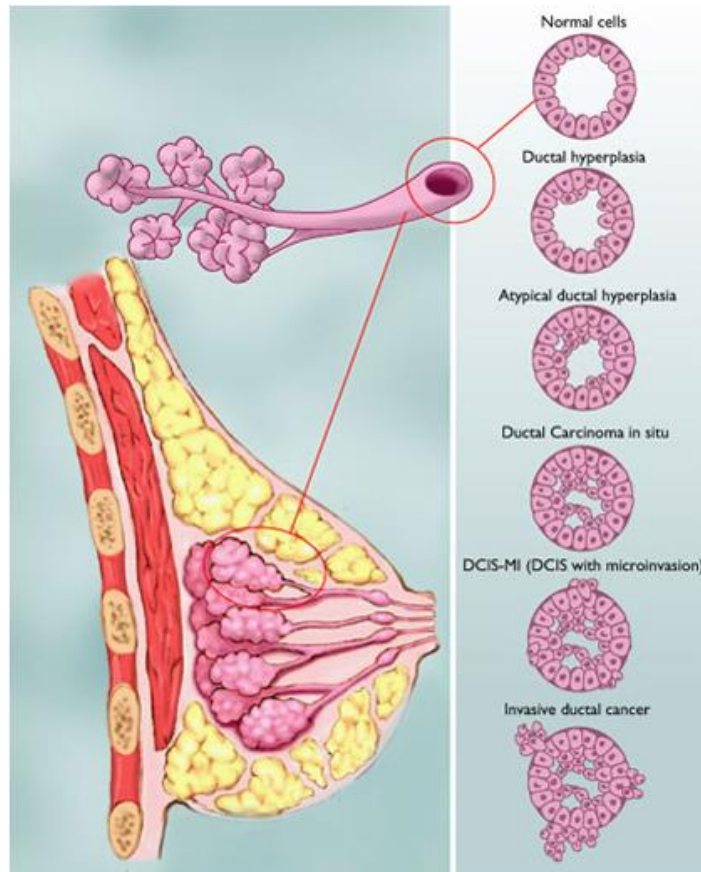


Figure 1.3: Left: The anatomical structure of the breast and chest wall. Right: The steps along the way towards the development of invasive ductal carcinoma. Reference [34].

The healthy lactiferous or milk duct is composed of a single layer of columnar epithelial cells surrounded by an intact basement membrane [35]. Atypical ductal hyperplasia results from the cellular proliferation and architectural abnormalities within one or more of the milk ducts. As the replication of cells within the milk ducts continues the pre-cancerous condition of DCIS develops (Section 1.6.1). Once the abnormally replicating cells infiltrate beyond the basement membrane IDC begins to develop. These tumours excite a pronounced fibroblastic stromal reaction to the invading tumour cells resulting in a palpable mass (normally larger than 1.5 cm in diameter) with a hard consistency being produced. The tumours show an infiltrative attachment to the surrounding structures and may cause dimpling of the skin (due to traction on suspensory ligaments) or nipple retraction. The cut surface of the tumour appears gritty and shows irregular margins with stellate infiltration and foci of yellow, chalky streaks. Histologically, the tumour cells are larger in diameter than normal epithelium, and can assume a variety of

patterns such as glandular formation, cords of cells, broad sheets of cells or a mixture of all these, usually within a dense stroma. The tumours range from well differentiated, in which there is glandular formation, to poorly differentiated, containing solid sheets of pleomorphic neoplastic cells [36].

Breast cancer staging is extremely important in the decision making of the clinician when deciding on patient treatments. The classification system most commonly used is the American Joint Committee on Cancer (AJCC) Tumour, Node and Metastasis (TNM) system. It is used to determine the size of the primary tumour (T), involvement of the lymph nodes (N) and the presence of metastasis (M). The system uses a combination of these three categories to grade and stage each tumour in the following way:

- 1) The letter T followed by a number from 0 to 4 describes the size of the tumour and if it has spread to the skin or to the chest wall under the breast. Higher T numbers mean a larger tumour and/or wider spread to tissues near the breast [37].
- 2) The letter N followed by a number from 0 to 3 indicates lymph node involvement. The number of lymph nodes involved is important in prognosis [37].
- 3) The letter M followed by a 0 or 1 indicates whether the cancer has spread to distant organs [37].

In addition to this gross classification of breast cancer tumours it is also necessary to perform genetic analysis of the cells to determine the presence of cell surface receptors which are important in determining the treatment a patient receives. This has led to the inclusion of molecular markers in the classification of cancer subtypes. These include oestrogen receptor (ER), progesterone receptor (PR), ErbB2 (Her2/neu) and p53 which has resulted in six specific groups being identified: basal-like, ErbB2+, normal breast like, Claudin-low, luminal A and luminal B [33, 38, 39] (Figure 1.4).

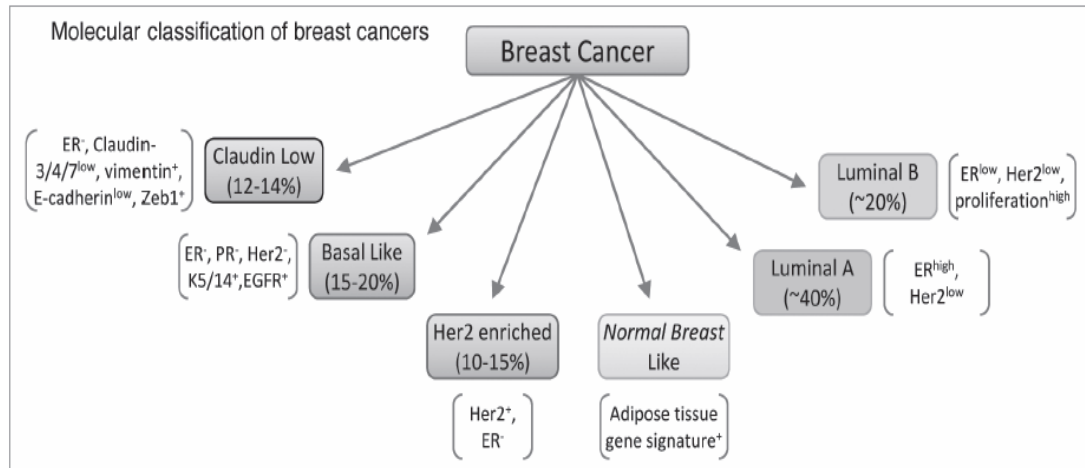


Figure 1.4: The molecular classification of breast cancers based on the intrinsic molecular subtypes of breast cancer identified by micro-array analysis. Reference [33].

The identification of cell surface receptors can significantly influence the course of treatment undertaken by the patient. The two most commonly identified receptors are Her-2 and ER. If these receptors are identified on the cell surface then the drugs Herceptin and Tamoxifen can be administered respectively. The use of these targeted therapies has been shown to significantly improve the overall patient outcome [40, 41].

1.6.1 Ductal Carcinoma in situ

Ductal carcinoma in situ is a disease which is characterised, histologically, by the proliferation of malignant-appearing cells which are located in the milk ducts of the breast. These cells have not invaded beyond the basement membrane into the normal breast parenchyma [42, 43]. The condition covers a broad spectrum from low-grade to high-grade DCIS and it can be associated with micro-invasion [43]. Micro-invasion is a term used to describe a borderline difference between completely contained DCIS and a minimally invasive ductal carcinoma. It can also be sub-divided into five recognised categories based on architectural features of the tumour which gives rise to: Comedo, Cribriform, Micro-papillary, Papillary and Solid [33]. It is estimated that DCIS accounts for between 10-20% of all breast malignancies detected by screening [44-46]. In 2009, the American Cancer Society predicted that over 62,280 new cases of breast carcinoma in situ would be diagnosed annually in the USA [47]. By 2014 this figure had

increased fractionally to 64,640 [12, 48], demonstrating that the detection rate remained constant following a rapid increase in cases during to 1980s and 1990s [43, 49]. DCIS is usually detected using high-resolution mammography which allows visualisation of the intra-ductal micro-calcifications that may be suggestive of DCIS [50]. It is a direct precursor to IDC, although the condition itself is not life-threatening. The exact time-frame over which DCIS may progress to invasive cancer is unclear. It has a 10-year survival rate of >95% with treatment [42]. The treatment options for a patient with biopsy-confirmed DCIS are similar to that of a patient with IDC although chemotherapy is not required. The primary treatment for localised DCIS is breast conservation surgery followed by radiation therapy. For more widespread DCIS, the definitive treatment is complete mastectomy with or without reconstructive surgery [42].

1.6.2 Breast Cancer Detection

It is estimated that breast cancer results in 40,000 deaths (39,210 women, 410 men) annually in the USA [12]. The method by which breast cancer is detected can occur as follows:

1. Physical Examination for a palpable mass
 - a) Patient
 - b) Physician
2. Imaging
 - a) Mammography
 - b) Ultrasound
3. Biopsy
 - a) Surgical
 - b) Fine-needle Aspiration
 - c) Core-needle Biopsy
4. Histologic confirmation

If a patient has a suspected tumour on a mammographic image they will undergo a surgical, fine-needle aspiration or more commonly a core-needle biopsy (CNB). This extracts a representative sample of tissue from the breast and is usually performed under ultra-sound guidance to aid with needle placement to ensure correct sampling of the target lesion. These samples

are then processed in the histology laboratory and examined histologically by a pathologist to confirm the presence of malignant tumour cells.

1.6.2.1 X-ray Mammography

Mammography has over time become the “gold standard” target population screening tool for early breast cancer detection. The technique uses low-levels of ionizing radiation to generate an image of the breast which aids in the detection of cancerous masses or characteristic micro-calcifications suggestive of DCIS. The introduction of mammography has been proven to detect breast cancer at an early stage and, when followed up with appropriate diagnosis and treatment, to reduce mortality from breast cancer [51]. The average size at which breast cancer tumours can be detected with mammographic screening is 7.5 mm compared to 15 mm without screening [52]. Prior to the introduction of a national breast screening programme in Ireland (1994-1999) the 5-year survival rate for women with breast cancer was 74.3%. Women who were diagnosed between 2006 and 2011 had a five-year survival rate of 84.7% [53]. This increase in patient survival cannot entirely be attributed to the introduction of the mammographic screening programme. However, the ability to detect breast cancers at an earlier stage, allows a patient to undergo treatment as soon as possible which increases the likelihood of survival.

1.6.2.2 Limitations of Mammography

Mammography does however have some significant limitations including, relatively low sensitivity and specificity (79% and 90% respectively) which are both significantly reduced in young patients (less than 40 years old) due to the increased breast density [54-56]. There are two major problems surrounding mammographic screening. The first of these is radiologically occult disease. This manifests as breast cancer tumours which cannot be detected using mammography. The second significant issue is the interpretation of mammography results which requires highly trained, specialist radiologists to systematically review each individual mammogram. Misinterpretation of mammography results can alter either the sensitivity

(disease is present but not detected) or the specificity (disease is absent but interpreted as being present) of the screening test.

A comprehensive review of clinical trial data relating to screening programmes for breast cancer detection determined significant increases in the rates of over-diagnosis and over-treatment of up to 30%. In reality this figure is hard to quantify and is probably much lower than 30%. A number of drawbacks are associated with breast cancer screening including an increase in psychological distress which can include anxiety, worry, despondency and sleeping problems [57-60]. The report also suggested that the number of mastectomies can increase by up to 20% as a result of screening programs [58]. A recent independent review conducted by a panel in the United Kingdom noted that there were significant methodological limitations to the Cochrane Review and that the true rate of over-diagnosis is likely to be closer to 11% for women invited to attend a screening programme and approximately 19% for those who actually attend a screening [61]. In a study by Berg *et al.* (2004), the team assessed the specificity and sensitivity of a number of cancer detection modalities individually and in combinations. They determined, using 258 proven lesions, that mammography on its own had a sensitivity of 67%, specificity of 75% and a positive predictive value of 85.7% [55]. They then determined the effectiveness of mammography by breast tissue composition (extremely dense, heterogeneously dense, minimal scattered fibro-glandular densities and predominantly fatty). As before 258 histologically proven lesions were used of which mammography was only able to detect 45% (21/47) in extremely dense tissue compared with 100% (8/8) in predominantly fatty breasts [55]. A limitation of this study was that only a small number of patients were analysed.

The current imaging modalities used to further evaluate mammographically suspicious lesions are magnetic resonance imaging (MRI) [56, 62], and ultrasound (US) [62]. Computed tomography (CT) and positron emission tomography (PET) [62] are not routinely used in clinical practice for evaluation of breast lumps or abnormal mammographic findings. The major limitation of these technologies is the significant cost of both the hardware

and the procedures. PET/CT scanning, as with mammogram, uses low doses of ionising radiation during the procedure which is a potential limiting factor for its use in cancer patients. It is primarily used in the detection of metastatic diseases [62]. MRI on the other hand does not use any radiation and instead utilises an intravascular injection of a contrast agent such as gadolinium diethylene tri-amine penta-acetic acid (GdDTPA) [63, 64] but MRI has limitations with its cost, potential adverse reactions and nephrotoxicity to contrast media and an unacceptably high false positive rate [65].

1.7 Prostate Cancer Detection

Prostate cancer in men has many similarities to breast cancer in women in terms of number of new cases per year, gender affected and confirmation of cancer type. The American Cancer Society estimates that 233,000 and 232,670 new cases of prostate and female breast cancer respectively will be diagnosed in the USA in 2014 [12]. This shows that the incidence rate for these two cancers is almost identical. Approximately 99% of all breast cancer occurs in women while 100% of prostate cancer occurs in men. The current method of detecting prostatic malignancy is a histological examination of core-needle tissue samples removed during a trans-rectal biopsy. This method of using CNB to extract tissues for histological analysis is the same as that used to determine the presence of breast cancer. Prior to the CNB procedure a patient will likely have had a combination of a digital rectal examination (DRE), a prostate specific antigen (PSA) test showing elevated levels and a trans-rectal US [66]. There are a number of concerns surrounding the ability of both DRE and PSA tests to accurately predict the presence of prostate cancer in patients [67-69]. The use of DRE is limited due to the inability to palpate the entire prostate gland and is not sufficient in the detection of cancers which have not progressed to the prostatic capsule [69]. These deficits are compounded by a low sensitivity (53.2%) and specificity (83.6%) of the test when used in isolation [68]. PSA testing was first developed by Kuriyama *et al.* in 1980 [70] and has since become one of the major tools used in the assessment of prostate cancer. An abnormal test occurs when a serum PSA level of ≥ 4.1 ng/ml, however studies have shown

that individuals can present with elevated PSA levels but subsequent biopsy revealed no identifiable cancerous lesion [71, 72]. This is due to a naturally higher baseline level of PSA. One of the major downsides of PSA usage is the lack of sensitivity which has been calculated as part of a recent meta-analysis to be 72.10% with a specificity of 93.10% [67]. The random sampling of the prostate during the procedure may result in a tumour being missed and the patient receiving an incorrect diagnosis. The authors of that review illustrate a number of potential limitations to the clinical trials on which the analysis was based citing a lack of a control group receiving no screening or treatment and a lack of biopsy results for all of the involved patients. As a result, they state that the figures for sensitivity and specificity are potentially biased due to the aggressiveness of the biopsy procedure and variations in PSA determination and DRE findings [67]. Another significant downside to the use of PSA testing for the determination of prostate cancer is the overlap with benign prostate hyperplasia. It has been shown that between 21-47% of patients with a pathologically confirmed benign condition have serum levels above the cut-off of ≥ 4 ng/ml, while as many as 48% of men with prostate cancer have antigen concentrations below the 4 ng/ml threshold [67]. A number of novel electrical impedance devices have focused on prostate cancer detection and are outlined in later sections.

1.8 Unmet user needs

Current CNB needles are passive devices that provide no objective feedback as to the needle tip location during advancement or at the time of biopsy which is where the requirement for ultra-sound guidance arises. There is an unmet user need with regard to the identification of the tissue type into which the tip of a biopsy needle and a wire-localisation device are inserted. This potential, combined with the ability to distinguish between healthy and cancerous tissues in real-time would greatly improve the biopsy procedure and sample acquisition. It may also avoid the need for a formal biopsy of benign lesions which account for almost 95% of lesions that develop within the breast [73]. Current research in this area needs to involve clinicians who can identify a technological deficit in their field and can guide the research

necessary to test a prototype medical device in a clinical setting. This is an area that appears to be ideally suited to the use of electrical bio-impedance.

1.9 Electrical Impedance

The flow of direct current through an electrical circuit is impeded only by the resistance presented by the circuit. In systems utilizing alternating current, which is a sinusoidal signal, the opposition to a current is the impedance, which takes into account both the magnitude of the opposition to the applied current and the phase shifts between the current and voltage caused by the components of the circuit [74, 75]. Electrical impedance (Z), measured in Ohms (Ω), is the total opposition to current flow in an alternating circuit and is defined in terms of three individual components: resistance (R), inductance (L) and capacitance (C). The angular frequency of the current is represented by ω , and j is the square root of (-1) [22, 74, 76]. Impedance may be expressed as a complex number (Equation 1.1).

$$Z = R + j(\omega L - 1/\omega C)$$

Equation 1.1: Equation for the determination of electrical impedance (Z). R – resistance, j – square root of -1 , ω – angular frequency, L – inductance and C – capacitance.

Resistance is a property that opposes current flow and conductance is the inverse of resistance. Capacitance is the opposition of a change in voltage or electrical potential across an object and acts to store energy. A capacitor consists of two conductors; each oppositely charged and separated by a dielectric material. Permittivity is a property of the dielectric material and reflects the ability of charges in the material to move in response to an electric field [77]. Capacitance is a function of the permittivity and the physical geometry of the object. The capacitance formula for a two-plate capacitor is:

$$C = \epsilon A/d$$

Equation 1.2: Formula for the calculation of value of a two plate capacitor. C – capacitance, ϵ – permittivity, A – area of each plate, d – distance between plates. Reference [77].

The modulus of the impedance, $|Z|$, is the ratio of the magnitudes of the voltage and current (V/I). For the purpose of this thesis only the modulus of the impedance will be investigated as the study is only interested in

assessing the difference in the resistive element of impedance to provide a relative measurement capable of differentiating between biological tissue types.

The measurement of electrical impedance has been investigated for breast analysis since the early 20th century when Fricke and Morse first described altered capacitance values of breast cancer tissue compared to normal breast tissue in 1926 [78]. In the last two decades the utility of impedance in discrimination between biological samples has been extensively investigated. The term bio-impedance is used to describe the response of a living organism to an externally applied electric current, and is a measure of the opposition to the flow of that electric current through tissues [31, 74]. Each cell type in the human body is composed of different chemical and physical elements which result in the production of distinctive impedance signals generated by each variant [79, 80]. This is also true of diseased, cancerous tissues which have been shown to have a lower impedance value when compared to healthy cells of the same type [15, 18, 79]. Most benign lesions have been shown to exhibit impedance similar to healthy tissues. This finding could provide a potential method of differentiating between benign and cancerous lesions during screening of breast cancer patients [81-83].

The differential electrical properties associated with cancerous tissues result from increased cellular water and salt content, amount of extracellular fluid, altered membrane permeability, changed packing density and orientation of cells [84-87]. Tissues within the human body provide two forms of resistance to an applied electrical current. Capacitive R (reactance) results from the lipid bilayer cell membrane while resistive R is due to the extra- and intracellular fluid present in the tissue of interest [88]. A number of equivalent circuit models of biological tissues have been proposed to explain this behaviour. The most commonly used simple equivalent circuit arranges intracellular fluid R (R_i) and cell membrane capacitance (C_m) in series with extracellular fluid R (R_e) in parallel in an R(RC) circuit (Figure 1.5) [79, 88].

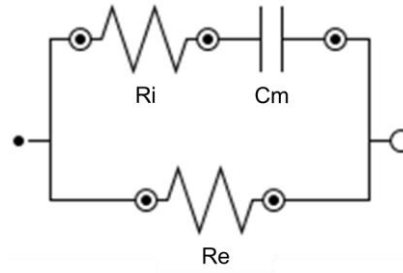


Figure 1.5: A simple equivalent circuit model of biological tissues. R_i – intracellular resistance, C_m – cell membrane capacitance, R_e – extracellular resistance. Figure is Author's own.

Another equivalent circuit model of cell and tissue behaviour can be described as an $(([C_R)(C_R)](C_R))$ circuit (Figure 1.6). In this system both the resistance and capacitance of the extracellular fluid, intracellular fluid and the cell membrane are taken into account [79].

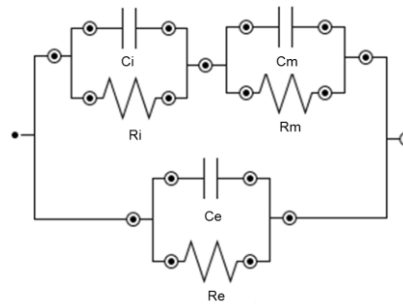


Figure 1.6: An equivalent circuit model of biological cell behaviour. R_i – intracellular resistance, R_e – extracellular resistance, R_m – cell membrane resistance, C_i – intracellular capacitance, C_e – extracellular capacitance, C_m – cell membrane capacitance. Figure is Author's own.

At zero (to low) frequency, the applied current does not penetrate the cell membrane, which acts as an insulator, and as a result the current is transferred exclusively across the extracellular fluid. At very high frequencies the cell membrane is charged as a near perfect capacitor which results in the dielectric properties of the tissue resulting from the combined impedance of the extra- and intracellular fluid [80, 88]. The electrical properties of tissues vary according to applied frequency as seen from α -, β - and γ -dispersion [84, 89, 90]. α - (10 Hertz [Hz] – 10 kHz) and β -dispersions (10 kHz – 10 MHz) are of relevance to medical applications as the changes between pathological and normal tissue typically occur in these ranges [84, 91]. The α -dispersions

are associated with electrical double-layers and surface ionic conduction effects at the membrane boundaries [89]. The β -dispersion results from a combination of the capacitive shorting-out of membrane resistance and rotational relaxations of bio-macromolecules [89]. The γ -dispersion arises from the relaxation of bulk water in the tissue [89].

There are two branches of electrical impedance measurement which have evolved gradually in the last number of years: electrical impedance tomography (EIT) and invasive impedance detection.

1.10 Electrical Impedance Tomography

1.10.1 TransScan TS 2000

Electrical impedance tomography is an imaging modality that estimates the electrical properties of an object from measurements made on its surface [92]. The technique has been investigated for the detection of breast cancer. The difference between the electrical storage potential of normal and pathologically altered tissues allows an image of conductance and permittivity to be produced from measurements on the skin surface [93]. A number of devices have been developed to test the effectiveness of skin surface impedance recordings at visualising a cancerous growth in breast tissue. In 1999, the Food and Drug Administration approved the use of the TransScan TS 2000 (Siemens Medical, Germany and TransScan, Ramsey, NJ, USA) as an adjunct to mammographically equivalent patients to aid biopsy recommendation [94]. This system utilised a reference electrode placed in the patients hand and an 8 x 8 electrode array contained on a hand-held probe that would be placed firmly against the breast to ensure adequate skin-electrode contact. Although the initial product introduced by TransScan Medical Inc. was granted approval, a subsequent model TS 2000ED (Mirabel Medical Systems, Inc.) was rejected due to concerns relating to device sensitivity, the size and population of the study, number of cancers detected in study patients, and risks associated with additional screening events [95].

1.10.2 Mammography Electrical Impedance Device

Another EIT device, which was developed by the Institute of Radio Engineering and Electronics in Russia, was designed using a 256-electrode array and a hand-held external reference electrode (Figure 1.7). One electrode is used to administer a 0.5 mA current at 50 kHz frequency which is detected across the skin surface by the other electrodes present on the device.

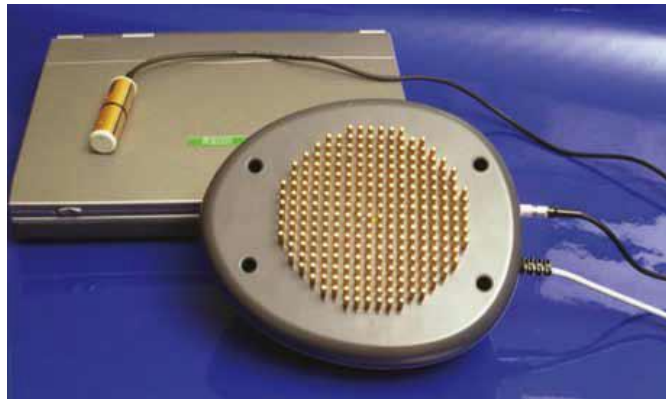


Figure 1.7: The electrical impedance mammography device with the 256-electrode design. Reference [93].

This generates a grey-scale image in which areas of hyper- and hypo-impedance can be distinguished. In 2001, Cherepenin *et al.* (2001) conducted an initial clinical trial of the mammography electrical impedance (MEIK) device which involved 21 women with tumours, between 1.5 and 5 cm on x-ray mammogram. The imaging scans revealed 14 focal abnormalities across the 21 patients studied which accounted for 67% of the total tumours. When the team combined these results with 4 images without clear abnormalities, they were able to fully or partially diagnose 86% of confirmed lesions in the study [96]. The researchers describe a number of limitations to the technology including a decrease in scanning area associated with increased measurement depth. Poor image resolution at the corners of the recording device was due to poor contact between the skin and the electrodes [96]. A further study conducted using the MEIK system was conducted by Prasad *et al.* (2008), in which the team examined a group of 88 patients with a range of breast abnormalities. These included fibrocystic disease, mastitis, cysts, fibroadenoma and carcinoma which were

assessed using mammography, ultra-sound and EIT. Of the 88 patients, 59 were determined to have a suspicious finding using at least one of the imaging techniques. Across each of the detectable lesions EIT fared best only for the detection of cysts where it correctly identified 21/21 (100% specificity) [97]. However, this was matched by ultra-sound which also detected all of the lesions successfully, whereas mammography could only determine 17 of the 21 cases (81%) [97]. For each of the remaining categories being investigated EIT showed a lower sensitivity than either mammography or ultra-sound. For the detection of carcinoma, the sensitivities were determined to be 100% for mammography and ultra-sound but only 75% for EIT [97]. The team noted that further investigation involving larger numbers of patients would be required to more accurately determine the specificity and sensitivity of the MEIK device and its potential use as an adjunct to the currently available diagnostic techniques.

In a study by Raneta *et al.* (2012) the team used the device to test a population of 808 randomly selected patients (aged 18-94; mean 54 years) who presented with abnormalities which had previously been detected by mammography and/or sonography [93]. The group determined the sensitivity and specificity of the device and compared it to mammography (657 patients) and ultrasonography (571 patients) [93]. When used to detect breast cancer the MEIK system had a reported sensitivity, specificity and negative predictive value (NPV) of 87%, 85% and 96% respectively [93]. When combined with traditional mammography these values increased to 96% and 99% for sensitivity and NPV; the specificity declined slightly to 79% [93]. The advantages of this technology include its non-invasive nature, zero exposure to ionizing radiation, along with it being portable and relatively inexpensive. However, some disadvantages include a limited depth of field and low spatial resolution.

1.10.3 Dartmouth Ag/AgCl Device

One of the major research groups in the area of electrical impedance spectroscopy (EIS) comes from Dartmouth University where the team have been investigating devices for the detection of breast cancer for a number of

years. Their initial clinical trial was a study of 26 women who underwent both mammography and EIS to determine the presence of breast abnormalities. The device used in the experiment was a radially translatable circular array of 16 silver/silver chloride (Ag/AgCl) electrodes that were placed around the patient's breast while they lay in a prone position [98]. The team divided the patients into three groups based on their American College of Radiology (ACR) Breast Imaging-Reporting and Data System (BIRADS) score: ACR 1 (38 patients); ACR 2-5 (13 patients); and the six most serious lesions were classified as ACR 4-5. Each group was analysed using the EIS method described by the team and the sensitivity of the technique was calculated as 73%, 83% and 79% for ACR 1, 2-5 and 4-5 respectively [98]. The team also investigated a numerical identification method for determining the presence breast abnormalities but this resulted in sensitivity values lower than the visual interpretation of the EIS images. They did acknowledge that the numerical estimation was in its infancy and that significant improvement would be required to match the capability of the visual method [98].

A follow up study conducted by the Dartmouth team was conducted in 2008 in which the group tested a newly designed EIT device which contained 64 Ag/AgCl electrodes in a circular arrangement of 16 electrodes across 4 layers. This allowed the electrodes to adjust to the size of each patient's breasts while maintaining maximum electrode contact on the patient's skin [99]. The clinical trial undertaken by the team involved the EIT imaging of 96 women in the Dartmouth-Hitchcock Medical Centre. The women were divided into 4 groups based on the composition of their breast tissue upon mammographic interpretation. The EIT based breast imaging system presented in this study provided a novel design concept for this type of device. The results of the clinical trial were mainly limited to system performance tests. The team reported the results of conductivity tests performed on areas of peripheral fatty tissue and centrally located fibroglandular tissue. In all cases analysed, the fatty tissue displayed a lower conductivity than that of the fibroglandular tissue [100].

Unfortunately, the use of EIS for breast cancer detection has disadvantages that outweigh the advantages. The images produced are not as effective as

the currently accepted imaging modalities of mammography and ultra-sound. For this reason there have been more recent efforts to develop invasive needle electrodes for the measurement of impedance values below the surface of the skin.

1.11 Invasive Breast Cancer Detection

One of the earliest investigations carried out using invasive bio-impedance measurement devices was conducted by Morimoto *et al.* (1993). They utilised a co-axial needle in conjunction with an external plate electrode to measure three parameters: R_e , R_i and C_m . The team investigated a total of 111 patients who were admitted to the University of Tokushima, Department of Surgery between April 1986 and September 1988. Fifty four of these were due to undergo resection of breast tumours and the remaining 57 scheduled for thoracotomy (which is an incision into the pleural space of the chest) [79]. In each patient, between 3 and 5 frequency sweep impedance recordings were conducted in three tissue types in the breast resection cases: fatty tissue, mammary tissue and breast tumour. The research group found that the R_e and R_i were not significantly different between areas of fibroadenoma and healthy tissue however there was a significant ($p=0.01$) difference between these two tissues and breast carcinoma [79]. Fatty tissue was shown to have the highest recorded R_e and R_i values as well as the lowest C_m value which were significantly different from cancerous tissues and fibroadenoma and normal tissue. The results of this very early trial highlighted a potential application for invasive measurement of bio-impedance in the determination of both benign and malignant breast conditions.

A follow-up study was conducted by Kinouchi *et al.* in 1998. The aim of the research was to show the speed at which *in vivo* impedance measurements of local tissues could be obtained using invasive needle electrodes. The team used a similar electrode set-up to the 1993 study with the addition of 3 extra needle electrodes, while retaining the surface plate reference electrode [16]. By utilising this configuration the team were able to obtain extremely fast impedance measurements from 0-200 kHz. The 0.5 mm outer diameter

of the needle electrode provided a minimally invasive tool for the measurement of electrical impedance values *in vivo* [16]. However the placement of four stainless electrodes in to the region of interest detracts significantly from this benefit. Therefore it is still necessary to reduce the total size of any invasive measurement device to maximise the benefit to the patient.

Another study conducted by Mäki *et al.* demonstrated a prototype biopsy instrument for use in tissues of different origin including breast. The device design built on the work of Mishra *et al.* (Section 1.12.2) to use a functional CNB needle and insulate the trocar and the cannula from each other in a novel geometry (Figure 1.8).

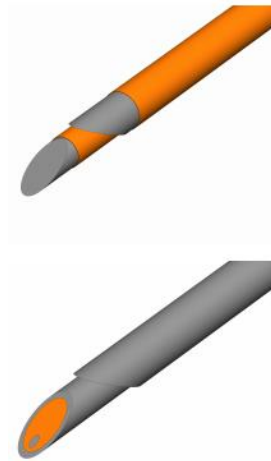


Figure 1.8: The two geometries used by Mäki *et al.* to design an electrical impedance biopsy needle. Reference [101].

By utilising their unique needle geometry the team were able to increase the total measurement sensitivity obtained from directly in front of the needle to 98.3% compared to 4.85% using the previously tested prototype [101]. This enabled more spatially accurate measurements, which were more representative of the originating sample. Using the prototype bioimpedance probe the team showed promising results in differentiating between adipose, muscle, liver and kidney tissues in an anesthetized piglet. The future development of this prototype device may provide a significant advancement in CNB sampling and accuracy.

A 2015 article by Kang et al. showed the most advanced research into invasive electrical impedance detection of breast cancer. The team describe a novel method of patterning gold electrodes on to a 27 gauge needle. They utilised a flexible parylene-C photolithography mask to allow deposition of interdigitated electrode (IDE) layouts on to the curved needle substrate (Figure 1.9) [102].

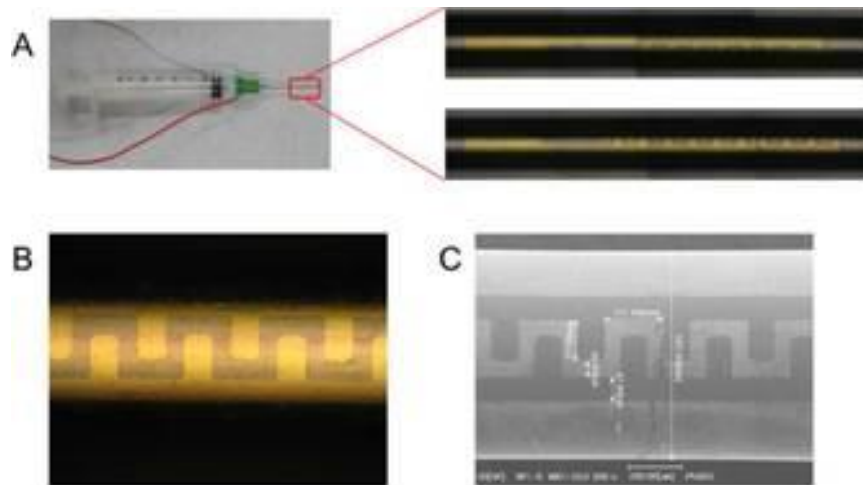


Figure 1.9: Images of the IDE electrodes on the curved surface of the needle; (A) IDE electrodes on the needle assembled with syringe (B) microscopic image for detailed view, and (C) SEM image showing the projected boundaries of the needle. Reference [102].

They outlined the initial electrical impedance measurements undertaken using the novel EIS-on-a-needle prototype. A range of phosphate-buffered saline (PBS) phantoms and slaughtered pork fat, muscle and skin samples were used to examine the ability of the probe to differentiate between solutions and tissues of varying conductivity [102]. The team showed a statistically significant difference ($p < 0.001$) between each of the pork tissues tested (muscle < fat < skin) across a frequency range of 1 MHz – 1 KHz. The final experiment outlined in the article involves the recording of electrical impedance measurements from *ex vivo* breast tissue samples containing cancerous lesions. The research team showed that a statistically significant difference existed between the normal and cancerous breast tissue measured using their prototype device. The data presented demonstrates that for both the resistance and reactance components of the measured impedance, the cancer tissue impedance was less than that of the normal tissue controls across most of the frequency range from 1 MHz to 1

kHz. The future development of this prototype device could be extremely promising given the novel deposition method employed in its assembly. By allowing the electrodes to be patterned directly on to a hypodermic needle it significantly increases the probes usability within a clinical setting.

1.12 Prostate Cancer Detection

1.12.1 Dual-needle

A number of research groups worldwide have investigated invasive probes for the detection of prostate cancer for use as an adjunct to current screening methods. The team of Lee *et al.* (1999) designed a minimally invasive technique for the localisation of prostate cancer. Two 30 mm long, 1 mm diameter stainless steel probes, coated with non-conducting epoxy were used. The distal 1 mm remained exposed/un-insulated for impedance recording and the probes were secured in an insulated fibreglass cylinder in parallel alignment with 1 mm separating the two (Figure 1.10) [17]. The recordings were then taken using a range of frequencies (100 kHz – 4 MHz), at a depth of 3 mm, across 16 locations in freshly excised prostate sections [17]. The injection sites were then stained for histologic examination by a pathologist to confirm the presence or absence of cancer at the point of injection [17]. The group showed that the observed impedance values of cancerous tissue was greater across all electrical current frequencies tested [17].

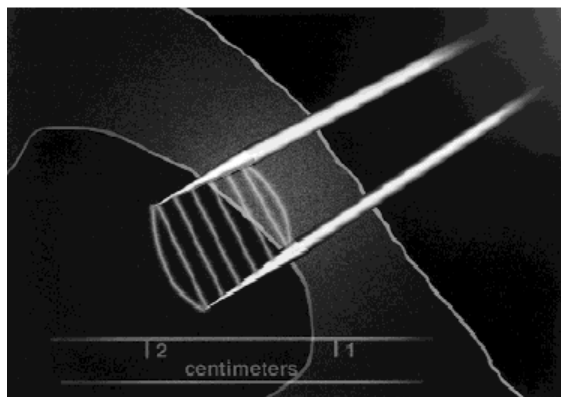


Figure 1.10: A bio-impedance needle probe constructed from two stainless steel needles, each 1 mm in diameter and tapered to a point. Reference [17].

1.12.2 Tip-exposure

This research group designed a standard stainless steel biopsy needle in which the component parts of the needle were electrically insulated from each other using polyimide. The tip of both the trocar and the cannula were not coated with polyimide and were therefore available for bipolar impedance measurement (Figure 1.11) [103].

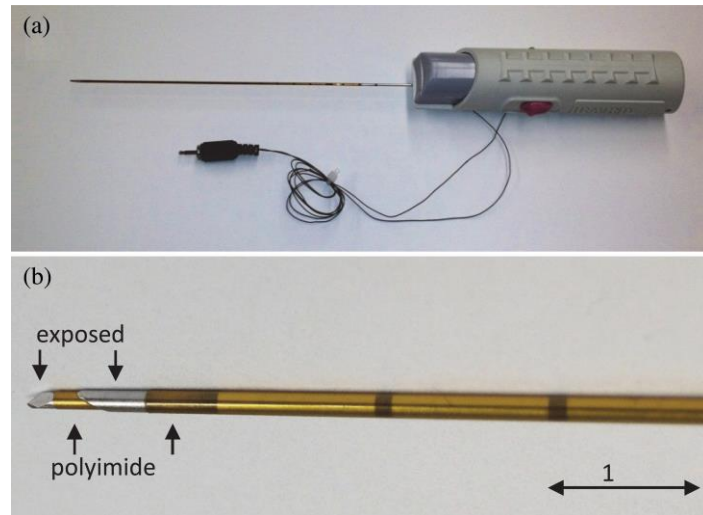


Figure 1.11: The EIS-Biopsy probe design (a), with polyimide insulation and the exposed tips (b). Reference [103].

This device was designed to induce a 1 mA current across the two electrically isolated components of the needle while concurrently measuring the voltage [103]. The research group simulated a standard 12-core biopsy procedure by suspending surgically removed prostate samples in a specially designed chamber filled with 0.01 S/m saline to mimic the conductivity of the pelvic cavity [103]. Results from this set of experiments suggested that the device was capable of distinguishing between cancerous and healthy tissues within *ex vivo* prostate samples. The team did stress that the *in vivo* application of such a device may be susceptible to a number of physiological parameters such as blood flow, cellular metabolism, higher temperatures and cellular hydration status [103]. In a set of follow-up experiments the team used their device to determine the optimal frequency at which to measure resistivity and reactivity in the *ex vivo* prostate samples being tested. They showed the specificity and sensitivity of their device was fairly modest at 75.4% and 71.4% respectively [18]. As with the previous study there were a

number of limitations associated with the experimental design which may have affected the outcome [18]. This device showed potential as a clinically useful device but has so far only been tested experimentally in a research setting.

1.13 Impedance in the Brain

The first evidence of micro-fabrication technologies being employed in the area of impedance detection was by a research group from the *Centro Nacional de Microelectrónica* (CNM-IMB) in Barcelona, Spain. This group developed and manufactured a novel device which utilises silicon and platinum for the needle and electrodes respectively [23]. These materials were chosen both for their structural and electrical properties but also because they are bio-compatible. There are two major benefits achieved by the reduction in both the electrode and device design. The first is that the device is minimally destructive to healthy tissue adjacent to the target lesion. The second is that the tissue-to-electrode ratio is increased which should result in more precise localised impedance measurements [23]. The original device produced by the team at CNM-IMB used a four electrode system arranged in a paired, linear formation along the length of the silicon shaft (Figure 1.12).

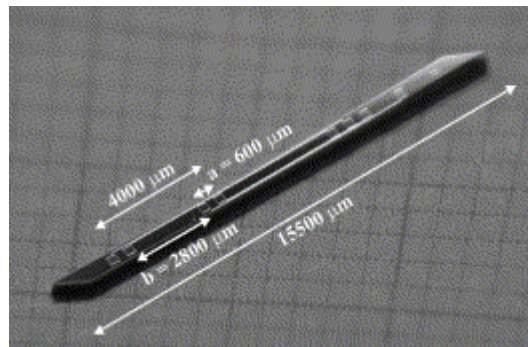


Figure 1.12: The probe design in which the platinum electrodes are placed at non-constant inter-electrode separation distances. Reference [23].

Further research at the institute led to the development of a variation of this design using a tapered ultra-fine micro-needle body. This was made using SU-8 photoresist and a precision machined tip which contained four micro-electrodes arranged in a diamond formation (Figure 1.13). The final

measurements of the device were provided in their 2010 paper (Table 1.3) [25].

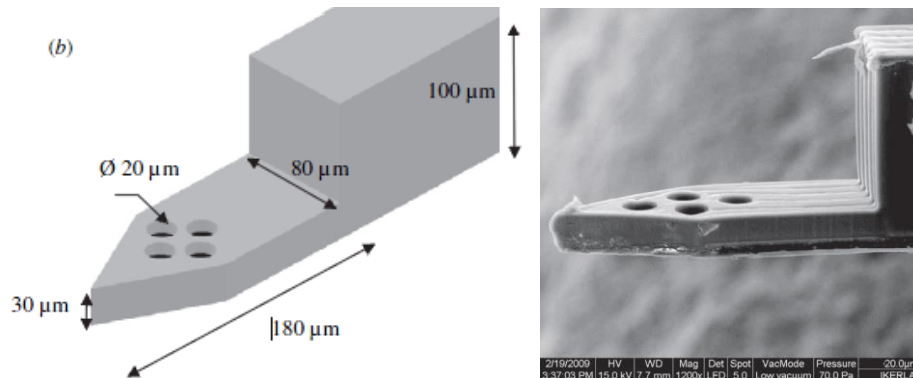


Figure 1.13: The design and dimensions of the micro-electrode tip and a scanning electron micrograph image of a SU-8 micro-needle tip. Reference [25].

The focus of this group's research was to design a probe for neural impedance measurement. However, the initial testing was conducted on ischaemic-kidney models in rats [23].

Table 1.3: The size of each aspect of the micro-needle probe. Reference [25].

Unit	Parameter	Measurement
Probe (Total)	Length	2-3 cm
	Thickness	100 μm
Connection Head	Width	3.8 mm
	Length	6.4 mm
Insertion Area	Width	80 μm
	Length	180 μm
	Thickness	30 μm

In the later studies by Altuna *et al.*, they tested the SU-8 micro-needles by injecting them into Cornu Ammonis 3 (CA3) hippocampal slices and obtaining impedance measurements. This group of researchers showed that it is possible to manufacture a functional impedance device that is both suitable for *in vivo* human and animal testing and also contains electrodes as small as 20 μm in diameter. They also concluded that in order to maximise

the functionality of these micro-needle probes obstacles needed to be overcome in regards to the fabrication process and signal recording [24, 25]. One of the major limitations of this proposed device for use in the detection of cancer would be that the materials chosen were designed to be flexible for use in neural applications to reduce serious damage to important structures within the brain. Most cancer detection would require a more robust device of sufficient length that would allow penetration into the deeper structures of the body and into the target lesion itself.

1.14 Device Solutions

The background research presented in the previous sections has shown that it is possible to utilise electrical impedance to differentiate between healthy and cancerous tissues in humans. It also provides the basis for the research presented in this thesis where it is hoped that a combination of semi-conductor and MEMS manufacturing processes and electrical impedance can be used to produce a novel biomedical device for the detection and screening of benign and cancerous breast lesions. The inclusion of gold microelectrodes on to a rigid substrate such as a CNB needle would allow the impedance device to be inserted directly in to the region of interest with minimal damage to the surrounding tissues. This would provide a real-time indication of probe advancement and tissue differentiation during a biopsy procedure for which no technology is currently approved for clinical use. This would provide a significant advancement to the current best practice of US-guided CNB for tissue extraction. It was envisioned that the novel probe device, developed as part of this Ph.D. project, would act as an adjunct technology to mammography screening which is currently utilised for breast cancer detection (Figure 1.14). This would potentially significantly improve the process of obtaining tissue for histological examination as well as removing the need for patients with benign breast lesions to undergo unnecessary procedures. The design of the proposed device was chosen to maximise the expertise within the Tyndall National Institute (TNI) in the fabrication, packaging and testing of prototypes using semi-conductor manufacturing techniques including photolithography, metal evaporation and

deposition. The electrochemical testing facilities and cell culture laboratories available in the Institute were also vital to the completion of this project.

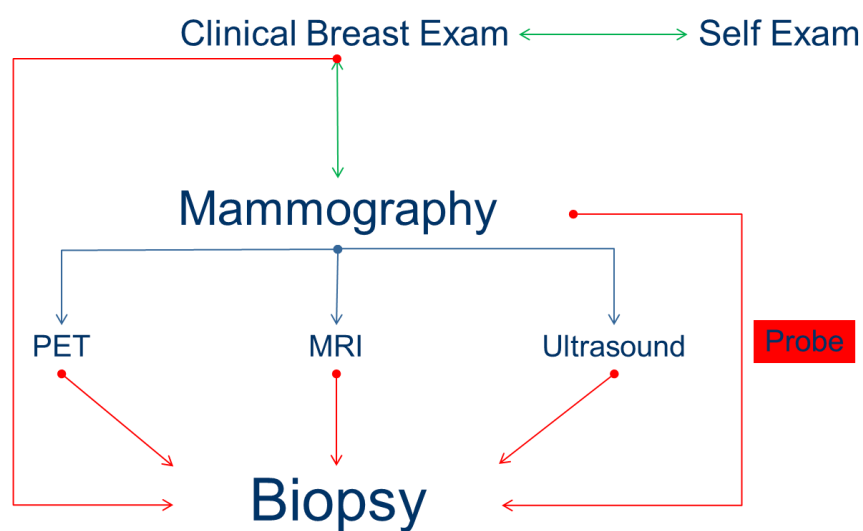


Figure 1.14: A schematic overview of the breast cancer detection pathway and the area in which the novel probe device fits within the pathway. Figure is Author's own.

1.15 References

1. De Bona, F. and E.T. Enikov, *Microsystems mechanical design*. Vol. 478. 2006: Springer Science & Business Media.
2. P&S Market Research, *Global Self-Monitoring Blood Glucose (SMBG) Devices Market is Expected to Grow With 6% CAGR During 2015 - 2022: P&S Market Research*. 2015: PR Newswire.
3. World Health Organization. *Country and regional data on diabetes*. 2015 [cited 2016 04 January]; Available from: http://www.who.int/diabetes/facts/world_figures/en/.
4. Turner, A.P., *Biosensors: sense and sensibility*. Chemical Society Reviews, 2013. **42**(8): p. 3184-3196.
5. Chan, M., D. Estève, J.-Y. Fourniols, C. Escriba, and E. Campo, *Smart wearable systems: Current status and future challenges*. Artificial Intelligence in Medicine, 2012. **56**(3): p. 137-156.
6. Wang, J., *Electrochemical biosensors: Towards point-of-care cancer diagnostics*. Biosensors and Bioelectronics, 2006. **21**(10): p. 1887-1892.
7. Bohunicky, B. and S.A. Mousa, *Biosensors: the new wave in cancer diagnosis*. Nanotechnology, Science and Applications, 2011. **4**: p. 1.
8. Mohanty, S.P. and E. Kougiannos, *Biosensors: a tutorial review*. Potentials, IEEE, 2006. **25**(2): p. 35-40.
9. Huang, X., D. Greve, D. Nguyen, and M. Domach. *Impedance based biosensor array for monitoring mammalian cell behavior*. in *Sensors, 2003. Proceedings of IEEE*. 2003. IEEE.
10. International Agency for Research on Cancer, *World Cancer Report 2014*, ed. B.W.S.C.P. Wild. 2014: International Agency for Research on Cancer. 630.
11. World Health Organization. *The top 10 causes of death Fact Sheet N°310*. 2014 May 2014 [cited 2014 08 September]; Available from: <http://www.who.int/mediacentre/factsheets/fs310/en/>.
12. American Cancer Society, *Cancer Facts & Figures 2014*. 2014, American Cancer Society, Inc.: Atlanta.
13. BreastCheck, *Annual Report 2000-2001*. 2002. p. 24.
14. BreastCheck, *BreastCheck Programme Report 2013/14*. 2015. p. 13.
15. Morimoto, T., Y. Kinouchi, T. Iritani, S. Kimura, Y. Konishi, N. Mitsuyama, K. Komaki, and Y. Monden, *Measurement of the electrical bio-impedance of breast tumors*. Eur Surg Res, 1990. **22**(2): p. 86-92.
16. Kinouchi, Y., T. Iritani, T. Morimoto, and S. Ohyama, *Fast in vivo measurements of local tissue impedances using needle electrodes*. Medical and Biological Engineering and Computing, 1997. **35**(5): p. 486-492.
17. Lee, B.R., W.W. Roberts, D.G. Smith, H.W. Ko, J.I. Epstein, K. Lecksell, and A.W. Partin, *Bioimpedance: novel use of a minimally invasive technique for cancer localization in the intact prostate*. Prostate, 1999. **39**(3): p. 213-8.
18. Mishra, V., A.R. Schned, A. Hartov, J.A. Heaney, J. Seigne, and R.J. Halter, *Electrical property sensing biopsy needle for prostate cancer detection*. Prostate, 2013. **73**(15): p. 1603-13.

19. Keshtkar, A., A. Mesbahi, P. Mehnati, and A. Keshtkar, *Surface fluids effects on the bladder tissue characterisation using electrical impedance spectroscopy*. Med Eng Phys, 2008. **30**(6): p. 693-9.
20. Keshtkar, A., Z. Salehnia, A. Keshtkar, and B. Shokouhi, *Bladder cancer detection using electrical impedance technique (tabriz mark 1)*. Patholog Res Int, 2012. **2012**: p. 470101.
21. Keshtkar, A., A. Keshtkar, and R.H. Smallwood, *Electrical impedance spectroscopy and the diagnosis of bladder pathology*. Physiological Measurement, 2006. **27**(7): p. 585.
22. Hernandez, D.J., V.A. Sinkov, W.W. Roberts, M.E. Allaf, A. Patriciu, T.W. Jarrett, L.R. Kavoussi, and D. Stoianovici, *Measurement of bio-impedance with a smart needle to confirm percutaneous kidney access*. J Urol, 2001. **166**(4): p. 1520-3.
23. Ivorra, A., R. Gomez, N. Noguera, R. Villa, A. Sola, L. Palacios, G. Hotter, and J. Aguilo, *Minimally invasive silicon probe for electrical impedance measurements in small animals*. Biosens Bioelectron, 2003. **19**(4): p. 391-9.
24. Altuna, A., E. Bellistri, E. Cid, P. Aivar, B. Gal, J. Berganzo, G. Gabriel, A. Guimera, R. Villa, L.J. Fernandez, and L. Menendez de la Prida, *SU-8 based microprobes for simultaneous neural depth recording and drug delivery in the brain*. Lab Chip, 2013. **13**(7): p. 1422-30.
25. Altuna, A., G. Gabriel, L.M.d.I. Prida, M. Tijero, A. Guimerá, J. Berganzo, R. Salido, R. Villa, and L.J. Fernández, *SU-8-based microneedles for in vitro neural applications*. Journal of Micromechanics and Microengineering, 2010. **20**(6): p. 064014.
26. Fernández, L.J., A. Altuna, M. Tijero, G. Gabriel, R. Villa, M.J. Rodríguez, M. Batlle, R. Vilares, J. Berganzo, and F.J. Blanco, *Study of functional viability of SU-8-based microneedles for neural applications*. Journal of Micromechanics and Microengineering, 2009. **19**(2): p. 025007.
27. Sanchez, B., G. Vandersteen, I. Martin, D. Castillo, A. Torrego, P.J. Riu, J. Schoukens, and R. Bragos, *In vivo electrical bioimpedance characterization of human lung tissue during the bronchoscopy procedure. A feasibility study*. Med Eng Phys, 2013. **35**(7): p. 949-57.
28. Kimura, S., T. Morimoto, T. Uyama, Y. Monden, Y. Kinouchi, and T. Iritani, *Application of electrical impedance analysis for diagnosis of a pulmonary mass*. Chest Journal, 1994. **105**(6): p. 1679-1682.
29. Laufer, S., A. Ivorra, V.E. Reuter, B. Rubinsky, and S.B. Solomon, *Electrical impedance characterization of normal and cancerous human hepatic tissue*. Physiol Meas, 2010. **31**(7): p. 995-1009.
30. Keshtkar, A., Z. Salehnia, M.H. Somi, and A.T. Eftekharsadat, *Some early results related to electrical impedance of normal and abnormal gastric tissue*. Phys Med, 2012. **28**(1): p. 19-24.
31. Ching, C.T., T.P. Sun, S.H. Huang, C.S. Hsiao, C.H. Chang, S.Y. Huang, Y.J. Chen, C.S. Cheng, H.L. Shieh, and C.Y. Chen, *A preliminary study of the use of bioimpedance in the screening of squamous tongue cancer*. Int J Nanomedicine, 2010. **5**: p. 213-20.
32. Sun, T.-P., C.T.-S. Ching, C.-S. Cheng, S.-H. Huang, Y.-J. Chen, C.-S. Hsiao, C.-H. Chang, S.-Y. Huang, H.-L. Shieh, W.-H. Liu, C.-M. Liu,

- and C.-Y. Chen, *The use of bioimpedance in the detection/screening of tongue cancer*. *Cancer Epidemiology*, 2010. **34**(2): p. 207-211.
33. Malhotra, G.K., X. Zhao, H. Band, and V. Band, *Histological, molecular and functional subtypes of breast cancers*. *Cancer Biol Ther*, 2010. **10**(10): p. 955-60.
 34. breastcancer.org. *IDC- Invasive Ductal Carcinoma*. 2015 [cited 2015 04 December]; Available from: <http://www.breastcancer.org/symptoms/types/idc>.
 35. Gray, H., *Gray's Anatomy: With original illustrations by Henry Carter*. 2009: Arcturus Publishing.
 36. University of Virginia. *VI. Malignant Neoplasms*. 2015 [cited 2015 04 Decmeber]; Available from: <https://www.med-ed.virginia.edu/courses/path/gyn/breast6.cfm>.
 37. Edge, S.B., D.R. Byrd, C.C. Compton, A.G. Fritz, F.L. Greene, and A. Trotti, *AJCC cancer staging manual*. Vol. 649. 2010: Springer New York.
 38. Perou, C.M., T. Sorlie, M.B. Eisen, M. van de Rijn, S.S. Jeffrey, C.A. Rees, J.R. Pollack, D.T. Ross, H. Johnsen, L.A. Akslen, O. Fluge, A. Pergamenschikov, C. Williams, S.X. Zhu, P.E. Lonning, A.L. Borresen-Dale, P.O. Brown, and D. Botstein, *Molecular portraits of human breast tumours*. *Nature*, 2000. **406**(6797): p. 747-52.
 39. Sorlie, T., C.M. Perou, R. Tibshirani, T. Aas, S. Geisler, H. Johnsen, T. Hastie, M.B. Eisen, M. van de Rijn, S.S. Jeffrey, T. Thorsen, H. Quist, J.C. Matese, P.O. Brown, D. Botstein, P.E. Lonning, and A.L. Borresen-Dale, *Gene expression patterns of breast carcinomas distinguish tumor subclasses with clinical implications*. *Proc Natl Acad Sci U S A*, 2001. **98**(19): p. 10869-74.
 40. Higgins, M.J. and J. Baselga, *Targeted therapies for breast cancer*. *The Journal of clinical investigation*, 2011. **121**(10): p. 3797.
 41. Rojo, F., J. Albanell, A. Rovira, J.M. Corominas, and F. Manzarbeitia. *Targeted therapies in breast cancer*. in *Seminars in diagnostic pathology*. 2008. Elsevier.
 42. Boughey, J.C., R.J. Gonzalez, E. Bonner, and H.M. Kuerer, *Current treatment and clinical trial developments for ductal carcinoma in situ of the breast*. *Oncologist*, 2007. **12**(11): p. 1276-87.
 43. Badruddoja, M., *Ductal carcinoma in situ of the breast: a surgical perspective*. *Int J Surg Oncol*, 2012. **2012**: p. 761364.
 44. Ernster, V.L., J. Barclay, K. Kerlikowske, H. Wilkie, and R. Ballard-Barbash, *Mortality among women with ductal carcinoma in situ of the breast in the population-based surveillance, epidemiology and end results program*. *Arch Intern Med*, 2000. **160**(7): p. 953-8.
 45. Lee, R.J., L.A. Vallow, S.A. McLaughlin, K.S. Tzou, S.L. Hines, and J.L. Peterson, *Ductal carcinoma in situ of the breast*. *Int J Surg Oncol*, 2012. **2012**: p. 123549.
 46. Kumar, A.S., V. Bhatia, and I.C. Henderson, *Overdiagnosis and overtreatment of breast cancer: rates of ductal carcinoma in situ: a US perspective*. *Breast Cancer Res*, 2005. **7**(6): p. 271-5.
 47. Jemal, A., R. Siegel, E. Ward, Y. Hao, J. Xu, and M.J. Thun, *Cancer statistics, 2009*. *CA Cancer J Clin*, 2009. **59**(4): p. 225-49.

48. American Cancer Society, *Breast Cancer Facts & Figures 2013-2014*. 2013, American Cancer Society, Inc.: Atlanta.
49. Li, C.I., J.R. Daling, and K.E. Malone, *Age-specific incidence rates of in situ breast carcinomas by histologic type, 1980 to 2001*. *Cancer Epidemiol Biomarkers Prev*, 2005. **14**(4): p. 1008-11.
50. Schulze-Garg, C., J. Lohler, A. Gocht, and W. Deppert, *A transgenic mouse model for the ductal carcinoma in situ (DCIS) of the mammary gland*. *Oncogene*, 2000. **19**(8): p. 1028-37.
51. Saslow, D., C. Boetes, W. Burke, S. Harms, M.O. Leach, C.D. Lehman, E. Morris, E. Pisano, M. Schnall, and S. Sener, *American Cancer Society guidelines for breast screening with MRI as an adjunct to mammography*. *CA: a cancer journal for clinicians*, 2007. **57**(2): p. 75-89.
52. Michaelson, J., S. Satija, R. Moore, G. Weber, E. Halpern, A. Garland, D.B. Kopans, and K. Hughes, *Estimates of the sizes at which breast cancers become detectable on mammographic and clinical grounds*. *Journal of Womens Imaging*, 2003. **5**: p. 3-10.
53. National Cancer Registry Ireland. *Breast Cancer Survival Statistics*. 2012 [cited 2015 15 December]; Available from: <http://www.ncri.ie/data/survival-statistics>.
54. National Cancer Institute. *Mammograms*. 2012 27 July 2012 [cited 2013 22 October]; Available from: <http://cancer.gov/cancertopics/factsheet/detection/mammograms>.
55. Berg, W.A., L. Gutierrez, M.S. Ness-Aiver, W.B. Carter, M. Bhargavan, R.S. Lewis, and O.B. Ioffe, *Diagnostic accuracy of mammography, clinical examination, US, and MR imaging in preoperative assessment of breast cancer*. *Radiology*, 2004. **233**(3): p. 830-49.
56. Biglia, N., V.E. Bounous, L. Martincich, E. Panuccio, V. Liberale, L. Ottino, R. Ponzzone, and P. Sismondi, *Role of MRI (magnetic resonance imaging) versus conventional imaging for breast cancer presurgical staging in young women or with dense breast*. *Eur J Surg Oncol*, 2011. **37**(3): p. 199-204.
57. Brodersen, J., H. Thorsen, and S. Kreiner, *Validation of a condition-specific measure for women having an abnormal screening mammography*. *Value Health*, 2007. **10**(4): p. 294-304.
58. Gotzsche, P.C. and M. Nielsen, *Screening for breast cancer with mammography*. *Cochrane Database Syst Rev*, 2011(1): p. CD001877.
59. Fallowfield, L.J. and A. Hall, *Psychosocial and sexual impact of diagnosis and treatment of breast cancer*. *Br Med Bull*, 1991. **47**(2): p. 388-99.
60. Brewer, N.T., T. Salz, and S.E. Lillie, *Systematic review: the long-term effects of false-positive mammograms*. *Ann Intern Med*, 2007. **146**(7): p. 502-10.
61. Independent UK Panel on Breast Cancer Screening, *The benefits and harms of breast cancer screening: an independent review*. *Lancet*, 2012. **380**(9855): p. 1778-86.
62. Prasad, S.N. and D. Houserikova, *The role of various modalities in breast imaging*. *Biomed Pap Med Fac Univ Palacky Olomouc Czech Repub*, 2007. **151**(2): p. 209-18.

63. Degani, H., M. Chetrit-Dadiani, L. Bogin, and E. Furman-Haran, *Magnetic resonance imaging of tumor vasculature*. Thromb Haemost, 2003. **89**(1): p. 25-33.
64. Furman-Haran, E., F. Kelcz, and H. Degani, *Magnetic resonance imaging of breast cancer angiogenesis: a review*. J Exp Clin Cancer Res, 2002. **21**(3 Suppl): p. 47-54.
65. Hillman, B.J., S.E. Harms, G. Stevens, R.G. Stough, A.B. Hollingsworth, K.F. Kozlowski, and L.J. Moss, *Diagnostic performance of a dedicated 1.5-T breast MR imaging system*. Radiology, 2012. **265**(1): p. 51-8.
66. de Abreu, D.S., *Bioimpedance and chronoamperometry as an adjunct to prostate-specific antigen screening for prostate cancer*. Cancer Manag Res, 2011. **3**: p. 109-16.
67. Mistry, K. and G. Cable, *Meta-analysis of prostate-specific antigen and digital rectal examination as screening tests for prostate carcinoma*. J Am Board Fam Pract, 2003. **16**(2): p. 95-101.
68. Ilic, D., M.M. Neuberger, M. Djulbegovic, and P. Dahm, *Screening for prostate cancer*. Cochrane Database Syst Rev, 2013. **1**: p. Cd004720.
69. Gambert, S.R., *Screening for prostate cancer*. Int Urol Nephrol, 2001. **33**(2): p. 249-57.
70. Kuriyama, M., M.C. Wang, L.D. Papsidero, C.S. Killian, T. Shimano, L. Valenzuela, T. Nishiura, G.P. Murphy, and T.M. Chu, *Quantitation of prostate-specific antigen in serum by a sensitive enzyme immunoassay*. Cancer Res, 1980. **40**(12): p. 4658-62.
71. Arcangeli, C.G., D.K. Ornstein, D.W. Keetch, and G.L. Andriole, *Prostate-specific antigen as a screening test for prostate cancer. The United States experience*. Urol Clin North Am, 1997. **24**(2): p. 299-306.
72. Catalona, W.J., J.P. Richie, F.R. Ahmann, M.A. Hudson, P.T. Scardino, R.C. Flanigan, J.B. deKernion, T.L. Ratliff, L.R. Kavoussi, B.L. Dalkin, and et al., *Comparison of digital rectal examination and serum prostate specific antigen in the early detection of prostate cancer: results of a multicenter clinical trial of 6,630 men*. J Urol, 1994. **151**(5): p. 1283-90.
73. Health Service Executive. *Breast Lump*. 2015 [cited 2015 19 November]; Available from: <http://www.hse.ie/eng/health/az/B/Breast-lump/Symptoms-of-a-breast-lump-.html>.
74. Coffman, F.D. and S. Cohen, *Impedance measurements in the biomedical sciences*. Stud Health Technol Inform, 2013. **185**: p. 185-205.
75. Banica, F.-G., *Chemical sensors and biosensors: fundamentals and applications*. 2012: John Wiley & Sons.
76. Roberts, W.W., O.E. Fugita, L.R. Kavoussi, D. Stoianovici, and S.B. Solomon, *Measurement of needle-tip bioimpedance to facilitate percutaneous access of the urinary and biliary systems: first assessment of an experimental system*. Invest Radiol, 2002. **37**(2): p. 91-4.
77. Hope, T.A. and S.E. Iles, *Technology review: the use of electrical impedance scanning in the detection of breast cancer*. Breast Cancer Research, 2004. **6**(2): p. 69-74.

78. Fricke, H. and S. Morse, *The electric capacity of tumors of the breast*. The Journal of Cancer Research, 1926. **10**(3): p. 340-376.
79. Morimoto, T., S. Kimura, Y. Konishi, K. Komaki, T. Uyama, Y. Monden, Y. Kinouchi, and T. Iritani, *A study of the electrical bio-impedance of tumors*. J Invest Surg, 1993. **6**(1): p. 25-32.
80. Surowiec, A.J., S.S. Stuchly, J.B. Barr, and A. Swarup, *Dielectric properties of breast carcinoma and the surrounding tissues*. IEEE Trans Biomed Eng, 1988. **35**(4): p. 257-63.
81. Jossinet, J., *Variability of impedivity in normal and pathological breast tissue*. Med Biol Eng Comput, 1996. **34**(5): p. 346-50.
82. Jossinet, J., *The impedivity of freshly excised human breast tissue*. Physiol Meas, 1998. **19**(1): p. 61-75.
83. Malich, A., T. Bohm, M. Facius, M. Freessmeyer, M. Fleck, R. Anderson, and W.A. Kaiser, *Additional value of electrical impedance scanning: experience of 240 histologically-proven breast lesions*. Eur J Cancer, 2001. **37**(18): p. 2324-30.
84. Zou, Y. and Z. Guo, *A review of electrical impedance techniques for breast cancer detection*. Med Eng Phys, 2003. **25**(2): p. 79-90.
85. Scholz, B. and R. Anderson, *On electrical impedance scanning—principles and simulations*. Electromedica, 2000. **68**(1): p. 35-44.
86. Rigaud, B., J.P. Morucci, and N. Chauveau, *Bioelectrical impedance techniques in medicine. Part I: Bioimpedance measurement. Second section: impedance spectrometry*. Crit Rev Biomed Eng, 1996. **24**(4-6): p. 257-351.
87. Cuzick, J., R. Holland, V. Barth, R. Davies, M. Faupel, I. Fentiman, H.J. Frischbier, J.L. LaMarque, M. Merson, V. Sacchini, D. Vanel, and U. Veronesi, *Electropotential measurements as a new diagnostic modality for breast cancer*. Lancet, 1998. **352**(9125): p. 359-63.
88. Kyle, U.G., I. Bosaeus, A.D. De Lorenzo, P. Deurenberg, M. Elia, J.M. Gomez, B.L. Heitmann, L. Kent-Smith, J.C. Melchior, M. Pirlich, H. Scharfetter, A.M. Schols, and C. Pichard, *Bioelectrical impedance analysis--part I: review of principles and methods*. Clin Nutr, 2004. **23**(5): p. 1226-43.
89. Pethig, R., *Dielectric properties of body tissues*. Clinical Physics and Physiological Measurement, 1987. **8**(4A): p. 5.
90. Blad, B., P. Wendel, M. Jonsson, and K. Lindstrom, *An electrical impedance index to distinguish between normal and cancerous tissues*. J Med Eng Technol, 1999. **23**(2): p. 57-62.
91. Blad, B. and B. Baldetorp, *Impedance spectra of tumour tissue in comparison with normal tissue; a possible clinical application for electrical impedance tomography*. Physiol Meas, 1996. **17 Suppl 4A**: p. A105-15.
92. Saulnier, G.J., R.S. Blue, J.C. Newell, D. Isaacson, and P.M. Edic, *Electrical impedance tomography*. Signal Processing Magazine, IEEE, 2001. **18**(6): p. 31-43.
93. Raneta, O., D. Ondrus, and V. Bella, *Utilisation of electrical impedance tomography in breast cancer diagnosis*. Klin Onkol, 2012. **25**(1): p. 36-41.
94. U. S. Food and Drug Administration, *TransScan Medical Inc.'s T-Scan 2000 Information for Prescribers*, U. S. Food and Drug Administration,

- Editor. 1999, U. S. Food and Drug Administration: Silver Spring, MD. p. 1-9.
95. U. S. Food and Drug Administration. *Obstetrics and Gynecology Devices Panel*. 2006 31 July 2013 [cited 2013 22 October]; Available from:
<http://www.fda.gov/AdvisoryCommittees/CommitteesMeetingMaterials/MedicalDevices/MedicalDevicesAdvisoryCommittee/ObstetricsandGynecologyDevices/ucm125145.htm>.
96. Cherepenin, V., A. Karpov, A. Korjenevsky, V. Kornienko, A. Mazaletskaya, D. Mazourov, and D. Meister, *A 3D electrical impedance tomography (EIT) system for breast cancer detection*. *Physiol Meas*, 2001. **22**(1): p. 9-18.
97. Prasad, S.N., D. Houserkova, and J. Campbell, *Breast imaging using 3D electrical impedance tomography*. *Biomed Pap Med Fac Univ Palacky Olomouc Czech Repub*, 2008. **152**(1): p. 151-4.
98. Kerner, T.E., K.D. Paulsen, A. Hartov, S.K. Soho, and S.P. Poplack, *Electrical impedance spectroscopy of the breast: clinical imaging results in 26 subjects*. *IEEE Trans Med Imaging*, 2002. **21**(6): p. 638-45.
99. Halter, R., A. Hartov, and K.D. Paulsen, *Design and implementation of a high frequency electrical impedance tomography system*. *Physiol Meas*, 2004. **25**(1): p. 379-90.
100. Halter, R.J., A. Hartov, and K.D. Paulsen, *A broadband high-frequency electrical impedance tomography system for breast imaging*. *IEEE Trans Biomed Eng*, 2008. **55**(2 Pt 1): p. 650-9.
101. Mäki, S., J. Kari, P. Ahonen, T. Elomaa, P. Annus, and K. Kronström, *Biopsy Needle Including Bioimpedance Probe with Optimized Sensitivity Distribution*. 2015.
102. Kang, G., J. Yun, J.-S. Cho, J. Yoon, and J.-H. Lee, *Micro Electrical Impedance Spectroscopy (μ EIS) Fabricated on the Curved Surface of a Fine Needle for Biotissue Discrimination*. *Electroanalysis*, 2015: p. n/a-n/a.
103. Mishra, V., H. Bouayad, A. Schned, A. Hartov, J. Heaney, and R.J. Halter, *A real-time electrical impedance sensing biopsy needle*. *IEEE Trans Biomed Eng*, 2012. **59**(12): p. 3327-36.

Chapter 2

Impedance Probe Fabrication, Characterisation and Validation

2. Impedance Probe Fabrication, Characterisation and Validation

2.1 Objectives

The main objective of this chapter is to report the design and fabrication of a prototype electrical impedance transducer device, suitable for impedance testing of biological tissue samples. It was important to develop a device, which would be sufficiently robust to withstand repeated testing and cleaning, as well as being biocompatible for future use in human studies. A series of experiments were designed to determine the electrical and surface characteristics of the new probe (Table 2.1).

Table 2.1: The experimental methods that will be used in Chapter 2 and the purpose of each of them.

Surface Characterisation	Purpose
Scanning Electron Microscopy	Imaging of surface to show any deposition defects
Energy-dispersive X-ray	Elemental analysis of the deposited layers
Focused-ion Beam	Thickness of the deposited layers
Atomic Force Microscopy	Calculation of the total surface roughness
Optical Profilometry	Calculation of the total surface roughness
Breakage Strength	Force required to cause critical failure
Short-circuit Testing	Gold continuity and presence of shorts
Electrical Characterisation	Purpose
Cyclic Voltammetry	Determination of cleaning protocol effectiveness and electron charge transfer
Electrical Impedance	Determine the sensitivity of the probe to changes in layer conductivity.

2.2 Introduction

This chapter will discuss the design, fabrication and characterisation of a novel impedance probe which will be used to aid in tissue differentiation. The development of the probe sought to maximise the technology and capabilities available in the TNI including silicon fabrication, photolithography, electrical packaging and electrochemical testing. The construction of this device involved the utilisation of techniques including

photolithography, metal deposition, lift-off and plasma etching to allow the deposition of gold on to an insulated substrate [1]. Insulation of the substrate material is required to prevent conduction of an electrical current from the electrodes through the substrate. The characterisation of the probe involved the use of a number a key techniques including SEM, FIB milling, AFM, EDX, CV and electrical impedance which will all be discussed further in this chapter.

2.2.1 Impedance Probe Design

The design and layout of the probe devices was initially undertaken as part of a National Access Programme (NAP) grant that was subsequently funded by a Technology Innovation Development Award (TIDA) which was operated by Science Foundation Ireland (SFI). The concept was formulated by Dr Walter Messina and the layout drawings were completed by Mr Richard Murphy both of TNI, University College Cork. These designs were used to fabricate the photolithography masks required during the metal deposition and etching processes involved in the fabrication of both the stainless steel and silicon devices. The prototype device which was chosen for development during this project consisted of two gold micro-electrodes patterned on to a passivated substrate. The fabrication materials chosen for the development of the prototype device were required to provide good biocompatibility and sustain long-term stimulation and sensing [2]. During the course of this study both silicon and stainless steel substrates were tested because of their fabrication convenience and conformity with specific requirements of the semiconductor processes (ability to withstand heating cycles, a flat substrate and a chemically inert surface) [3]. The electrode material chosen for microelectrode devices are usually noble metals such as platinum or in the case of this study gold. This is due to the specific properties of these metals including high resistance to corrosion and low chemical reactivity which makes them ideally suited to electrical stimulation and sensing both *in vitro* and *in vivo* [3-7]. The use of the two microelectrode design meant that the need for an external reference electrode (which is a necessary component of many of the devices mentioned in Chapter 1) was removed. The overall probe size can be maintained at a cross-sectional area of approximately 144

mm² which could potentially limit tissue damage upon insertion due to its small size. The specific dimensions of the electrode layout were chosen to allow the electrochemical sensors to be integrated on to a standard stainless steel hypodermic needle. This would make it possible to determine the electrical impedance of tissues as the needle is advanced within the human body in real-time and may allow for tissue discrimination.

The photolithography mask design drawings were created using CleWin4 layout design software by Mr Richard Murphy (Figure 2.1-2.4). The image files were sent to Compugraphics International Ltd (Fife, United Kingdom) and used to manufacture a series of fused silica glass and chrome photolithography masks. The design specifications for each probe were (Table 2.2):

Table 2.2: The probe specifications and dimensions used in the design of the photolithography masks.

Probe Specifications	Dimensions
Total Length	39 mm
Pitch	3.7 mm
Output Electrode Width	500 μ m
Output Electrode Length	2 mm
Recording Electrode Width	200 μ m
Recording Electrode Length	1 mm
Track Width	100 μ m
Track Separation	100 μ m

These masks were used in the fabrication of both the silicon and stainless steel prototype devices. A different mask was used in each step of the process to produce a specific deposition pattern for each of the materials. These masks were reused in multiple fabrication runs for the production of both the silicon and stainless steel prototype devices. This meant that during the production of these devices the material deposition should produce almost identical electrodes across each of the probes created.

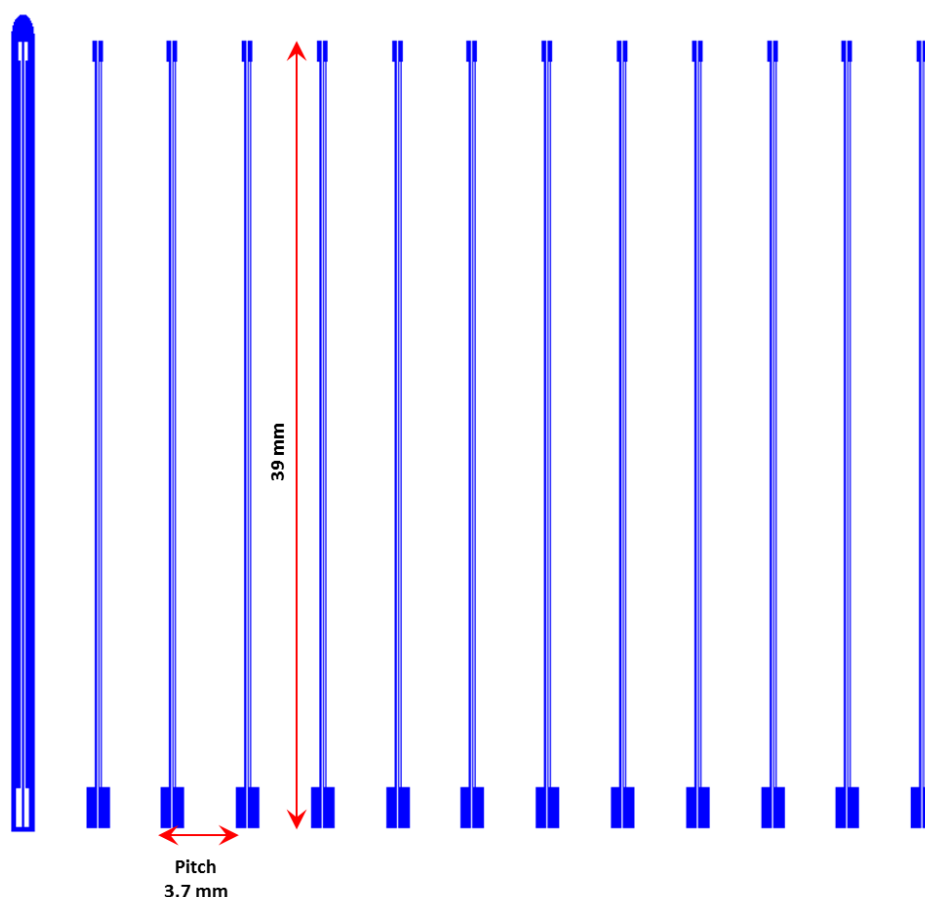


Figure 2.1: The design pattern for the masks used in the production of the stainless steel and silicon probes. The total length of the patterned probes is 39 mm and the pitch between probes is 3.7 mm.

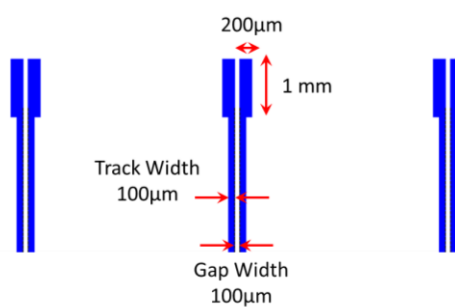


Figure 2.2: A close-up of the design pattern for the recording electrodes for the stainless steel and silicon probes. The dimensions of the electrode pads and the gold tracks are shown.

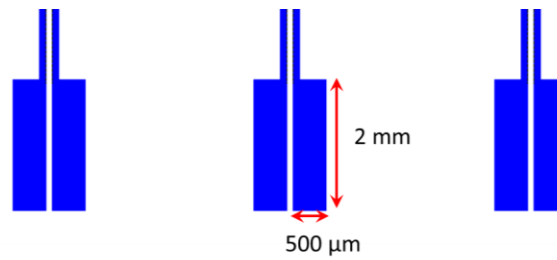


Figure 2.3: A close-up of the design pattern for the connection pads for the stainless steel and silicon probes. The dimensions of the output pads are shown.

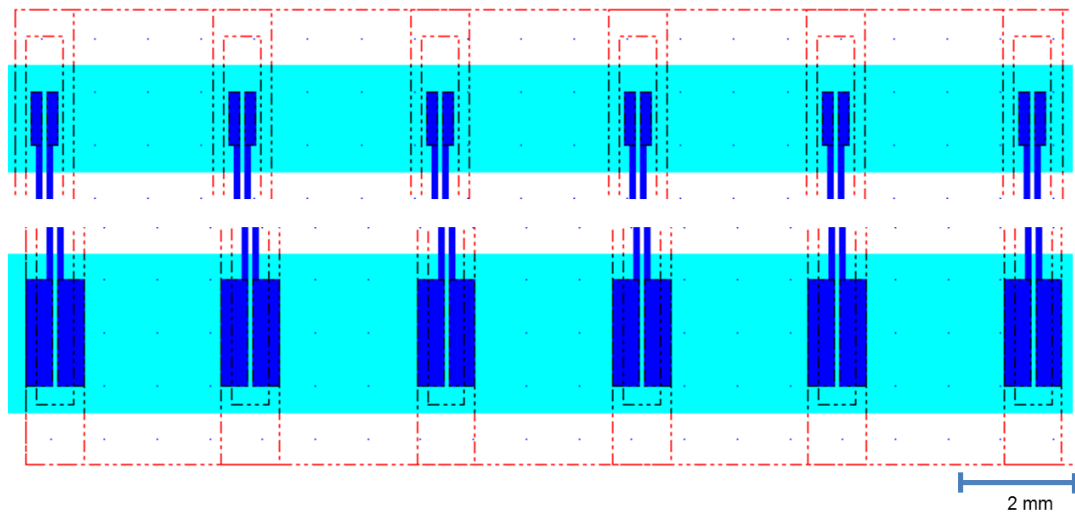


Figure 2.4: The outline (light blue) of the mask used during the passivation process for both the recording and output electrode pads. This area is etched to remove the Si₃N₄ to expose the electrodes and allow electrical signals to be conducted.

A small section of the gold tracts were left exposed during the passivation process (Figure 2.4). As a result, the functional area of the recording electrodes on each probe was slightly larger than the rectangular area of the patterned electrode pads. The actual dimensions of the recording electrodes are outlined in Table 2.3:

Table 2.3: The total calculated recording surface area of each of the gold electrodes.

Recording Electrode	Area (μm^2)	Total Area (μm^2)
Rectangular Electrode	$1,000 \times 200 = 200,000$	250,000
Gold Tract	$500 \times 100 = 50,000$	

2.3 Instrumentation and Techniques

2.3.1 Scanning Electron Microscope

Scanning Electron Microscopy (SEM) involves the use of an electron gun to generate a stream of electrons which are directed at the sample being imaged. The electrons are deflected by the sample being imaged and these scattered electrons are detected by a back-scattered electron detector. Unlike a conventional light microscope which uses glass lens to focus light, an SEM uses a series of electromagnetic lenses to focus the electron beam [8, 9]. The use of electrons as the illumination source rather than light allows significantly higher magnification and resolution images to be obtained [10, 11]. The primary use of SEM during the course of this work was to provide high resolution images of the surface of the gold electrodes on the silicon and stainless steel substrates. It was also used to image the growth of immortalised cells on the surface of the silicon probe (See Section 3.5.1.5). Figure 2.5 shows an FEI Quanta 650 FEG SEM which is used in the Electron Microscopy and Analysis Facility (EMAF) in the TNI.



Figure 2.5: An example of an FEI Quanta 650 FEG SEM. Reference [12].

2.3.2 Energy-dispersive X-ray Analysis

Energy-dispersive X-ray analysis (EDX) is an adjunct technique to SEM imaging. The primary electron beam, used for image generation, causes an increase in the energy states of electrons at the surface of the material [13,

14]. This increase in energy moves the electrons to higher energy orbitals [13, 14]. Over time these electrons return to their lowest available orbitals. The difference in energy between the two states can be emitted in states such as heat, visible light, vibration, or x-rays which is the case in EDX [13]. The resultant energy emissions are detected by a specialist EDX spectrometer. Each element on the periodic table will generate a distinct spectra based on the orbitals to which the electrons in each atom can move. These spectra can then be analysed to determine the elements present at the surface of a material.

2.3.3 Focused-ion Beam

The technique of focused-ion beam (FIB) can be used for high resolution imaging and/or precision milling and sputtering. In a process similar to SEM imaging, FIB uses gallium (Ga^+) ions to bombard the surface of the material of interest. At a lower primary beam current, FIB machines can achieve image resolution up to 5 nm [15, 16]. At higher currents, FIB can be used for the precision removal of surface material, a process known as milling [17]. For the purpose of this research the high current milling was used. The most common application of FIB is for the preparation of cross-sectional samples for SEM and transmission electron microscope imaging. For analysis of planar samples it is often necessary to deposit a layer of metal such as platinum or tungsten on to the area of interest prior to milling [18]. Chemical vapour deposition is used to deposit the desired material on the substrate being analysed [17, 19]. The addition of a platinum or tungsten layer has two functions, the first of which is to protect the material surface from spurious sputtering [19]. The second function is to provide layer contrast for the discrimination of material layers when the sample is analysed using SEM. Following metal deposition, high-energy Ga^+ ions are bombarded across the surface of the region of interest. This results in the sputtering and subsequent removal of the surface molecules through each of the material layers. The area of interest is then imaged using conventional SEM. Using this combination of FIB milling and SEM imaging it is possible to get approximate measurements of each of the layers deposited during the

fabrication process. Figure 2.6 shows an FEI Quanta 3D Dual Beam FIB which is used in the EMAF in the TNI.



Figure 2.6: An example of an FEI Quanta 3D Dual Beam FIB. Reference [20].

2.3.4 Atomic Force Microscopy

Atomic Force Microscopy (AFM) was developed in the early 1980s by Gerd Binnig and Henrich Rohrer. It was designed as a tool to enable precise imaging and measurement of ultra-small forces on particles as small as single atoms [21]. Images are produced by measuring the strength of force of interaction between the sharp tip of a cantilever (Figure 2.7) made of silicon or silicon nitride (Si_3N_4) and the surface atoms of the material [22]. The precision of the technique means that the presence of one atom on the surface of the material can cause the cantilever to be deflected.

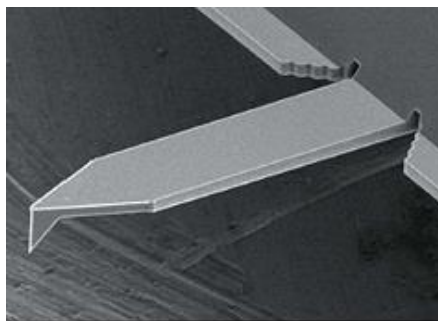


Figure 2.7: An example of an AFM cantilever and tip. Reference [23].

The forces that can be measured include mechanical contact, van der Waals, capillary, chemical bonding, electrostatic, piezo responses and magnetic forces. Many commercial AFM devices use a process of optical

beam deflection to measure the response of the cantilever as it is scanned across the surface of a material [24]. When the tip is brought into the proximity of a sample the interaction with the surface chemistry leads to a deflection of the cantilever. A laser diode light source is directed by a prism onto the back of the cantilever. The beam is reflected by a mirror towards a photodiode detector which is used to determine the vertical deflection experienced by the cantilever [24]. AFM instruments obtain measurements in three dimensions to produce a 3D image of the surface. The resolution which can be obtained in the x and y plane ranges from 0.1 to 1.0 nm and in the z direction of 0.01 nm [22].

2.3.5 Cyclic Voltammetry

Cyclic voltammetry (CV) is a type of measurement first described by John Randles in 1948 [25]. The technique involves cycling the applied potential between two fixed points at a constant rate in an unstirred solution and measuring the resulting current [26]. The sweep rate applied can vary from a few millivolts per second to a hundred volts per second. It is an effective approach for the evaluation of a redox system's electron transfer in reactions, such as provision of data relating to kinetics and formal reduction, reversibility, stability and oxidation potentials in a system [27]. A reference electrode such as an Ag/AgCl electrode is used to maintain the potential of the working electrode being tested. The potential is applied as a linear potential scan with a triangular waveform. The voltage increase begins at V_1 until it reaches V_2 at which point the scan is reversed until it reaches V_1 again (Figure 2.8) [28]. The important parameters of CV measurements include the magnitude of the peak currents I_{pa} (anodic peak current) and I_{pc} (cathodic peak current) and the potential at which the peaks occur at E_{pa} and E_{pc} .

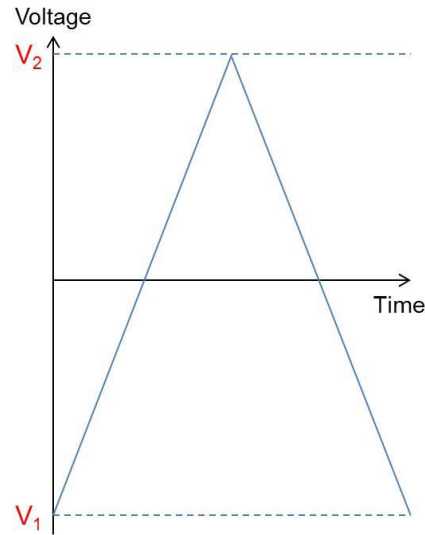


Figure 2.8: The forward and reverse potentials versus time of a typical cyclic voltammogram. Redrawn from reference [28].

For reversible electrochemical reactions there are four characteristics which must be present [28, 29]:

- 1) Voltage separation between peak currents is (Equation 2.1):

$$\Delta E = E_p^a - E_p^c = \frac{59}{n} \text{ mV}$$

Equation 2.1: The relationship between the anodic and cathodic peak currents. n = number of electrons transferred.

- 2) The positions of peak voltage do not alter as a function of voltage scan rate
- 3) The ratio of peak currents is equal to one (Equation 2.2):

$$\left| \frac{i_p^a}{i_p^c} \right| = 1$$

Equation 2.2: The ratio of the peak anodic and cathodic peak current which equals 1 for reversible chemical reactions.

- 4) The peak currents are proportional to the square root of the scan rate (Figure 2.9):

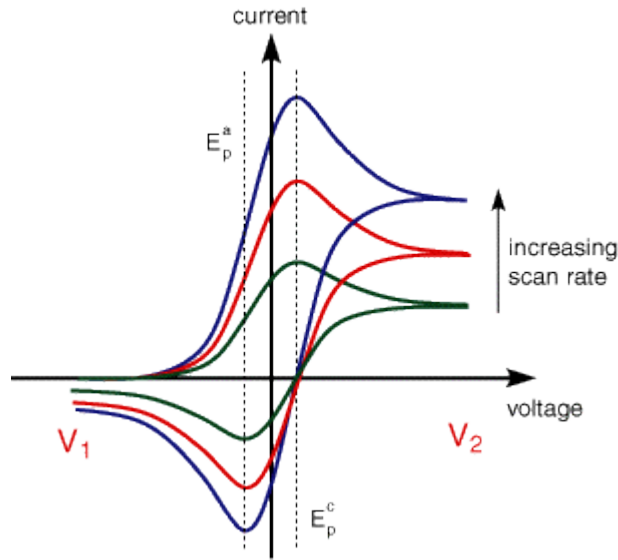


Figure 2.9: The effect of increasing scan rate on the peak current response of reversible electrochemical reaction. Reference [28].

The peak current for a reversible system is described by the Randles-Sevcik equation for the forward sweep of the first cycle (Equation 2.3) [26, 30].

$$i_p = (2.69 \times 10^5) n^{3/2} A D^{1/2} C v^{1/2}$$

Equation 2.3: The Randles-Sevcik equation for the calculation of peak current in a reversible system.

i_p is the peak current (A), n is electron stoichiometry, A is the electrode area (cm^2), D is the diffusion coefficient (cm^2/s), C is the concentration (mol/cm^3) and v is the scan rate (V/s). Therefore, i_p increases with $v^{1/2}$ and is directly proportional to the concentration. For quasi-reversible systems, the current is controlled by both the mass transport and charge transfer. The voltammograms produced are more extended and exhibit a larger peak separation compared to a reversible system [30, 31].

An electrochemical cell used during CV typically consists of a three electrode set-up: A working electrode composed of inert materials such as carbon, gold, platinum or graphite; a counter electrode most commonly a platinum wire; and a reference electrode such as Ag/AgCl or a saturated calomel electrode. The potentiostat to which the three electrodes are connected

applies the desired potential between the working and reference electrodes. The current required to sustain the electrolysis at the working electrode is provided by the counter electrode (Figure 2.10) [26]. The current measured during the process is often normalised to the electrode surface area and is referred to as the current density. A cyclic voltammogram is produced by plotting the current density at the working electrode surface during the voltage sweep against the applied potential [32]. A peak in the measured current is seen at the potential that is characteristic of an electrode reaction taking place. The peak width and height for a particular process may depend on the sweep rate, electrolyte concentration and the electrode material [33].

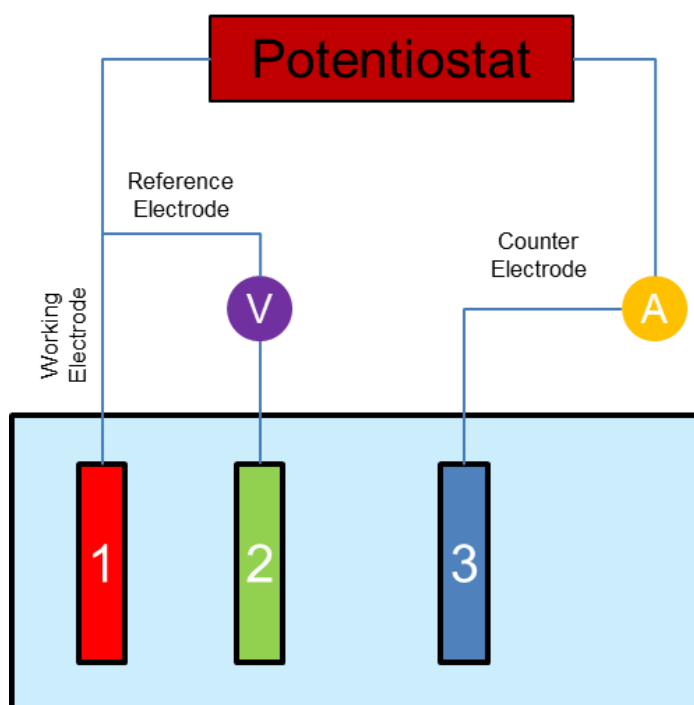


Figure 2.10: A simple schematic of a three-electrode electrochemical cell, showing the working electrode, reference electrode and counter electrode immersed in solution. The electrodes are all connected to a potentiostat so that the potential differences between the electrodes can be measured. Figure is Author's own.

2.4 Experimental Details

2.4.1 Reagents and Materials

Silicon Dioxide, MicroChem S1805 Imaging Resist, Microposit MF319 Developer and Microposit R1165 Resist Stripper, Silicon Nitride (Si_3N_4) (All purchased from Shipley Europe Ltd., Coventry, United Kingdom); Stainless steel wafers (Mechanical Workshop, Tyndall National Institute); Silicon Wafers (Silicon Fabrication Unit, Tyndall National Institute); Gold Powder (Pi-Kem Ltd., Staffordshire, United Kingdom); Titanium (Umicore N.V., Brussels, Belgium); Single-core wire, Multi-core wire and 2-part Araldite Rapid T Hardener Epoxy, Kapton® Tape (all from Radionics Ltd., Dublin, Ireland); Ablebond 84-1LM1SR4 Silver Epoxy (Farnell Ltd., Leeds, United Kingdom); Tetrafluoromethane, Isopropyl alcohol, 20 ml universal collection tube, Petri Dish, Carbon Tape, Microscope slides, Potassium Ferricyanide, Potassium Chloride, resazurin sodium salt (all from Sigma-Aldrich Ltd., Dublin, Ireland); Scalpel (Swann Morton, Sheffield, United Kingdom).

2.4.2 Instrumentation

FEI Quanta 650 FEG Scanning Electron Microscope with EDX (FEI UK Ltd., Cambridgeshire, United Kingdom), FEI Quanta 3D Dual Beam Focused-Ion Beam (FEI UK Ltd., Cambridgeshire, United Kingdom), Asylum Research MFP-3D Classic Atomic Force Microscope (Oxford Instruments, Oxfordshire, United Kingdom), Palmsens Potentiostat (Palmsens BV, Utrecht, The Netherlands), Instron 5960 Dual-column Testing System (Instron, Buckinghamshire, United Kingdom), Temescal FC-2000 (Scotech Ltd., Renfrewshire, Scotland), STS310 PC Plasma-enhanced Chemical Vapour Deposition (SPTS Newport (UK), Newport, United Kingdom), Karl Suss MA1006 Mask Aligner (Suss Microtec AG, Garaching, Germany), PICO Ashing (CF_4), Disco DAD3350 (Disco Hi-Tec U.K. Ltd., West Sussex, United Kingdom), Silver Epoxy Oven (Heraeus VT5042EK vacuum oven, Heraeus Holding GmbH, Hanau, Germany); Ultrawave QS3 Ultrasonic Water Bath (Ultrawave Ltd., Cardiff, United Kingdom), Harrick Plasma PDC-002 Extended Plasma Cleaner (Harrick Plasma, New York, U.S.A.); Wild M3Z Stereo Microscope (Wild Heerbrugg AG, Gais, Switzerland), CHI111

Ag/AgCl Reference Electrode and Platinum Wire Counter Electrode (CH Instruments Inc., Austin, Texas, USA); Fluke 16 Multimeter (Fluke UK Ltd., Norfolk, United Kingdom); Autolab PGSTAT204 with FRA32M module (Metrohm UK Ltd, Runcorn, United Kingdom); Zyga NewView 5032 (ZygoLOT GmbH, Darmstadt, Germany).

2.5 Procedures

2.5.1 Fabrication

2.5.1.1 Silicon Probes

The silicon probes were fabricated using the Fabrication Facilities in the TNI. The 100 mm diameter silicon wafers were obtained from the Silicon Fabrication Unit in the TNI. The silicon probes were fabricated using the Fabrication Facilities in the TNI by Mr Dan O'Connell. The initial thickness of the wafer was 525 μm . A variable-wet-oxide layer was applied to each of the wafers. The process was conducted at 1,100°C for 16 min to produce a 3,000 angstrom (300 nm) oxide layer. Figure 2.11 shows a conceptualised drawing of the three layers of the probe which are deposited onto the silicon substrate (SiO_2 , gold/titanium and Si_3N_4).

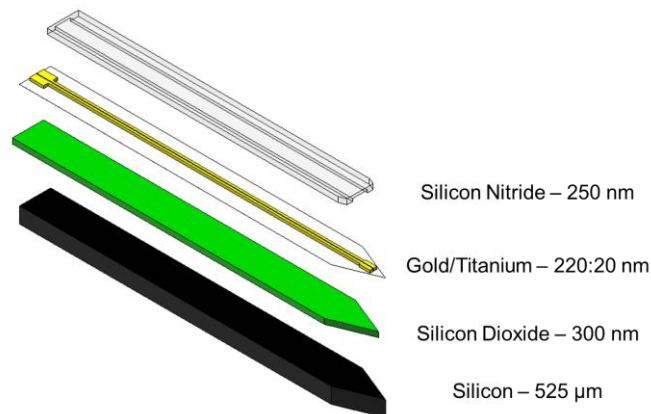


Figure 2.11: An expanded view conceptualised drawing of the individual layers deposited during the fabrication of the silicon probes. Black – 525 μm Silicon Substrate; Green – 300nm SiO_2 ; Yellow – 20 nm/220 nm Titanium/Gold; White – 250 nm Si_3N_4 . Figure was produced by Dr Walter Messina.

The silicon wafers were spin-coated with MicroChem LOR3A lift-off resist at 3,000 rpm and baked on a hot plate for 3 min at 150°C. MicroChem S1805 imaging photoresist was applied to the entire surface of the wafer at 3,000

rpm for 50 seconds and the wafers were baked again for 2 min at 115°C. The pre-designed masks were aligned with the wafers in a Karl Suss MA1006 mask-aligner. The wafers were exposed to UV light at a dosage of 40 mW/cm². The wafers were placed in a Microposit MF319 developer for 1 min to activate the positive resist in the pattern of the electrodes. Deionised water was used to rinse the wafers which were then baked in an oven for 30 min at 90°C. A layer of titanium and gold (20 nm:220 nm) was then evaporated on top of the photoresist layer. The titanium layer was used as an adhesive layer to aid in the attachment of the evaporated gold. The metal deposition was conducted using e-beam evaporation in a Temescal FC-2000 (Scotech, Renfrewshire, Scotland) at a pressure of $<5 \times 10^{-7}$ Torr. Excess metal and photoresist were removed using Microposit R1165 resist stripper. A passivation layer of Si₃N₄ was applied by plasma-enhanced chemical vapour deposition (PECVD) in a STS310 PC system (SPTS, Newport, United Kingdom). A photolithography mask was designed to pattern this layer so that both the recording electrodes and the connection pads would be exposed after the overlying passivation layer was etched in tetrafluoromethane (CF₄) plasma in a PICO Ashing system.

Once each of the deposition processes had been completed the wafers were then diced into approximately 3.7 mm wide sections, using a Disco DAD3350 automatic dicing unit (Disco Hi-Tec U.K Ltd., West Sussex, United Kingdom), by Mr Paul Tassie to release the individual probes from the wafers. This was completed in the Packaging Laboratory in TNI. To permit the insertion of the diced probes into tissue, the probe tips were pointed using an electrical sander.

2.5.1.2 Stainless Steel

The stainless steel probes were fabricated using the Fabrication Facilities in the TNI by Mr Dan O'Connell. The substrates used for the probe development were 100 mm diameter and 1 mm thick stainless steel wafers which were obtained from the Mechanical Workshop in the TNI. The deposition process previously described for the silicon prototypes was used to pattern the stainless steel substrates. Insulation layers of silicon dioxide

ranging from 250 nm to 1 μm were deposited on the surface of the wafers to prevent conduction of an electrical current through the steel substrate. Once each of the deposition processes had been completed the wafers were then diced using a Disco DAD3350 automatic dicing unit (Disco Hi-Tec U.K Ltd., West Sussex, United Kingdom), by Mr Paul Tassie to release the individual probes from the wafers. This was completed in the Packaging Laboratory in TNI.

2.5.1.3 Probe Packaging

After the silicon probes had been shaped they were packaged to allow electrical recordings to be performed. Both single-core and multi-core wires were used in the development of the silicon probes. The insulation coating was first removed from the end of the electrical wires using a scalpel to allow a direct contact with the connection pads located on the devices. The wires were positioned on a glass microscope slide and held in place using Kapton® Tape. The silicon probes were then aligned beneath the wires and also held in place with Kapton® Tape. The wires were bonded to the gold output pads with a conductive silver epoxy which was applied under a light microscope. A compressed air supply line was attached to the tube of silver epoxy to allow it to be dispensed in a controlled manner. When both wires were connected, the probes were placed in an oven at 120°C for 2 hours to allow the epoxy to cure (Figure 2.13). Plastic Pasteur pipettes were then cut to size using a scalpel to provide a protective covering over the wire bond (Figure 2.12). A 2-part epoxy (Araldite Rapid T Hardener, Radionics Ltd., Dublin, Ireland) was mixed in equal parts in a plastic weigh-boat before being transferred in to an open syringe tube. This was capped and attached to a compressed air supply. The epoxy was then used to fill the tubing and allowed for harden for 20 minutes until dry.



Figure 2.12: A packaged probe showing the plastic tubing filled with hardened 2-part epoxy covering the electrical connects.



Figure 2.13: The Heraeus VT5042EK vacuum oven used in the probe packaging process.

2.5.2 Probe Cleaning

Each silicon probe was cleaned prior to electrochemical, cell culture or meat and human tissue testing. The devices were cleaned using ultrasonic isopropyl alcohol (IPA) and deionised water washes as this combination was able to remove contaminants without damaging the probe surface [34-36]. The devices were placed in a 20 ml tube which was filled with IPA and placed in an ultrasonic water-bath (QS3, Ultrawave Ltd., Cardiff, United Kingdom) for 10 min at 25 °C (Figure 2.14).



Figure 2.14: The Ultrawave QS3 ultrasonic water-bath used during the probe cleaning protocol.

The IPA was removed and discarded according to laboratory protocols. The probes were rinsed 3 times using 18.2 M Ω nano-pure water and the waste was discarded. The tube was filled with nano-pure water and placed in the ultrasonic bath for a further 10 minutes at 25 °C. The water was discarded and the probes were rinsed 3 times with nano-pure water. The devices were then placed on a sheet of lint-free cleanroom paper in a fume-hood. Compressed nitrogen gas was used to remove any remaining water from the probe. The devices were placed in an oxygen-plasma cleaner (PDC-002, Harrick Plasma, New York, U.S.A.) and the chamber was pumped out using the attached vacuum pump (Figure 2.15). The gas inlet valves were then opened to allow oxygen into the cleaning chamber which was maintained between 800-1000 microns for 20 min to remove any organic contaminants. Once completed the plasma cleaner was switched off and the gas valves were carefully opened to prevent damage of the probes. The devices were then placed in a clean petri dish before being used in experiments.

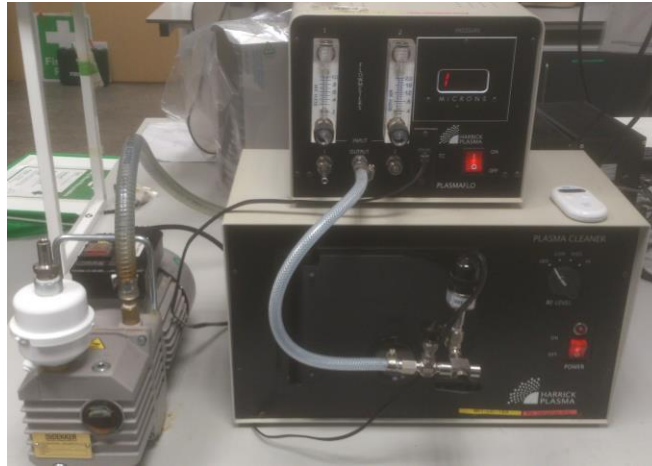


Figure 2.15: The Harrick Plasma oxygen-plasma cleaner and vacuum pump used during the silicon probe cleaning protocol.

2.5.3 Continuity Testing

A handheld multi-meter (Figure 2.16) was used to determine if the diced probes were short-circuited by measuring electrical continuity. The multimeter was set-up to determine continuity and would alarm at less than $25\ \Omega$ resistance. The positive cable (red) was placed on one of the gold output pads. The negative cable (black) was then placed on the recording electrode on the same side as the output under a light microscope to ensure correct placement. An alarm signalled a continuous circuit along the length of the gold tract. The multimeter probes were moved to the other recording and output pads to test the continuity of the opposite gold tract. If the alarm sounded when the probes were placed on any other point on the device outside of the recording and output pads a short circuit was present. If no alarm sounded when the multimeter probes were positioned correctly that would indicate that the gold track was not continuous along its entire length. This technique was used to qualitatively determine the continuity of the gold electrodes to assess if each probe was suitable for packaging.



Figure 2.16: A Fluke 16 multimeter which was used to determine if a short-circuit existed in the stainless steel and silicon probes.

2.5.4 Material Characterisation

2.5.4.1 Scanning Electron Microscope

Two probes were chosen as representative samples of both the silicon and stainless steel devices to be imaged by SEM. The probes were attached to the chuck of the microscope stage using carbon tape. The SEM chamber was then closed and pumped out to create a vacuum inside. A voltage of 20 kV generated the stream of electrons used for imaging. The probes were imaged across a range of magnifications from 140-100,000x and a stage tilt of either 0° or 45°. The purpose of this was to obtain high resolution images of the electrode layout, probe surface and the gold deposition. Representative images will be shown in the results section. All SEM images were obtained using a FEI Quanta 650 FEG scanning electron microscope (FEI, Cambridge, United Kingdom) by Mr Vince Lodge in the EMAF in the TNI.

2.5.4.2 Energy-dispersive X-ray Analysis

This technique was used to determine the composition of the electrodes that were fabricated as part of the probe manufacture. The electrodes were placed in the vacuum chamber of the SEM as previously described. The EDX unit was inserted in to the chamber. The recording parameters were setup using the software associated with the EDX unit. The left and right

electrode of each probe was analysed each time. The EDX analysis was performed by Mr Vince Lodge in the EMAF in TNI.

2.5.4.3 Focused-ion Beam

The FIB milling associated with this project was performed using an FEI Quanta 3D Dual Beam FIB instrument (FEI, Cambridge, United Kingdom) by Mr Vince Lodge in the EMAF in TNI. An area of platinum approximately $20\text{ }\mu\text{m}^2$ ($4\text{ }\mu\text{m} \times 5\text{ }\mu\text{m}$) was deposited on the surface of the gold electrode. The FIB instrument was then used to mill through each of the deposition layers. Once the milling was complete the probe was imaged using the FEI Quanta SEM as previously described using the following parameters (Table 2.4):

Table 2.4: The SEM imaging parameters used after the FIB milling procedure

Parameter	Value
Magnification	20,000 and 150,000 x
Tilt	45°
Electron Charge	30 kV

2.5.4.4 Atomic Force Microscopy

Atomic force microscopy imaging was performed by Dr Lynette Keeney using an Asylum Research MFP-3D Classic Atomic Force Microscope (Oxford Instruments, Oxfordshire, United Kingdom). The silicon probes were imaged in AC (intermittent contact) mode using AC240TS silicon cantilevers (Al reflex coated, $\sim 70\text{ kHz}$ resonant frequency). The scan parameters used to image the silicon probes are shown in Table 2.5.

Table 2.5: The AFM imaging parameters used in the analysis of the gold electrode surface.

Scan Rate	Scan Angle	Set Point	Integral Gain	Drive Amplitude	Drive Frequency	Scan Points
1 Hz	90°	$\sim 0.2\text{ V}$	10	$\sim 0.3\text{ V}$	$\sim 72\text{ kHz}$	256

Five measurement points were selected on each of the two gold electrodes on one silicon probe. A forward and reverse scan was performed over an area of $25\text{ }\mu\text{m}^2$ ($5\text{ }\mu\text{m} \times 5\text{ }\mu\text{m}$). The root-mean squared (RMS) values from each of the recordings were averaged and a total surface roughness value for each of the individual electrodes was determined.

2.5.4.5 Break Strength Testing

The instrument used to test the force applied to the probe to cause a critical failure in the silicon was an Instron 5960 Dual column testing system (Instron, Buckinghamshire, United Kingdom). The silicon probe was placed vertically in a piece of Blu-tack™ on the lower plate of the machine. The upper plate was then lowered until it contacted the top of the probe. The system was zeroed prior to a force being applied to the probe. The instrument was started and an increasing force was applied to the upper plate until a breakage in the probe occurred. The maximum applied force in Newton (N) required to break the silicon probe was then calculated.

2.5.4.6 Optical Profilometry

The Zyga NewView 5032 instrument was used to image the surface topography of the bare stainless steel wafer. The wafer was placed on the microscope stage and was aligned using the motorised stage control. The 20x Mirau objective lens was used during the measurement process. Four measurement points were selected on one stainless steel wafer. A forward and reverse scan was performed over an area of 0.091 mm^2 ($0.35 \text{ mm} \times 0.26 \text{ mm}$). The root-mean squared (RMS) values from each of the recordings were averaged and a total surface roughness value for the stainless steel wafer was determined.

2.5.5 Electrochemical Characterisation

2.5.5.1 Potassium Ferri/Ferrocyanide Solution

A 1M solution of potassium chloride (KCl) was first made up by adding 14.91 g of KCl salt to 200 ml of deionised water and mixed thoroughly to ensure a homogenous mixture. 100 ml of the solution was divided into two separate 200 ml Duran® bottles. Potassium Ferricyanide salt, $\text{K}_3[\text{Fe}(\text{CN})_6]$, (0.1645 g), was weighed out and added to one of the Duran® bottles containing KCl solution. 0.211 g of Potassium Ferrocyanide ($\text{K}_4[\text{Fe}(\text{CN})_6]$) was then weighed out and added to the other KCl solution bottle. The two solutions were thoroughly mixed to ensure a homogenous mixture. The ferricyanide and ferrocyanide solutions were then mixed in a clean 500 ml Duran® bottle and

was inverted a number of times to mix the two solutions. This produced a 5 mM Potassium Ferri/Ferrocyanide solution in 1 M KCl.

2.5.5.2 Cyclic Voltammetry Setup

A three-electrode set-up was used during this experiment. One of the gold electrodes acted as the working electrode along with a platinum wire counter and an Ag/AgCl reference electrode. The measurements were performed using a PalmSens potentiostat (Palmsens BV, Utrecht, The Netherlands) (Figure 2.17).



Figure 2.17: The equipment setup for the CV measurements using a PalmSens potentiostat and a three electrode circuit.

5 ml of the Potassium Ferri/Ferrocyanide and KCl solution was pipetted into a 10 ml glass beaker and placed on a retort stand. The Ag/AgCl reference electrode was attached to the reference cable, the platinum wire counter to the counter cable and one of the gold electrodes to the working cable which were connected to the PalmSens instrument. The electrodes and the silicon probe were then suspended from the retort stand in the ferri/ferrocyanide solution (Figure 2.18).



Figure 2.18: The Ag/AgCl and platinum wire electrodes and a silicon probe in a solution of potassium ferri/ferrocyanide and KCl during CV measurement.

A scan protocol was setup using the PSTrace software associated with the PalmSens instrument (Table 2.6):

Table 2.6: The parameters used for the cyclic voltammetry measurements performed using a three-electrode set-up with the silicon probes, a Ag/AgCl reference and a platinum counter electrode.

Parameter	Setting
Equilibration Time	2 sec
E Initial	-0.3 V
E Vertex 1	-0.3 V
E Vertex 2	0.6 V
E Step	0.002 V
Scan Rate	0.1 V/s
Number of Scans	2

The probes were cleaned using the previously described cleaning protocol and were tested at a fixed scan rate of 0.1 V/s. The probes were tested again after use in meat tissue and were considered unclean. Each of the gold electrodes acted as a working electrode so cyclic voltammograms were measured independently on the left electrode and then the right electrode each time. Variation between the two was identified by overlaying the generated plots which will be presented in the results section.

In the second set of experiments a selection of 5 probes were cleaned using the previously described cleaning protocol and were tested at a fixed scan rate 0.1 V/s. Each of the gold electrodes acted as a working electrode so cyclic voltammograms were measured independently on the left electrode and then the right electrode each time. Variation between the 5 probes was identified by overlaying the generated plots from the left electrode of each probe which will be presented in the results section. The purpose of this was to identify intra-batch variability between the different probes.

The final set of experiments conducted using CV was to determine the effect of a varying scan rate on the current response. The same electrode set-up and analyte solution was used as in the previous experiment. The parameters of the CV measurement were maintained as previously described except for the applied scan rate which was varied between 0.01 V/s and 0.1 V/s in 0.01 V increments. As in the previous experiments the left electrode was tested first and then the right electrode each time.

2.5.5.3 Electrical Impedance Testing

400 ml of water, in a glass beaker, was heated to approximately 70°C on a hotplate. A total of 56 g of powdered gelatine (Gelatine, Dr Oetker, Leeds, United Kingdom) was weighed out and added to the heated water. The solution was then stirred to ensure a homogenous mixture. A plastic lunchbox was lined with cling-film and the entire gelatine mixture was poured into it and placed in a fridge at 4°C and allowed to set until firm. 250 g of Frytex Lard (JDS Foods Ltd., Cork, Ireland) was added to a clean 600 ml glass beaker and placed on a hotplate at 190°C. The lard was stirred continuously and allowed to melt completely. The gelatine was removed from the fridge and liquid lard was poured directly on top. The lunchbox was then placed in the fridge at 4°C to allow the lard to set firm. The gel and lard slab was removed and brought to the Bioanalysis Laboratory to perform the electrical impedance measurements. Silicon probes were connected to the Autolab potentiostat and fixed frequency measurements were performed at 4,500 Hz and 10 mV peak amplitude. A total of 60 individual points were recorded each time. The probe which was initially placed in the gelatine layer

was moved to the lard layer after approximately 30 seconds. After each subsequent 30 seconds the probe was moved to the opposite layer. The purpose of this experiment was to determine if the silicon probes were capable of determining the change in electrical impedance between a conductive (gelatine) and an insulating material (lard) over time.

2.6 Results and Discussion

2.6.1 Silicon Probes

2.6.1.1 Wafer Fabrication

The patterned silicon wafers (Figure 2.19) were produced using the previously described semi-conductor fabrication methods. Visually, the patterned wafers appeared to be free of defects. The wafers were diced to release the individual probes so that they could be packaged.

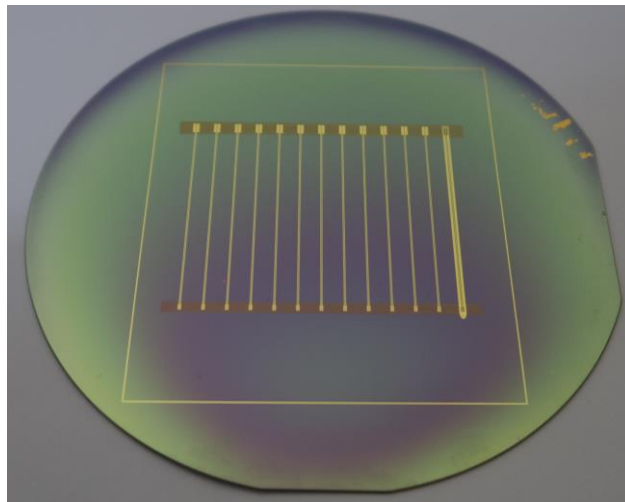


Figure 2.19: A silicon wafer after the entire deposition process had been completed.

The use of silicon wafers as the base substrate for the deposition of the gold electrodes was found to result in reproducibility across the fabrication and packaging processes. The key reason for this was the uniformity of the silicon surface which provided an exceptionally smooth surface on to which the fabricated layers were deposited. The result of this was a very high percentage of the fabricated devices were able to undergo packaging to allow them to be used for the purpose of electrical recordings. The major drawback to using a silicon substrate was the overall brittleness of the

material which meant that the finished probes were very easily broken during the cleaning and testing procedures. For this reason the long term future of the prototype will require the substitution of the silicon substrate for a more robust and biocompatible alternative.

2.6.1.2 Silicon Probe Packaging

As previously described the process of packaging the silicon devices involved a number of stages. Figure 2.20 shows three stages of the development process. On the left is a diced probe having been removed from the wafer, while the middle one is a fully shaped probe. The probe on the right was a fully packaged prototype capable of recording electrical signals.



Figure 2.20: The stages of the device packaging process including diced, shaped and electrically packaged.

2.6.1.3 Scanning Electron Microscope

The high resolution SEM images provided an idea of the surface topography of the gold electrodes and the surrounding silicon substrate. The micrographs of the silicon probes clearly illustrated the deposition of the gold across the electrode surface. The first two images in Figure 2.21 (A and B) show relatively low magnification SEM images of the gold electrodes and the underlying silicon substrate. These images showed the precision with which the electrode patterns are created as well as showing the thickness of the silicon substrate and the deposited SiO_2 . The higher magnification images (Figure 2.21 C-E) acquired using this method showed a relatively uniform layer of gold across the electrode surface. This indicated that the metal deposition used during the fabrication of the devices was satisfactory and that the devices produced were defect free. This should provide the best possible surface to perform the electrochemical and impedance testing for

which the devices were created. The use of SEM as a characterisation tool was particularly useful in assessing the metal deposition and surface topography of the stainless steel and silicon devices. The SEM images showed the cleanliness of the probe surface after the cleaning protocol had been performed. This was extremely important for future testing involving the prototype device in human and meat tissue samples. The results of the SEM imaging of the silicon probes were correlated with the results of the AFM testing which will be outlined in Section 2.6.1.6.

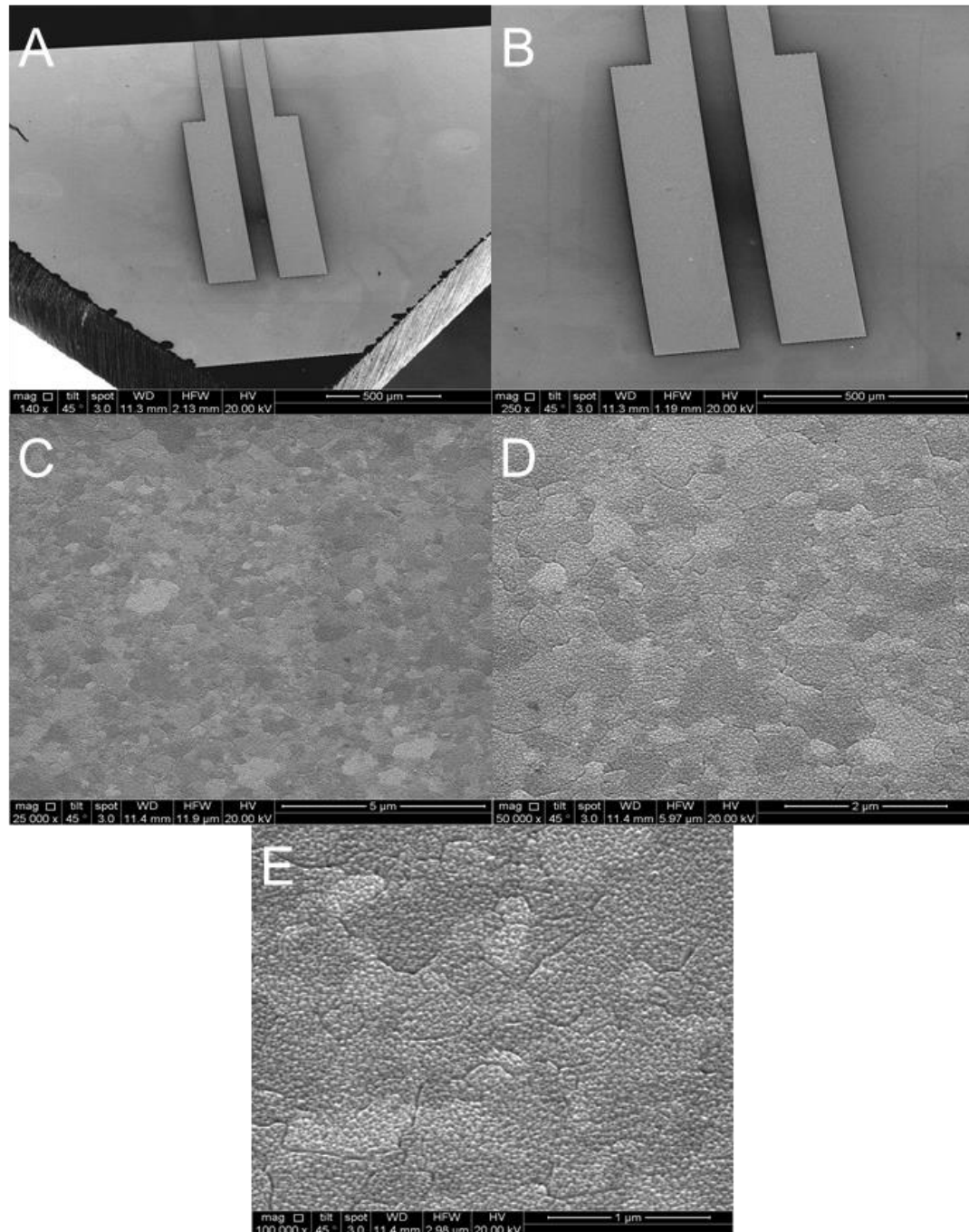


Figure 2.21: A) A 140x magnification SEM image of the gold electrode surface and underlying silicon substrate. B) A 250x magnification SEM image of the gold electrode surface and underlying silicon substrate. C) A 25,000x magnification SEM image of the gold electrode surface. D) A 50,000x magnification SEM image of the gold electrode surface. E) A 100,000x magnification SEM image of the gold electrode surface.

2.6.1.4 Energy-dispersive X-ray Analysis

The EDX unit was used in conjunction with the SEM to analyse the surface material of the electrodes patterned on the silicon substrates. The surface of one electrode was measured on two different silicon probes and the spectra

produced are shown in Figure 2.22 A and B. The peaks which were determined show the presence of gold, silicon and potentially titanium. These results were to be expected as gold was the deposition metal used to pattern the electrode, titanium was used as an adhesion layer for the gold and silicon is the major substrate upon which the probes were created. The spectra produced on the different probes were almost identical which was a positive result as it proved that the multiple deposition processes used during the device fabrication resulted in uniform layers across the surface of both of the electrodes.

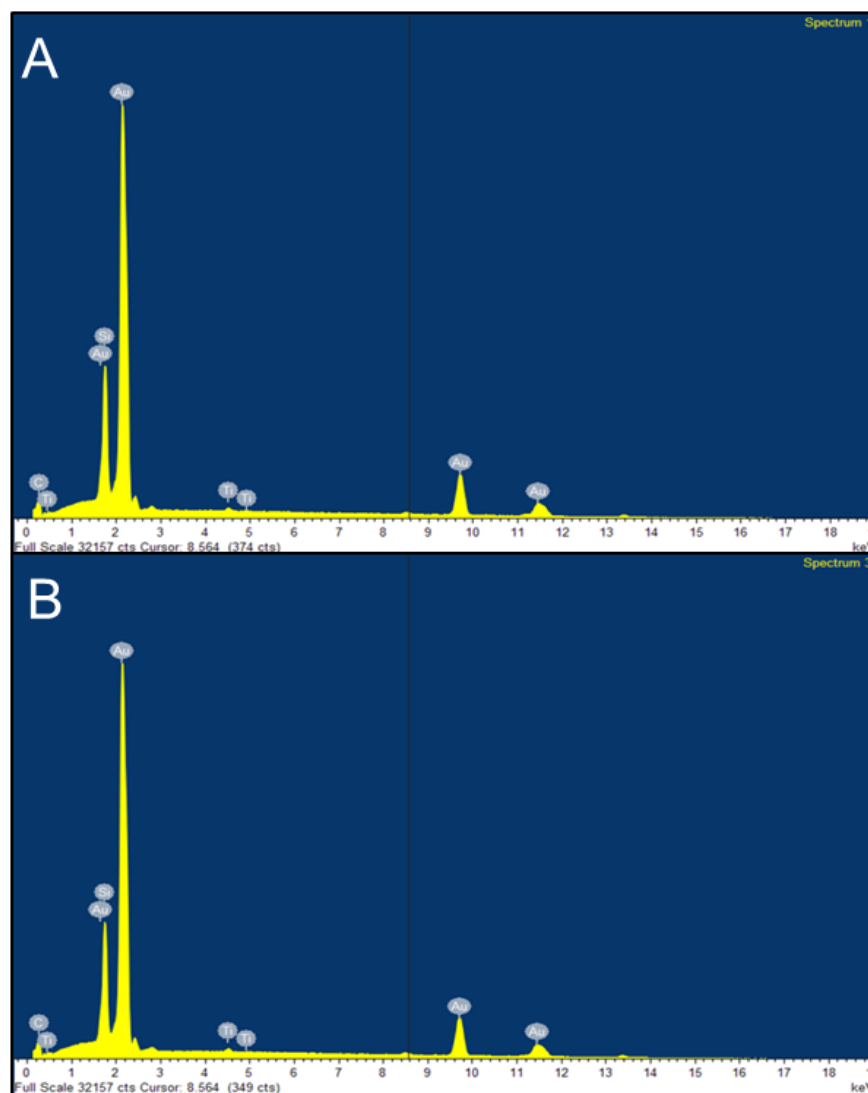


Figure 2.22: A) The EDX spectrum of the surface of a gold electrode from a silicon probe. B) The EDX spectrum from the surface of a gold electrode on a different silicon probe from the one analysed in A).

2.6.1.5 Focused-ion Beam

The area that was milled during the FIB procedure was imaged using an SEM to obtain the highest resolution image possible. The use of this technique allowed for the approximation of the individual layer thickness of each of the deposited materials on the silicon substrate. This provided a cross-sectional image of each layer of the probe. It was then possible to estimate the true thickness of each layer which could then be compared to the specified value. Figure 2.23a showed the area which was etched out using the FIB instrument. The area of platinum overlaid on the gold electrode surface was used to provide contrast during the SEM imaging.

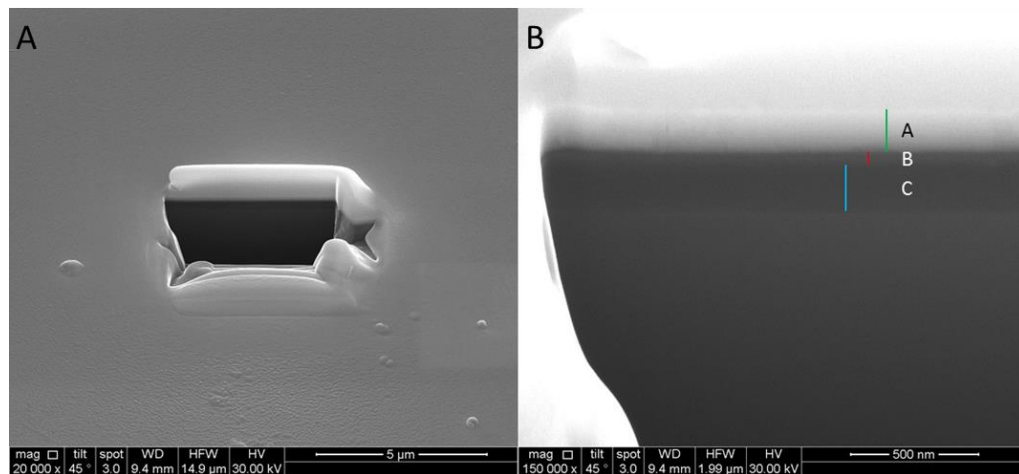


Figure 2.23: A) A 20,000x magnification SEM image of the focused-ion beam milling site on the gold electrode. B) A 150,000x magnification SEM image of the hole milled using the FIB instrument. The approximate layer thickness of the gold (A), titanium (B) and SiO₂ (C) layers are also shown.

The SEM image used for the determination of the layer thickness was taken at 150,000x magnification. Figure 2.23b shows the approximate dimensions of each of the layers that could be visualised using this technique. The topmost layer is the gold electrode which should have been 220 nm thick. The approximate thickness of the gold was 239.0 nm. As this value was only an approximation of the true value it was possible that the real thickness was closer to that of the target 220 nm. The layer immediately below the gold was titanium which was used as an adhesion layer for the gold. The approximate thickness of this layer was measured as 63.20 nm. The theoretical height of this layer was 20 nm. The final layer which could be visualised in this image

was the underlying insulation layer of SiO₂. The estimated value obtained during the SEM measurement is 263.8 nm while the target value was 300 nm. All of these approximations of layer thickness were close to the specified values that were planned in the fabrication protocol at the outset of the production process (Table 2.7). This technique provided an insight into the accuracy of the metal deposition process and also estimated the real dimensions of the material layers.

Table 2.7: The theoretical and approximate values of the deposition layers observed on the silicon probes using SEM imaging.

Deposition Layer	Target Value (nm)	SEM Image Value (nm)
Gold	220	239
Titanium	20	63
Silicon Dioxide	300	263

2.6.1.6 Atomic Force Microscopy

The use of AFM in this project was to determine the approximate surface roughness of the gold electrodes after fabrication. This provided an indication of the relative uniformity of the gold across the probe surface. The major benefit of using the AFM was the ability to obtain a quantitative measurement of the surface roughness of the gold electrode which could be correlated with the surface topography imaging provided by the SEM technique. A total of 20 measurements across 10 different areas on two electrodes were performed. Images were obtained to show the probe location at each of the recording sites. Figure 2.24 shows the silicon cantilever at the site of the first recording on the gold electrode.

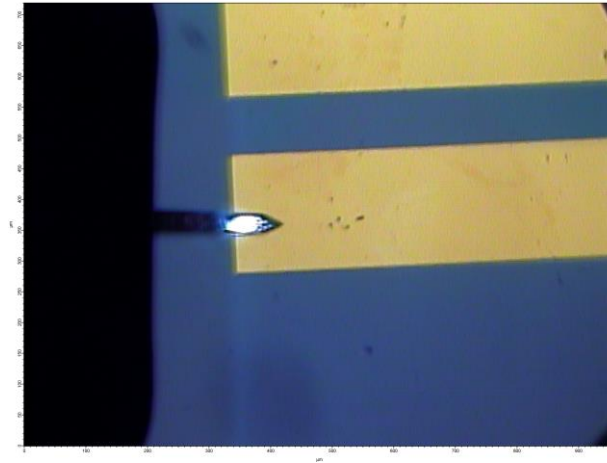


Figure 2.24: The position of the AFM cantilever during one of the measurement recordings.

For each of the recordings performed a two-dimensional grey scale image was produced which represented the total deflection encountered by the AFM probe tip as it moved across the surface. Figure 2.25 shows a representative grey scale image from one of the scans performed across a $25\ \mu\text{m}^2$ area of the gold electrode.

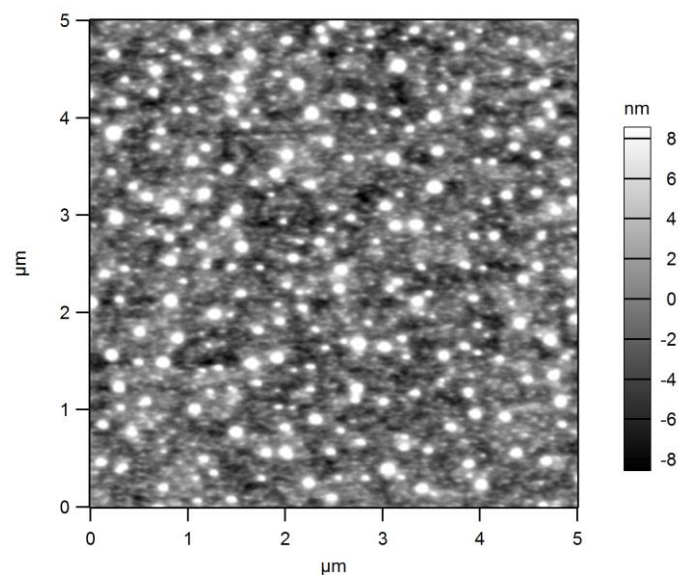


Figure 2.25: A representative image from one of the AFM scans performed on the gold surface of the silicon probe.

The calculated RMS data obtained from each of the AFM scans was averaged for each of the measurement sites and then averaged to produce a combined value for each of the electrodes. The RMS roughness is similar to the roughness average, with the only difference being the mean squared

absolute values of surface roughness profile [37]. These values were then graphed as the $\text{RMS} \pm \text{Standard Deviation (S.D.)}$ for each of the individual electrodes (Figure 2.26). The mean values for the left and right electrodes were 5.0 nm and 4.9 nm respectively. These values correlated well with the images obtained from the SEM which showed that the deposition of gold across the electrode surface was extremely smooth. The combination of the data obtained from both the AFM and SEM showed that fabrication of the gold electrodes on the silicon substrates was successful. As a result, the electrode surface should be suitable for electrochemical recording as it is defect free and should act as a planar electrode during recording. Any significant deviation in the surface roughness of the electrode would change the total surface area of the electrodes and would impact on the recordings obtained using that electrode.

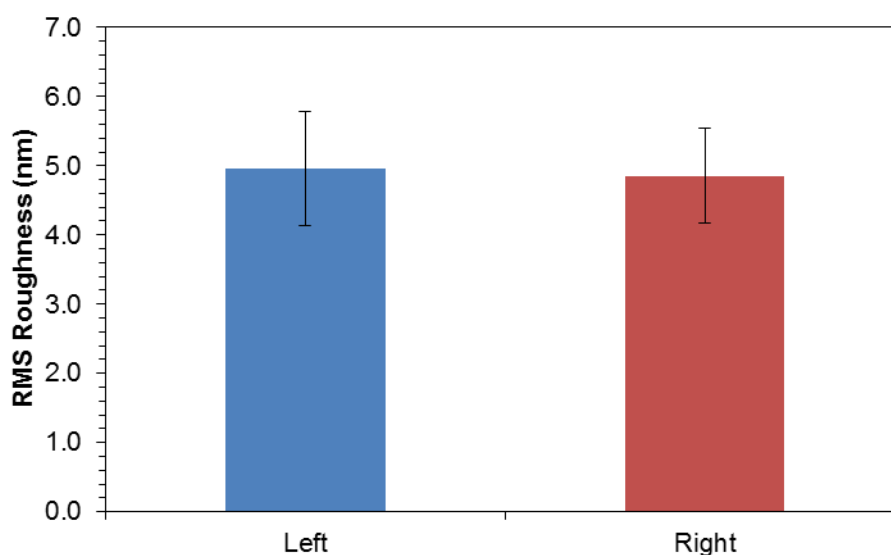


Figure 2.26: The mean RMS roughness of the left and right electrodes obtained using AFM. $N=1$; Mean \pm S.D.

2.6.1.7 Breakage Tests

The breakage analysis testing was performed using an Instron 5960 dual column testing system. Each of the silicon devices were placed upright between the two plates of the machine on which the force was applied (Figure 2.27).

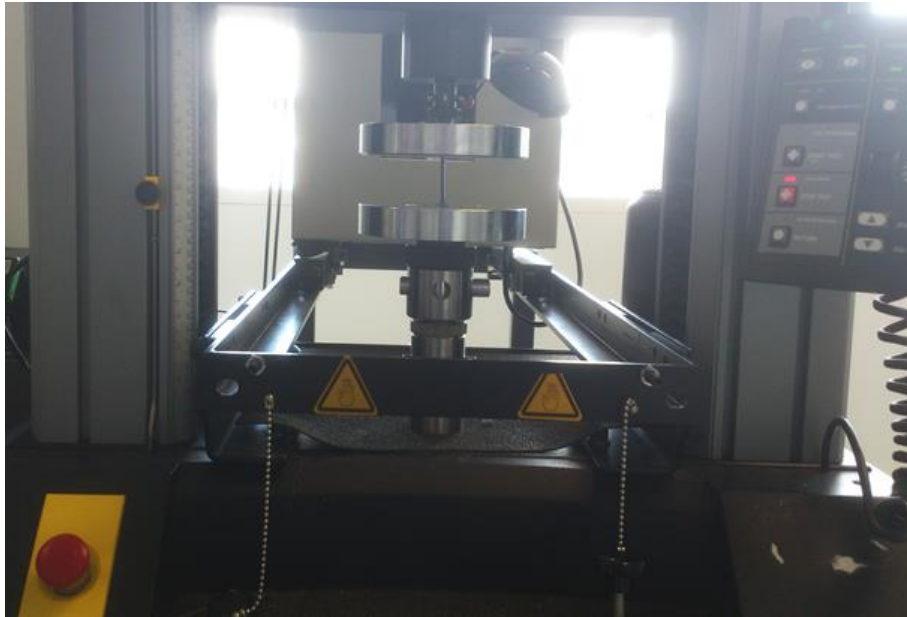


Figure 2.27: A silicon probe held in position between the two plates of the Instron force testing instrument.

The results of a number of probe breakages can be seen in Table 2.8. The figures obtained from 5 separate probes showed a mean value of 50.39 N of force applied to produce a critical failure in the devices. This was an approximation of the true breaking strength of the silicon probes when the force was applied directly on the pointed tip in a vertical direction. This setup was used to replicate the force which would be applied to the tip of the probe when it was inserted in to *ex vivo* tissues which would be the most likely cause of failure in each of the devices. The variability in the results obtained may have resulted from the initial set-up of the probes in the testing instrument. The devices were placed in the machine by hand and approximately vertical to the base plate. Minor variations in the angle of applied force may account for the differences in the results presented in Table 2.8.

Table 2.8: The values of the applied force in Newton obtained during the silicon probe breaking force tests.

Probe	Force Applied (N)
1	47.33
2	48.66
3	42.75
4	58.45
5	54.74
Mean	50.39
Standard Deviation	6.22

The results obtained for the silicon probe could be compared to future prototype devices to demonstrate if the new devices have a higher breakage threshold. This would indicate that the device would be more capable of being inserted directly in to *ex vivo* tissues.

2.6.1.8 Cyclic Voltammetry

Cyclic voltammetry measurements were performed to determine the effective charge transfer at the electrode surface for each of the packaged devices. The electrochemical response of the gold electrode devices was analysed using the accepted technique of CV [38, 39]. The first set of experiments was designed to show the effect of fouling on the surface of the electrode as a result of experimental use in the testing of meat tissues and to validate the effect of the cleaning protocol applied prior to testing. Voltammograms were obtained at a scan rate of 0.1 V/s for each electrode. Two sweeps were performed each time and the second one was graphed for each electrode. The overlay of the left and right electrodes showed extremely similar scans which showed good stability across both (Figure 2.28).

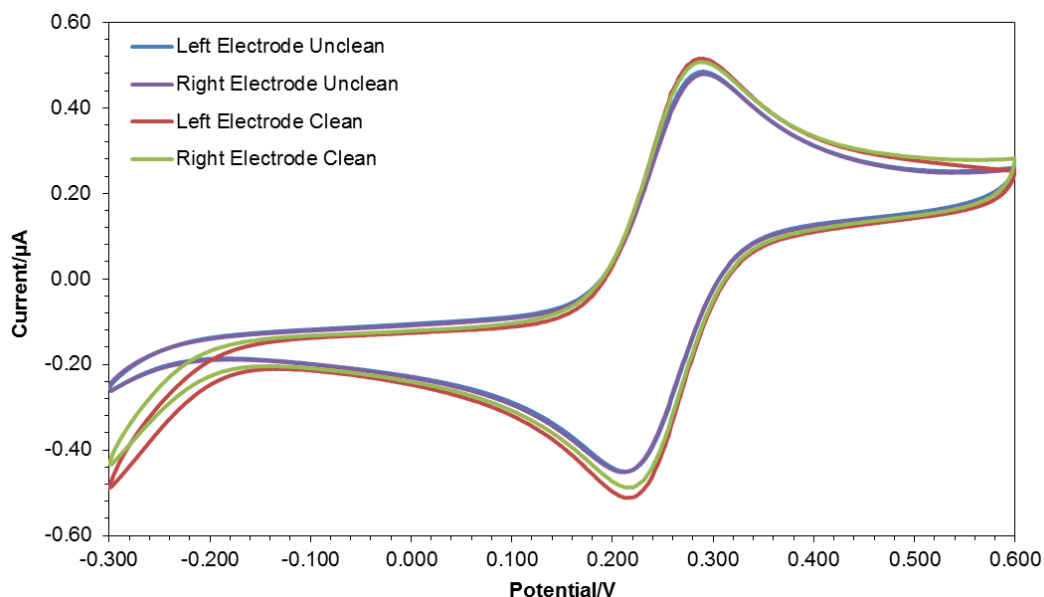


Figure 2.28: A cyclic voltammogram of the left and right electrodes of a gold probe prior to cleaning and directly after cleaning. The cleaning protocol resulted in an increase in both the anodic and cathodic peak currents.

An increase in both the anodic and cathodic peak currents can clearly be seen. The difference in the peak currents was used to determine if imperfections or contaminations existed at the electrode surface. The theoretical value achievable for single electron transfer reactions, such as in the $[\text{Fe}(\text{CN})_6]^{3-/4-}$ couple, on a perfect gold surface should $\Delta E = 58 \text{ mV}$ [30, 40]. The differences between the anodic and cathodic peaks are shown in Table 2.9. The values for the left and right electrode after cleaning was 0.062 V (62 mV) and the value for the unclean electrodes was 0.07 V (70 mV). Both of the clean electrodes showed an improvement of 8 mV compared to the unclean electrodes. This indicated that the cleaning protocol used was effective at removing surface contaminants which resulted in an increase in electron transfer across the electrode surface. The ΔE obtained for the clean electrodes of 62 mV compares favourably with the theoretical value of 58 mV which could be achieved for a perfect gold surface. These results indicated that the surfaces of the electrodes tested were virtually free of imperfections and that cleaning protocol was effective at removing surface contaminants.

Table 2.9: The anodic and cathodic peak voltages and peak differences of the clean and unclean electrodes measured using cyclic voltammetry.

Electrode Status	Peak	Peak Voltage (V)	$\Delta E = \Delta E_A - \Delta E_C$
Left Electrode Clean	Anodic	0.282	0.062
	Cathodic	0.22	
Left Electrode Unclean	Anodic	0.286	0.07
	Cathodic	0.216	
Right Electrode Clean	Anodic	0.282	0.062
	Cathodic	0.22	
Right Electrode Unclean	Anodic	0.286	0.07
	Cathodic	0.216	

The second experiment was designed to demonstrate the intra-batch variability that was present across probes fabricated from the same batch. These probes were all packaged at the same time using the previously described method. Each of the cleaned probes was scanned in 5 mM Ferri/Ferrocyanide in 1 M KCl, as previously described, at a rate of 0.1 V/s. The second scan from each of the five probes was overlaid and the results are shown in Figure 2.29.

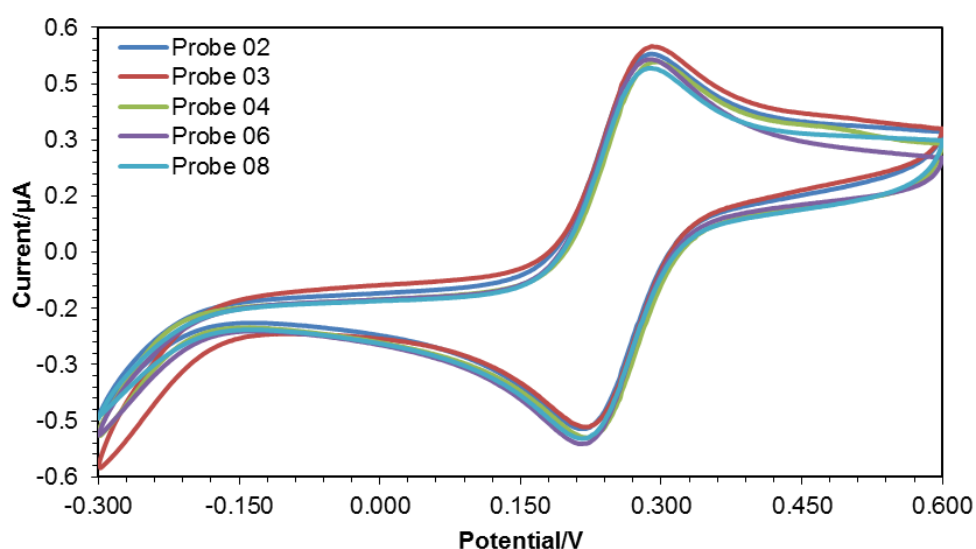


Figure 2.29: The overlaid CV graphs from the left electrode of 5 silicon probes from the same batch.

The peak potential values for each of the anodic and cathodic peaks were calculated and the ΔE was determined (Table 2.10). The maximum peak difference observed was probe 3 (0.068 V) while both probe 6 and 8 showed a difference of 0.062 V. The difference between the highest and lowest ΔE values observed is 0.006 mV which is a percentage difference of 9.7 which should not significantly affect the observed values during experimental recordings.

Table 2.10: The peak anodic and cathodic potentials and differences for the five silicon probes from the same batch scanned at a rate of 0.1 V/s.

Probe No.	ΔE_A	ΔE_C	$\Delta E = \Delta E_A - \Delta E_C$	% Difference
2	0.286	0.22	0.066	6.5
3	0.29	0.222	0.068	9.7
4	0.29	0.224	0.066	6.5
6	0.282	0.22	0.062	0
8	0.282	0.22	0.062	0

The final set of experiments conducted using CV was to determine the effect of varying scan rate on the peak current response of the probe. If the transfer of electrons at the electrode surface is diffusion controlled then there will be a linear relationship observed between the peak current and the square root of the scan rate. The same electrode set-up and analyte solution was used as in the previous experiments. The applied scan rate was varied from 0.01 V/s to 0.1 V/s in 0.01 V increments. A total of two scans were performed at each rate and the second scan each time was used to graph the current versus potential. The left and right electrodes were graphed in Figure 2.30a and 2.31a respectively. It can clearly be seen from each of the graphs that the peak current achieved in each of the scans shows a step wise increase with respect to increasing scan rate. This was an expected result as an increase in scan rate should produce an increase in peak current [28, 41]. As in the previous experiment investigating the cleaning protocol and fouling, the probes tested showed extremely stable quasi-reversible curves at each scan rate analysed. This was a positive result as it showed that the prototype devices could obtain stable recordings across the measurement parameters.

In order to determine the linearity of the current response to varying scan rate the peak current values were graphed versus the square root of the scan rate for the left and right electrodes respectively (Figure 2.30b and 2.31b). By observing the peak currents of the $[\text{Fe}(\text{CN})_6]^{3-/4-}$ reaction in figures 2.30a and 2.31a it is clear to see that the electron transfer at the surface of the gold electrodes undergoes a quasi-reversible one-electron redox reaction. Both the left and right electrodes which were measured independently of each other showed a linear relationship between peak current and the square root of the scan rate when varied between 10 mV/s and 100 mV/s (Figure 2.30b and 2.31b).

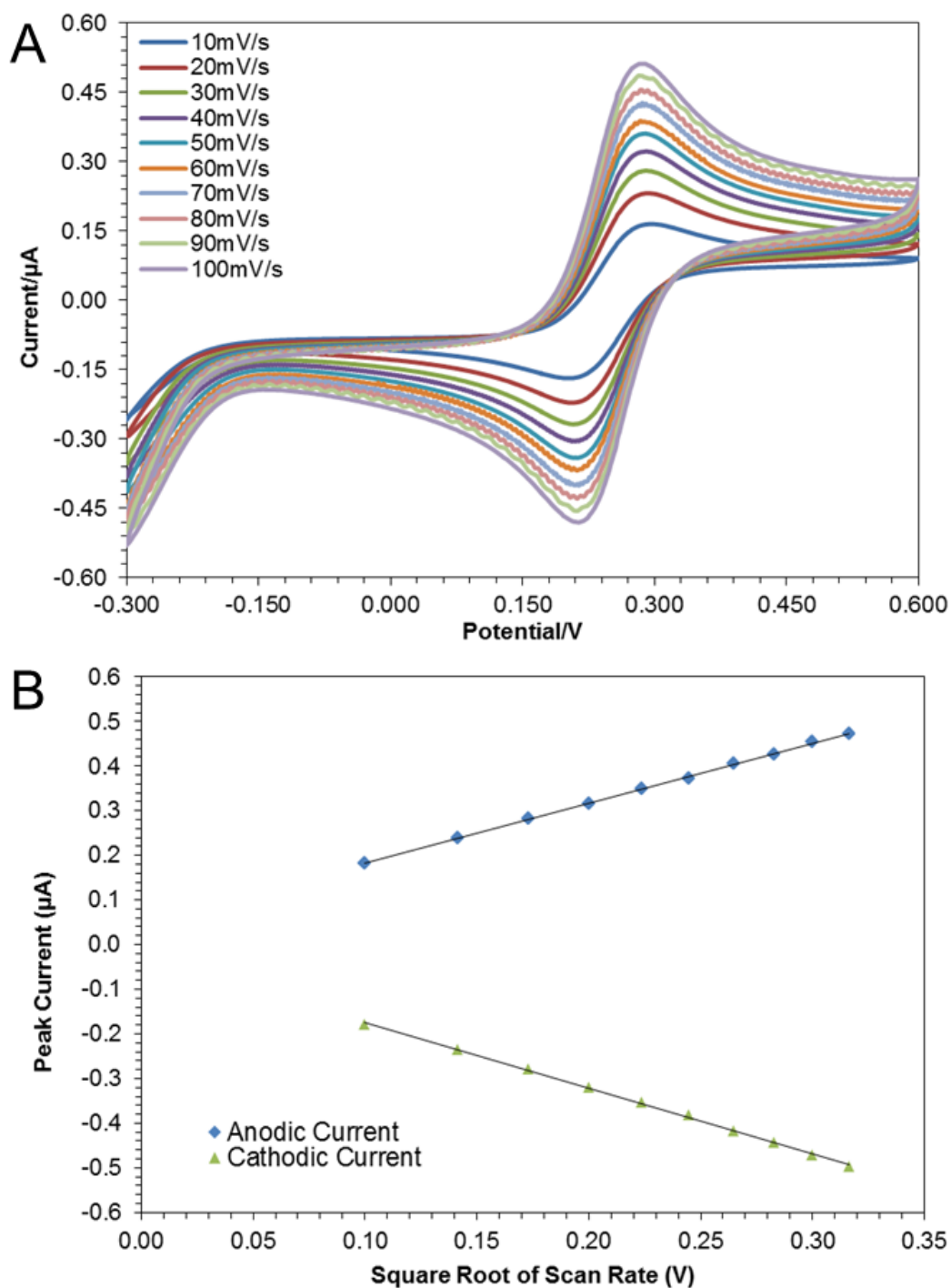


Figure 2.30: A) Cyclic voltammograms of a left working electrode displaying an increase in peak current with increasing scan rate from 10 mV/s to 100 mV/s. B) A graph of the redox peak currents -v- the square root of the scan rate from 10 mV/s to 100 mV/s.

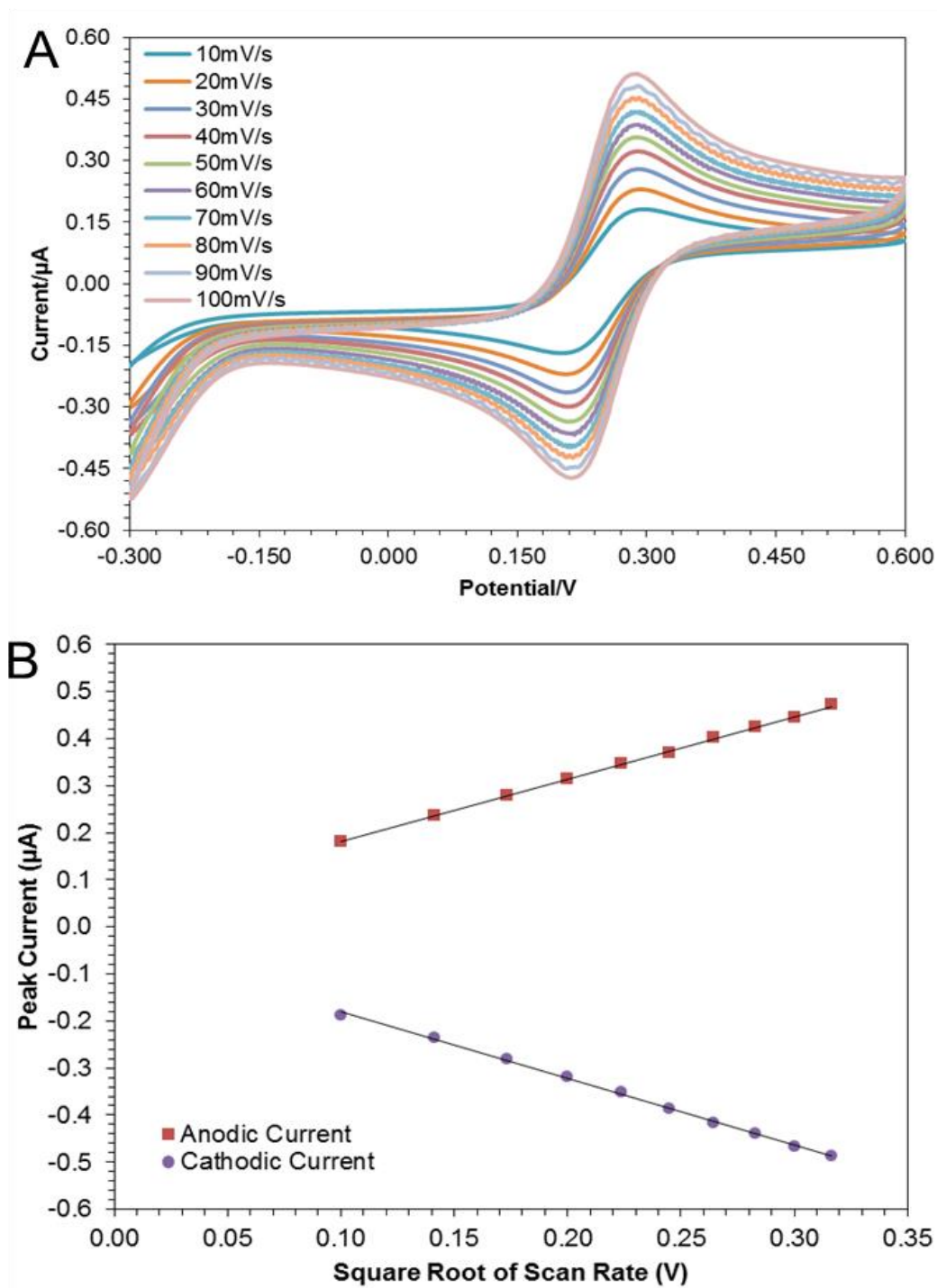


Figure 2.31: A) Cyclic voltammograms of a right working electrode, from the same probe as in Figure 2.34, which shows the increase in peak current with increasing scan rate from 10 mV/s to 100 mV/s. B) A graph of the redox peak currents -v- the square root of the scan rate from 10 mV/s to 100 mVs.

Table 2.11: The linear regression equations for the anodic (I_{pa}) and cathodic (I_{pc}) peak current -v- square root of the scan rate for the left and right working electrodes for a gold probe. The test solution used was 5mM $[Fe(CN)_6]^{3-/4-}$ in 1 M potassium chloride (KCl).

Electrode	Linear Regression Equation	R^2 Value
Left	$I_{pa} (\mu A) = 1.3443x + 0.0483$	0.9995
	$I_{pc} (\mu A) = -1.4768x - 0.0269$	0.999
Right	$I_{pa} (\mu A) = 1.3283 + 0.0487$	0.9996
	$I_{pc} (\mu A) = -1.4216x - 0.0373$	0.9987

The results shown here indicated that the electron transfer process was diffusion controlled across both the left and right electrodes (Table 2.11). The differences in peak heights were 1.013 and 1.016 μA for the left and right electrodes respectively. This showed that there was no significant variation between the electro-active surface areas of either to the two electrodes. This was to be expected as the initial design was the same for both. It also indicated that the metal deposition process did not differ significantly between the left and right side of the probe. This meant that either of the electrodes could be used as the working electrode in a two- or three-electrode system.

Cyclic voltammetry was the technique used to assess the viability of the prototype probes for use as electrical recording devices. The experiments were able to show the effective current transfer across the two electrodes which resulted in a complete electrical circuit being created. They were also used to demonstrate the effect of the cleaning protocol on electron transfer as well as demonstrate the linear relationship between the peak current and a variable scan rate. Finally, the CV technique was used to demonstrate the intra-batch variability in the probes. When the peak currents obtained were compared with the theoretical values for gold electrodes there was only a 6 mV difference between the two. This shows that the surface of the gold electrodes tested was in extremely good condition and the cleaning protocol was efficient at removing surface contamination. The use of CV to determine the electrochemical characteristics is a widely accepted technique that can produce a significant amount of information about each electrode tested. In

relation to this project the most significant finding was the comparability between the left and right electrodes of each probe which showed little to no difference electrochemically. This meant that it did not matter whether the left or right electrode was used during an experiment as they would produce almost identical results. It was also shown that individual probes from the same fabrication batch showed differences in the peak voltage of less than 10% when measured at the same scan rate after cleaning. This finding in combination with the surface characterisation techniques previously discussed show that the prototype device fabrication methods produced stable and reproducible probes which could be used for the purpose of recording electrochemical signals during future experimental testing.

2.6.1.9 Electrical Impedance Testing

The final experiment in this section was carried out to determine the sensitivity of the silicon probes when moving between layers of different conductivity. The materials chosen to create the layers were gelatine and lard. These were used because of the significant difference in the expected modulus of the impedance between the two materials. The left and right electrodes of three probes were tested in triplicate. The average value for one probe is shown in Figure 2.33. Figure 2.32 shows a silicon probe inserted in to the gelatine layer during the electrical impedance testing experiment. The layer of lard (white) can clearly be seen immediately above the gelatine layer (orange).

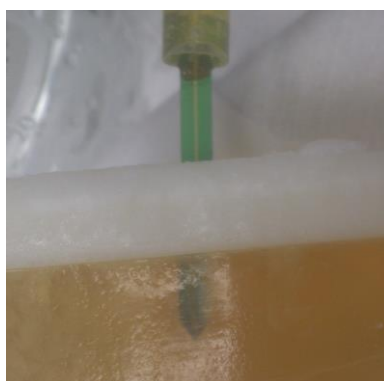


Figure 2.32: A silicon probe inserted in to the gelatine (orange) and lard (white) model during the electrical impedance testing.

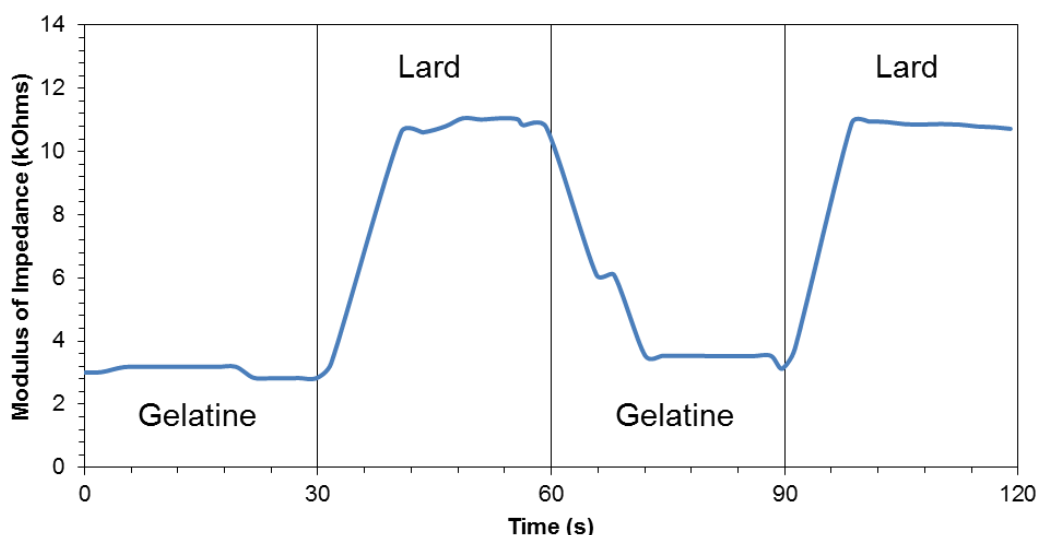


Figure 2.33: The average of the fixed frequency (4,500 Hz) recordings obtained as one of the silicon probes was moved between layers of gelatine and lard at 30 second intervals.

The results displayed here showed that the silicon probe was extremely good at detecting the change in the modulus of the impedance at the tip of the device immediately after it was moved. This was a positive result as it showed that the probes were able to maintain a steady state of recording in a homogenous substance while instantly detecting a change upon probe movement. It is possible that there was some carry-over of material when the device was moved from one layer to the other. However, from the data presented this does not appear to have affected the probes ability to detect the change the layer impedance. The major obstacle in this experiment was the Autolab potentiostat instrument. This apparatus did not allow each of the fixed frequency measurements to be taken at set time intervals. This meant that the repeated recordings had a different number of data points accounting for the 120 second period after the initial recording. In order to overcome this problem the recordings were divided into four sections according to the corrected time value determined by the Nova 1.10 software (Table 2.12).

Table 2.12: The corrected time values for each of the gelatine and lard layers tested.

Layer	Corrected Time (s)
Gelatine (1)	0-30
Lard (1)	31-60
Gelatine (2)	61-90
Lard (2)	91-120

The corrected time value for each data point was averaged across each of the triplicate recordings to provide a uniform value for the graph of the average impedance values. For future testing involving the Autolab instrument it would be necessary to design a protocol for the fixed frequency recordings that would be more suitable for multi-layer testing such as this. A period of adjustment after the movement of the probe to the lard layer was clearly evident in most of the recordings as the potentiostat adjusted to the significant change in the impedance of each layer. This resulted in some recordings being as many as 10 seconds apart which would be unacceptable in the clinical setting in which we envisage these probes being used.

2.6.2 Stainless Steel Probes

The development of a prototype electrical impedance device involved a number of different strategies. One of these strategies was to fabricate used a stainless steel substrate deposited with gold electrodes. Figure 2.34 shows a stainless steel wafer that was patterned with 12 pairs of gold electrodes and passivated probe tracts. In the first fabrication run using the stainless steel wafers an insulation layer of 250 nm of SiO_2 was deposited on to the surface. It was discovered after the fabrication process was completed that the deposition process had not been successful due to short-circuits present in the probes. It was suspected that the insulation layer deposited on to the stainless steel was not sufficient to provide to isolate the substrate from the electrode metals. It was decided to increase the SiO_2 layer thickness to $1\mu\text{m}$ in order to try and produce a usable prototype stainless steel impedance probe. The increase in insulation layer thickness did not prevent the short-circuiting of the probes when tested using a multimeter device which will be

described in a later section. Further analysis of the probes surface using SEM imaging was undertaken to determine if a cause of the short-circuiting could be determined and the results of this will be presented in a later section in this chapter. Dicing of the wafer proved to be particularly difficult given the hardness of the stainless steel and specialist cutting blades were required for this task. It was not possible to shape the recording ends of each of the probes which would have aided the insertion of the prototypes into tissue samples.

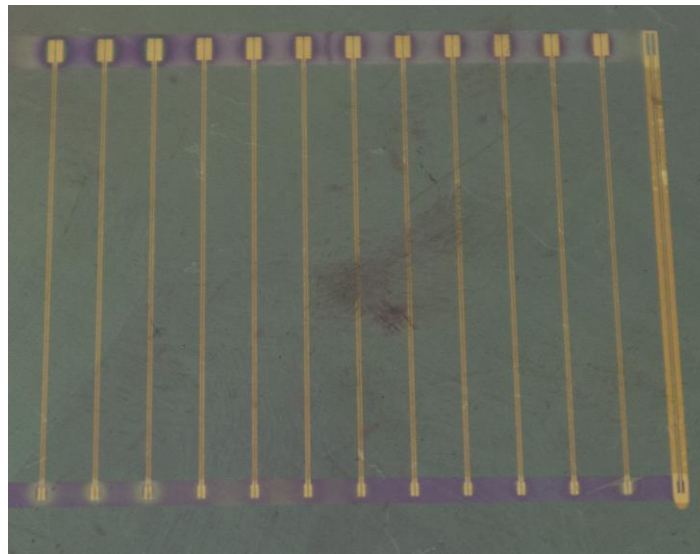


Figure 2.34: A close-up view of a patterned stainless steel wafer with 12 electrode pairs.

2.6.2.1 Scanning Electron Microscope

The fabricated stainless steel probes were imaged using the SEM to determine the cause of the short-circuiting in the devices. Figures 2.34 and 2.35 show a selection of the high-resolution micrograph images obtained from the patterned stainless steel probes. Figures 2.35 A and B showed the electrode surface of a stainless steel probe at 288 and 1,500x magnification. A significant defect in the gold electrode surface could clearly be seen and was measured as having an approximate diameter of 29.92 μm . This defect penetrated through the entire thickness of the gold and possibly the underlying titanium layer as well. This type of defect would certainly be significant enough to cause a critical short-circuit in the packaged devices.

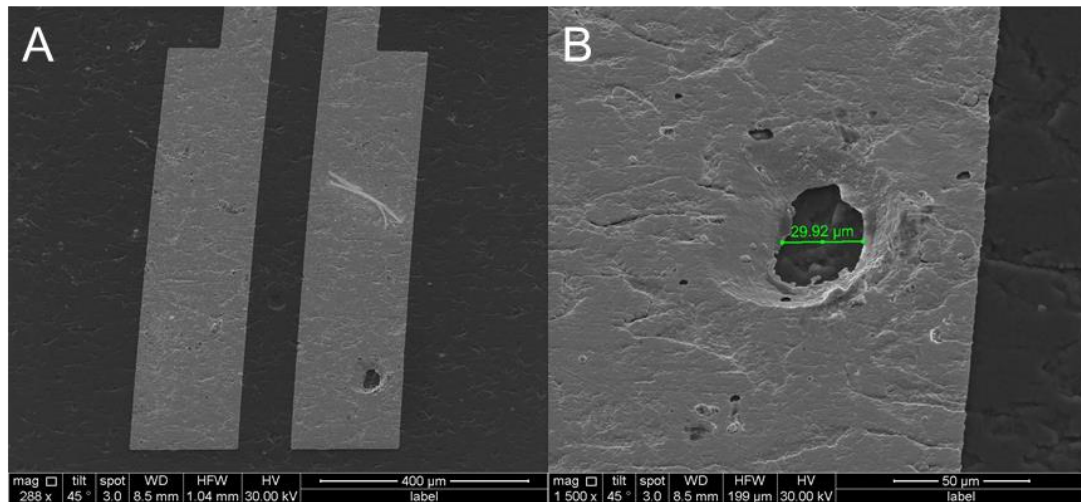


Figure 2.35: A) A 288x magnification SEM image of the recording electrode pads of a stainless steel prototype device. B) A 1,500x magnification SEM image of a surface defect identified in the left electrode of the stainless steel probe imaged in A). An approximate measurement of the width of defect is displayed on the image.

Figure 2.36 showed a 305x magnification image of the dual gold tracks of a stainless steel device. It was clearly evident that the gold was not continuous along the entire length of either track. The insulation layer which was deposited over the gold electrode tracks should have protected the gold from significant mechanical damage. Therefore, it was possible that either the damage occurred during the fabrication process before the insulation layer was deposited or that the underlying materials did not provide a suitable attachment point for the gold. It was clearly evident from the image that the gold tracks were not continuous and would not be capable of conducting an electrical signal from the recording electrodes to the output electrodes at the opposite end of the probe.

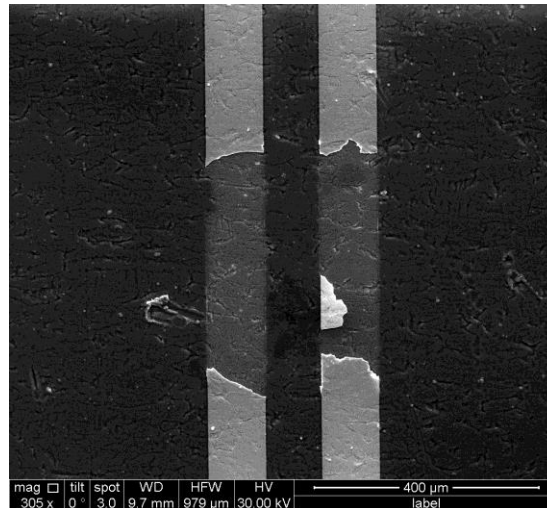


Figure 2.36: A 305x magnification SEM image of the insulated gold tracks of a stainless steel probe.

From the SEM micrographs it was clear to see that a number of critical defects were present in the devices that were imaged. The images obtained of the surface of the stainless steel probes showed significant defects in the gold electrode pads and tracts as well as the surrounding substrate. It was hypothesised that the cause of the short circuiting of the stainless steel probes was as a result of these critical defects distributed across the probe surfaces. These defects produce a path of least resistance along which the electrical current can flow which prevents the recordings being obtained for the recording electrodes. Optical profilometry of the bare stainless steel wafers was conducted to investigate this hypothesis and the results are presented in Section 2.6.2.4.

2.6.2.2 Energy-dispersive X-ray Analysis

An EDX detection unit was used in conjunction with the SEM to analyse the materials presents on the surface of a stainless steel probe. A spectrum was produced by analysing the surface of one of the gold electrodes deposited on the substrate (Figure 2.37).

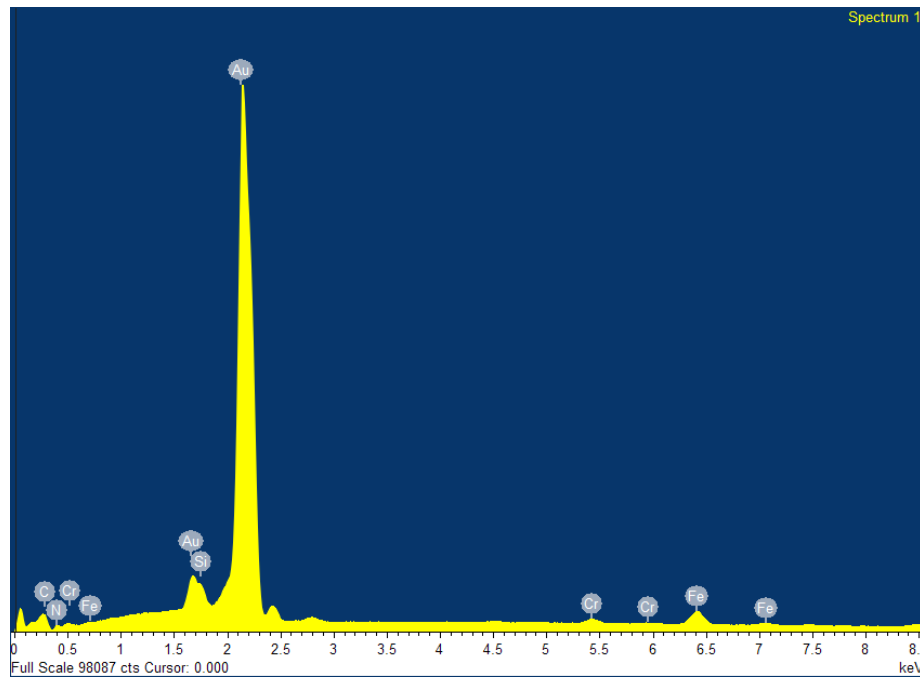


Figure 2.37: An EDX spectrum of a gold electrode on a stainless steel substrate.

The peaks which were determined showed the presence of gold, silicon, chromium, iron, carbon and nitrogen. These results were as expected because gold was the deposition metal used to pattern the electrode and stainless steel was the major substrate upon which the probes were created. The exact composition of stainless steel varies depending on its manufactured grade but will certainly include a mixture of iron, carbon and chromium. The spectra produced on the different probes analysed were almost identical to the one displayed. This was a positive result as it meant that the multiple deposition processes were successful in patterning the required materials on to the substrate surface.

2.6.2.3 Continuity Testing

Using the previously described protocol (Section 2.5.3), the multimeter probe was used to test the continuity of the electrical tracks and identify any possible short-circuits. This test was used as a qualitative analysis of the electrical conductivity of the stainless steel probes. As a result, quantitative data was not collected. Any of the probes which were identified as having an issue with continuity were discarded as they were not suitable to be packaged for performing electrical recordings. The initial batch of patterned

stainless steel wafers contained no functional probes which indicated that there was a significant issue with the fabrication process. In order to overcome this problem it was decided to increase the thickness of the insulation layer deposited during the fabrication process. However, an increase in the thickness of the SiO₂ insulation layer from 250 nm to 1 µm was not sufficient to prevent this problem. It was possible that the thickness of the materials deposited on the surface of the stainless steel was not sufficient to overcome a very large surface roughness of the stainless steel wafer.

2.6.2.4 Optical Profilometry

Optical Profilometry was used to quantitatively assess the surface roughness of the bare stainless steel wafer used in the fabrication process. The major benefit of using the optical profilometer was the ability to obtain a measurement of the surface roughness which could not be done using AFM as described for the gold electrodes on the silicon probes. A total of 5 measurements across 4 different areas one stainless steel wafer were performed. For each of the recordings performed a two-dimensional colour image was produced which represented the combined constructive and destructive interference from the light reflected from the surface of the wafer and the reference mirror. Figure 2.38 shows a representative image from one of the scans performed across a 0.091 mm² area of the stainless steel surface.

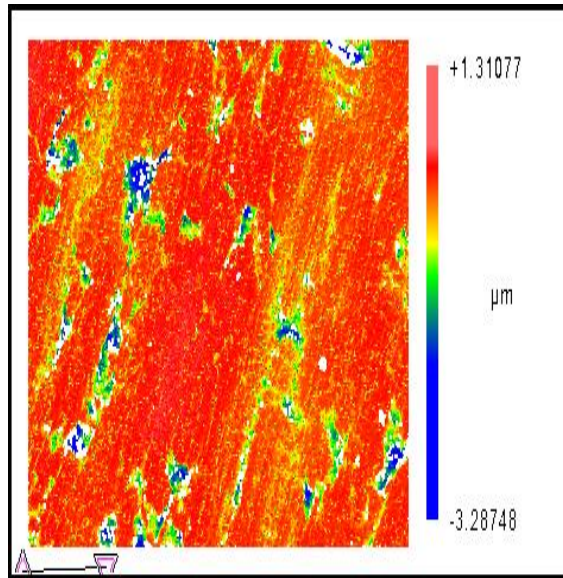


Figure 2.38: A representative image from one of the optical profilometry scans performed on the surface of the bare stainless steel wafer.

The values obtained from each of the five measurements were averaged to show the surface topography profile across the stainless steel wafer. The maximum height difference across the recorded areas was 1.01 μm . The graph showed that the surface of the stainless steel wafer contained many significant peaks and crevices which could inhibit the deposition of material on to the surface during fabrication (Figure 2.39).

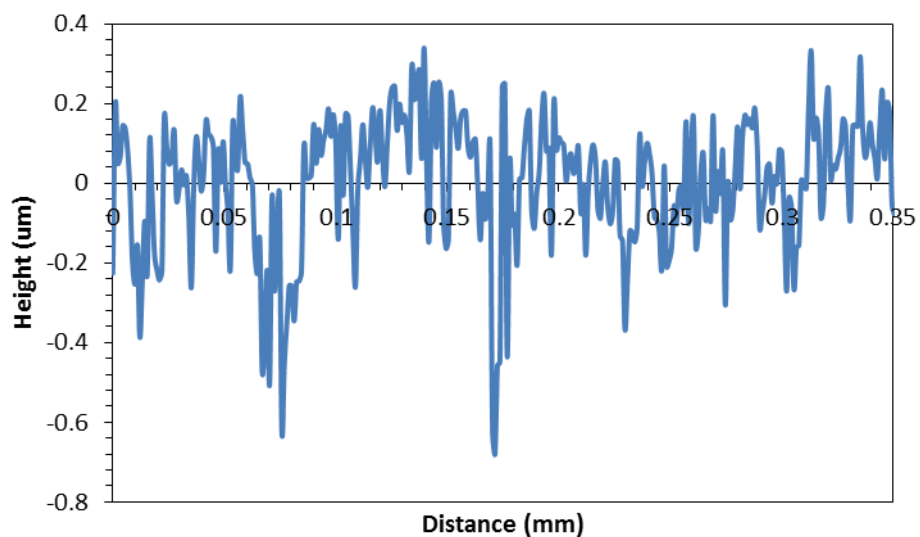


Figure 2.39: A graph of topographical profile of the surface of the bare stainless steel wafer.

The calculated RMS data obtained from each of the optical profilometer scans was averaged for each of the measurement sites and then averaged to produce a combined value for surface of the stainless steel. This value was then graphed as the $\text{RMS} \pm \text{S.D.}$ (Figure 2.40). The mean value for the stainless steel wafer was 314 nm. This value correlated well with the images obtained from the SEM which showed that the deposition of gold across the electrode surface was significantly inhibited and may have been as a result of the initial surface roughness of the stainless steel wafer.

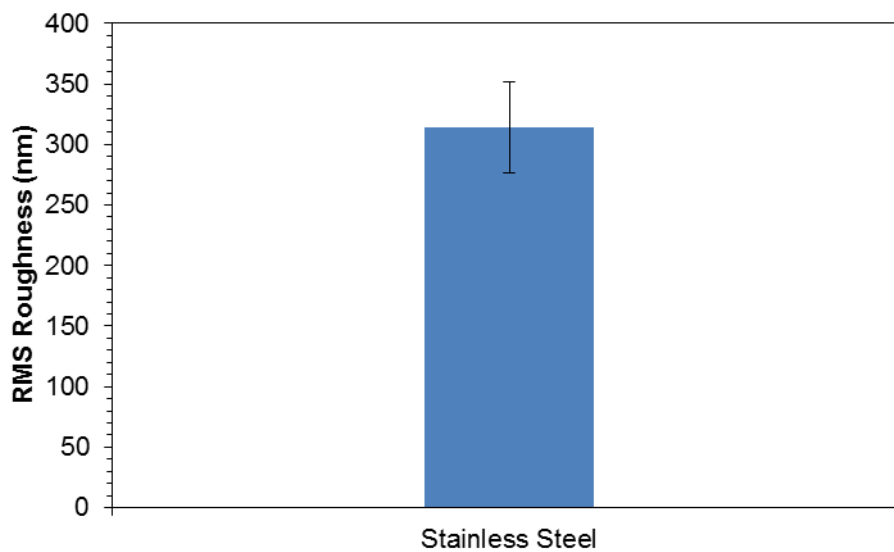


Figure 2.40: The mean RMS roughness of the surface of the stainless steel wafer obtained using optical profilometry. $N=1$; Mean \pm S.D.

2.6.2.5 Breakage Testing

It was hoped that breakage strength testing could be performed on the stainless steel probes. This was not possible as the application of vertical force on to the stainless steel would not result in a critical failure of the device. Therefore, it was not possible to conduct this analysis and it was not possible to compare the values obtained for the silicon probes to the stainless steel ones.

2.7 Conclusions

In this chapter a novel microelectrode for use in testing biological tissues was fabricated on to silicon and stainless steel substrates using semiconductor fabrication techniques including photolithography and etching [1, 42-44]. The

configuration included two gold microelectrodes. One of the most significant obstacles encountered during the course of this entire project was the issue of device construction using stainless steel as the base substrate. The original concept was to use metal deposition processes to pattern the dual-electrode structure on to off-the-shelf hypodermic needles. This would have provided a sufficiently strong base material that would also have been suitable for use in the clinical environment. The first problem that was encountered was that the methods of metal deposition used in semiconductor fabrication were only suitable for use with flat substrates. This immediately ruled out the use of hypodermic needles for prototype assembly as reproducible electrode tracts could not be fabricated on to the curved needle shaft. The first alternative to the needles was to use flat stainless steel wafers as the substrate for the electrodes. This would remove the problem of the curved surface presented by the needles. However, the final stainless steel probes were unusable due to an issue with short-circuiting that developed following metal deposition. It was hypothesised that the reason for this was as a result of the initial surface roughness being too high to allow reliable metal deposition. The results of the optical profilometry measurements showed that the surface roughness of the stainless steel wafer was sufficiently high to significantly impact on the deposition of material across the surface of the wafer. Using the profilometry instrument it was possible to obtain an approximate surface roughness measurement but it was important to note that there were crevices distributed across the wafer which may have been as deep as 3 μm or more. The total thickness of the deposited materials is approximately 790 nm which was insufficient to overcome the issue of the crevices found across the wafer surface. These significant defects in the surface of the stainless steel would be sufficient to impede the uniform deposition of materials on to the wafer that was apparent using SEM imaging of the patterned devices. Given the time constraints associated with this project it was not possible to investigate any potential methods of resolving this methodological challenge which meant that it was not possible to use the stainless steel probes for the purpose of the electrical recordings described in later sections. It was decided to replace the stainless steel substrate with a silicon wafer to improve the success rate of the

fabrication process and to produce reliable and functional electrochemical devices. The main body of work in this chapter focused on the surface and electrochemical characterisation of the silicon prototypes. Using a number of experimental techniques the probes were shown to be clean, defect free and electrochemically stable. The results outlined in this chapter show that by utilising the silicon substrate instead of the stainless steel substrate it was possible to produce a functional prototype device that was suitable for performing electrochemical measurements.

2.7.1 Future Work

The future of prototype development in the production of this impedance probe must focus heavily on the substitution of silicon as the substrate material. Currently accepted biomedical materials such as stainless steel or titanium could be investigated as they have been shown to have properties applicable to a range of clinical challenges. In particular the tensile strength of these materials would far exceed that of silicon which would reduce breakage of the devices. This would significantly reduce the number of broken packaged devices as well as reduce the potential risk of the device failing while under strain in a patient's body. It is also envisaged that the currently used packaging of the device would be evaluated and refined to produce a "plug-and-play" device which could be fitted directly into an adapter which would contain the electrical contacts [45, 46]. This would significantly reduce the handling time for each probe during the production phase. It would also reduce the risk of cross-contamination as the probe would become a disposable device that could be disconnected and discarded after each use. The construction of a very streamlined and easy to use device is essential given the niche in the market which this device is trying to fill. The device must be functional at the bedside during the breast cancer screening process. It must have minimal effect on patient comfort while increasing the amount of information available to the doctor at the bedside. The final iteration of the impedance probe must be as minimally intrusive to the screening timeline while maximally improving the screening and detection of breast cancer in patients. It would also be important to engage with the manufacturers of the potentiostat instrument to better align

the two technologies and to provide a seamless user experience for the clinician at the bedside.

2.8 References

1. Huang, X.J., A.M. O'Mahony, and R.G. Compton, *Microelectrode arrays for electrochemistry: Approaches to fabrication*. Small, 2009. **5**(7): p. 776-788.
2. Lin, S.P., J.J. Chen, J.D. Liao, and S.F. Tzeng, *Characterization of surface modification on microelectrode arrays for in vitro cell culture*. Biomed Microdevices, 2008. **10**(1): p. 99-111.
3. Heiduschka, P. and S. Thanos, *Implantable bioelectric interfaces for lost nerve functions*. Prog Neurobiol, 1998. **55**(5): p. 433-61.
4. Yagi, T., Y. Ito, H. Kanda, S. Tanaka, M. Watanabe, and Y. Uchikawa. *Hybrid retinal implant: fusion of engineering and neuroscience*. in *Systems, Man, and Cybernetics, 1999. IEEE SMC '99 Conference Proceedings. 1999 IEEE International Conference on*. 1999.
5. O'Shaughnessy, T.J., B. Zim, W. Ma, K.M. Shaffer, D.A. Stenger, K. Zamani, G.W. Gross, and J.J. Pancrazio, *Acute neuropharmacologic action of chloroquine on cortical neurons in vitro*. Brain Res, 2003. **959**(2): p. 280-6.
6. Nam, Y., D.W. Branch, and B.C. Wheeler, *Epoxy-silane linking of biomolecules is simple and effective for patterning neuronal cultures*. Biosens Bioelectron, 2006. **22**(5): p. 589-97.
7. Ingebrandt, S., C.-K. Yeung, M. Krause, and A. Offenhäusser, *Cardiomyocyte-transistor-hybrids for sensor application*. Biosensors and Bioelectronics, 2001. **16**(7-8): p. 565-570.
8. Nixon, W., *The general principles of scanning electron microscopy*. Phil. Trans. Royal Soc. London B, 1971. **261**: p. 45-50.
9. Egerton, R., *Physical principles of electron microscopy: an introduction to TEM, SEM, and AEM*. 2006: Springer Science & Business Media.
10. Ruska, E., *The Development of the Electron Microscope and of Electron Microscopy (Nobel Lecture)*. Angewandte Chemie International Edition in English, 1987. **26**(7): p. 595-605.
11. Bogner, A., P.H. Jouneau, G. Thollet, D. Basset, and C. Gauthier, *A history of scanning electron microscopy developments: Towards "wet-STEM" imaging*. Micron, 2007. **38**(4): p. 390-401.
12. Helmholtz-Zentrum Geesthacht. *FEI Quanta 650 FEG Scanning Electron Microscope*. 2015 [cited 2015 17 July]; Available from: http://www.hzg.de/institutes_platforms/materials_research/materials_mechanics/solid_state_joining_processes/techniques/index.php.en?print.
13. Russ, J.C., *Fundamentals of Energy Dispersive X-Ray Analysis: Butterworths Monographs in Materials*. 2013: Butterworth-Heinemann.
14. Frankel, R.S. and D.W. Aitken, *Energy-Dispersive X-Ray Emission Spectroscopy*. Applied Spectroscopy, 1970. **24**(6): p. 557-566.
15. Orloff, J., L.W. Swanson, and M. Utlaut, *Fundamental limits to imaging resolution for focused ion beams*. Journal of Vacuum Science & Technology B, 1996. **14**(6): p. 3759-3763.
16. Castaldo, V., C.W. Hagen, P. Kruit, E. van Veldhoven, and D. Maas, *On the influence of the sputtering in determining the resolution of a*

- scanning ion microscope*. Journal of Vacuum Science & Technology B, 2009. **27**(6): p. 3196-3202.
17. Reyntjens, S. and R. Puers, *A review of focused ion beam applications in microsystem technology*. Journal of Micromechanics and Microengineering, 2001. **11**(4): p. 287.
 18. Kwong, W. and W. Zhang. *Electron-beam assisted platinum deposition as a protective layer for FIB and TEM applications*. in *Semiconductor Manufacturing, 2005. ISSM 2005, IEEE International Symposium on*. 2005. IEEE.
 19. Giannuzzi, L.A. and F.A. Stevie, *A review of focused ion beam milling techniques for TEM specimen preparation*. Micron, 1999. **30**(3): p. 197-204.
 20. Oregon State University. *FEI QUANTA 3D dual beam SEM/FIB*. 2010 [cited 2015 17 July]; Available from: <http://www.science.oregonstate.edu/emfacility/?q=node/Facilities/FIB>.
 21. Binnig, G., C.F. Quate, and C. Gerber, *Atomic Force Microscope*. Physical Review Letters, 1986. **56**(9): p. 930-933.
 22. Blanchard, C.R., *Atomic Force Microscopy*. THE CHEMICAL EDUCATOR, 1996. **1**(5): p. 1-8.
 23. Olympus. *Standard Silicon Cantilever*. 2015 [cited 2015 17 July]; Available from: http://probe.olympus-global.com/en/product/img/standardsiliconE_01.jpg.
 24. Bhushan, B. and O. Marti, *Scanning Probe Microscopy – Principle of Operation, Instrumentation, and Probes*, in *Nanotribology and Nanomechanics I*, B. Bhushan, Editor. 2011, Springer Berlin Heidelberg. p. 37-110.
 25. Randles, J.E.B., *A cathode ray polarograph*. Transactions of the Faraday Society, 1948. **44**(0): p. 322-327.
 26. Kissinger, P.T. and W.R. Heineman, *Cyclic voltammetry*. Journal of Chemical Education, 1983. **60**(9): p. 702.
 27. Kounaves, S.P., *Voltammetric techniques*. 1997, Prentice Hall, Upper Saddle River, NJ, USA. p. 709-726.
 28. University of Cambridge. *Linear Sweep and Cyclic Voltammetry: The Principles*. 2015 [cited 2015 16 February]; Available from: <http://www.ceb.cam.ac.uk/research/groups/rg-eme/teaching-notes/linear-sweep-and-cyclic-voltammetry-the-principles>.
 29. Bott, A.W., *Characterization of chemical reactions coupled to electron transfer reactions using cyclic voltammetry*. Current Separations, 1999. **18**(1): p. 9-16.
 30. Bard, A.J. and L.R. Faulkner, *Electrochemical methods: fundamentals and applications*. Vol. 2. 1980: Wiley New York.
 31. Wang, J., *Analytical electrochemistry*. 2006: John Wiley & Sons.
 32. Bartlett, P.N., C.S. Toh, E.J. Calvo, and V. Flexer, *Modelling Biosensor Responses*, in *Bioelectrochemistry*. 2008, John Wiley & Sons, Ltd. p. 267-325.
 33. Sinclair, I., *Sensors and transducers*. 2000: Newnes.
 34. Dongming, H., M.A. Shannon, and N.R. Miller, *Micromachined silicon electrolytic conductivity probes with integrated temperature sensor*. Sensors Journal, IEEE, 2005. **5**(6): p. 1185-1196.

35. Hutchison, J.E., T.A. Postlethwaite, and R.W. Murray, *Molecular films of thiol-derivatized tetraphenylporphyrins on gold: film formation and electrocatalytic dioxygen reduction*. Langmuir, 1993. **9**(11): p. 3277-3283.
36. Harnett, E.M., J. Alderman, and T. Wood, *The surface energy of various biomaterials coated with adhesion molecules used in cell culture*. Colloids and Surfaces B: Biointerfaces, 2007. **55**(1): p. 90-97.
37. De Oliveira, R., D. Albuquerque, F. Leite, F. Yamaji, and T. Cruz, *Measurement of the nanoscale roughness by atomic force microscopy: basic principles and applications*. 2012: INTECH Open Access Publisher.
38. Moulton, S.E., J.N. Barisci, A. Bath, R. Stella, and G.G. Wallace, *Studies of double layer capacitance and electron transfer at a gold electrode exposed to protein solutions*. Electrochimica Acta, 2004. **49**(24): p. 4223-4230.
39. Patel, J., L. Radhakrishnan, B. Zhao, B. Uppalapati, R.C. Daniels, K.R. Ward, and M.M. Collinson, *Electrochemical Properties of Nanostructured Porous Gold Electrodes in Biofouling Solutions*. Analytical Chemistry, 2013. **85**(23): p. 11610-11618.
40. Fischer, L.M., M. Tenje, A.R. Heiskanen, N. Masuda, J. Castillo, A. Bentien, J. Émneus, M.H. Jakobsen, and A. Boisen, *Gold cleaning methods for electrochemical detection applications*. Microelectronic engineering, 2009. **86**(4): p. 1282-1285.
41. Mabbott, G.A., *An introduction to cyclic voltammetry*. Journal of Chemical Education, 1983. **60**(9): p. 697.
42. Mamouni, J. and L. Yang, *Interdigitated microelectrode-based microchip for electrical impedance spectroscopic study of oral cancer cells*. Biomed Microdevices, 2011. **13**(6): p. 1075-88.
43. Chang, J., G. Brewer, and B. Wheeler, *Microelectrode Array Recordings of Patterned Hippocampal Neurons for Four Weeks*. Biomedical Microdevices, 2000. **2**(4): p. 245-253.
44. Yang, L., A. Guiseppi-Wilson, and A. Guiseppi-Elie, *Design considerations in the use of interdigitated microsensor electrode arrays (IMEs) for impedimetric characterization of biomimetic hydrogels*. Biomedical Microdevices, 2011. **13**(2): p. 279-289.
45. Yao, J., R. Schmitz, and S. Warren, *A wearable point-of-care system for home use that incorporates plug-and-play and wireless standards*. Information Technology in Biomedicine, IEEE Transactions on, 2005. **9**(3): p. 363-371.
46. Falck, T., H. Baldus, J. Espina, and K. Klabunde, *Plug'n play simplicity for wireless medical body sensors*. Mobile Networks and Applications, 2007. **12**(2-3): p. 143-153.

Chapter 3

Validation of Biocompatibility and Impedance in Biological Samples

3. Validation of Biocompatibility and Impedance in Biological Samples

3.1 Objectives

The objectives of this experimental chapter are to evaluate the biocompatibility of the prototype devices and to determine their ability to differentiate between tissue types using *ex vivo* meat samples. In addition, it was planned to evaluate the prototype probes in cell culture media, to investigate the electrical impedance of immortalised cell lines. The outcome of these experiments would provide the foundation for a first in-human clinical trial to differentiate between healthy and cancerous tissue in surgically removed breast cancer samples.

3.2 Introduction

In this chapter the previously fabricated and characterised silicon and stainless steel probes will be assessed for biocompatibility and impedance functionality. The experiments were performed in the Cell Culture and Bioanalysis facilities in TNI. In recent years there has been a significant amount of research conducted using cancer cell lines for the study of early cancer diagnosis and the development of novel cancer therapies [1]. In the first part of this chapter a number of different immortalised cell lines were utilised during the testing process. These included A549 lung cancer [2], HT-29 colorectal cancer [3] and most significantly Michigan Cancer Foundation 7 (MCF-7) [4] which is a female breast cancer cell line. These cells were grown on the surface of the devices and imaged using three techniques: light, fluorescence and SEM. In addition to the imaging of cells on the device surface a resazurin assay was performed on fragments of the silicon probes to determine the percentage cell viability of the MCF-7 cells grown for 24 hr. This provided a quantitative analysis of the biocompatibility of the silicon devices and confirmed the qualitative images obtained previously. In order to obtain impedance modulus recordings from the seeded MCF-7 cells on the packaged silicon prototypes it was necessary to design and fabricate device holders that would maintain a defined volume of liquid on the probe surface. The holders were produced in the Mechanical Workshop in TNI and used to

aid in the culturing of cells on the probe surface and the results of the experiments are outlined in this chapter.

In the second section of this chapter the working silicon prototypes were used to record impedance modulus data from a range of meat tissue samples including beef, lamb and pork. In each case areas of fat and muscle were tested and compared to determine if the probe was capable of differentiating between the two tissue types. Experiments were also carried out to determine the effect of applying external pressure on the probe during testing as well as the effect of penetration depth on the electrical recordings obtained.

3.2.1 Cell Culture

Cell culture is a term used to describe the method by which primary and immortalised cell lines can be grown and maintained in an aseptic environment in a laboratory setting. The cell culture facility in the TNI is composed of two separate laboratories. One is used for the growth of primary cell lines and the other is used for the culture of immortalised cell lines. The immortalised cell culture laboratory was used to perform the experimental work described in this chapter. The laboratory contains specialist instruments including:

- 1) SpectraMax Gemini EM Microplate Reader
- 2) Airstream Class II Biological Safety Cabinet E-Series
- 3) Panasonic MCO-18AC-PE CO₂ Incubator
- 4) Hettich Universal 320 Centrifuge
- 5) Bright-Line™ Haemocytometer
- 6) Olympus CKX41 Inverted Microscope

Each of these components is required to allow the aseptic growth environment to be maintained throughout the experimental process.

Primary cell lines are isolated from tissues of interest and are grown under artificial conditions until they reach confluency. Once these cells have been subcultured in to a new flask they become a cell line. The number of replications these cells can undergo is limited by genetic factors. Eventually,

senescence will occur, the cell will fail to replicate and will die [5]. The major influencer of cellular senescence is the enzyme telomerase which maintains telomere end length during replication. Somatic cells which contain little or no telomerase experience successive telomere shortening which eventually elicits a senescence checkpoint [6, 7]. Through a process known as transformation, finite cell lines can be modified to allow them to replicate indefinitely [5]. These are known as immortalised cell lines. The development of these cell lines which have almost unlimited replication potential has resulted in their use across many research applications. These include cell growth and migration; drug toxicity and compound screening; gene regulation and biocompatibility testing [8, 9]. The increasing use of cell culture to determine drug effect and toxicity has coincided with the worldwide push to reduce the number of animals used for screening new compounds and products [9]. A number of assays have been developed that utilise cell culture techniques to determine the biocompatibility of medical device components [10]. One of the most common outcomes of biocompatibility assays is to determine cell viability using a quantitative analysis method. The resazurin cell viability assay is an example of this type of test.

3.2.2 Resazurin Assay

A resazurin cell viability assay, which was performed as part of this research, measures the reduction of blue non-fluorescent 1,2,3 Resazurin dye (7-hydroxy-3H-phenoxazin-3-one10-oxide) to pink fluorescent resorufin by metabolically active cells. This is achieved by the action of the mitochondrial electron transport chain, and indicates cell viability [11, 12]. Cell health can be monitored by numerous methods. Plasma membrane integrity, DNA synthesis, DNA content, enzyme activity, presence of adenosine triphosphate (ATP) and cellular reducing conditions are known indicators of cell viability and cell death. Resazurin assays are used as cell health indicators by using the reducing power of living cells to quantitatively measure the proliferation of human and animal cell lines, bacteria, plant, and fungi. It also allows the establishment of the relative cytotoxicity of agents within chemical classes [13]. When cells are alive they maintain a reducing environment within the cytosol of the cell. Resazurin is a non-toxic, cell

permeable compound that is blue in colour and non-fluorescent. Upon entering cells, resazurin is reduced to resorufin, a compound that is red in colour and highly fluorescent. Living cells continuously convert resazurin to resorufin, increasing the overall fluorescence and colour of the media surrounding the cells. The reduction of resazurin correlates with the number of live mammalian cells present. The level of reduction was quantified through measurements with a spectrophotometer at 445 nm and 590 nm emission frequencies [14].

3.2.3 Cell Culture Holders

In order to obtain impedance modulus measurements from immortalised cell lines using the silicon probe devices, the design and fabrication of a 2-part Perspex holder was necessary. The holder was designed in collaboration with Dr Walter Messina, Life Science Interface Group, Tyndall National Institute. The purpose of the unit was to provide a suitable volume in which to culture the cell lines, while providing a level surface on which to grow the cells. This was not previously possible due to the manner in which the electrical wires were packaged. This meant that any cell suspension or media applied to the probe would dissipate from the surface immediately. The holders were fabricated in the Mechanical Workshop, TNI by Mr Donal O'Sullivan. The design drawings submitted for the work (Figure 3.1 A-C) display the expanded, constructed and side-view profiles of the holder. The lower part of the holder contained a recess that matched the width and depth of the individual silicon probes. This allowed the surface of each probe to sit flush with the surface of the holder. The upper part of the holder contained a well that allowed 1 ml of culture media to be maintained above the surface of the probe. At the bottom of the well was a hole to allow the transfer of liquid and cells on to the silicon device. Immediately below this opening a rubber O-ring was inserted which would form a watertight seal between the probe surface and the media well. The maximum dimension of this O-ring was limited by the width of the silicon probes. This resulted in a very narrow opening through which the culture media could pass. The two parts of the holder were secured together with four screws inserted at each of the

corners. The dimensions for the cell culture holders are outlined in Appendix 6.7.

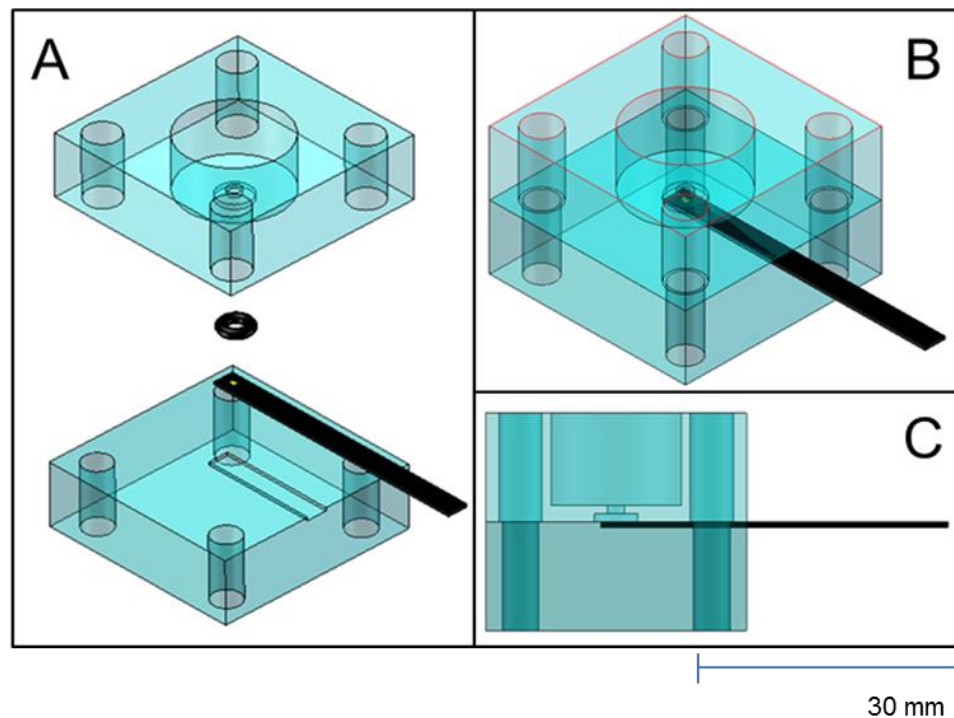


Figure 3.1: A) The expanded view of the cell culture probe holder including an O-ring which forms a water-tight seal. B) The design drawing of the constructed cell culture holder and probe. C) The side-profile view of the cell culture probe holder.

3.2.4 Pressure Testing

One of the investigations undertaken during this project was to determine the effect of externally applied pressure on the measurement of impedance modulus recordings in meat tissue samples. Due to the nature of the tissues tested using the prototype silicon probe it was sometimes necessary to make an incision into the tissue to allow device placement. These tissues were then apposed to the probe surface by pressing them together by hand. This could potentially result in a variable pressure being applied to the electrode surface during the impedance recordings. In order to determine the effect of this pressure on the values obtained, a series of recordings were performed with different sources of externally applied pressure. The testing was performed using two different probes, which had previously been cleaned; to measure beef rib fat and muscle at room temperature. The purpose of this experiment was not to determine the pressure which was being applied to

the probe surface but to assess if variably and constantly applied pressure produced the same impedance modulus values.

3.2.5 Depth Testing

In addition to the investigation of the effect of externally applied pressure on impedance recordings an experiment was carried out to determine if the depth of probe insertion had an effect on the impedance obtained values. The design of the silicon probes provided an insulation layer over the length of the gold tracts with the exception of the electrodes and output pads which were left exposed. This should mean that the depth of insertion does not influence the recordings obtained. However, it was necessary to confirm if an increase in the depth of recording caused a change in the impedance modulus measurements. In order to determine the effect of depth on the observed values, a silicon probe was tested at a number of depths in a block of gelatine with multiple frequency sweep recordings taken each time.

3.3 Experimental Details

3.3.1 Reagents and Materials

MCF-7 cells, Minimum Essential Media Eagle (MEME), Trypsin, Ethylenediaminetetraacetic acid (EDTA), Foetal Calf Serum, L-Glutamine, Non-essential amino acid (NEAA), A549 cells, T75 cell culture flask, 1 ml cryogenic vials, 15 ml centrifuge tube, Hank's balanced salt solution (HBSS), Dulbecco's Modified Eagle Medium: Nutrient Mixture F-12 (DMEM/F12), Penicillin, Streptomycin, HT-29 cells, McCoy's 5A media, 80% ethanol, Propidium iodide (PI), Petri Dish, Plastic Pipette, 6-well plate, poly-L-lysine, Primary fixative solution containing glutaraldehyde and paraformaldehyde, sodium cacodylate/HCl buffer, osmium tetroxide (OsO_4), Acetone, Tetramethylsilane (TMS), Double-sided carbon tape, Resazurin sodium salt, 0.45 nm pore syringe filter, Triton-x (All chemicals and reagents were sourced from Sigma-Aldrich Ltd., Dublin, Ireland and were analytical grade); Beef, lamb and pork samples (were all sourced from O'Mahony Butchers, Cork, Ireland); Powdered gelatine (Vege-gel and Gelatine) (was purchased from Dr Oetker, Leeds, United Kingdom). Viton O-rings (were sourced from Radionics, Dublin, Ireland).

3.3.2 Instrumentation

Quorum Q150T Turbo-pumped Sputter Coating System (Quorum Technologies Ltd., East Sussex, United Kingdom); Jeol JSM 5510 Scanning Electron Microscope (Jeol (U.K.) Ltd., Herts, United Kingdom); Autolab PGSTAT204 with FRA32M module (Metrohm UK Ltd, Runcorn, United Kingdom); Data-Therm IR thermometer (Guangzhou Jinxinbao Electronic Co. Ltd., Guangzhou, China); SpectraMax Gemini EM Microplate Reader (Molecular Devices (UK) Ltd., Berkshire, United Kingdom); Airstream Class II Biological Safety Cabinet E-Series (Esco GB Ltd, Yorkshire, United Kingdom); Inverted-phase contrast microscope, Weitlaner Tissue Retractor (Aesculap Inc., Pennsylvania, USA); MCO-18AC-PE CO_2 Incubator (Panasonic Biomedical Sales Europe B.V., Leicestershire, United Kingdom); Hettich Universal 320 Centrifuge (DJB Labcare Ltd., Buckinghamshire, United Kingdom); Bright-Line™ Haemocytometer (Sigma-Aldrich Ltd.,

Dublin, Ireland); Olympus BX51-P Fluorescent Microscope (Mason Technologies Ltd., Dublin, Ireland); Olympus CKX41 Inverted Microscope (Mason Technologies Ltd., Dublin, Ireland), Cimatec SP131325Q Ceramic Hotplate (Fisher Scientific Ltd., Dublin, Ireland); Grant SUB Aqua 18 Plus Waterbath (Grant Instruments (Cambridge) Ltd, Cambridgeshire, United Kingdom).

3.4 Procedures

3.4.1 Cell Culture

Three different immortalised cell lines were used during this series of experiments. The cell types used were:

- 1) A549 – A human alveolar adenocarcinoma basal epithelial cell line derived from an explanted tumour of a 58 year old Caucasian male.
- 2) HT-29 – A human colorectal adenocarcinoma epithelial cell line derived from a 44 year old Caucasian female.
- 3) MCF-7 – A human adenocarcinoma epithelial cell line derived from a pleural effusion of a metastatic invasive breast ductal carcinoma tumour from a 69 year old female.

Each cell type had specific culture media requirements and subculture procedures which will be described in the following sections. The MCF-7 cell line was chosen as it is commonly used as a model of breast cancer for *in vitro* testing. The A549 and HT-29 cell lines were used to validate the results obtained with the MCF-7 cell line.

3.4.1.1 MCF-7 Cell Culture Preparation

The MCF-7 cells used during this project were purchased from Sigma-Aldrich Ltd. (Dublin, Ireland) and were stored in liquid nitrogen prior to being cultured. All cell culture work was performed in a Class II biological safety cabinet (Airstream Class II Biological Safety Cabinet E-Series, Esco GB Ltd, Yorkshire, United Kingdom) in a dedicated immortalised cell culture laboratory (Figure 3.2).



Figure 3.2: The Class II biological safety cabinet in the Tissue Culture Facility in Tyndall National Institute.

To begin growth of the cells they were first removed from liquid nitrogen storage and defrosted in a water bath at 37°C (Grant SUB Aqua 18 plus Waterbath, Grant Instruments (Cambridge) Ltd, Cambridgeshire, United Kingdom). The entire contents (1 ml) of the cryogenic vial were then pipetted into a T75 cell culture flask. The MCF-7 cells were cultured in MEME complete media (Sigma-Aldrich Ltd., Dublin, Ireland) as per the manufacturer's guidelines (Table 3.1). 30 ml of the complete media was added to the flask which was then placed in an incubator at 37°C and 5% carbon dioxide (CO₂) until the cells reached approximately 70% confluency [15].

Table 3.1: MEME complete media composition.

MEME Complete Media	Volume (ml)
MEME Media	440
Foetal Calf Serum	50
L-Glutamine	5
NEAA	5
Total	500

To remove the cells from the flask the culture media was first removed using a sterile plastic pipette and the flask was rinsed with 4 ml of pre-warmed Trypsin/EDTA. 3ml of trypsin/EDTA was added to the flask which was then incubated for 8 min to allow the cells to detach. 7 ml of MEME complete

media was then added to inactivate the trypsin/EDTA. The cell suspension was removed and placed in a clean 15 ml centrifuge tube and the cells were centrifuged for 5 min at 1,000 rpm. The supernatant was removed and the cell pellet was re-suspended in 5 ml of fresh complete media. A cell count was performed as described in Equation 3.1. 10 μ l of the suspension was added to 90 μ l of complete media.

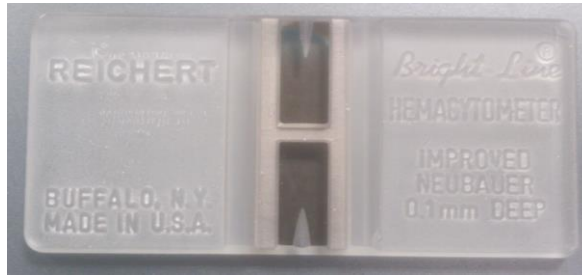


Figure 3.3: The haemocytometer used during the cell culture counts.

10 μ l of this solution was then pipetted onto a haemocytometer (Figure 3.3) and a glass coverslip was placed on top. In total five boxes were counted for each sample (Figure 3.4).

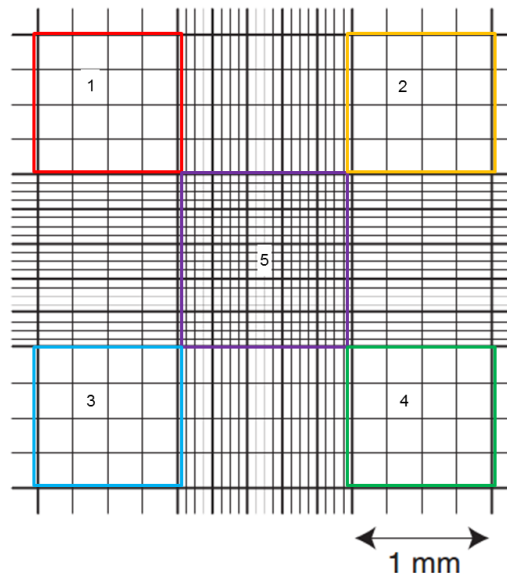


Figure 3.4: The layout of a haemocytometer with the 5 large boxes highlighted which are counted during a cell count. Modified by Author from Reference [16].

The equation was used to estimate the total cell number in suspension (Equation 3.1):

$$\text{Cells/ml} = \frac{\text{No. of Cells} \times 10(\text{Dilution Factor}) \times 10^4 (\text{Constant})}{5 (\text{Boxes Counted})}$$

Equation 3.1: Calculation of number of cells per millilitre of cell suspension.

The total number of cells counted was multiplied by the dilution factor and the haemocytometer constant of 10^4 . This value is then divided by 5 which was the number of boxes counted in each case. The final value provided an approximation of the number of cells per millilitre of cell suspension. To continue the growth of the cell line, 1 ml of cell suspension was pipetted in to a clean T75 flask and 29 ml of complete media was added. The flask was then placed in an incubator at 37°C and 5% CO₂ for 48 hours.

3.4.1.2 A549 Cell Culture Preparation

The A549 cells used during this project were initially stored in liquid nitrogen in the Life Science Interface laboratory, Tyndall National Institute. To begin growth of the cells they were first removed from storage and defrosted in a water bath at 37°C. The A549 cells were cultured in DMEM/F12 complete media (Sigma-Aldrich Ltd., Dublin, Ireland) as per the manufacturer's guidelines (Table 3.2). The entire contents (1 ml) of the cryogenic vial were then pipetted into a T75 cell culture flask. 30 ml of the complete media was added to the flask which was then placed in an incubator at 37°C and 5% CO₂ until the cells reached approximately 70% confluency [17].

Table 3.2: DMEM/F12 complete media composition.

DMEM/F12 Complete Media	Volume (ml)
DMEM/F12 Ham Media	440
Foetal Calf Serum	50
L-Glutamine	5
Penicillin/Streptomycin	5
Total	500

To remove the cells from the flask the culture media was first removed using a sterile plastic pipette and two washes were performed with pre-warmed HBSS (Sigma-Aldrich Ltd., Dublin, Ireland) and 4ml of trypsin/EDTA was

added. The flask was then incubated for 5 min to allow the cells to detach. 6 ml DMEM/F12 complete media was then added to inactivate the trypsin/EDTA. The cell suspension was removed and placed in a clean 15 ml centrifuge tube and the cells were centrifuged for 5 min at 1,000 rpm. The supernatant was removed and the cell pellet was re-suspended in 5 ml of fresh complete media after which the cells were then counted using a haemocytometer as previously described. To continue the growth of the cell line, 1 ml of cell suspension was pipetted in to a clean T75 flask and 29 ml of complete media was added. The flask was then placed in an incubator at 37°C and 5% CO₂ for 48 hours.

3.4.1.3 HT-29 Cell Culture Preparation

The HT-29 cells used during this project were stored in liquid nitrogen prior to being cultured. To begin growth of the cells they were first removed from storage and defrosted in a water bath at 37°C. The HT-29 cells were cultured in McCoy's 5A complete media (Sigma-Aldrich Ltd., Dublin, Ireland) as per the manufacturer's guidelines (Table 3.3). The entire contents (1 ml) of the cryogenic vial were then pipetted into a T75 cell culture flask. 30 ml of the complete media was added to the flask which was then placed in an incubator at 37 °C and 5% CO₂ until the cells reached 70% confluency [18].

Table 3.3: McCoy's 5A complete media composition.

McCoy's 5A Complete Media	Volume (ml)
McCoy's 5A Media	450
Foetal Calf Serum	50
Total	500

To remove the cells from the flask the culture media was first removed using a sterile plastic pipette and two washes were performed with pre-warmed HBSS and 3 ml of trypsin/EDTA was added. The flask was then incubated for 25 min to allow the cells to detach. 7 ml of McCoy's 5A complete media was then added to inactivate the trypsin. The cell suspension was removed and placed in a clean 15 ml centrifuge tube and the cells were centrifuged for 5 min at 1,000 rpm. The supernatant was removed and the cell pellet was re-

suspended in 5 ml of fresh complete media. A cell count was performed as described previously. To continue the growth of the cell line, 1 ml of cell suspension was pipetted in to a clean T75 flask and 29 ml of complete media was added. The flask was then placed in an incubator at 37°C and 5% CO₂ for 48 hours.

3.4.1.4 Silicon Biocompatibility

In order to assess the biocompatibility of the silicon probes, unpackaged devices were seeded with cells in a plastic Petri dish. MCF-7 and HT-29 cells were seeded at an optimum density of 400,000 cells per silicon. A control device containing media only was used each time. The required volume of cell suspension was carefully pipetted onto each probe and the Petri dishes were placed in the incubator at 37°C and 5% CO₂ for 1 hr to allow the cells to attach. The final volume in each dish was then made up to 14 ml with the appropriate complete media. The devices were placed on the incubator for either 24 or 48 hr before being imaged.

3.4.1.5 Resazurin Assay

Resazurin sodium salt (Sigma-Aldrich Ltd., Dublin, Ireland) was dissolved in HBSS at a final concentration of 440 µM (Equation 3.2). The molecular weight of resazurin = 251.17 g/l.

$$440 \text{ } \mu\text{M} = 251.17 \text{ g} \times 440 \times 10^{-6} = 0.110515 \text{ g/l}$$

Equation 3.2: The calculation of the concentration of resazurin in solution.

Resazurin (440 µM) was sterile filtered using a syringe with 0.45 µm pores filters (Sigma-Aldrich Ltd., Dublin, Ireland) prior to use in cell culture. It was then diluted in complete media at 10% to provide a final concentration of 44 µM to be added to cells.

The resazurin assay was conducted by Ms Michelle Fitzgerald in the Cell Culture Laboratory in Tyndall National Institute. The MCF-7 cell line was used to demonstrate the biocompatibility of the silicon probe devices. The percentage viability of the cells was analysed using a spectrophotometer to assess the colour change produced by living cells. The cells were seeded on

sections of the silicon probes in a 24-well cell culture plate. The plate layout is shown in Table 3.4:

Table 3.4: The layout used for the resazurin assay experiments.

Variable	Replicate 1	Replicate 2	Replicate 3
1	Positive Control	Positive Control	Positive Control
2	Test	Test	Test
3	Negative Control	Negative Control	Negative Control
4	Resazurin Blank	Resazurin Blank	Resazurin Blank

An optimum density of 500,000 cells was seeded in the positive, test and negative wells. Complete media was added to a final volume of 1 ml. The negative control wells had 10 μ l of Triton-x added with the complete media. Triton-x is a laboratory detergent which was used to kill cells in culture. At 24 hr the complete media was removed and 1 ml of 10% resazurin and complete media was added to each of the 12 wells shown in Table 3.4. The plate was left for 3 hours to allow the colour change to develop. Each well of the plate was then read using a spectrophotometer. The results were exported to Excel where they were analysed and graphed.

3.4.1.6 Scanning Electron Microscope

MCF-7 cells were cultured for seeding on the silicon devices for imaging using an SEM microscope. The cell number was initially optimised by Ms Michelle Fitzgerald in the Cell Culture Facility in Tyndall National Institute. The cells were grown in T75 cell culture flasks and then seeded at a density of 450,000 cells per device as previously described. The probes were incubated at 37°C for 24 hours before being fixed for evaluation by SEM. The cell media was removed and substituted with a primary fixative solution containing glutaraldehyde and paraformaldehyde in 0.1 M sodium cacodylate/HCl buffer pH 7.2. After the cells had been immersed in the fixative for 90 minutes, they were washed with an SEM buffer for 30 minutes before being immersed in OsO₄ for 120 minutes (Table 3.5). The OsO₄ is used as a stain for lipids in membranous structures and vesicles. Following this the samples were soaked again in SEM buffer overnight. The

dehydration process consisted of several consecutive washes with a solution containing an increasing concentration of acetone (Table 3.6).

Table 3.5: The cell fixation process required for SEM imaging.

Fixation	Day 1
Primary Fixative	90 min
Buffer Wash	30 min
OsO ₄	120 min
Buffer	Held Overnight

Table 3.6: The acetone dehydration process required for SEM imaging

Dehydration	Day 2
25% Acetone	15 min
50% Acetone	15 min
75% Acetone	15 min
100% Acetone	15 min
100% Acetone	15 min
100% Acetone	15 min
100% Acetone	15 min

Once the Acetone wash sequence was completed, the cells were transferred into a TMS solution for 15 minutes and then air-dried in a fume hood. The TMS solution has a low boiling point (26.3°C) and is used to allow tissue drying while significantly overcoming the deleterious effects of air-drying. Samples were then mounted on metal stubs using double-sided carbon tape and sputter coated with an approximate 5 nm layer of gold using a Quorum Q150T Turbo-pumped Sputter Coating System (Quorum Technologies Ltd., East Sussex, United Kingdom). The sputter coating prevents charging of the sample which would occur due to the accumulation of static electric fields. It also increases the amount of secondary electrons that can be detected from the surface of the specimen in the SEM and therefore increases the signal to noise ratio. The samples were imaged immediately using a Jeol JSM 5510 Scanning Electron Microscope (JEOL (U.K.) Ltd, Hertfordshire, United

Kingdom). The SEM imaging was performed by Ms Suzanne Crotty in the Biosciences Imaging Centre, University College Cork.

3.4.1.7 O-ring Biocompatibility

The Viton O-rings used as part of the design of the cell culture probe holder were tested to ensure they were biocompatible with cell growth. The MCF-7 cells were grown and cultured as previously described. They were seeded at an optimum density of 100,000 cells per well in 6 wells of a 24 well plate. Three of these wells contained the O-rings and 3 wells were seeded with just cells and were used as controls for comparison. The cells were incubated for 24 hr. After this time they were imaged using an Olympus CKX41 Inverted Microscope.

3.4.1.8 Impedance Modulus Measurements

Figure 3.5 shows each of the components of the Perspex cell culture holder and an unpackaged silicon probe prior to assembly. Figure 3.6 shows a top and bottom view of the cell culture holder with a silicon probe inserted prior to seeding with cells.

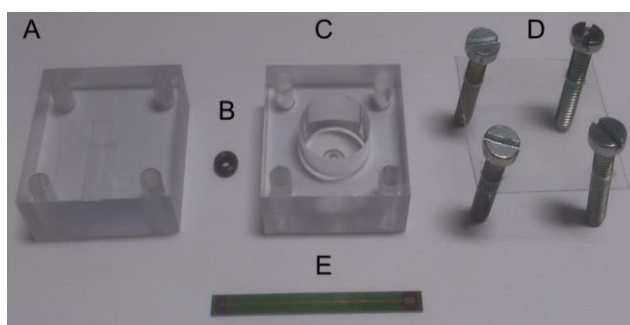


Figure 3.5: The individual components of the cell culture probe holder. A) Bottom of holder, B) O-ring, C) Top of holder, D) Plastic film cover and screws, E) An unpackaged silicon prototype.

The A549 cells were cultured as previously described and were seeded on each of the silicon devices contained in the cell culture holder at densities of 50,000-200,000 cells per well. This value had previously been optimised to ensure a confluent cell layer would be present on each of the electrodes at 24 hr. The cells were seeded on the devices for 1 hr and left in an incubator at 37 °C. The final volume of DMEM/F12 complete media was then added to

each well. The cells were placed in the incubator for 24 hr to allow cell attachment and growth prior to impedance modulus recordings being performed

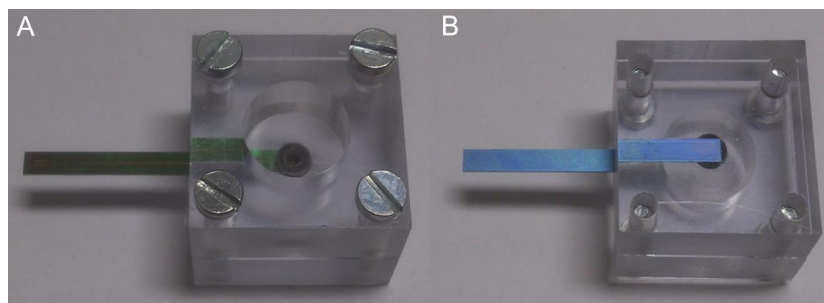


Figure 3.6: The assembled cell culture probe holder from the top A) and bottom B).

3.4.1.9 Stainless Steel Biocompatibility

Three plastic wells were attached to the surface of the wafer with biocompatible glue. Two of the wells were seeded with cells and a control well containing media only was used each time. A PI nuclear stain was used to visualise cell growth on the surface of the wafer. A549 cells were seeded at a density of 40- or 80- or 120,000 cells per well. The cells were initially grown in DMEM/F12 complete media. The cells were grown for either 24 or 48 hours at which point they were removed from the incubator to be fixed and stained. After each time point, the cells were washed 3 times in 600 μ l of 37°C HBSS. The cells were suspended in 500 μ l of HBSS. Ice-cold 80% ethanol (600 μ l) was then added to each well and the device was placed in the freezer at -20 °C for 35 min. The ethanol was used as a fixative for the cells prior to staining. The ethanol was then removed and 3 x 600 μ l of warm HBSS was added to each well to rinse the cells and remove any residual ethanol. The PI solution (600 μ l) was added to each well and incubated for 5 min at 37 °C. This was removed and 3 further HBSS washes were performed and the final wash was left in the well to prevent the samples from drying out. The device was then placed in a fridge at 4°C until being imaged using a fluorescent microscope.

3.4.2 Meat Tissue Recordings

3.4.2.1 Beef Recordings

Frequency sweep measurements were performed on beef rib samples in regions of fat and muscle tissue. Samples were obtained from O'Mahony Butchers (Cork, Ireland) on the day of testing. The samples were left for in the Bioanalysis Laboratory for approximately an hour prior to recording. This was to allow the tissue to equilibrate to the temperature of the room. The frequency range analysed was from 100,000 Hz to 1,000 Hz with an applied peak AC voltage of 10, 30 and 50 mV. An Autolab PGSTAT204 with an FRA32M module (Metrohm U.K. Ltd., Cheshire, United Kingdom) was used to conduct the measurements. A total of 30 values were obtained across the frequency range at each site tested. During the experiment 1 silicon probe (No. 13) was used to recorded triplicate values in both fat and muscle tissue in random sites across the beef rib sample. Between each tissue type the probe was cleaned by dipping it in nano-pure water and wiping it with lint-free paper twice. The values obtained for each scan were exported to Excel and IBM SPSS Statistics 20 (SPSS) software package where they were analysed and graphed. A total of n=9 for the fat and muscle samples was obtained.

3.4.2.2 Pressure Testing

To determine the effect of applied pressure on the modulus of the impedance of a sample, beef rib fat and muscle tissues (O'Mahony Butchers, Cork, Ireland) were tested. Sections of fat and muscle of approximately the same thickness were separated from each other and placed on the bench and maintained at room temperature. Silicon probes were tested in a number of ways which are described in Table 3.7.

Table 3.7: The different methods of applying pressure to the beef rib muscle and fat samples.

Pressure Applied	Description
Unsupported	Probe inserted into tissue and maintained under own weight
Handheld	The tissue was apposed by hand to the probe.
Clamp	Weitlaner tissue retractor (Notch 5) was used to appose the tissue to the probe
Clamp Tight (Muscle Only)	Weitlaner tissue retractor (Notch 4) was used to appose the tissue to the probe

A Weitlaner tissue retractor obtained from the Department of Surgery in CUH was used to apply the fixed pressure to the fat and muscle samples (Figure 3.7). The frequency range analysed was from 100,000 Hz to 1,000 Hz with an applied peak AC voltage of 10 mV. An Autolab PGSTAT204 with a FRA32M module was used to conduct the measurements. A total of 30 values were obtained across the frequency range at each site tested. The values obtained for each scan were exported to Excel and SPSS where they were analysed and graphed.



Figure 3.7: An example of a Weitlaner tissue retractor that was used in the pressure testing of the beef rib samples. Reference [19].

3.4.2.3 Depth Testing

500 ml of water was heated to approximately 70°C on a hotplate. A total of 56 g of powdered gelatine (Vege-Gel, Dr Oetker, Leeds, United Kingdom)

was weighed out and added to the heated water. The solution was then stirred to ensure a homogenous mixture. A plastic lunchbox was lined with cling-film and the entire gelatine mixture was poured into it and placed in a fridge at 4°C and allowed to set until firm. The gel was removed and brought to the Bioanalysis Laboratory to perform the impedance modulus measurements. A ruler, which was used to measure the depth of penetration, was placed parallel to the silicon probe and held in place with a retort stand (Figure 3.8). The device was connected to the Autolab potentiostat and the total probe length was measured (30 mm to bottom of the packaging). The probe was then inserted into the gel at increasing increments with triplicate measurements taken at each depth (10, 15 and 20 mm). The values obtained for each scan were exported to Excel where they were analysed and graphed to determine the overall effect of increasing depth on the impedance values obtained.

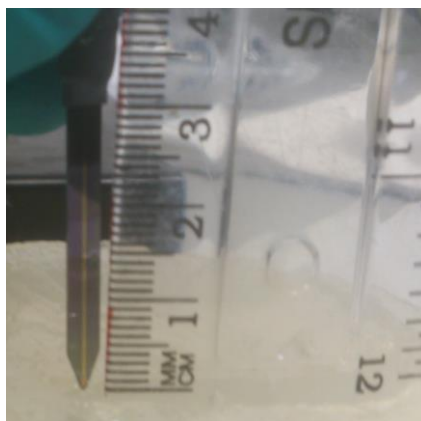


Figure 3.8: The total length of the silicon probe prior to insertion in the gelatine gel.

3.4.2.4 Parasitic Capacitance Testing

Frequency sweep measurements were performed using the silicon probes immersed in 10 ml of HBSS. The frequency range analysed was from 1 MHz - 1 Hz with an applied peak AC voltage of 10 mV. An Autolab PGSTAT204 with an FRA32M module was used to conduct the measurements. A total of 50 values were obtained across the frequency range. During the experiment 1 silicon probe (No. 13) was used to record five repeat values in the HBSS. Between each measurement the probe was cleaned by dipping it in nano-pure water and wiping it with lint-free paper twice. The values obtained for

each scan were exported to Excel where they were analysed and graphed. A total of $n=1$ was obtained. The value recorded for reactance (imaginary impedance) was used to calculate the figure for capacitive reactance using Equation 3.3.

$$C = -\frac{1}{2\pi f X_c}$$

Equation 3.3: The calculation for capacitance using reactance. f – Applied Frequency, X_c – Reactance, C – Capacitance.

3.4.2.5 Lamb Recordings

Frequency sweep measurements were performed on lamb centre loin samples in regions of fat and muscle tissue. Samples were obtained from O'Mahony Butchers (Cork, Ireland) on the day of testing. The samples were left for in the Bioanalysis Laboratory for approximately an hour prior to recording. This was to allow the tissue to equilibrate to the temperature of the room. The frequency range analysed was from 100,000 Hz to 1,000 Hz with an applied peak AC voltage of 10, 30 and 50 mV. An Autolab PGSTAT204 with an FRA32M module was used to conduct the measurements. A total of 30 values were obtained across the frequency range at each site tested. During the experiment 1 silicon probe (No. 14) was used to recorded triplicate values in both fat and muscle tissue in random sites across the lamb centre loin sample. Between each tissue type the probe was cleaned by dipping it in nano-pure water and wiping it with lint-free paper twice. The values obtained for each scan were exported to Excel and SPSS where they were analysed and graphed. A total of $n=9$ for the fat and muscle samples was obtained.

3.4.2.6 Pork Recordings

Frequency sweep measurements were performed on pork centre loin samples in regions of fat and muscle tissue. Samples were obtained from O'Mahony Butchers (Cork, Ireland) on the day of testing. The samples were left for in the Bioanalysis Laboratory for approximately an hour prior to recording. This was to allow the tissue to equilibrate to the temperature of the room. The frequency range analysed was from 100,000 Hz to 1,000 Hz with

an applied peak AC voltage of 10, 30 and 50 mV. An Autolab PGSTAT204 with a FRA32M module was used to conduct the measurements. A total of 30 values were obtained across the frequency range at each site tested. During the experiment 1 silicon probe (No. 13) was used to recorded triplicate values in both fat and muscle tissue in random sites across the pork centre loin sample. Between each tissue type the probe was cleaned by dipping it in nano-pure water and wiping it with lint-free paper twice. The values obtained for each scan were exported to Excel and SPSS where they were analysed and graphed. A total of $n=9$ for the fat and muscle samples was obtained.

3.4.3 Statistical Analysis

For the analysis of the fat and muscle tissues a paired-sample T test was performed to determine if a statistical significance existed between the tissue types. A paired T test is used when there is one measurement variable (frequency) and two nominal variables (fat and muscle). This test was chosen to see if the means of these two normally distributed interval variables differed from one another. The combined values of skewness and Kurtosis were used to test the normality of the data. This was performed on each of the data sets following analysis with the paired-samples T test. This was used to determine if the data was normally distributed which was necessary when performing a parametric statistical analysis. Values of < 2 and < 9 for skewness and Kurtosis have previously been described as being suitable for parametric analysis using a paired-samples T test [20]. The paired-samples T test was also used to optimise the measurement frequency at which fixed frequency measurements could be performed. The triplicate measurements in each tissue were averaged each time and the nine repeats were combined in the paired-samples T test with a confidence interval of 95%. A p value of < 0.05 would be indicative of a statistical significance between the two tissue types.

3.5 Results

3.5.1 Cell Culture

3.5.1.1 Silicon Biocompatibility

The MCF-7 and HT-29 cell lines were both grown on the surface of the silicon probes to demonstrate the overall biocompatibility of the devices. The experiment was repeated a number of times at both the 24 and 48 hour time point. A selection of the images taken using the bright-field setting on the microscope during this study can be seen in Figures 3.9 and 3.10. Figure 3.9 shows images taken of the silicon probes seeded with 400,000 HT-29 cells at 24 and 48 hours (B and C). A control probe, which contained only media and incubated for 24 hours, showed no cell growth as expected (Figure 3.9 A). A confluent cell layer was clearly evident at each of the time points analysed. This demonstrated that the entire surface of the silicon probes was compatible with the growth of HT-29 cells.

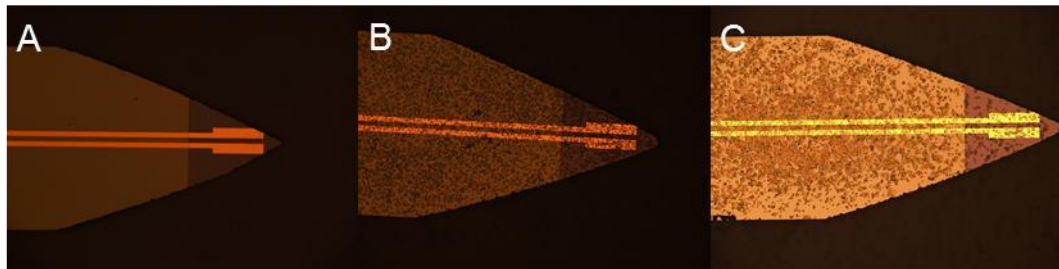


Figure 3.9: Micrographic images of the tip of the silicon probe seeded with control (no cells; A) and HT-29 cells (400,000 cells per device) for 24 hr (B) and 48 hr (C).

MCF-7 cells were also seeded on the silicon probes to show the biocompatibility and to compare with the findings of the HT-29 cells previously shown. They were seeded at an optimum density of 400,000 cells per device along with a control which contained no cells (Figure 3.10 A and B). Under the light microscope the cells were clearly visible across the entire probe surface including the gold electrodes. In order to quantitatively assess the biocompatibility of the silicon devices a resazurin cell viability assay was performed and the results are shown in the Section 3.5.1.2.

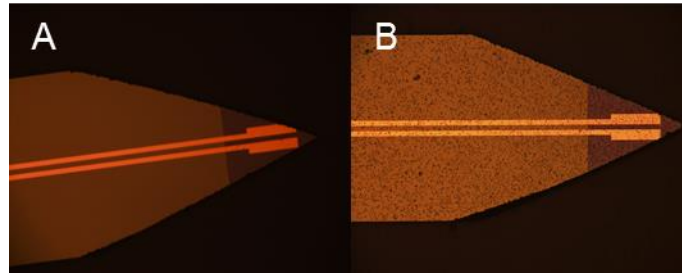


Figure 3.10: Micrographic images of the tip of the silicon probe seeded with control (no cells; A) and MCF-7 cells (400,000 cells per device) for 24 hr (B).

The significant amount of cell growth observed with each cell line was a positive result. It demonstrated that the silicon substrate probes did not adversely affect the growth of either cell line over a period 48 hours. This indicated that the fabricated devices were biocompatible. This result meant that silicon could be put forward as a potential alternative to stainless steel for *ex vivo* tissue measurement because of the reduced stress applied to the probes when measuring excised tissue samples. The initial investigations performed to test the biocompatibility of the silicon probes involved the growth of both the MCF-7 and HT-29 cells lines on the surface of the device. Light microscopy was used to confirm that a confluent cell layer was present on each of the probes that were seeded with cells. Further investigation in to the biocompatibility of the silicon probes was undertaken as they were the most promising prototype developed as part of this research project and the results are outlined in Sections 3.5.1.2 and 3.5.1.3.

3.5.1.2 Resazurin Cell Viability Assay

The resazurin cell viability assay was used to provide a quantitative measurement of the viability of the MCF-7 cells grown on the surface of the silicon devices. The results obtained showed that the percentage viability of cells grown on the silicon probe fragments was 98.7% compared to the positive control of cells seeded on the surface of the 24-well plate (Table 3.8). Figure 3.11 shows a bar chart displaying the mean \pm S.D. for the positive control, test and negative control wells that were analysed in each of the plates (N=4). This showed that the materials and fabrication processes used to produce the silicon probes were biocompatible and did not significantly inhibit cell growth. The assay results confirmed the results

obtained during the light microscopy and SEM investigations which showed a confluent MCF-7 cell layer present at 24 hr after seeding.

Table 3.8: The averaged results of each replication of the resazurin assay and the standard deviation.

Resazurin Assay	Positive Control	Test	Negative Control
Plate 1	100	104.433	1.108
Plate 2	100	90.399	1.527
Plate 3	100	103.795	0.943
Plate 4	100	96.180	1.222
Average	100	98.700	1.200
Standard Deviation	0	6.686	0.246

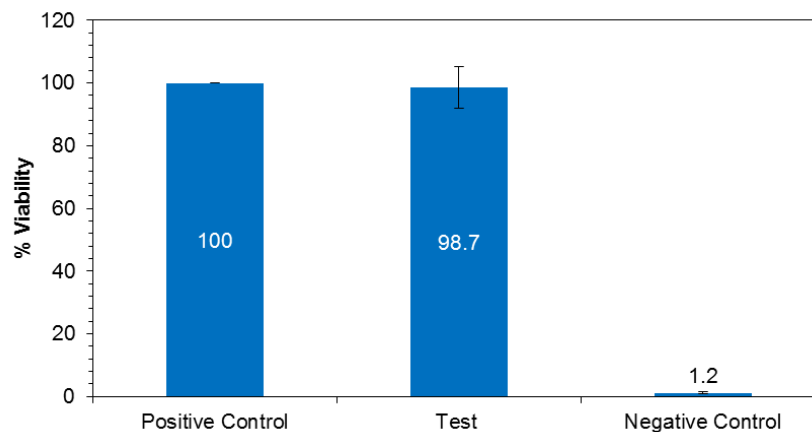


Figure 3.11: The result of the resazurin assay which shows the cell viability of MCF-7 cells grown on the silicon devices compared to both positive and negative controls. N=4 and each sample was tested in triplicate. Data shown is the average of the % viability value \pm S.D.

The resazurin cell viability assay was used to provide a quantitative analysis of the viability of the MCF-7 cells grown on the silicon devices [21]. The results of the experiment showed that the presence of fragments of the prototype silicon probes did not significantly reduce the percentage cell viability when compared with the positive control (Figure 3.11). This was to be expected given the preliminary findings from the light microscopy images and the known biocompatibility of the materials used in the fabrication process [22, 23]. The results also compared extremely well to a recently published study by Srinivasaraghavan *et al.* (2015) who showed that the

MCF-10A breast cell line displayed a $98.8 \pm 0.2\%$ viability when grown on silicon [24].

3.5.1.3 Scanning Electron Microscopy

The final biocompatibility experiment that was conducted with the silicon probes involved the SEM imaging of MCF-7 cells seeded at a density of 450,000 and cultured for 24 hours. The SEM images of the silicon probes and gold electrodes seeded with cells were taken using a Jeol JSM 5510 SEM in the Bioscience Imaging Centre, University College Cork. These high resolution images provided an insight in to the growth and distribution of the MCF-7 cells cultured across the electrode surface and the surrounding silicon substrate. The images clearly illustrated that the cells grew in a confluent layer across the entire electrode surface (Figure 3.12 A-D). At the lower kV values (A and B) it was not possible to see the gold electrode tracks as the electron beam was only focused across the surface of the cells. At the higher kV values (C and D) the depth of penetration of the electrons was significantly higher and the gold electrodes could be seen more clearly. The SEM images of MCF-7 cells seeded on to the silicon probe devices were used to visualise the three dimensional growth of the cells across the surface of the device. It was evident from these SEM images that the growth of cells was not impeded by any part of the surface of the silicon probe. This indicated that the fabricated devices and materials were biocompatible. The result presented here was in agreement with the findings of the resazurin and light microscopy experiments which showed no significant reduction in cell viability of MCF-7 cells grown on the prototype devices. The experiments performed to test the biocompatibility of stainless steel and silicon devices showed that cell growth and viability were not adversely affected by the prototype probes. This was an important milestone in the fabrication of the novel impedance probe because it indicated that the probe may be safe to use in a clinical setting without causing an adverse immune response in the patient. This result allowed the project to progress to the next experimental section which was the investigation of the impedance modulus measurements in meat tissues.

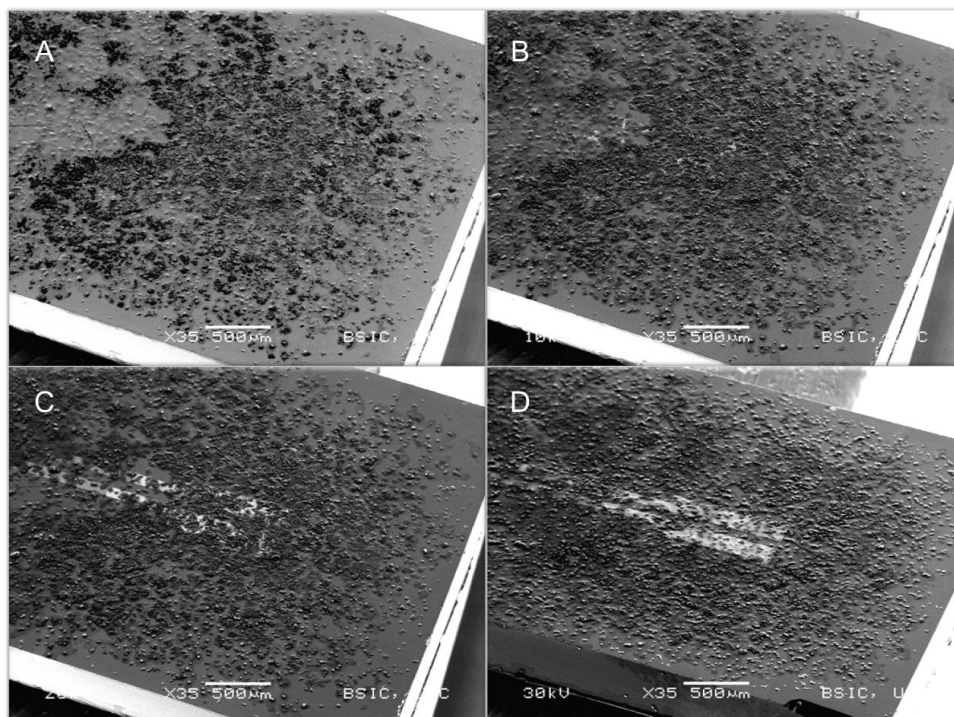


Figure 3.12: 35x magnification SEM images of a silicon probe seeded with MCF-7 cells at increasing voltage from a) 5, b) 10, c) 20 and d) 30 kV.

3.5.1.4 O-ring Biocompatibility

An inverted-phase contrast microscope was used to image the cells grown as part of the O-ring biocompatibility study. The representative images obtained during the study are shown in Figure 3.13 A-C. The images presented showed a layer of confluent cells was present in each of the wells. The presence of the O-ring in each of the three test wells did not inhibit the growth of cells in the surrounding area (Figure 3.13 A and B). A confluent cell layer was present in each of the control wells. This was expected as the necessary growth conditions were available (Figure 3.13 C). The result of this experiment showed that the O-rings chosen as part of the probe holder set-up were suitable for use during the experiment and would not impede the growth of cells across the silicon devices. This would allow a confluent layer of cells to form across the surface of the probe while also providing a water-tight seal to maintain the volume of media within the cell culture well.

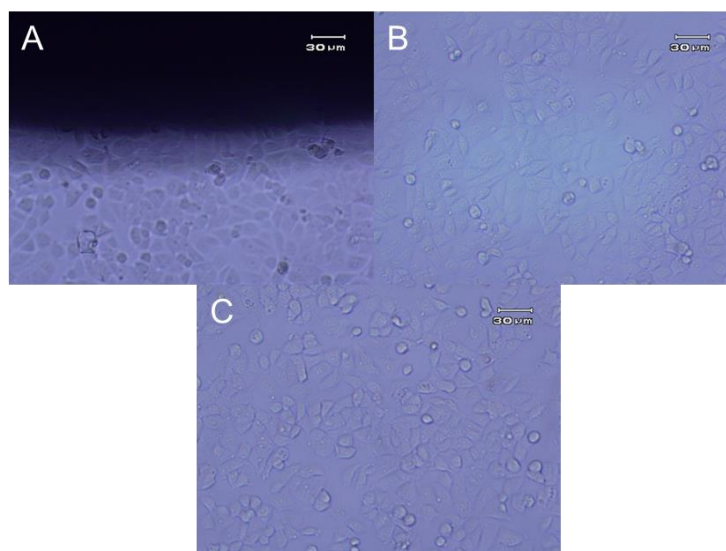


Figure 3.13: The images taken of the O-ring biocompatibility study. A) The outer edge of the O-ring in black with cells grown to confluence adjacent to it. B) An image taken from the same well as A) which shows growth across the entire well. C) An image of one of the control wells used in the experiment in which a confluent cell layer was present.

3.5.1.5 Culture of Cells on Silicon Probes

The silicon probes were inserted in the previously described cell culture holders and seeded with A549 cells. A rubber O-ring was used to provide a watertight seal between the probe and the holder. The A549 cells were initially grown on the devices to allow optimisation of the cell numbers and liquid volume necessary for confluent growth over a 24 hr period. After the cells were seeded for a day they were imaged using a light microscope (Figure 3.14 A-C). The representative images shown here displayed no significant growth at either 100,000 or 200,000 cell seeding density. The control showed no growth as expected. Multiple repeats of this experiment were unsuccessful in optimising the growth of a confluent cell layer on the silicon probes. During the imaging process it was necessary to remove the upper part of the probe holder. It was noticed on a number of occasions that the cell culture media was not in contact with the probe surface. This was most likely due to surface tension created by the opening in the O-ring being too small to allow sufficient transfer of the cell suspension onto the device. As a result it was not possible to get cell growth across the electrode surface on the silicon probe.

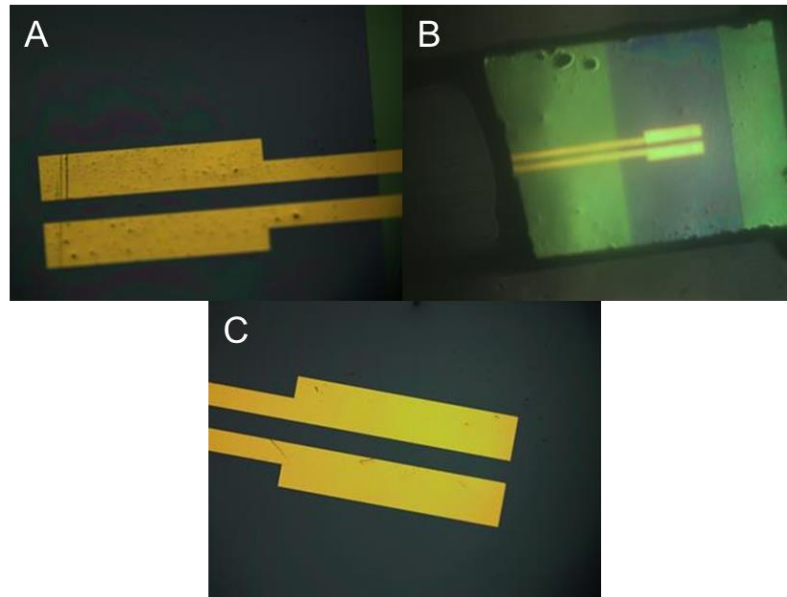


Figure 3.14: A) 10x magnification image of a silicon probe seeded with 100,000 A549 cells. B) 2.5x magnification image of a silicon probe seeded with 200,000 A549 cells. C) 10x magnification image of a silicon probe seeded with no cells as a control.

Due to time and resource constraints associated with this project it was not possible to re-design and manufacture new probe holders that would allow sufficient cell and media transfer. The width of the diced and packaged silicon probes was a limiting factor in the design of the cell culture holder and the size of O-ring used. In order to obtain impedance modulus recordings from cells cultured on to silicon devices it would have been necessary to completely redesign the silicon probes as well as the cell culture holder. The electrical packaging of the silicon probes meant that it was not possible for the probes to lie flat on the bottom of a cell culture dish. This meant that the culture media and cell suspension could not be maintained on the probe surface to allow optimum cell growth. The cell culture holder was designed to keep the probes level which provided a flat growth surface. However, the width at which the silicon probes were diced limited the maximum diameter of the O-ring that could be used to maintain the liquid seal around the electrode area. High surface tension across the opening of the O-ring did not allow the cell suspension and culture media to contact the probe surface. As a result, there was no cell adhesion or growth on the electrode surface. In order to increase the width of the O-ring opening it would have been necessary to increase the pitch between the patterned probes on the wafer

during fabrication. This would have required a complete redesign of the photolithography masks used to pattern the probe structures. This was not feasible given the time and resource constraints of the project. Ultimately, it was not possible to obtain *in vitro* impedance modulus recordings of the immortalised cancer cell lines. The principal reason for this was that the silicon probes were designed to obtain *ex vivo* tissue recordings rather than being used as cell culture impedance sensors. If it had been possible to obtain these recordings it would have proven that the silicon probes were capable of differentiating between cell lines of different origins using the modulus of the impedance. This would have provided a baseline measurement on which the future studies could have been developed. The lack of impedance data collected from this experimental section did not present a significant obstacle to the overall project progression as the primary research outcome was always to assess the ability of the probe to measure impedance in whole tissue samples. For measurement of cells in culture an ECIS set-up would be significantly more suitable and has previously been shown to be effective in a range of screening assays [25-27].

3.5.1.6 Stainless Steel Biocompatibility

Previously described results outlined that the stainless steel probes were unsuitable for conducting electrochemical recordings. However, a preliminary assessment of the biocompatibility of the stainless steel wafers was conducted in order to identify if the patterned structures were suitable for maintaining cell growth. This would provide an indication as to whether the stainless steel probes could be used for *in vivo* testing should the issue with the metal deposition be overcome in the future. A number of repetitions of biocompatibility testing of the stainless steel wafers were performed and the results obtained were as expected. The method of determining cell growth across the surface of the stainless steel wafer was the presence of PI nuclear stain. Propidium iodide is a fluorogenic compound that binds stoichiometrically to nucleic acids [28-30] which emits fluorescence proportional to the amount of DNA in the cell [31]. Using a fluorescent microscope it was confirmed that there was nuclear staining present and a corresponding absence in the control sample (Figure 3.15). The materials

used during the development were chosen because of the likely biocompatibility. The ability of cells to grow on the surface of the device was a positive step forward as it meant that not only the materials but also the processes were suitable for use in the assembly of the novel biomedical technology. Figure 3.15 shows A549 cells seeded at 80,000 (A) and 120,000 (B) on the surface of the stainless steel wafer. The cells were stained with PI and imaged using a fluorescent microscope. The outline of the recording electrodes could be seen in both images. This demonstrated that the cells were growing across the entire electrode surface and the surrounding substrate.

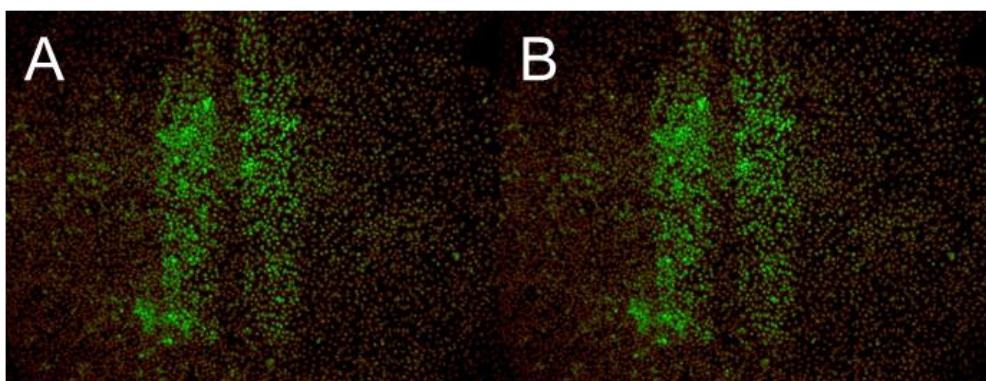


Figure 3.15: A549 cells seeded at 80,000 (A) and 120,000 (B) cells per well for a period of 24 hours on the stainless steel wafer with plastic cell culture wells attached. The cells are stained with propidium iodide (500nM) nuclear stain.

In this section, biocompatibility testing was carried out on the patterned stainless steel wafers. The tests involved the growth of A549 cells on the surface of a patterned stainless steel wafer to which wells had been attached. Propidium Iodide was previously shown to be effective in staining A549 cells, which was used to allow visualisation of the cells seeded on the surface of the material [32-34]. Confluent cell growth was shown at both 24 and 48 hr after seeding. There was an absence of cells in the control well which was to be expected as no cells were added. The result of this experiment showed that the stainless steel wafer which had been patterned with gold electrodes was biocompatible with cell growth. This was to be expected as the materials used during the fabrication process should not cause adverse reactions when in contact with cells. In particular, stainless steel and gold are commonly used materials for medical purposes [35-38]

and do not result in cell death *in vivo*. This initial experiment showed that the use of a stainless steel wafer in conjunction with silicon fabrication techniques is a potentially viable method of creating a prototype of this novel electrical impedance sensor.

3.5.2 Meat Tissue Results

3.5.2.1 Beef Impedance Recordings

One of the silicon probes (Number 13) was tested in fat and muscle samples of beef rib (Figure 3.16 A and B).

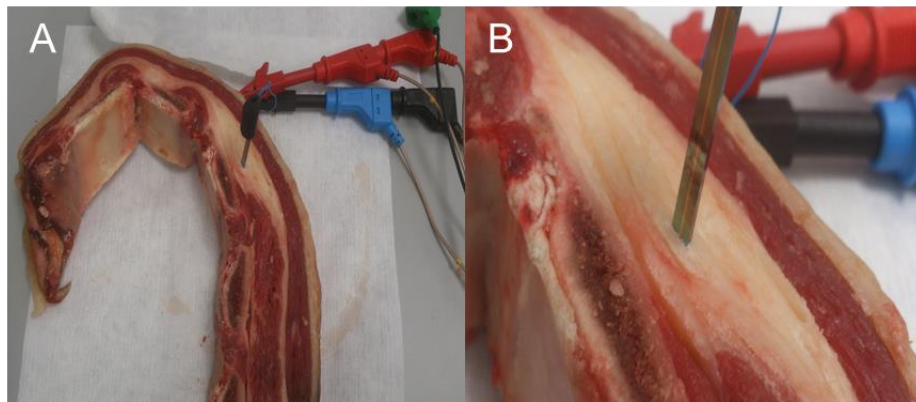


Figure 3.16: A) A silicon probe in the fat of a beef rib sample. B) A close up image of a silicon probe in a section of fat in a beef rib sample.

As part of the experiment to determine the prototype probes ability to differentiate between fat and muscle tissues, the effect of applied voltage was investigated. A series of three peak voltages 10, 30 and 50 mV were applied in triplicate at each of the measurement sites recorded. The graph shows the average values obtained at each of the applied voltages in one of the meat samples (Figure 3.17). The results showed that a negligible difference existed between the recordings obtained using each of the applied voltages. Therefore, it was decided to analyse the values obtained using the 10 mV peak amplitude as this was the lowest applied voltage which elicited a response.

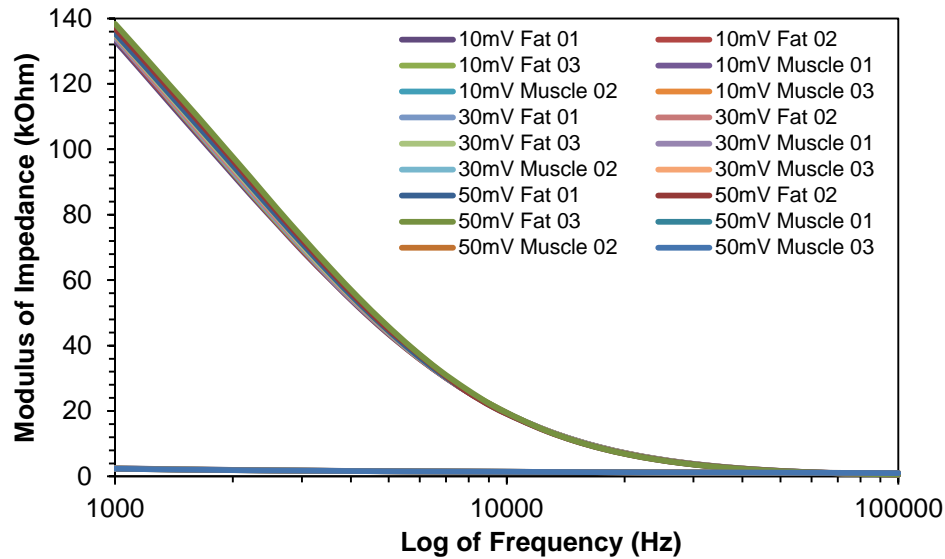


Figure 3.17: The triplicate impedance modulus values for beef fat and muscle obtained using 3 applied voltages (10, 30 and 50 mV peak voltage) across a frequency sweep from 100,000-1,000 Hz.

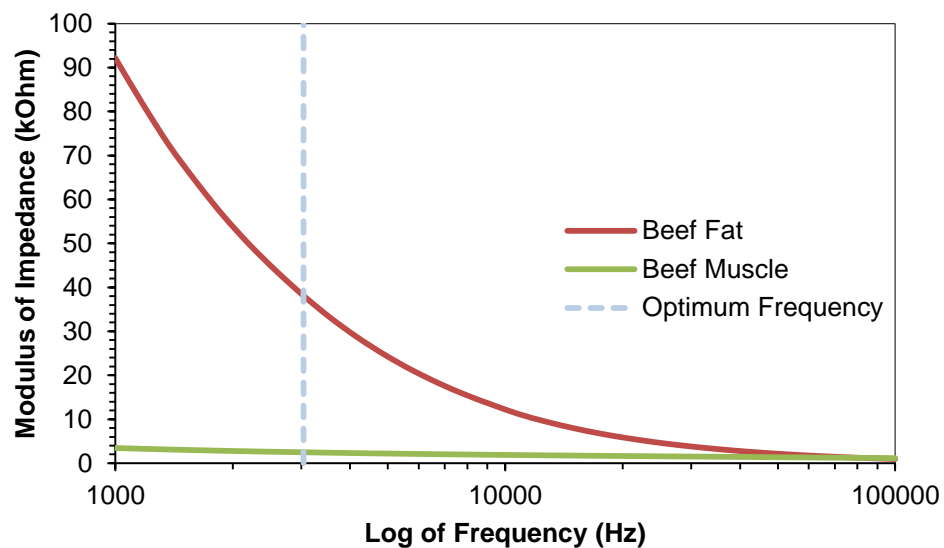


Figure 3.18: The Bode plot of the averaged values for beef rib fat and muscle frequency sweep recordings at 10 mV peak voltage. N=9.

The graph shows the averaged Bode plots of the beef samples across the frequency range at 10 mV peak amplitude (Figure 3.18). The results obtained showed that there was excellent separation between the fat and muscle tissues across the majority of the frequencies measured. A paired-samples T test was performed to determine the significance of the separation between the means of the fat and muscle impedance modulus results. For

each of the frequencies recorded below 38 kHz the observed p-value was ≤ 0.05 . Therefore, it was possible to use any of these frequencies as the optimum. Normality testing was performed using the 9 pairs of averaged data obtained from each of the meat samples at a frequency of 3 kHz. Table 3.9 shows the skewness and Kurtosis values generated from the beef fat and muscle averages for all the samples tested. For both tissue types the values for Kurtosis were below the upper limit of 9. The value for skewness for fat was below the threshold of 2 however the value for muscle was not. By combining the observed skewness Kurtosis values it was possible to assume data normality. Therefore, this data set was suitable for analysis using the paired-samples T test.

Table 3.9: The data output for the normality testing performed on average beef fat and muscle recordings at a frequency of 3 kHz. N=9.

Normality Test	Beef Fat	Beef Muscle
Skewness	0.946	2.393
Kurtosis	-0.179	5.866

Using the results from the paired-samples T test, it was decided that 3 kHz would be chosen for all future fixed frequency recordings. The mean separation between the two tissue types at 3 kHz (3,039 Hz) was 35,607 Ω ($p < 0.001$) (Appendix 6.8.1). Figure 3.19 shows the mean \pm S.D. for the beef fat and muscle samples obtained at 3 kHz (N=9). It was evident from the graph that significantly larger variability existed in the fat tissue compared to the muscle. Regardless of this, it was still possible to choose a frequency that was suitable for fixed frequency recordings that could differentiate between all fat and muscles samples of bovine origin.

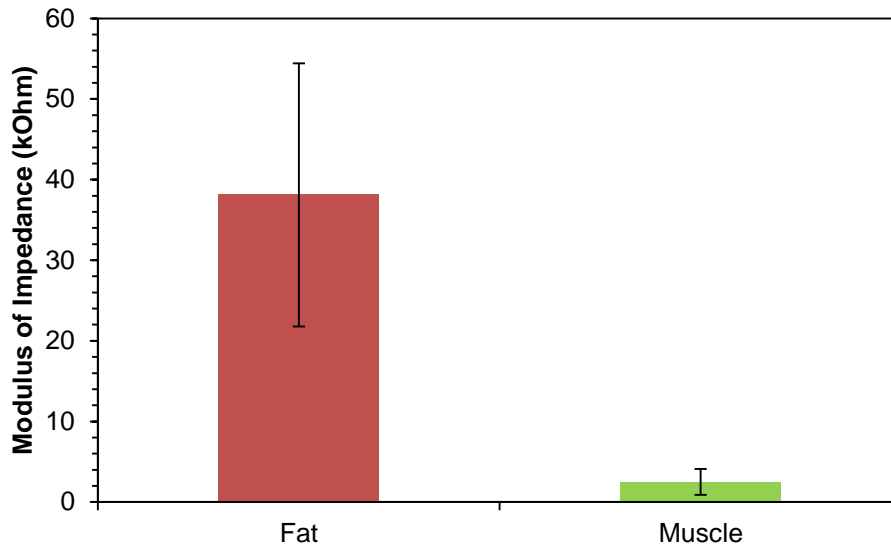


Figure 3.19: The result of the paired-samples T test to compare the means of the beef rib fat and muscle impedance modulus recordings at 3 kHz. Mean \pm S.D., N=9, $p < 0.001$.

The results outlined in this section showed that the prototype silicon probe was capable of differentiating between fat and muscle tissues of bovine origin. This provided the first confirmation of the devices ability to differentiate between *ex vivo* fat and muscle tissues. The optimum fixed frequency value chosen was 3 kHz. This value provided a statistically significant separation between the two tissue types and the data was shown to be suitable as demonstrated by the normality tests. Therefore, the effects observed are less likely to be either entirely resistive or capacitive. This result provided the basis for the clinical study that aimed to use electrical impedance to differentiate between healthy and cancerous breast tissue removed during surgery.

3.5.2.2 Pressure Testing

This experiment was conducted to determine the effect of applying pressure on tissues during electrical impedance recordings. Figure 3.20 shows the results of the pressure testing performed on the beef muscle samples. The results showed that for each of the pressures applied, there was very little variation between the observed impedance modulus values. There was a lack of variability between the clamp and clamp tight recordings which did not differ significantly from each other despite the increase in pressure applied by the Weitlaner tissue retractor. This suggested that for the purpose of

recording muscle tissue samples the effect of externally applied pressure does not appear to have an effect on the electrical impedance value obtained.

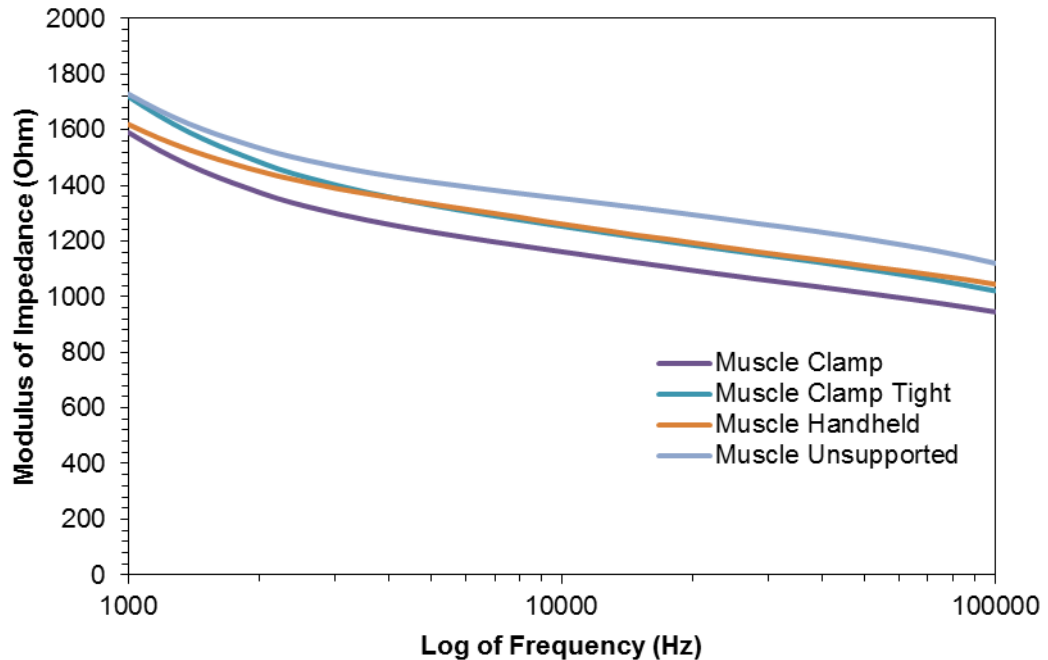


Figure 3.20: The average values for the test of pressure on the modulus of the electrical recordings obtained in a beef rib muscle sample. The averages of the triplicate recordings for each variable are shown.

The results for the fat measurements showed significant variability across the different experimental parameters (Figure 3.21). The clamped sample displayed higher impedance than the other two recordings. This indicated that the increase in externally applied pressure resulted in an increase in electrical impedance compared to the unsupported and handheld recordings. Due to the variability observed between the different fat recordings it is necessary to ensure that the type of pressure applied is the same for all recordings and is constant throughout the recording procedure.

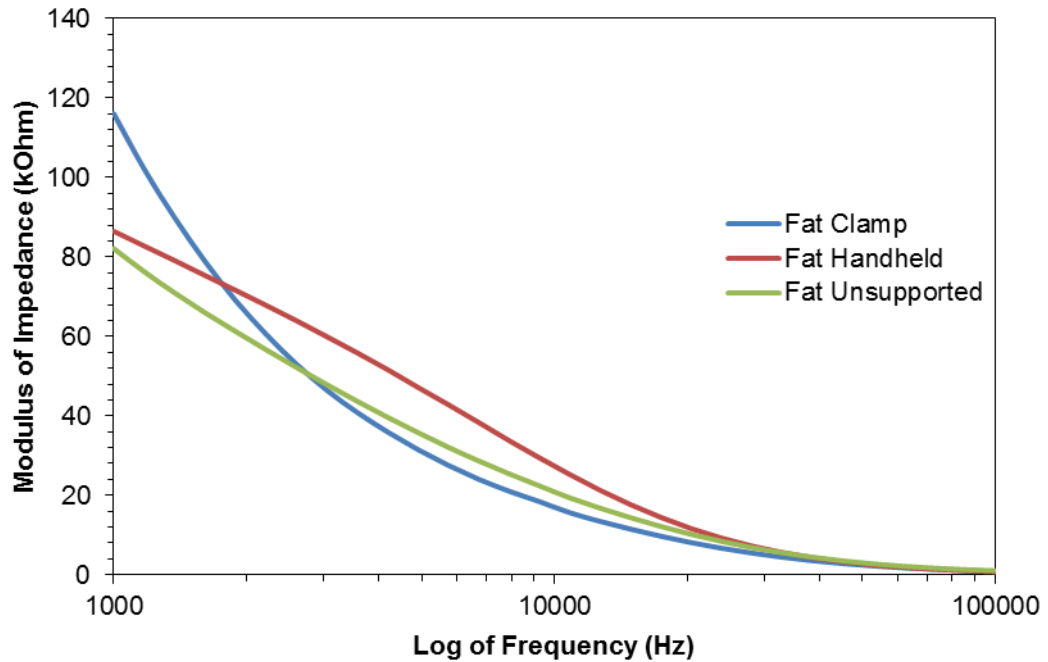


Figure 3.21: The average values for the test of pressure on the modulus of the electrical recordings obtained in a beef rib fat sample. Average of triplicate recordings for each variable.

The effect of externally applied pressure on electrical impedance values was investigated using the silicon prototype to measure beef rib fat and muscle samples. The results obtained showed that the effect of pressure was negligible during recording of muscle samples but that the electrical impedance of fat was variable according to pressure applied. A study by González-Correa *et al.* demonstrated that increased pressure applied to the electrical impedance probe could produce an increase in the recordings observed. However, the team noted that the effect of pressure was significantly less than the observed difference between the tissues of interest [20]. They suggested that the increase in impedance resulting from increased pressure may be caused by squeezing of the intracellular fluid with simultaneous reduction of extracellular spaces within the tissues [20]. An important observation of this study was the possibility that the recorded impedance values *in vitro* may not reflect the *in vivo* situation. This was due to the pressure distribution beneath the tissues being different because of a lack of support by a firm surface *in vivo* [20]. This point is particularly relevant to the future development of the current silicon prototype utilised in this

project. It will have to be able to penetrate tissue structures of the breast effectively without damaging the surrounding tissues and without externally applied pressure to ensure tissue contact with the electrode surface. The concern relating to the differences between *in vivo* and *ex vivo* samples is expanded on by Keshtkar and Keshtkar in their 2008 paper. They suggest that by applying an external pressure to tissues *in vivo*, it is possible to interrupt the blood supply and cause an increase in impedance by reducing the volume of fluid in the tissues [21]. Therefore it can be expected that higher impedance can be obtained from *in vivo* tissues compared to *ex vivo* tissue when the same external pressure is applied [21]. Both research groups propose that the primary loss of fluid in compressed tissues comes from the extracellular fluid compartments. Dodde *et al.* suggested that when soft tissues were compressed fluid loss must be seen as being composed of both intra- and extra-cellular fluid [22]. The most significant aspect of the research into the effect of pressure on electrical impedance recordings is that in both *ex vivo* and *in vivo* settings the same force must be applied to the probe during all measurements.

3.5.2.3 Depth Testing

This experiment was conducted using one of the silicon probes to determine if the depth at which a recording is taken has an effect on the measured impedance. Triplicate frequency sweep measurements were taken at three different depths 10, 15 and 20 mm from the surface of the gel (Figure 3.22 A-C). The probe was able to support itself in the gel and no external pressure was applied during the measurement phase.

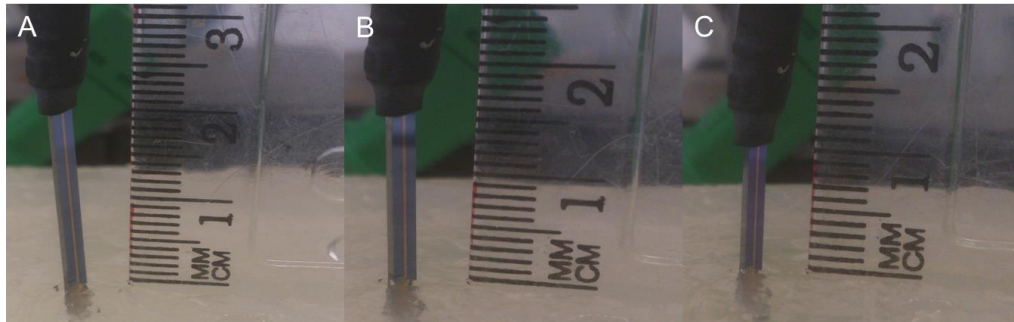


Figure 3.22: The probe and ruler used to measure the depth of penetration during experimentation at 10 mm (A), 15 mm (B) and 20 mm (C).

The results obtained during this experiment are shown in Figure 3.23. The graph shows the average of the triplicate recordings taken at each depth and overlaid on each other. It can clearly be seen that there was almost no separation between the lines. However, the maximum separation which occurs at 1,000 Hz is only 8.5 % of the total value in Ohms recorded.

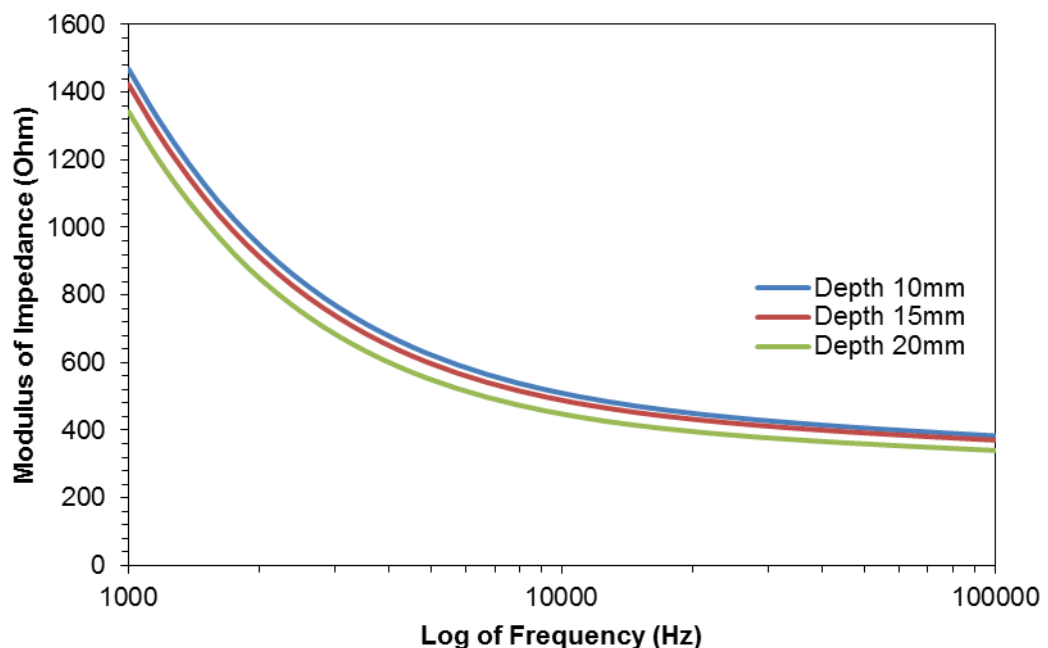


Figure 3.23: The results of the depth of penetration experiments at three depths 10, 15 and 20 mm. Values shown are averages of triplicate recordings at each depth.

The results obtained during the experiment were positive as it showed that for all frequencies tested there was almost no difference across the penetration depths. This was an expected result due to the design of the

probe which provided an insulation layer along the entire length the gold tracts. This prevented the detection of electrical impedance outside of the dual microelectrodes at the recording end of the device. This was important to note for future studies as *ex vivo* and *in vivo* measurements cannot always be taken at the same depth due to the nature of the sample and the tissue type of interest.

3.5.2.4 Parasitic Capacitance Testing

In order to assess whether parasitic capacitance was present across the frequency range being analysed using the silicon probe it was necessary to test the device in a standard buffered solution. The solution that was chosen was HBSS which had previously been used as part of the cell culture testing. The frequency range of interest was from 1,000 – 100,000 Hz at the optimum peak voltage of 10 mV. The left electrode of each silicon probe was tested a total of 5 times when placed in 10 ml of HBSS. The average capacitive reactance plot from one of the silicon probes is shown in Figure 3.24. The results show no evidence of parasitic capacitance across the frequency range of interest. This indicates that it is possible to use any of the frequencies within this range for the purpose of fixed frequency recordings.

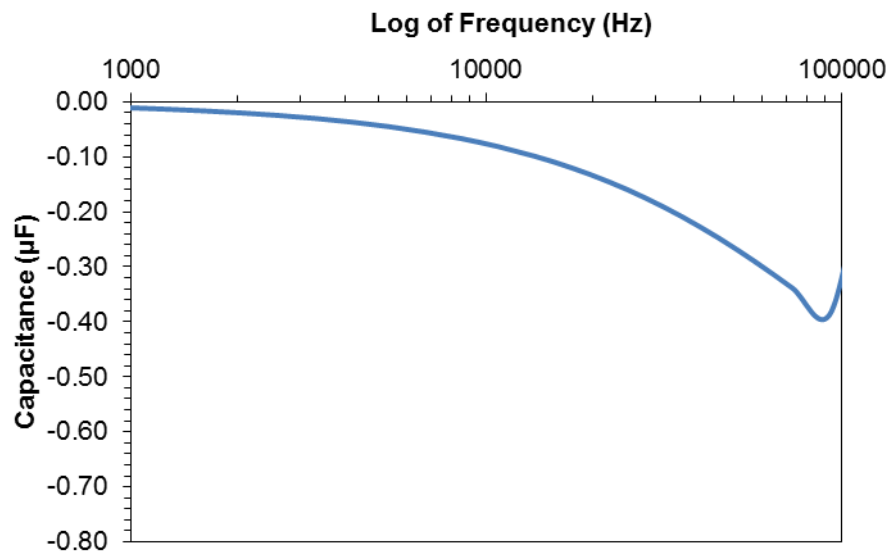


Figure 3.24: The average plot of the capacitive reactance response of a silicon probe in HBSS buffer. N=1.

3.5.2.5 Lamb Impedance Recordings

One of the silicon probes (Number 14) was tested in fat and muscle samples of lamb centre loin (Figure 3.25 A and B).

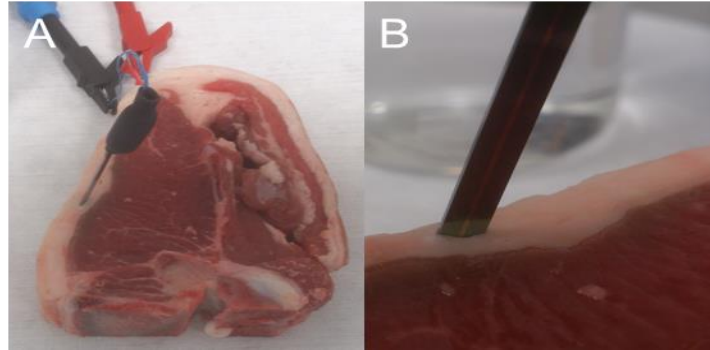


Figure 3.25: A) A silicon probe placed in an area of fat in a lamb centre loin sample. B) A close up of the probe in the fat tissue (right).

As with the beef rib samples, the effect of applied voltage was investigated using the lamb centre loin samples. A series of three voltages 10, 30 and 50 mV peak voltage was applied in triplicate at each of the measurement sites recorded. The graph shows the average values obtained at each of the applied voltages in one of the meat samples (Figure 3.26).

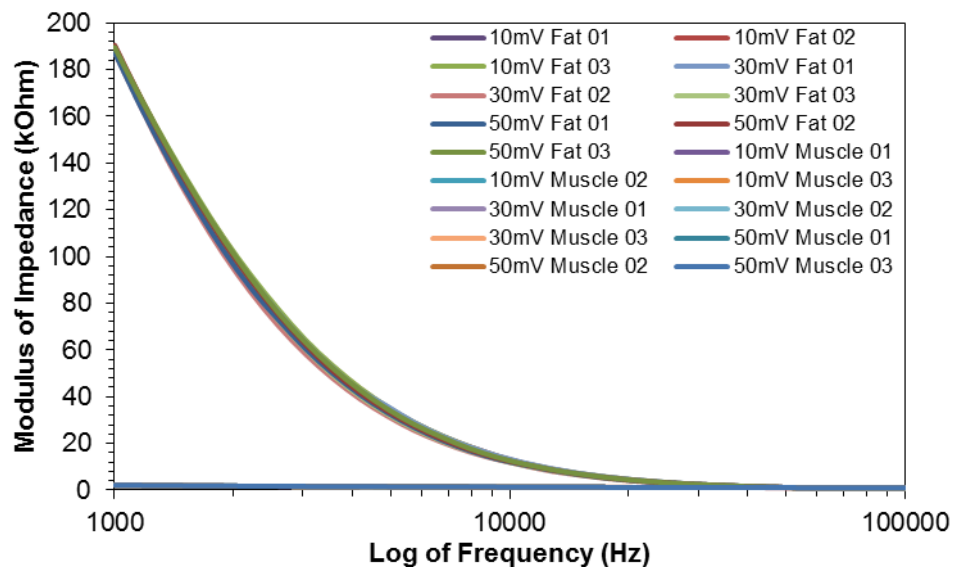


Figure 3.26: The triplicate electrical impedance modulus values for lamb fat and muscle obtained using 3 applied peak voltages (10, 30 and 50 mV) across a frequency sweep from 100,000-1,000 Hz.

The results showed that a negligible difference existed between the recordings obtained using each of the applied voltages. Therefore, it was decided to analyse the values obtained using the 10 mV peak amplitude as this was the lowest applied voltage which elicited a response.

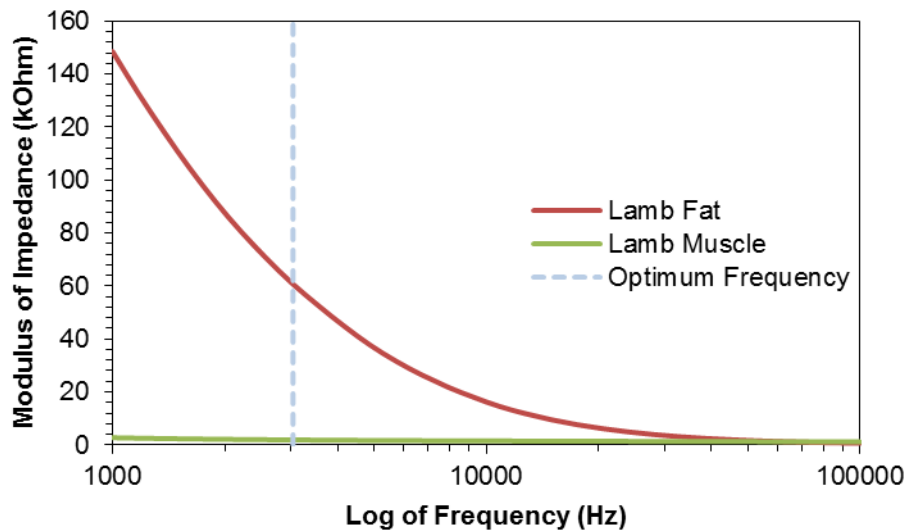


Figure 3.27: The Bode plot of the averaged values for lamb centre loin fat and muscle frequency sweep recordings at 10 mV peak amplitude. N=9.

The graph shows the averaged Bode plots of the lamb centre loin samples across the frequency range at 10 mV peak amplitude (Figure 3.27). The results obtained showed that there was excellent separation between the fat and muscle tissues across all of the frequencies below 52 kHz. A paired-samples T test was performed to determine the significance of the separation between the means of the fat and muscle impedance modulus results. Across each of the frequencies recorded below 52 kHz the observed p-value was <0.05 . Therefore it was possible to use any of the recorded frequencies as the optimum. Normality testing was performed using the 9 pairs of averaged data obtained from each of the lamb samples at a frequency of 3 kHz. Table 3.10 shows the skewness and Kurtosis values generated from the lamb fat and muscle averages obtained from each of the meat samples. For both tissue types the values were below the upper limit of 2 and 9 for skewness and Kurtosis respectively. Therefore, this data set was suitable for analysis using the paired-samples T test.

Table 3.10: The data output for the normality testing performed on average lamb fat and muscle recordings at a frequency of 3 kHz. N=9.

Normality Test	Lamb Fat	Lamb Muscle
Skewness	0.634	1.325
Kurtosis	-1.003	1.819

As with the beef recordings it was decided that 3 kHz would be chosen for all future fixed frequency recordings. The mean difference between the two tissue types at 3 KHz (3,039 Hz) was 58,816 Ω ($p < 0.001$) (Appendix 6.8.1). The graph shows the mean \pm S.D. at 3 KHz and 10 mV peak voltage for the lamb centre loin fat and muscle samples (N=9) (Figure 3.28). It was evident from the graph that a larger variability existed in the fat tissue compared to the muscle however this was much less than was observed in either the beef or pork fat tissue.

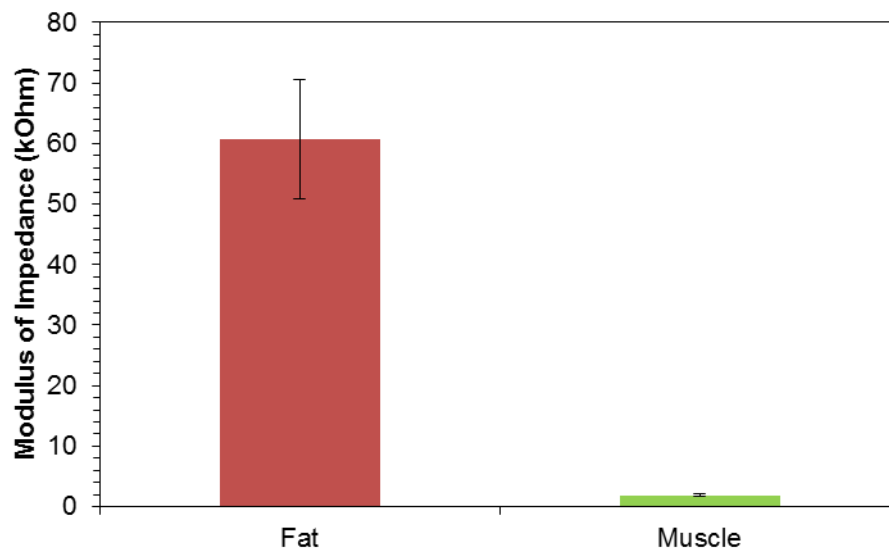


Figure 3.28: The result of the paired-samples T test to compare the means of the lamb centre loin fat and muscle impedance recordings at 3 kHz. Mean \pm S.D., N=9, $p < 0.001$.

The results outlined in this section showed that the prototype silicon probe was capable of differentiating between fat and muscle tissues of ovine origin. This provided additional confirmation of the devices ability to differentiate between *ex vivo* fat and muscle tissues. This result in combination with the previously described beef results provided the basis for the future clinical

study that aims to use electrical impedance to differentiate between healthy and cancerous breast tissue removed during surgery.

3.5.2.6 Pork Impedance Recordings

One of the silicon probes (Number 13) was tested in fat and muscle samples of pork centre loin (Figure 3.29). As with the beef and lamb samples, the effect of applied peak voltage was also investigated using the pork samples. A series of three peak voltages (10, 30 and 50 mV) were applied in triplicate at each of the recorded measurement sites. The graph shows the average values obtained for each of the applied voltages in one of the meat samples (Figure 3.30).

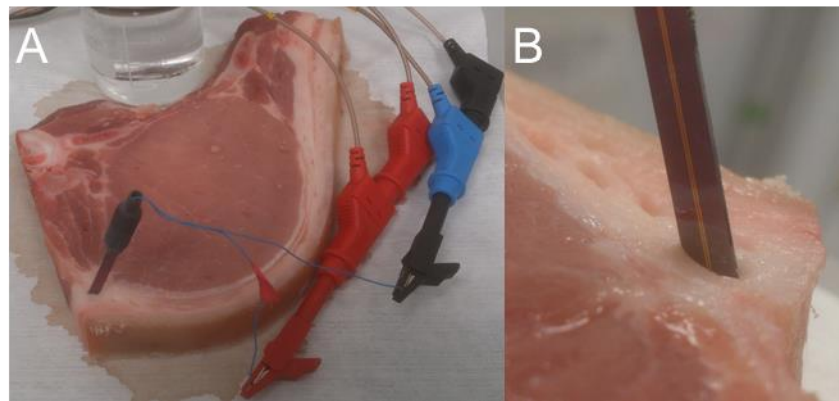


Figure 3.29: A) A silicon probe in a region of fat in a pork centre loin sample. B) A close up of the probe in the fat tissue (right).

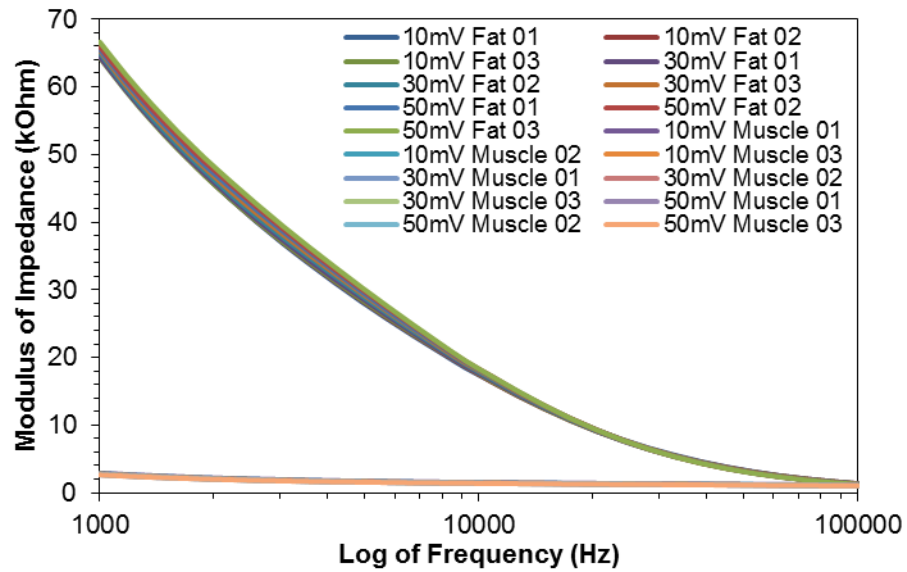


Figure 3.30: The triplicate electrical impedance values for pork fat and muscle obtained using 3 applied voltages (10, 30 and 50 mV peak voltage) across a frequency sweep from 100,000-1,000 Hz.

The results showed that a negligible difference existed between the recordings obtained using each of the applied voltages. Therefore, it was decided to analyse the values obtained using the 10 mV peak amplitude as it was the lowest applied voltage which elicited a response. The graph shows the averaged Bode plots of the pork centre loin samples across the frequency range at 10 mV peak amplitude (Figure 3.31). The results obtained showed that there was excellent separation between the fat and muscle tissues across all of the frequencies measured.

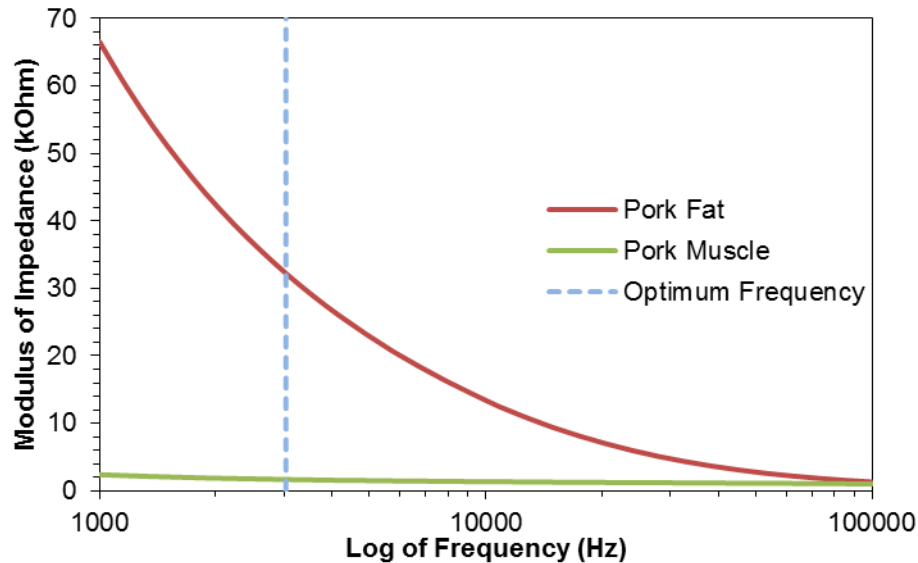


Figure 3.31: The Bode plot of the averaged values for pork centre loin fat and muscle frequency sweep recordings at 10 mV peak voltage. N=9.

A paired-samples T test was performed to determine the significance of the separation between the means of the fat and muscle impedance results. For all frequencies recorded except 100 kHz the observed p-value was <0.05 . Normality testing was performed using the 9 pairs of averaged data obtained from each of the pork samples at a frequency of 3 kHz. Table 3.11 shows the skewness and Kurtosis values generated from the pork fat and muscle averages obtained from each of the meat samples. For both tissue types the values were below the upper limit of 2 and 9 for skewness and Kurtosis respectively. Therefore, this data set was suitable for analysis using the paired-samples T test.

Table 3.11: The data output for the normality testing performed on average pork fat and muscle recordings at a frequency of 3 kHz. N=9.

Normality Test	Pork Fat	Pork Muscle
Skewness	0.050	-0.042
Kurtosis	-0.169	-0.110

It was decided that 3 kHz would be chosen for all future fixed frequency recordings as this would be in line with the optimum chosen for the beef and lamb samples while maintaining a significance of below 0.05. The mean separation between the two tissue types at 3 KHz (3,039 Hz) was 30,537 Ω

($p < 0.001$) (Appendix 6.8.1). The graph shows the mean \pm S.D. at 3 KHz and 10 mV peak amplitude for the pork fat and muscle samples ($N=9$) (Figure 3.32). It was evident from the graph that the pork fat displayed the largest variability of any of the recorded tissues in this study. It was clear at the time of recording that the pork fat was significantly less solid than either the beef or lamb fat tissues. This made the recording of the electrical impedance values more difficult and the variable composition of the fat at room temperature may have influenced the recorded values. Regardless of this it was still possible to choose a frequency that was suitable for fixed frequency recordings that could differentiate between all fat and muscles samples of porcine origin.

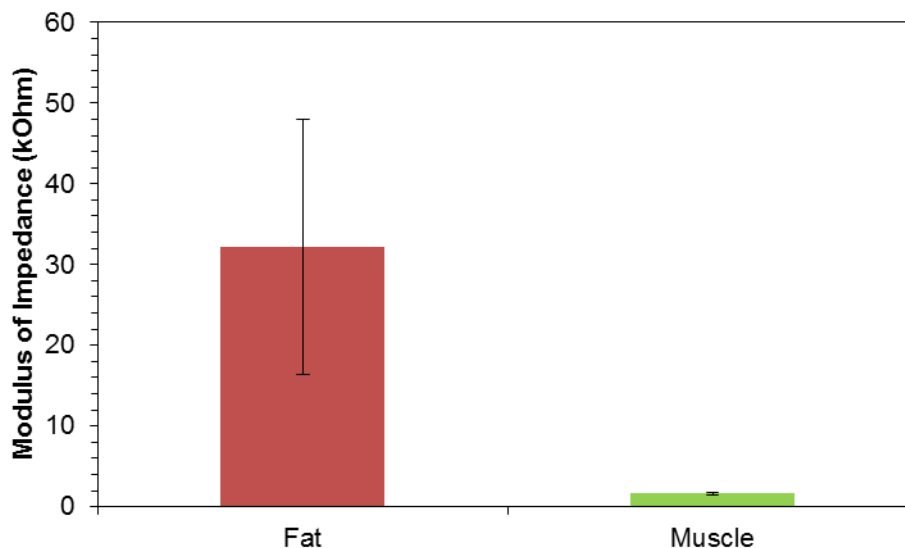


Figure 3.32: The result of the paired-samples T test to compare the means of the pork centre loin fat and muscle impedance recordings at 3 kHz. Mean \pm S.D., $N=9$, $p = 0.001$.

In order to determine if the silicon impedance probes were functioning in a stable manner across each of the recordings performed it was necessary to plot the individual phase angle data points for each of the pork measurements using a modified Bland-Altman plot. The mean \pm 1.96 S.D were calculated for pork fat and muscle separately and displayed in Figure 3.33 and 3.34.

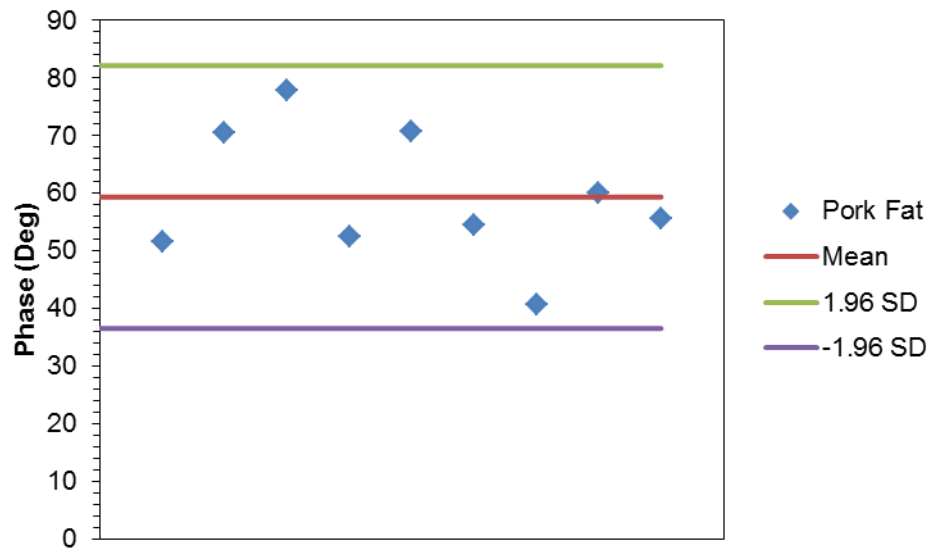


Figure 3.33: A modified Bland-Altman plot of the phase angle for each of the pork fat recordings. The mean \pm 1.96 S.D have been plotted on the graph.

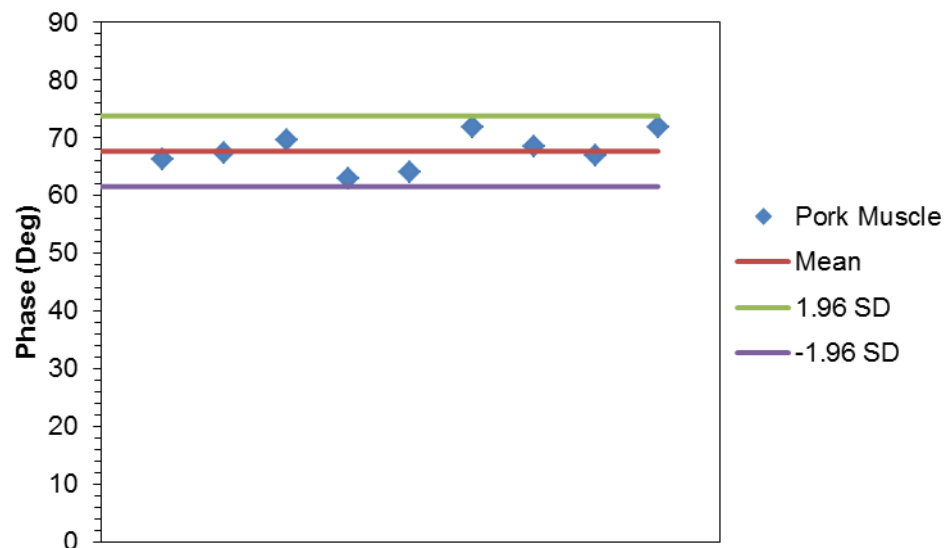


Figure 3.34: A modified Bland-Altman plot of the phase angle for each of the pork muscle recordings. The mean \pm 1.96 S.D have been plotted on the graph.

The results show that for both the fat and muscle recordings the phase angle associated with the impedance modulus recordings are within 1.96 S.D of the mean phase value. This indicated that the recorded phase values did not deviate significantly from the mean across any of the tissue recordings. It was evident from the graphs that pork fat recordings displayed a larger spread of phase angle compared to the muscle tissue but each of the average phase values still fell within the 1.96 S.D range. The results

demonstrated that the phase angle response observed when recording the biological tissue samples were stable enough for a comparison to be made between each of repeated experimental measurements. In particular, the measured phase angle for the muscle tissues showed a narrow range which was centred on the mean phase angle value for the combined muscle tissues. This finding is in keeping with the observed impedance modulus recordings which showed significantly less variability in the muscle recordings compared to the associated fat tissues.

The results outlined in this section showed that the prototype silicon probe was capable of differentiating between fat and muscle tissues of porcine origin. This provided further confirmation of the devices ability to differentiate between *ex vivo* tissues including fat and muscle. This result in combination with the previously described beef and lamb results provided the basis for the future clinical study that would aim to use electrical impedance to differentiate between healthy and cancerous breast tissue removed during surgery.

3.5.2.7 All Tissues Combined

In order to confirm if the origin of the tissue impacted on the ability of the silicon probe to differentiate between fat and muscle a paired-samples T test was performed on the combined data from all of the beef, lamb and pork samples. At the optimum frequency of 3 kHz it was shown that the combined data had a mean separation of 41,653 Ω ($p < 0.001$) (Figure 3.35). The results shown here demonstrated that when all of the tissues were combined it was possible to obtain a significant separation between the fat and muscle tissues. This showed that at the optimum frequency of 3 kHz, the silicon probe was capable of differentiating between fat and muscle tissue for each of the different animal sources.

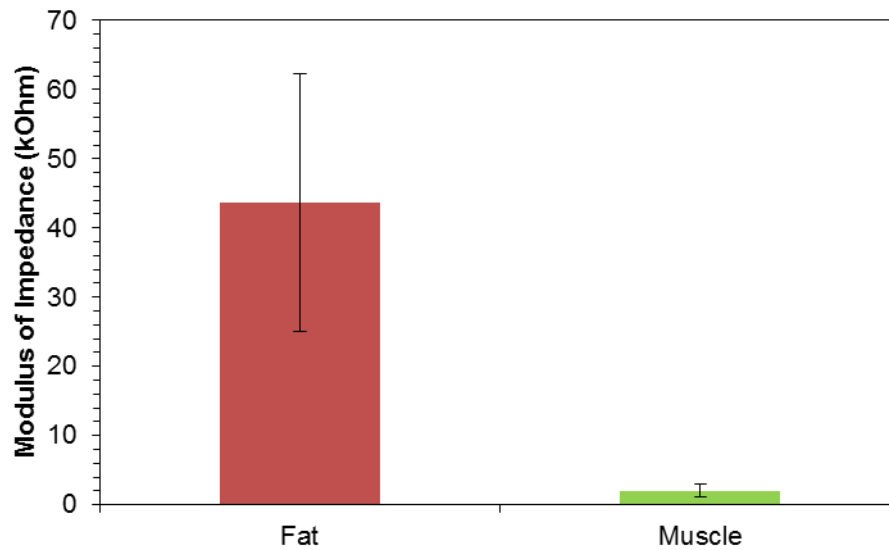


Figure 3.35: The result of the paired-samples T test to compare the combined beef, lamb and pork fat and muscle impedance recordings at 3 kHz. Mean \pm S.D., N=27, $p < 0.001$.

The results of the *ex vivo* measurements of meat tissues showed positive results. The prototype probe was proven to be capable of differentiating between fat and muscle tissue from three different animal sources which included cow, sheep and pig. The use of frequency sweep electrical impedance measurements at a fixed voltage showed that at all of the frequencies tested there was separation between the values obtained for fat and muscle. In each of the tissue samples tested there was increased separation as the frequency decreased. One of the most interesting findings observed was the level of variability encountered when measuring the fat tissues compared to muscle of same origin. This variation may be due to the difference in water content throughout the fat tissues and the variable increase in the temperature of the cells as they reach room temperature can potentially alter the recorded impedance value. The lower water content in fat tissues decreases the conductivity of the electrical current and therefore increases the electrical impedance [39, 40]. There was significantly less variation across each of the muscle samples which were analysed but this was to be expected due to significantly higher water content in each of the cells [39]. This resulted in increased conductivity which decreased the electrical impedance compared to the surrounding fat tissues.

3.6 Conclusions

The results outlined in this chapter demonstrate the biocompatibility and electrical impedance ability of the silicon probe prototypes. In the opening section it was shown that the devices were biocompatible with immortalised cell growth. This was proven using a number of techniques including light, fluorescence and SEM and a resazurin cell viability assay. By quantitatively measuring the number of living cells grown on the surface of the silicon probe fragments it was possible to determine the biocompatibility of the individual devices. It is not possible for resazurin to be reduced to resorufin by dead cells and therefore only cells which are alive at the time of analysis are measured when assessing cell viability. The results of this assay are compared with the light and scanning electron microscopy images to gain a complete understanding of the biocompatibility of the silicon probes. This was a positive result as it demonstrated that both the materials and fabrication procedures used in the production of these devices did not significantly inhibit cell growth and therefore it was determined that the silicon probes were biocompatible. Unfortunately it was not possible to complete the intended investigation of the electrical impedance of cultured cells on the silicon devices. This was due to a number of design constraints which inhibited the packaged probes use in a cell culture environment. In the second section of the chapter, the ability of the silicon probes to differentiate between fat and muscle tissues was shown. Samples of fat and muscle from beef, lamb and pork were repeatedly tested and it was demonstrated that the probes were capable of differentiating between the two tissue types. The tissues of three different origins were tested to validate the probes ability to differentiate between fat and muscle tissue and to ascertain if a significant difference existed between the different meats. It was shown that the beef and pork samples were similar in terms of mean impedance modulus values and fat variability. The lamb showed a higher mean impedance modulus value compared to either the beef or pork and displayed less variability in the fat recordings. By testing tissues from a number of different animal origins it was possible to show that the silicon probe could differentiate between fat and muscle tissue of very different cellular composition. This was a

significant milestone in this project as it definitively showed that the silicon probes were able to differentiate between tissue types in an *ex vivo* setting.

3.6.1 Future Work

The future work associated with this aspect of the research project would involve the measurement of a selection of biological tissues recorded at both room and physiological temperatures. This could create a database of healthy tissue electrical impedance recordings. These values could then be used to identify meat tissue samples as well as being used as a comparison to pathological tissues including cancerous tissue samples. Future iterations of this device may potentially be used in the detection and diagnosis of animal diseases but this would require specific research in this area and include trials using live animal models. This could open a new market for this sensor in the area of the animal health and veterinary medicine for the detection of pathological conditions. A significant redesign of the cell culture holders would allow for measurements to be obtained from seeded cells on the silicon probes. This would allow both primary and immortalised cells to be monitored during each stage of the cell growth, differentiation and death cycle using electrical impedance as the detection method. This would provide real-time analysis of changes in cell morphology and survival and would allow for testing of therapeutic substances on the cell cultures with feedback provided by impedance detection. However, this probe was designed for the purpose of recording electrical impedance measurements in *ex vivo* and *in vivo* tissues of animal and human origin. Therefore, the most appropriate future investigations would focus on differentiation of intact tissue structures with a focus on differential disease diagnosis.

3.7 References

1. Mamouni, J. and L. Yang, *Interdigitated microelectrode-based microchip for electrical impedance spectroscopic study of oral cancer cells*. Biomed Microdevices, 2011. **13**(6): p. 1075-88.
2. Giard, D.J., S.A. Aaronson, G.J. Todaro, P. Arnstein, J.H. Kersey, H. Dosik, and W.P. Parks, *In vitro cultivation of human tumors: establishment of cell lines derived from a series of solid tumors*. Journal of the National Cancer Institute, 1973. **51**(5): p. 1417-1423.
3. Fogh, J. and G. Trempe, *New human tumor cell lines*, in *Human tumor cells in vitro*. 1975, Springer. p. 115-159.
4. Soule, H., J. Vazquez, A. Long, S. Albert, and M. Brennan, *A human cell line from a pleural effusion derived from a breast carcinoma*. Journal of the National Cancer Institute, 1973. **51**(5): p. 1409-1416.
5. Campisi, J. and F. d'Adda di Fagagna, *Cellular senescence: when bad things happen to good cells*. Nat Rev Mol Cell Biol, 2007. **8**(9): p. 729-740.
6. Itahana, K., J. Campisi, and G. Dimri, *Mechanisms of cellular senescence in human and mouse cells*. Biogerontology, 2004. **5**(1): p. 1-10.
7. Dimri, G., H. Band, and V. Band, *Mammary epithelial cell transformation: insights from cell culture and mouse models*. Breast Cancer Res, 2005. **7**(4): p. 171-179.
8. Ouellette, M.M., L.D. McDaniel, W.E. Wright, J.W. Shay, and R.A. Schultz, *The establishment of telomerase-immortalized cell lines representing human chromosome instability syndromes*. Human Molecular Genetics, 2000. **9**(3): p. 403-411.
9. Allen, D.D., R. Caviedes, A.M. Cárdenas, T. Shimahara, J. Segura-Aguilar, and P.A. Caviedes, *Cell Lines as In Vitro Models for Drug Screening and Toxicity Studies*. Drug Development and Industrial Pharmacy, 2005. **31**(8): p. 757-768.
10. Pariente, J.-L., B.-S. Kim, and A. Atala, *In vitro biocompatibility evaluation of naturally derived and synthetic biomaterials using normal human bladder smooth muscle cells*. The Journal of urology, 2002. **167**(4): p. 1867-1871.
11. Martina Holst, C. and S.M. Oredsson, *Comparison of three cytotoxicity tests in the evaluation of the cytotoxicity of a spermine analogue on human breast cancer cell lines*. Toxicology in Vitro, 2005. **19**(3): p. 379-387.
12. Anoopkumar-Dukie, S., J.B. Carey, T. Conere, E. O'Sullivan, F.N. van Pelt, and A. Allshire, *Resazurin assay of radiation response in cultured cells*. Br J Radiol, 2005. **78**(934): p. 945-7.
13. Borra, R.C., M.A. Lotufo, S.M. Gaglioti, M. Barros Fde, and P.M. Andrade, *A simple method to measure cell viability in proliferation and cytotoxicity assays*. Braz Oral Res, 2009. **23**(3): p. 255-62.
14. Riss, T., R. Moravec, A. Niles, H. Benink, T. Worzella, and L. Minor, *Cell viability assays*. 2004.
15. Sigma-Aldrich. *MCF7 Cell Line human*. 2015 [cited 2015 24th August]; Available from:

- <http://www.sigmaaldrich.com/catalog/product/sigma/86012803?lang=en®ion=IE>.
16. LeGresley, M. and G. McDermott, *Counting chamber methods for quantitative phytoplankton analysis—haemocytometer, Palmer-Maloney cell and Sedgewick-Rafter cell*. Microscopic and molecular methods for quantitative phytoplankton analysis. UNESCO (IOC Manuals and Guides), 2010: p. 25-30.
 17. Sigma-Aldrich. *A549 Cell Line human*. 2015 [cited 2015 24th August]; Available from: <http://www.sigmaaldrich.com/catalog/product/sigma/86012804?lang=en®ion=IE>.
 18. Sigma-Aldrich. *HT29/219*. 2015 [cited 2015 24th August]; Available from: <http://www.sigmaaldrich.com/catalog/product/sigma/85061109?lang=en®ion=IE>.
 19. Platts & Nisbett Ltd. *Weitlaner Retractor*. 2015 [cited 2016 04 January]; Available from: http://www.plattsnisbett.com/weitlaner-retractor-pn0951-pn1094-pn0952_P3.html.
 20. Posten, H.O., *Robustness of the two-sample t-test*, in *Robustness of statistical methods and nonparametric statistics*. 1984, Springer. p. 92-99.
 21. Bae, Y., T.A. Diezi, A. Zhao, and G.S. Kwon, *Mixed polymeric micelles for combination cancer chemotherapy through the concurrent delivery of multiple chemotherapeutic agents*. Journal of Controlled Release, 2007. **122**(3): p. 324-330.
 22. Voskerician, G., M.S. Shive, R.S. Shawgo, H. Von Recum, J.M. Anderson, M.J. Cima, and R. Langer, *Biocompatibility and biofouling of MEMS drug delivery devices*. Biomaterials, 2003. **24**(11): p. 1959-1967.
 23. Kristensen, B.W., J. Noraberg, P. Thiébaud, M. Koudelka-Hep, and J. Zimmer, *Biocompatibility of silicon-based arrays of electrodes coupled to organotypic hippocampal brain slice cultures*. Brain Research, 2001. **896**(1–2): p. 1-17.
 24. Srinivasaraghavan, V., J. Strobl, and M. Agah, *Microelectrode bioimpedance analysis distinguishes basal and claudin-low subtypes of triple negative breast cancer cells*. Biomed Microdevices, 2015. **17**(4): p. 80.
 25. K'Owino, I.O. and O.A. Sadik, *Impedance Spectroscopy: A Powerful Tool for Rapid Biomolecular Screening and Cell Culture Monitoring*. Electroanalysis, 2005. **17**(23): p. 2101-2113.
 26. Opp, D., B. Wafula, J. Lim, E. Huang, J.-C. Lo, and C.-M. Lo, *Use of electric cell-substrate impedance sensing to assess in vitro cytotoxicity*. Biosensors and Bioelectronics, 2009. **24**(8): p. 2625-2629.
 27. Wegener, J., C.R. Keese, and I. Giaever, *Electric Cell-Substrate Impedance Sensing (ECIS) as a Noninvasive Means to Monitor the Kinetics of Cell Spreading to Artificial Surfaces*. Experimental Cell Research, 2000. **259**(1): p. 158-166.

28. Wallen, C.A., R. Higashikubo, and L.A. Dethlefsen, *Comparison of two flow cytometric assays for cellular RNA—acridine orange and propidium iodide*. Cytometry, 1982. **3**(3): p. 155-160.
29. Pollack, A. and G. Ciancio, *Cell Cycle Phase-Specific Analysis of Cell Viability Using Hoechst 33342 and Propidium Iodide after Ethanol Preservation*. Flow Cytometry.(Darzynkiewicz Z and Crissman HA, eds). London Academic Press Inc. I, 1991. **990**: p. 19-24.
30. Schmid, I., C.H. Uittenbogaart, B. Keld, and J.V. Giorgi, *A rapid method for measuring apoptosis and dual-color immunofluorescence by single laser flow cytometry*. Journal of immunological methods, 1994. **170**(2): p. 145-157.
31. Riccardi, C. and I. Nicoletti, *Analysis of apoptosis by propidium iodide staining and flow cytometry*. Nat. Protocols, 2006. **1**(3): p. 1458-1461.
32. Sung, J.-M., H.-J. Cho, H. Yi, C.-H. Lee, H.-S. Kim, D.-K. Kim, A.M. Abd El-Aty, J.-S. Kim, C.P. Landowski, M.A. Hediger, and H.-C. Shin, *Characterization of a stem cell population in lung cancer A549 cells*. Biochemical and Biophysical Research Communications, 2008. **371**(1): p. 163-167.
33. Rho, J.K., Y.J. Choi, J.K. Lee, B.-Y. Ryoo, I.I. Na, S.H. Yang, C.H. Kim, and J.C. Lee, *Epithelial to mesenchymal transition derived from repeated exposure to gefitinib determines the sensitivity to EGFR inhibitors in A549, a non-small cell lung cancer cell line*. Lung Cancer, 2009. **63**(2): p. 219-226.
34. Haggarty, S.J., K.M. Koeller, J.C. Wong, C.M. Grozinger, and S.L. Schreiber, *Domain-selective small-molecule inhibitor of histone deacetylase 6 (HDAC6)-mediated tubulin deacetylation*. Proceedings of the National Academy of Sciences, 2003. **100**(8): p. 4389-4394.
35. Edelman, E.R., P. Seifert, A. Groothuis, A. Morss, D. Bornstein, and C. Rogers, *Gold-coated NIR stents in porcine coronary arteries*. Circulation, 2001. **103**(3): p. 429-434.
36. Wang, Y., T.N. Truong, C. Yen, D. Bilecen, R. Watts, D.W. Trost, and M.R. Prince, *Quantitative evaluation of susceptibility and shielding effects of nitinol, platinum, cobalt-alloy, and stainless steel stents*. Magnetic Resonance in Medicine, 2003. **49**(5): p. 972-976.
37. Demann, E.T.K., P.S. Stein, and J.E. Haubenreich, *Gold as an Implant in Medicine and Dentistry*. 2005. **15**(6): p. 687-698.
38. Disegi, J.A. and L. Eschbach, *Stainless steel in bone surgery*. Injury, 2000. **31**, **Supplement 4**(0): p. D2-D6.
39. Bera, T.K., *Bioelectrical Impedance Methods for Noninvasive Health Monitoring: A Review*. Journal of Medical Engineering, 2014. **2014**: p. 28.
40. Gabriel, S., R.W. Lau, and C. Gabriel, *The dielectric properties of biological tissues: II. Measurements in the frequency range 10 Hz to 20 GHz*. Physics in Medicine and Biology, 1996. **41**(11): p. 2251.

Chapter 4

Human Breast Tissue Clinical Trial

4. Human Breast Tissue Clinical Trial

4.1 Objectives

The objective of this chapter is to give a comprehensive overview of the work undertaken in the first-in-human clinical study using the silicon probe. The aim of the clinical study was to determine the efficacy of the silicon prototype probes at differentiating between tissue types in excised breast tissue after surgical removal. The electrical impedance of macroscopically normal and macroscopically abnormal (cancerous and benign breast lesions) were recorded. The impedance data produced was subsequently correlated with histological findings.

4.2 Introduction

This chapter will outline research undertaken in a clinical trial conducted in Cork University Hospital (CUH), Cork, Ireland from March 2015 - March 2016. The purpose of this trial was to determine the ability of the silicon probe devices to differentiate between normal breast tissue, cancerous and benign lesions in breast specimens excised at surgery. These samples were obtained from patients who underwent surgery as part of their breast cancer or benign breast lesion treatment. The innovative silicon probes were used to measure electrical impedance in freshly excised tissue samples in the Histopathology department in CUH. This process was performed in parallel with the routine tissue processing involved in preparing excised samples for microscopic analysis. The ability to perform continuous, real-time tissue analytics in a label free and non-destructive manner is a major potential advantage of using bioimpedance in evaluation of breast lesions [1].

4.2.1 Ethical Approval

Ethical approval was sought from the Clinical Research Ethics Committee of the Cork Teaching Hospitals (CREC). This organisation is responsible for processing submissions prior to the commencement of clinical trials within any of the four teaching hospitals in Cork, Ireland. As part of this application a number of documents were generated:

- 1) Application Form
- 2) Clinical Trial Protocol (Section 4.2.2)
- 3) Summary of C.V. for Chief Investigator (Appendix 6.3)
- 4) Research Participate Information Sheet (Appendix 6.1)
- 5) Research Participate Consent Form (Appendix 6.2)

The clinical trial protocol is outlined in section 4.2.2 and the remainder of the ethical approval documents are presented in the appendices (Section 6.1-6.3). In a letter dated 21 May 2014 the CREC committee decided to grant full approval for the study subject to receipt of a number of revised documents and clarifications including:

- 1) Clarify the rationale for the study
- 2) Clarify who discusses the study with the patient
- 3) Revised Patient Information Sheet – Patients need to be informed that extra tissue will not need to be taken

In a letter dated 23 June 2014 the necessary clarifications were outlined to the committee and a revised copy (Version 1.4) of the patient information leaflet was submitted for the approval of the committee. By satisfying the concerns outlined by the CREC committee full approval for conducting the clinical trial was received.

4.2.2 Clinical Trial Protocol

The clinical trial protocol is a standardised procedure by which the electrical impedance recordings of human tissue samples (obtained from CUH) were carried out. It was designed to ensure optimal sample recording while minimising the risk of a misdiagnosis of the patient's sample by the histology team. The initial ethical approval application specified that 100 patients would be recruited to the trial and that the clinical data would be reviewed after every 25 patients. Each patient took part in the trial on a voluntary basis and was free to withdraw their consent at any time at which point their data would be removed from the analytical process. The following section (4.2.2.1) shows a copy of the clinical trial protocol that was completed for

each recruited patient. The purpose of the protocol document was to standardise the collection of biographical and specimen data relating to each sample recorded as part of the clinical trial. This would ensure that a complete data set was obtained for each patient and would enable each sample to be tracked once it had been stained and analysed by the consultant pathologist.

4.2.2.1 Clinical Trial Protocol Sample

Protocol for Sampling Fresh Breast Cancer Tissue for Research Purposes

Version 3.6 09 Mar. 15

1. Consent

Informed consent is to be obtained from the patient before surgery on admission to the hospital on the morning of the surgery.

2. Preparation prior to surgery

- i. Contact the Department of Pathology, Cork University Hospital the morning of the surgery to finalise arrangements for sample processing. The resection specimen must **NOT** be placed in formalin fixative after removal but transported fresh **WITHOUT DELAY** to the Department of Pathology, Cork University Hospital.
- ii. **Histopathology Lab, CUH:** Prepare supplies for the collection procedure:
 - A. Disposable sterile surgical gloves
 - B. Clean laboratory coat
 - C. Digital thermometer
 - D. Plastic container for tissue samples
 - E. Permanent Marker
 - F. Digital Camera
 - G. Nano-pure Water (20ml)
 - H. Lint-free Tissue

LSI Lab Tyndall: Prior to use of each prototype the surface of the probes will be cleaned 1 times with isopropyl alcohol (IPA) and 1 times with nano-pure water (18.2 MΩ) in an ultrasonic water-bath for 20 min @ 20°C each. The probes are then oxygen plasma treated for 20 min @ 50W.

3. Tissue Collection

- i. Decide that the specimen is suitable for sampling. The surgeon will only consent patients whose tumours/specimens are likely to be of sufficient size to permit tumour testing. The final suitability of a specimen for testing will be determined by the pathology laboratory staff to avoid compromising clinical care.
- ii. Tumour tissue will be surgically excised by the surgical team according to Standard Operating Procedures and in keeping with the surgical care required by the patient.
- iii. **NOTE:** Samples are **NOT** to be placed in formalin fixative prior to impedance testing. They will be transported immediately dry in plastic medical specimen containers.
- iv. The medical scientist in breast cut-up will be notified prior to the sample being removed so that to ensure minimal delay prior to impedance recordings.

4. Impedance Testing and Processing

- iii. Samples will be immediately transferred to the Department of Pathology laboratory, CUH.
- iv. The fresh tissue samples will be oriented and macroscopically described by a medical scientist in the cut-up laboratory.
- v. The prototype probe device will be attached to the Autolab PGSTAT204 potentiostat and laptop computer which will be calibrated before use.
- vi. The whole tissue sample will then be dissected into a number of sections by the medical scientist as per current routine protocol.
- vii. **Note:** Recording of healthy tissue will be done before cancerous tissue to avoid cross-contamination.
- viii. The probe will be inserted to a depth of approximately 2 mm into the regions of interest (both within the cancerous lesion and the surrounding healthy tissue) that will be visually identified by the medical scientist prior to probe insertion and impedance recordings will be taken at 2 sites (1 cancerous; 1 healthy) over a frequency range of 1000 Hz – 100000 Hz and at the optimal fixed frequency over a period of 5-10 minutes. A digital thermometer will be inserted adjacent to

the probe to investigate the tissue temperature at the time of recording. Probe will be cleaned using nano-pure water and lint-free tissue between each measurement.

- ix. Representative photographic images will be acquired of the probe in situ to ensure precise probe placement and this will be confirmed by the medical scientist at the time the image is taken.
- x. The area immediately surrounding the needle tip will be inked and submitted for processing and slide preparation and the individual slide and block number will be recorded in the pathology notes and the data sheet attached.
- xi. Each section will be stained using Haematoxylin and Eosin in accordance with the Standard Operating Procedures currently in place in the department of pathology. This will enable the diagnosis and also microscopic characterisation of the area surrounding the probe insertion point.
- xii. After impedance analysis the samples will be placed in formalin for routine tissue processing by the pathology department according to the Standard Operating Procedures in place in the department.
- xiii. After staining the samples will be imaged using a light microscope and will then be analysed by the medical scientist to confirm the presence or absence of cancerous tissue surrounding each probe insertion point. This information will then be correlated with the impedance data generated during recording.
- xiv. After imaging, each of the samples will be archived in accordance with the current department of pathology guidelines.

5. Specimen Tracking

Following tissue sampling, the data below should be recorded and stored in a logbook.

- A. Name of the surgeon and medical scientist
- B. Date of surgery and procedure type
- C. Corresponding pathology number of the resected specimen
- D. Slide and block number of specimen into which the probe was inserted
- E. Types of tissue collected (tumour or normal) and anatomical location of each
- F. Storage location of each sample

6. Further Information

The data collected are to be solely used for research purposes as part of a Ph.D. project. All specimens are to be stored in the Department of Pathology, CUH under standard protocols

Breast Tissue Sampling Protocol Checklist

1. Before Surgery

Item Required	Yes	No
Disposable Surgical Gloves		
Laboratory Coat		
Digital Thermometer (Tissue)		
Tissue Containers		
Permanent Marker		
70% Ethanol		
Digital Camera		
Nano-pure Water (20 ml)		
Lint-free Tissue		
Probes x2 (Cleaned)		

Signed Consent Form	Yes	No
----------------------------	-----	----

If No, experimental recordings cannot be taken from the sample

2. Patient Information

Patient Name	
Date of Birth	
MRN	

3. During surgery

Item	Yes		No
Sample Removal	Yes	No	Time (hh:mm)
X-ray (Theatre)	Yes	No	Time (hh:mm)
X-ray (Radiology)	Yes	No	Time (hh:mm)
Samples Labelled			
Notify Medical Scientist			

4. Specimen Tracking

Surgical Team	1) 2) 3)	
Date		
Surgical Procedure		
Breast	Left	Right
Tissue Collected (Healthy/Cancerous)		
Sample Weight (g)		

5. Pathology Lab

Item	Yes		No
Disinfect Autolab Instrument			
Probe Set-up			
Instrument Calibration			
Medical Scientist Name			
Medical Scientist description			
Sample Temperature	Yes	No	Temperature (°C)
Tissue Hand-Over			
Time of First Measurement			
Total Number of Recordings			
Types of Recordings	Healthy:		Cancer:
Specimen Pathology Number			
Slide Number(s)			
Block Number(s)			

Niall Savage

Date

Medical Scientist

Date

4.3 Experimental

4.3.1 Materials

Latex gloves, disposable lab coat, dry specimen container, scalpel and formalin (all sourced from the Histopathology Department, CUH), 18.2M Ω nano-pure water (Life Science Interface Laboratory, Tyndall National Institute) and lint-free tissue.

4.3.2 Instrumentation

Autolab PGSTAT204 with FRA32M module (Metrohm UK Ltd, Runcorn, United Kingdom), Data-Therm IR thermometer (Guangzhou Jinxinbao Electronic Co. Ltd., Guangzhou, China, Ultrawave QS3 Ultrasonic Water Bath (Ultrawave Ltd., Cardiff, United Kingdom), Harrick Plasma PDC-002 Extended Plasma Cleaner (Harrick Plasma, New York, U.S.A.) and silicon probes.

4.4 Procedures

4.4.1 Device Cleaning

The silicon probes used throughout the duration of the clinical trial were cleaned each time prior to analysing each patients' tissue sample. The previously mentioned IPA and nano-pure water cleaning protocol was used to remove any contaminants from the electrode surface (Section 2.5.2). The devices were then oxygen-plasma treated for 20 min before use. The cleaned probes were stored in a clean 20 ml tube for transport to the hospital laboratory.

4.4.2 Before Surgery

In accordance with the clinical trial protocol outlined, electrical impedance recordings of *ex vivo* human tissue samples were conducted in CUH over the course of a number of months. Prior to the commencement of each surgery, patients who fulfilled the inclusion criteria were invited to participate in the study. Tumour size was one of the major exclusion criteria. Patients with tumours less than 1.5 cm in diameter as determined during the pre-operative assessment were not included in the trial, as these tumours were too small to

be reliably identified macroscopically in the histopathology laboratory. Each potential study participant was informed of the procedure involved and made aware of the potential risks associated with their sample being analysed. Once patients agreed to participate in the study, formal written consent was obtained. Two copies of the most recent version of the clinical trial consent form were signed in the presence of Niall Savage. One copy was placed in the patients' medical file and the other was stored with the other clinical trial documentation in the office of Dr Brian O'Donnell in CUH. After consent was obtained, the medical scientists in the histopathology department were informed and a clean, dry specimen container was brought to the surgical theatre.

4.4.3 During Surgery

During the surgical procedure the relevant information relating to the breast specimen was documented according to the Protocol for Sampling Fresh Breast Cancer Tissue which has previously been described (Section 4.2.2.1). Of particular importance were the sample removal time and the specimen tracking information. For breast conserving surgery samples the standard operating procedure states that the sample is x-rayed twice i.e. specimen mammography. The first time is in theatre and then in the main radiology department in the hospital. Mastectomy samples do not require specimen mammography. All samples were then placed in a dry specimen container without formalin to ensure the sample was not fixed prior to recording. The surgical nursing team were responsible for sample labelling and cross-checking before the specimens could leave the theatre and be brought to the Histopathology laboratory.

4.4.4 Histopathology Laboratory

Once the breast tissue specimens were received in the histopathology laboratory the medical scientists were required to check-in the samples and assign an accession number to each case. The accession number was logged in the clinical sampling record at the time of processing. The medical scientists then performed an initial tissue description in accordance with the standard operating procedure in the breast cut-up area of the histopathology

laboratory. This involves anatomical orientation of the tissue, tumour localisation and marking of the relevant tissue margins with ink prior to dissection. In the case of the majority of the specimens tested the tissues were only partially inked prior to the recordings being taken. The rest of the inking was done after the tissues had been formalin fixed. Six different coloured inks are used to mark each of the margins as follows: Lateral – Yellow; Medial – Orange; Inferior – Green; Posterior – Black; Anterior – Blue; Superior – Red. For each specimen the area of cancer-free tissue was analysed before the cancerous lesion to prevent contamination. An area of macroscopically normal, cancer free breast tissue was then identified away from the cancerous lesion on the margin of the specimen. An incision was made to allow the insertion of the probe in to the tissue of interest. Once the location of the tumour had been identified a scalpel was used to make an incision to expose the inside of the tumour. This allowed the accurate placement of the silicon probe on to the cut face of the tumour. The Autolab PGSTAT instrument was set-up on the dissection bench. A calibration protocol was run each time to ensure the potentiostat was functioning correctly. The electrodes were attached to the calibration box in the “C” configuration and the “Test FRA” method was used to record 50 measurements across a range of frequencies. Once the calibration scan was completed the electrodes were then connected in a two-electrode system. The left electrode of the silicon probe was attached to the sense connector each time. The right electrode of the probe was connected to the reference electrode each time. The device was then inserted into the incision site and the tissue was apposed to the electrode surface by hand (Figure 4.1).



Figure 4.1: The placement of a packaged probe in a cancerous lesion in a wide-local excision sample obtained from Study Participant 05.

Frequency sweep measurements were performed on each of the patient samples. The reason for this was because no previous recordings had been performed on breast tissue using this probe. Therefore, it was necessary to obtain impedance recordings across a range of frequencies. This data was then statistically analysed to determine an optimum frequency at which all future recordings could be performed. Triplicate recordings were obtained at each location across 30 frequencies from 100,000-1,000 Hz at 10 mV peak amplitude. An infra-red thermometer was used to measure the temperature of the tissue surface prior to taking the first recording. The probes were cleaned twice using 18.2 M Ω nano-pure water and lint-free tissue between the healthy and cancerous recordings. The data was then exported to SPSS for analysis.

4.4.5 After Recording

Once the final bioimpedance recording was taken, the sample was returned to the medical scientist. The sample was covered with formalin and processed routinely the following day. Six different coloured inks were applied to each of the relevant tissue margins (superior, inferior, superficial, deep, medial and lateral), as per departmental protocols. The entire specimen was then sectioned in to approximately 1 mm thick slices. Each area relevant to the pathological diagnosis was placed in a separate tissue cassette. Each section was then paraffin embedded to allow them to be sectioned and stained. Once the fixation process was completed the paraffin-embedded tissue was sectioned using a microtome. The sections were then

floated to remove wrinkles. A selection of the microtome sections were placed on glass slides for haematoxylin and eosin staining. A consultant pathologist microscopically analysed the samples and provided a pathologic description of the cells present in each. As part of the bioimpedance clinical study, the site of each probe recording was individually analysed to microscopically confirm the tissue type. The histological findings were aligned with the electrical impedance recordings, thereby facilitating a correlation of bioimpedance and histologic data. From the pathologists report it was possible to determine both the tumour type and grade present in each of the study participant's tissue samples and how this correlated to the impedance values obtained.

4.4.6 Statistical Analysis

A statistical analysis was performed on the data obtained during the clinical trial. The first test conducted was an inter-rater reliability (IRR) analysis. This was used to determine the correlation between the repeated measurements taken at each of the healthy and cancerous locations. The triplicate data sets for each patient were assessed individually using the SPSS software package. Each of the tissue margin and cancerous values were arranged in individual columns and a reliability analysis was performed using a two-way random model to determine the intra-class correlation coefficient with a 95% confidence interval. The value of correlation was measured from 0 to 1, with 1 being the highest degree of correlation between the data sets. The IRR analysis was also performed on the complete healthy, cancerous and fibroadenoma data sets to determine the total cohort IRR values.

The second statistical analysis performed was a paired-samples T test. This was used to determine if the difference between the means of the healthy and cancerous recordings was significant at a specific frequency. The data was arranged in descending order according to frequency (100,000-1,000Hz) and sequentially by patient number (Patient 02, 03, 04...). A paired-samples T test was used to analyse the data sets as there was one measurement variable (frequency) and two nominal variables (normal and abnormal tissue). This test was chosen to see if the means of these two normally

distributed interval variables differed from one another. The combined values of skewness and Kurtosis were used to test the normality of the data. This was performed on each of the data sets following analysis with the paired-samples T test. This was used to determine if the data was normally distributed which was necessary when performing a parametric statistical analysis. Values of < 2 and < 9 for skewness and Kurtosis have previously been described as being suitable for parametric analysis using a paired-samples T test [2]. The paired-samples T test was also used to optimise the measurement frequency at which fixed frequency measurements could be performed. The triplicate measurements in each tissue were averaged each time and the repeats were combined in the paired-samples T test with a confidence interval of 95 %. A p value of < 0.05 would be indicative of a statistical significance between the two tissue types.

4.5 Results and Discussion

4.5.1 Consented Patients

A total of 33 patients were consented to the electrical impedance clinical trial over the course of the project. Of these patients, 10 were lost to follow-up as the surgical samples obtained were not suitable for electrical impedance recordings to be taken. Reasons for sample removal from the study for each of the patients were as follows:

- 1) Tumour size too small and too close to deep margin
- 2) Tumour size too small and differential diagnosis only available microscopically
- 3) No solid tumour mass present; only areas of calcifications
- 4) Tumour size too small and wire-guide *in situ* prevented dissection of fibroadenoma
- 5) No solid tumour mass and differential diagnosis only available microscopically
- 6) Tumour size too small and neoadjuvant chemotherapy may have decreased tumour size prior to surgery
- 7) Tumour too deep in specimen and guide-wire was *in situ*
- 8) Tumour too deep in specimen and guide-wire was *in situ*
- 9) Patient presented with DCIS which was required to be mapped in its entirety and therefore could not be cut in to.
- 10) Tumour size too small and 2 guide-wires were *in situ*

All of the information obtained relating to these patients was confidentially maintained and stored securely in accordance with the ethical approval application. A total of 23 patients' surgical samples were suitable for electrical impedance recordings to be performed. These included tissue obtained during mastectomy, central and wide-local excision surgeries. Figure 4.2 shows the specimen obtained from Study Participant 05 that was

removed by wide-local excision. The tumour present was approximately 3 cm in diameter but is not visible in the image. The short superior (right) and long lateral (left) orientation sutures are readily identifiable in Figure 4.2.



Figure 4.2: A wide-local excision sample obtained from Study Participant 05 which contained a tumour of approximately 3 cm diameter. The orientation sutures can clearly be seen at two locations on the sample.

Each of the patients consented to the trial and the procedure they underwent is documented in Table 4.1.

Table 4.1: The details of the participants recruited to the breast cancer clinical study

Participant No.	Procedure	Side	Recordings
1	Mastectomy	Bilateral	No
2	Wide-local Excision	Right	Yes
3	Mastectomy	Right	Yes
4	Wide-local Excision	Left	No
5	Wide-local Excision	Left	Yes
6	Wide-local Excision	Left	No
7	Central Excision	Left	Yes
8	Wide-local Excision	Left	Yes
9	Mastectomy	Right	Yes
10	Mastectomy	Right	Yes
11	Wide-local Excision	Left	Yes
12	Mastectomy	Bilateral (Left)	Yes
13	Mastectomy	Right	Yes
14	Mastectomy	Left	Yes
15	Central Excision	Right	Yes
16	Wide-local Excision	Right	No
17	Wide-local Excision	Left	Yes
18	Mastectomy	Bilateral (Right)	Yes
19	Wide-local Excision	Left	Yes
20	Wide-local Excision	Left	Yes
21	Chest Resection	Left	No
22	Mastectomy	Left	No
23	Wide-local Excision	Left	No
24	Wide-local Excision	Left	No
25	Mastectomy	Right	No
26	Wide-local Excision	Left	Yes
27	Wide-local Excision	Right	Yes
28	Mastectomy	Left	Yes
29	Wide-local Excision	Left	No
30	Mastectomy	Right	Yes
31	Mastectomy	Left	Yes
32	Wide-local Excision	Right	Yes
33	Wide-local Excision	Left	Yes

4.5.2 Impedance Modulus Recordings

The medical scientists were responsible for macroscopically identifying the area of interest with regard to the cancerous lesion and the surrounding healthy tissue. Figure 4.3 shows the partially inked specimen obtained from Study Participant 11 into which an incision had been made to reveal the

tumour surface. There were three areas identified by the medical scientist that were visible in the Figure 4.3:

- 1) Red – Cancerous tumour
- 2) Green – Fat Necrosis from previous CNB. This area was not analysed as part of the study
- 3) Blue – Area of macroscopically normal breast tissue

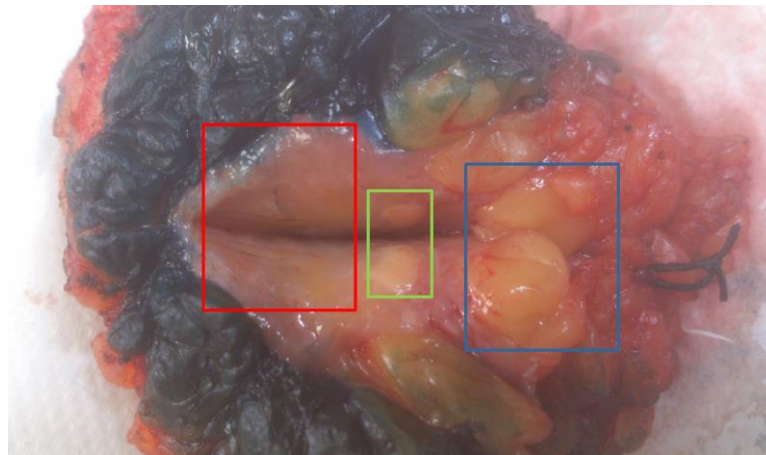


Figure 4.3: The areas of interest in the wide-local excision sample of study participant 11. The areas are the cancerous lesion (Red), fat necrosis (Green) and normal tissue (Blue).

Of the 33 patients consented to the study 2 patients presented for surgery with a breast fibroadenoma. Figure 4.4 shows US wire-guided diagnostic excision biopsy sample obtained from Study Participant 08. The white area in the centre of the image shows the point of incision into the fibroadenoma. This type of tumour is normally benign and may potentially produce different impedance values to either the cancerous or normal breast tissue. This may be useful in diagnosing the type of tumour present at the point of insertion.

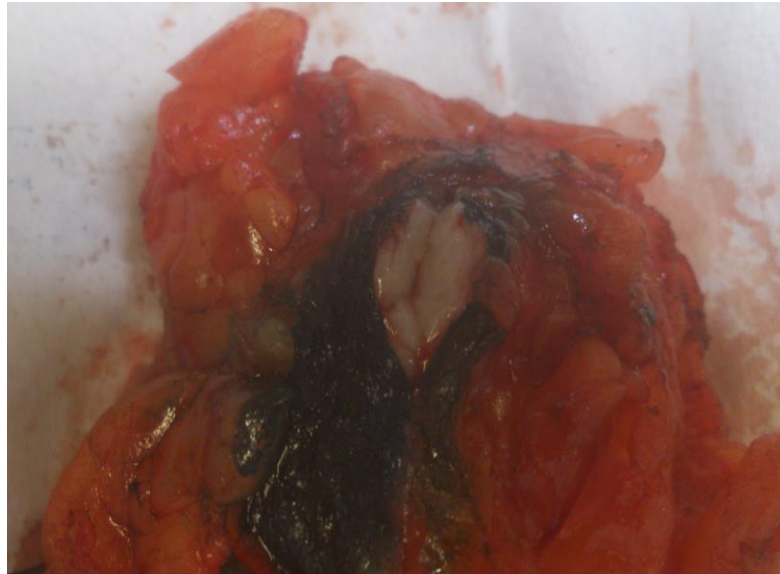


Figure 4.4: A partially inked ultrasound wire-guided diagnostic excisional biopsy specimen with an incision made in to an area of fibroadenoma shown in white from study participant 08.

4.5.3 Pathology Findings

Microscopic images were taken of each of the slides containing the tissue at the site of each electrode recording. Figure 4.5a shows the microscopic image from the site of the tissue margin impedance modulus recordings from Study Participant 02. The image contains two features associated with normal breast tissue. The red square highlights an area of normal perilobular adipose tissue which is evident across the majority of the section. The black square highlights a normal breast lobule. The lobules of the human breast are formed by ductules containing three cell types: basal cells, luminal cells, and myoepithelial cells which are all present in the area highlighted [3]. Figure 4.3b displays evidence of hyperchromatic staining, pleomorphic cells and dense fibrotic tissue which is indicative of cancerous invasion [3]. The microscopic images correlated with the macroscopic probe placement in each of the 17 cases analysed by the consultant pathologist to date (See Appendix 6.6.2). This was to be expected as the majority of the patients consented to the clinical trial had large well-circumscribed tumours that were readily identifiable by the medical scientists and pathologists in the department.

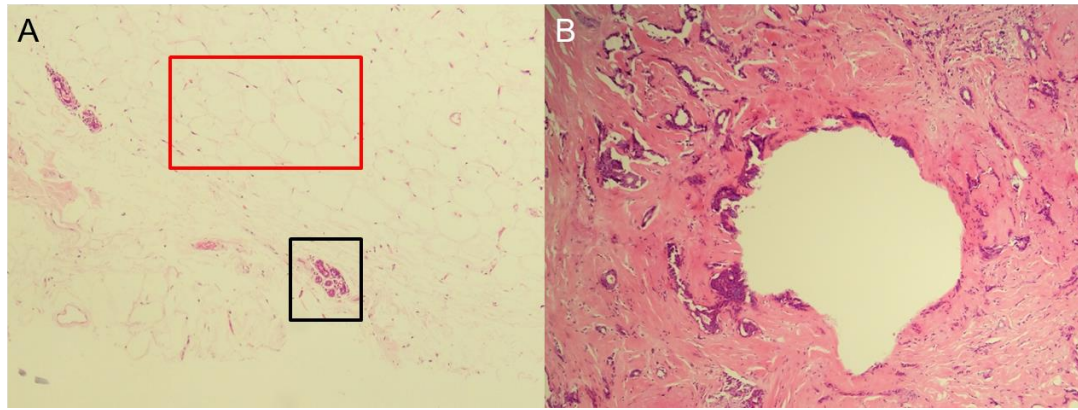


Figure 4.5: The microscopic images obtained from the healthy tissue margin (A) and the cancerous lesion (B) of study participant 02 as confirmed by a consultant pathologist.

The tissue type confirmation at the recording electrode placement site was necessary to ensure that the electrical impedance recordings obtained were being interpreted correctly (Table 4.2).

Table 4.2: The patient age, type and grade of the tumour samples analysed during the study.

Participant No.	Age	Tumour Type	Grade
2	58	Invasive Ductal Carcinoma	2
3	65	Invasive Lobular Carcinoma	2
5	83	Metastatic Squamous Cell Carcinoma	N/A
7	50	Invasive Ductal Carcinoma	3
8	21	Fibroadenoma	N/A
9	62	Invasive Ductal Carcinoma	2
10	63	Invasive Ductal Carcinoma	3
11	65	Invasive Ductal Carcinoma	3
12	34	Invasive Ductal Carcinoma	3
13	72	Invasive Ductal Carcinoma	3
14	78	Invasive Ductal Carcinoma	3
15	70	Invasive Ductal Carcinoma	2
17	64	Mixed Invasive Ductal and Lobular Carcinoma	2
18	50	Invasive Ductal Carcinoma	2
19	50	Fibroadenoma	N/A
20	88	Invasive Mucinous Carcinoma	2
26	51	Invasive Ductal Carcinoma	3
27	79	Mixed Invasive Ductal and Lobular Carcinoma	2
28	81	Invasive Ductal Carcinoma	3
30	60	Invasive Ductal Carcinoma	3
31	52	Mixed Invasive Ductal and Lobular Carcinoma	2
32	59	Invasive Ductal Carcinoma	3
33	58	Invasive Ductal Carcinoma	2

4.5.4 Inter-rater Reliability Analysis

The first statistical test performed was an IRR analysis. This was used to identify discrepancies between the triplicate recordings obtained in each of the tissue locations. Each patient's data sets were tested separately both with and without any data thought to be an outlier compared to the other recordings. If the intra-class correlation improved to above 0.900 then the outlying data would be omitted from the final analysis. During the analysis, three sets of patient's data were found to contain outlying data.

Table 4.3: The IRR analysis of the cancerous recordings obtained from study participant 05 including 3 healthy recordings including the outlying values.

	Intra-class Correlation	95% Confidence Interval		F Test with True Value 0			
		Lower Bound	Upper Bound	Value	df1	df2	Sig
Single Measures	.616	.419	.776	5.804	29	58	.000
Average Measures	.828	.684	.912	5.804	29	58	.000

Table 4.4: The IRR analysis of the cancerous recordings obtained from study participant 03 including 2 cancerous recordings excluding the outlying values.

	Intra-class Correlation	95% Confidence Interval		F Test with True Value 0			
		Lower Bound	Upper Bound	Value	df1	df2	Sig
Single Measures	.997	.994	.999	745.124	29	29	.000
Average Measures	.999	.997	.999	745.124	29	29	.000

The results in Tables 4.3 and 4.4 shows the data output from the IRR analysis with and without one of the repeated values. After removing one of the triplicate repeat values the intra-class correlation coefficient increased from 0.828 to 0.999. This showed that the value obtained for one of the repeat recordings was significantly different from the other impedance values from that location. This set of data was therefore omitted as it did not provide a representative repeat value that could be averaged appropriately. The cancerous recordings for patient 07 were shown to contain an outlying data set which was not included in the future statistical analysis (Table 4.5)

Table 4.5: The average measures output from the IRR analysis of study participant 07 before and after data set 01 was removed.

	Intra-class Correlation	95% Confidence Interval		F Test with True Value 0			
		Lower Bound	Upper Bound	Value	df1	df2	Sig
Avg Measures Before	.117	-.619	.550	1.133	29	58	.336
Avg Measures After	.877	.742	.941	8.133	29	29	.000

Although the intra-class correlation value did not increase above the 0.90 threshold, the removal of the outlying data set did significantly improve the overall correlation. The upper bound of the 95% confidence interval does however go beyond the required threshold and therefore it was decided to omit the outlying data set from any future statistical analysis. The IRR data output for Study Participant 09 was found to contain an outlying data set which was subsequently removed from the future analysis (Table 4.6).

Table 4.6: The average measures output from the IRR analysis of study participant 09 before and after data set 01 was removed.

	Intra-class Correlation	95% Confidence Interval		F Test with True Value 0			
		Lower Bound	Upper Bound	Value	df1	df2	Sig
AvgMeasures Before	.064	-.634	.511	1.069	29	87	.393
AvgMeasures After	.958	.924	.979	24.039	29	58	.000

As with the analysis of the two previous patients, the results of the IRR analysis of patient 09 showed an improvement in both intra-class correlations (0.064 – 0.958) and p value significance ($p = 0.393 - p < 0.001$). It was therefore decided to omit the outlying data set. The IRR analysis was repeated for all of the data sets obtained to determine the reliability of the values from the whole cohort. The first data set analysed was the entire tissue margin samples obtained from each patient (Table 4.7). The data output shows that the intra-class correlation across of the recorded values was 0.984 ($p < 0.001$) which is a positive result. This suggests that the

repeated measurements obtained correlated well across all of the patients analysed.

Table 4.7: The IRR analysis for the entire tissue margin recordings obtained from the total patient cohort.

	Intra-class Correlation	95% Confidence Interval		F Test with True Value 0			
		Lower Bound	Upper Bound	Value	df1	df2	Sig
Avg Measures	.984	.975	.991	63.894	28	1820	.000

The next data set that was analysed was all of the cancer recordings which did not include the two patients with fibroadenomata, which are benign. The statistical output of the IRR analysis is displayed in Table 4.8 which shows the intra-class correlation for all the cancer recordings performed to be .997 ($p < 0.001$). As with the tissue margin recordings, there was a positive correlation between all of the data sets obtained for the patients with breast cancer.

Table 4.8: The IRR analysis for all of the cancer recordings obtained during the clinical study.

	Intra-class Correlation	95% Confidence Interval		F Test with True Value 0			
		Lower Bound	Upper Bound	Value	df1	df2	Sig
Avg Measures	.984	.975	.991	62.50	29	1769	.000

The final IRR analysis performed was on the data obtained for the fibroadenoma recordings. Table 4.9 shows the data obtained for the reliability analysis of the electrical impedance recordings taken from the two fibroadenoma specimens. The intra-class correlation obtained was .999 ($p < 0.001$) which was a positive result and there was almost a perfect correlation across the recorded values.

Table 4.9: The IRR analysis for all of the fibroadenoma recordings obtained from two patients.

	Intra-class Correlation	95% Confidence Interval		F Test with True Value 0			
		Lower Bound	Upper Bound	Value	df1	df2	Sig
Avg Measures	.999	.999	1.000	1655.9	29	145	.000

4.5.5 Paired-samples T Test Analysis

4.5.5.1 Optimum Frequency Selection

In order to determine the optimum frequency at which to record fixed frequency impedance modulus recordings it was necessary to assess each of the individual paired-samples T Test analyses that were performed. It was then possible to choose a frequency which would provide the most statistically significant separation between the mean impedance modulus values for the normal and abnormal breast tissue. In choosing the optimum it was necessary to exclude frequencies at either end of the recorded spectrum. This was to avoid choosing frequencies that would only contain either resistive or capacitive elements as this would not provide a true reflection of the difference in impedance modulus between the two tissue types despite potentially having a larger mean separation. The optimum frequency outputs for each of the paired-samples T test analyses are shown in Appendix 6.8.2.

4.5.5.2 All Study Participants

Normality testing was performed using the 23 pairs of averaged data obtained from each of the patients at a frequency of 20,434 Hz. Table 4.10 shows the skewness and Kurtosis values generated from the tissue margin and lesion averages for the entire patient cohort. For both sample types the values were below the upper limit of 2 and 9 for skewness and Kurtosis respectively (Table 4.10). Therefore, this data set was suitable for analysis using the paired-samples T test.

Table 4.10: The data output for the normality testing performed on average tissue margin and lesion recordings for each patient. N=17.

Normality Test	Tissue Margin	All Lesions
Skewness	.252	1.942
Kurtosis	-1.446	4.960

A paired-samples T test was used to determine the level of significance between the averaged values for the tissue margin and lesion recordings from all of the study participants. This provided an overall indication of the probes ability to differentiate between tissue margins and both benign and cancerous breast lesions. The data obtained from the paired-sample T test indicated that the optimum frequency for recording of the combined tissue margin and lesions was 20,434 Hz. The mean difference between the tissue margin and lesion recordings was 4,340 Ω with $p < 0.001$. This demonstrated that for the combined averages across all of the study participants the separation of the means between the tissue margins and lesions was significantly different. The triplicate average values for each patient recorded were combined and an average value for the healthy and non-healthy recordings was graphed (Figure 4.6).

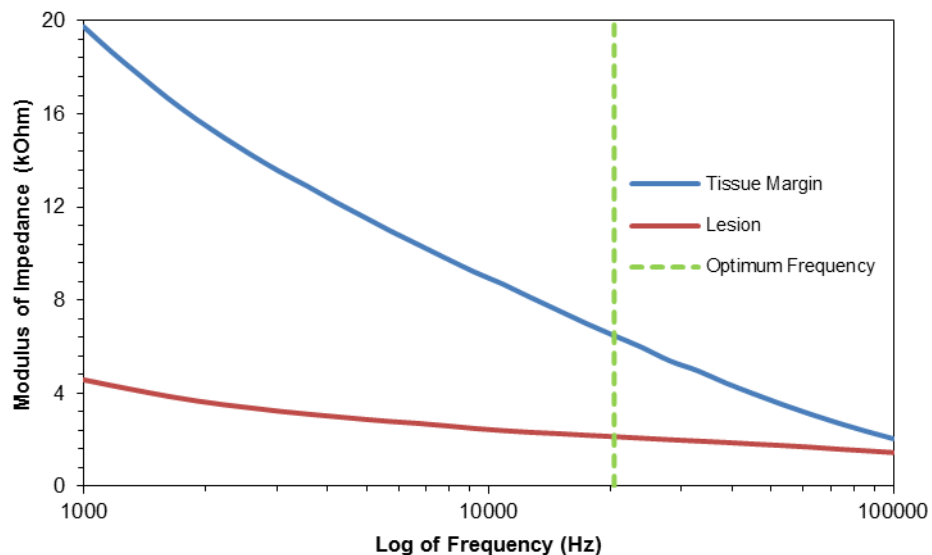


Figure 4.6: The Bode plot of the average impedance values for the tissue margin and lesion. N=23.

The graph of the electrical impedance tissue results showed separation across all of the frequencies tested. This correlates with the results of the T test analysis previously shown. The statistical analysis of all 23 study participants combined showed that in all cases the silicon probe was able to differentiate between the healthy tissue margin and the area of the breast lesion in the case of both benign and cancerous lesions at a frequency of 20,434 Hz and a peak voltage of 10 mV. This finding demonstrated that the probe could measure impedance in excised breast tissue. The impedance values obtained were sufficiently different to suggest the utility of the probe in tissue type identification.

4.5.5.3 All Cancers

In order to determine the silicon probes effectiveness at determining the difference between only cancerous and normal tissues the values obtained for benign fibroadenoma lesions were removed and the paired-sample T test analysis was repeated. The skewness and Kurtosis normality tests were repeated with the fibroadenoma values removed and the results are displayed in Table 4.11. The values obtained were all below the acceptable limits for parametric testing.

Table 4.11: The data output for the normality testing performed on average tissue margin and cancer recordings for each patient. N=21.

Normality Test	Tissue Margin	All Cancer
Skewness	.337	1.802
Kurtosis	-1.553	4.284

The statistical analysis of the 21 patient samples showed that at the optimum frequency of 20,434 Hz the mean separation between the tissue margins and the cancerous lesions was 4,187 Ω ($p < 0.001$). The Bode plot of the average cancer and tissue margin impedance values showed a separation across all of the frequencies measured each time (Figure 4.7). The results demonstrated that for the combined cancer and tissue margin recordings the prototype device was capable of differentiating between the two tissue types.

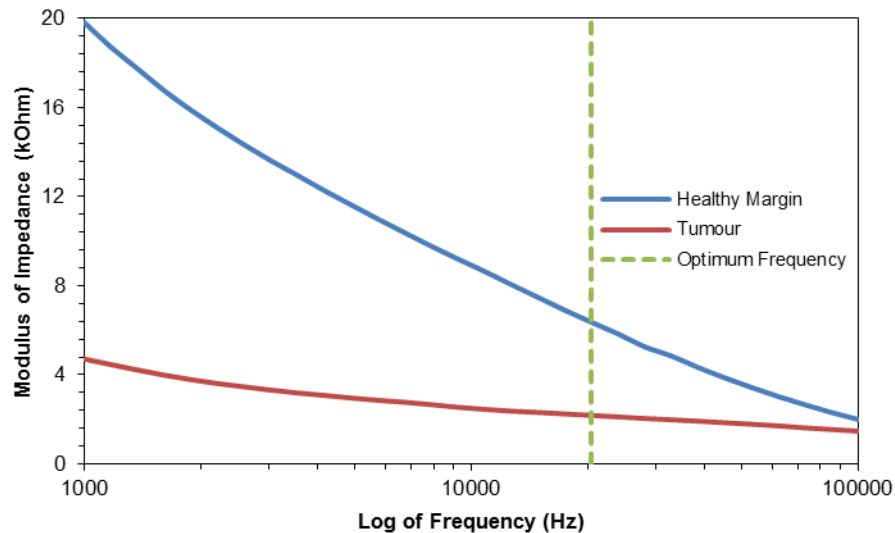


Figure 4.7: The Bode plot of the average impedance values for the tissue margin and cancer tumours. N=21.

4.5.5.4 All Primary Breast Cancers

A further series of paired-sample T tests were performed to determine if the types of lesions being analysed affected the probes ability to differentiate between normal and abnormal breast tissue. For this analysis only primary breast tumours were included which meant that the metastatic squamous cell carcinoma was excluded. Normality testing was performed on the data sets obtained at a frequency of 20,434 Hz (Table 4.12). The values generated from the normality testing allowed the paired-samples T test to be used to statistically analyse the primary breast cancer data.

Table 4.12: The data output for the normality testing performed on average tissue margin and cancer recordings for each patient. N=20.

Normality Test	Tissue Margin	All Cancer
Skewness	.434	1.743
Kurtosis	-1.427	4.073

The paired-sample T test showed that the mean separation between the breast cancer tumours and the healthy tissue margins was $3,845\Omega$ ($p < 0.001$). The combined analysis of all of the primary breast tumours and the associated tissue margins showed that across all of the frequencies tested

there was a significant separation between the two tissue types as illustrated in the Bode plot in Figure 4.8.

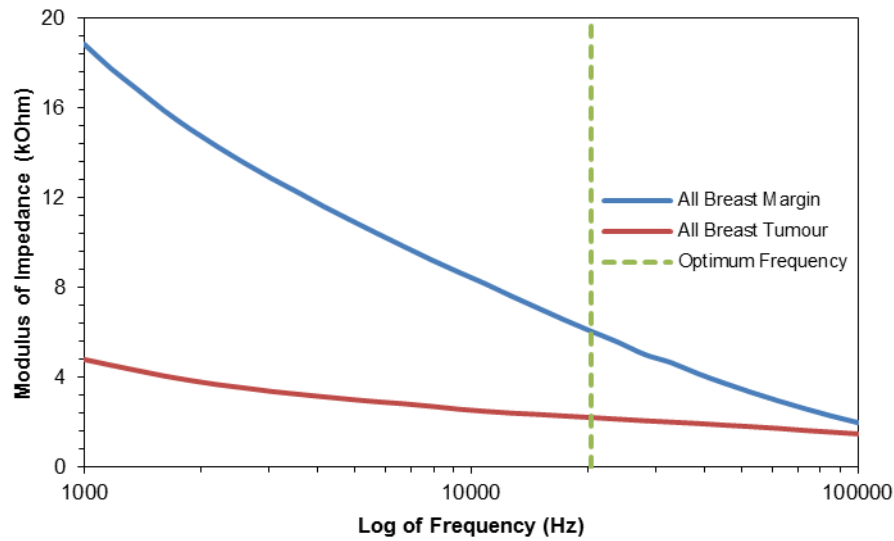


Figure 4.8: The average impedance values for the tissue margin and tumour for primary breast cancers. N=20.

4.5.5.5 All Invasive Ductal Cancers

The final combined grouping of cancer recordings to be analysed was the IDCs. These accounted for 15 of the 23 study participant samples that were recorded. This group of samples was composed of 11 patients who presented with IDC grade 3 and 4 samples were confirmed as being IDC grade 2. As with the previous data sets the normality of the distribution was assessed. The values of skewness and Kurtosis were deemed to be within the acceptable range for use with parametric statistics (Table 4.13).

Table 4.13: The data output for the normality testing performed on average tissue margin and cancer recordings for each patient. N=15.

Normality Test	Tissue Margin	All Cancer
Skewness	.477	.819
Kurtosis	-1.620	1.165

The Bode plot of the averaged electrical impedance values obtained from all of the IDC samples showed that an excellent separation existed between the tissue margins and the cancerous lesions (Figure 4.9).

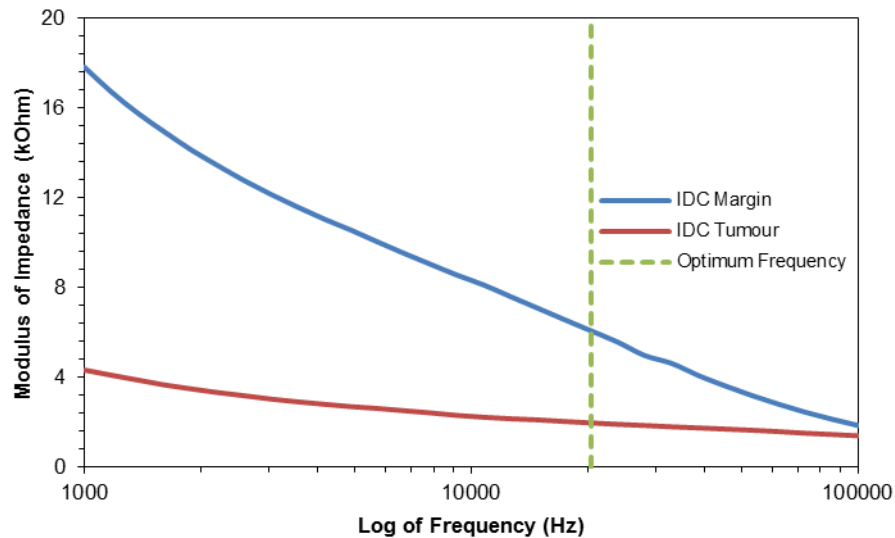


Figure 4.9: The average impedance values for the tissue margin and tumour for primary breast cancers. N=15.

The results of the paired-samples T test demonstrated that a statistically significant difference existed between the mean impedance modulus values for the combined IDC and the associated tissue margins (4,102 Ω ; $p = 0.002$).

4.5.5.6 Differentiation by Cancer Type

In order to determine if the electrical impedance response produced by the tissues was affected by the type of cancer and grade, the study participants were subdivided based on their pathological report findings and the analysis of the sections obtained from the site of recording. In total the tissues were separated into 7 categories and each subtype was statistically analysed individually:

- 1) Invasive ductal carcinoma – Grade 3
- 2) Invasive ductal carcinoma – Grade 2
- 3) Mixed invasive ductal and lobular carcinoma – Grade 2
- 4) Invasive lobular carcinoma – Grade 2
- 5) Invasive mucinous carcinoma (IMC) – Grade 2
- 6) Metastatic squamous cell carcinoma (MSCC)
- 7) Fibroadenoma

4.5.5.6.1 Invasive Ductal Carcinoma Grade 3

The most common cancer type observed during the study was IDC grade 3 with a total of 11 patients presenting with it (Figure 4.10). This was to be expected as the tumours of interest to the study needed to be 1.5 cm or larger in diameter. Large tumour mass is commonly associated with an advanced grade of cancer [4]. The normality of the data distribution was assessed for each of the 11 patients who presented with IDC grade 3. The values obtained for skewness and Kurtosis are displayed in Table 4.14. These values were acceptable to allow the IDC grade 3 data to be analysed with the paired-samples T test.

Table 4.14: The data output for the normality testing performed on average tissue margin and cancer recordings for each patient. N=11.

Normality Test	Tissue Margin	All Cancer
Skewness	-.088	.972
Kurtosis	-2.035	1.938

The results displayed here show that a separation exists between the cancer and tissue margin recordings across all of the frequencies measured. This indicated that it was possible to differentiate between tissue types in patients who presented with IDC grade 3. A paired-samples T test was used to determine if a statistically significant difference existed between the tissue margin and the cancerous tumour (5,111 Ω). A value of $p = 0.004$ obtained by the analysis showed that the difference between the mean impedance values at the optimum frequency of 20,434 Hz was statistically significant.

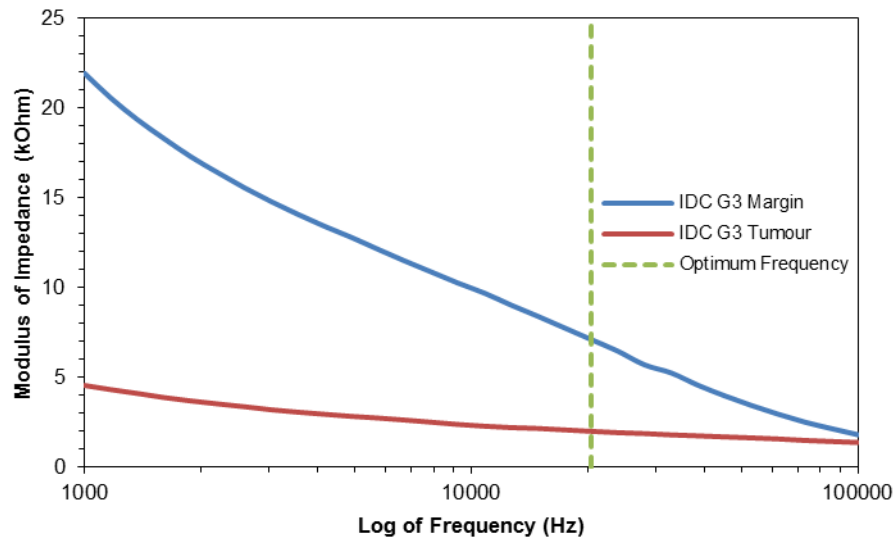


Figure 4.10: The Bode plot of the averaged electrical impedance results of the invasive ductal carcinoma grade 3 samples recorded during the clinical trial. N=11.

The group of patients consented to the trial with IDC Grade 3 constituted the largest sample population in the study. In order to assess whether a statistical similarity existed across the 11 patients the interclass correlation coefficient was determined using an inter-rater reliability test across the entire frequency range tested. The results are presented in Table 4.15.

Table 4.15: The IRR analysis for all of the IDC Grade 3 tissue margin and cancer recordings obtained during the clinical study.

	Intra-class Correlation	95% Confidence Interval		F Test with True Value 0			
		Lower Bound	Upper Bound	Value	df1	df2	Sig
Avg Measures Tissue Margin	.934	.872	.964	15.103	29	290	.000
Avg Measures IDC Grade 3	.881	.806	.935	8.383	29	290	.000

The results presented show that despite the variability observed between each of the individual patient samples and environmental factors encountered during impedance modulus recordings there is statistical evidence to support a correlation between each of the IDC Grade 3 samples. The intra-class correlation results for the tissue margin and cancer recordings were 0.934 and 0.881 respectively. Although the value for the

cancer recordings is below the threshold of 0.9 the upper bound of the 95% confidence interval does cross this threshold.

4.5.5.6.2 Invasive Ductal Carcinoma Grade 2

The second most common cancer in the study was IDC Grade 2 which was determined to be present in 4 of the patients samples recorded as part of the study. As with the previous data sets the normality of the distribution was assessed. The values of skewness and Kurtosis were deemed to be within the acceptable range for use with parametric statistics (Table 4.16).

Table 4.16: The data output for the normality testing performed on average tissue margin and cancer recordings for each patient. N=4.

Normality Test	Tissue Margin	All Cancer
Skewness	-.173	.428
Kurtosis	-.660	-.027

The graph showed that a difference existed between the tissue margins and the tumour of patients who presented with IDC grade 2 across all of the measured frequencies (Figure 4.11). A paired-samples T test was used to determine if the result obtained showed a statistically significant difference between the tissue margin and the cancerous tumour. At the optimum frequency of 20,434 Hz a mean separation of 1,329 Ω with an associated p-value of 0.027 was observed.

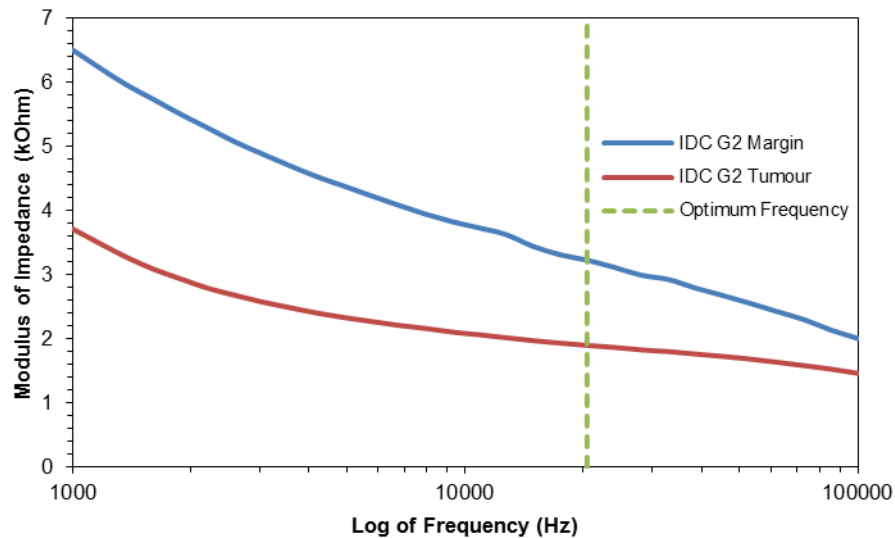


Figure 4.11: The Bode plots of the averaged electrical impedance results of the invasive ductal carcinoma grade 2 patients consented to the clinical trial. N=4.

4.5.5.6.3 Mixed Invasive Ductal and Lobular Carcinoma Grade 2

Of the 23 patients consented to the clinical study only 3 were determined to have a mixed invasive cancer composed of both ductal and lobular carcinoma cell types. It was not possible to assess the normality of the data distribution as the sample size was too small. The results displayed here show that a separation exists between the cancer and tissue margin recordings across all of the frequencies measured. This indicated that it was possible to differentiate between tissue types in patients who presented with mixed IDC and ILC grade 2 tumours. A paired-samples T test was used to determine if a statistically significant difference existed between the tissue margin and the cancerous tumour

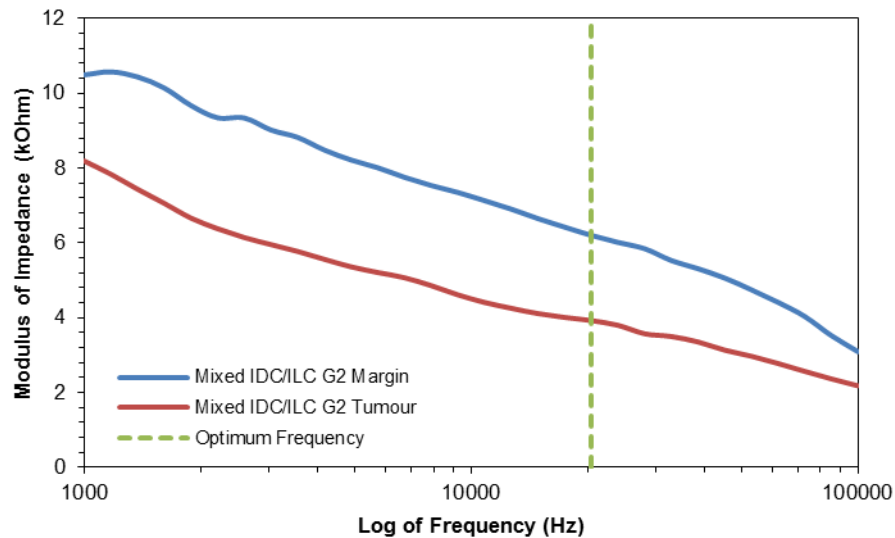


Figure 4.12: The electrical impedance results from the mixed invasive ductal and lobular carcinoma grade 2 sample. N=3.

At the optimum frequency of 20,434 Hz a mean separation of 2,278 Ω with an associated p-value of 0.426 was observed. The analysis showed that the difference between the mean impedance modulus values at the optimum frequency was not statistically significant. However, the sample size for mixed carcinomas was very small and would need more patient samples to draw appropriate conclusions.

4.5.5.6.4 Invasive Lobular Carcinoma Grade 2

The second most common cancerous lesion subtype within the breast is ILC. During this study 1 patient was consented to the trial with this cancer type (Figure 4.13). The Bode plot shows the average of the triplicate recordings obtained at the two recording sites. There was separation observed across all of the frequencies measured which was a positive result.

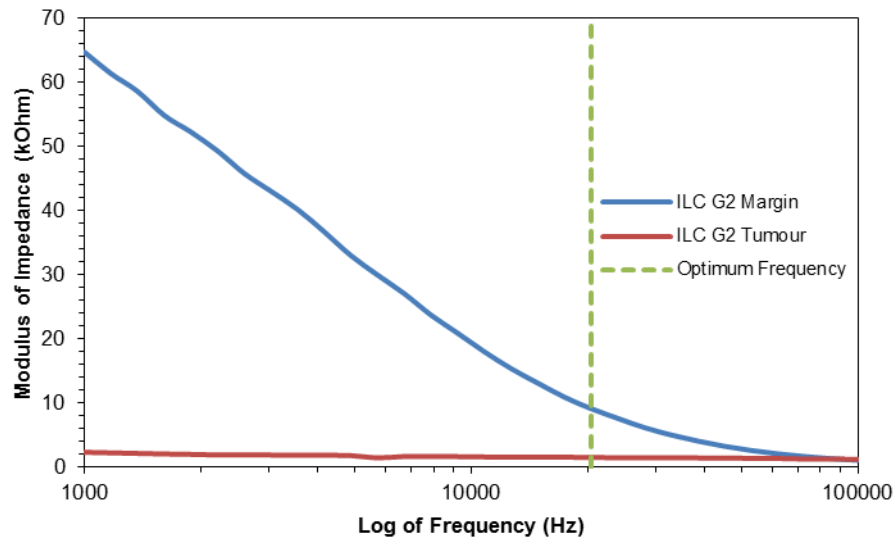


Figure 4.13: The averaged electrical impedance result of the invasive lobular carcinoma (ILC) grade 2 patient consented to the clinical trial. N=1.

The result outlined here indicated that the probe was capable of differentiating between the tissue margins and the tumour of a patient who presented with ILC grade 2 across each of the frequencies tested. A paired-samples T test was not able to be performed on the data without at least one more specimen of the same category. However, the mean values for the recordings obtained at the optimum frequency of 20,434 Hz showed a separation of 7,610 Ω (Figure 4.14). This indicates that the probe was capable of differentiating between a tumour and normal breast tissue in a patient with ILC Grade 2. In order to assess the statistical difference between the mean impedance modulus values it will be necessary to obtain many more patient samples with this particular cancer type and grade.

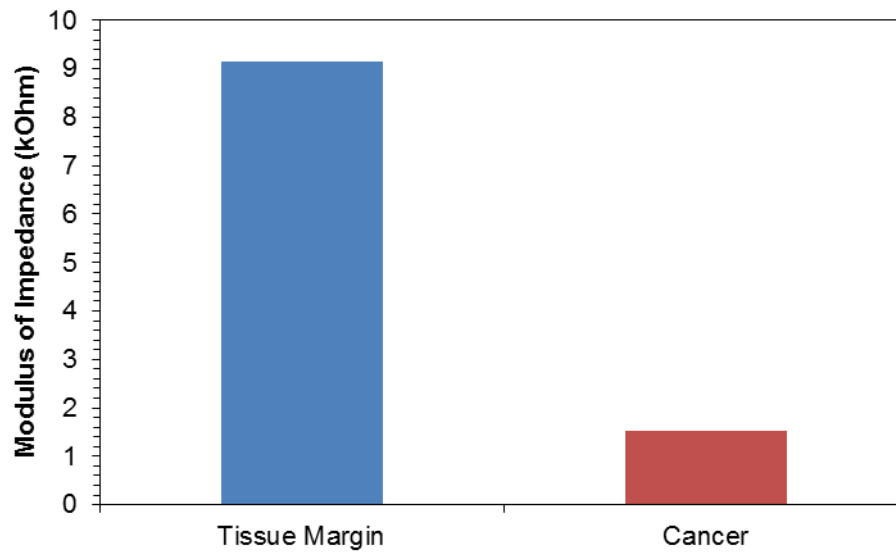


Figure 4.14: The mean values of the tissue margin and lesion recordings obtained at a frequency of 20 kHz from the tissue margins and cancer from the ILC Grade 2 specimen. N=1.

4.5.5.6.5 Invasive Mucinous Carcinoma Grade 2

One patient who was consented to the study was found to have an invasive mucinous carcinoma grade 2 upon pathological assessment. The Bode plot of the recorded impedance values showed that a clear separation was present across all 30 data points obtained (Figure 4.15).

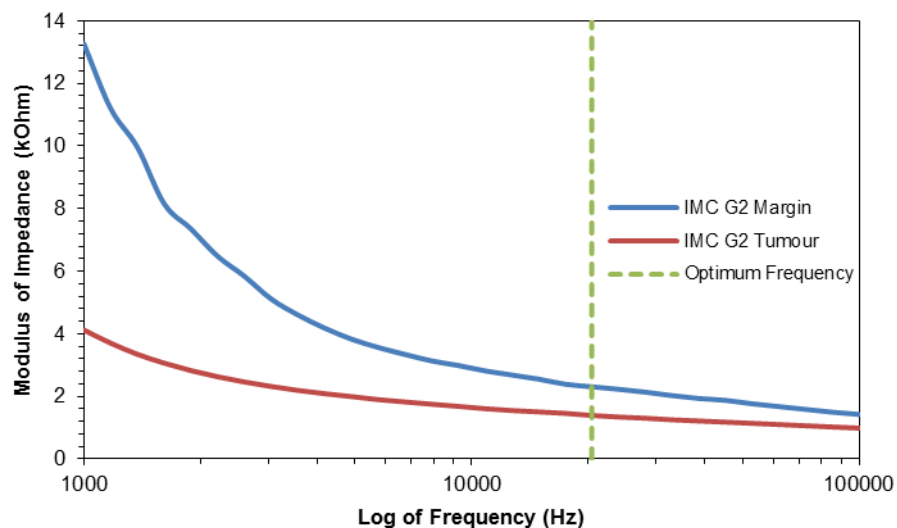


Figure 4.15: The electrical impedance results of the invasive mucinous carcinoma (IMC) grade 2 patients consented to the clinical trial. N=1.

The data outlined here showed a separation of 918 Ω between the tissue margins and the tumour of the patient who was determined to have IMC grade 2. It was not possible to perform either a paired-samples T test or a normality of distribution test on the data obtained from the IMC sample as only one sample was obtained. However, the data provided from the Bode plot shows a separation between the two tissue types. The mean separation observed at the optimum frequency of 20,434 Hz showed separation also (Figure 4.16).

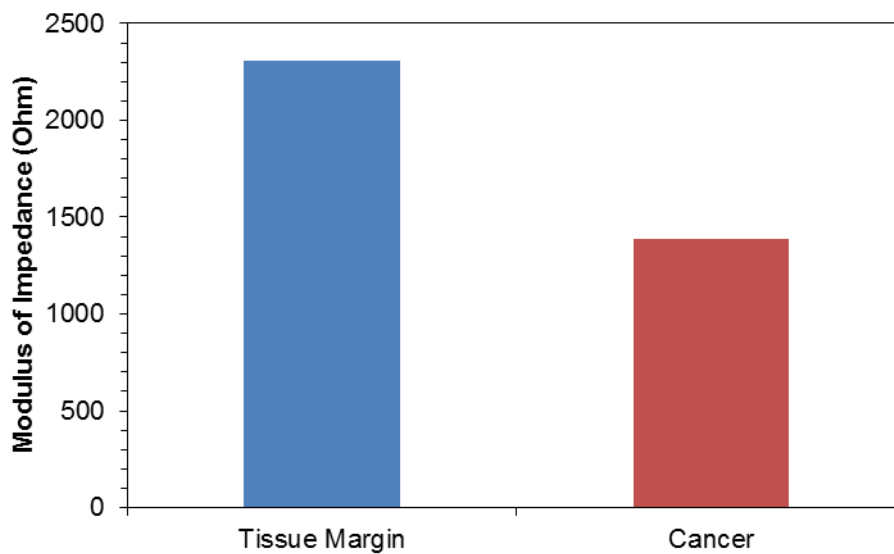


Figure 4.16: The mean values of the tissue margin and lesion recordings obtained at a frequency of 20 kHz from the tissue margins and cancer from the IMC Grade 2 sample. N=1.

4.5.5.6.6 Metastatic Squamous Cell Carcinoma

One patient consented to the trial presented with a secondary breast tumour. This was confirmed pathologically to be a metastatic squamous cell carcinoma. The histological analysis of this specimen showed evidence that the tumour had developed as a lymph node metastasis. Although this sample was not a case of primary breast cancer it was included as part of the study to demonstrate the probes ability to differentiate between tumours that originated outside of the breast and the surrounding healthy breast tissue margin (Figure 4.17).

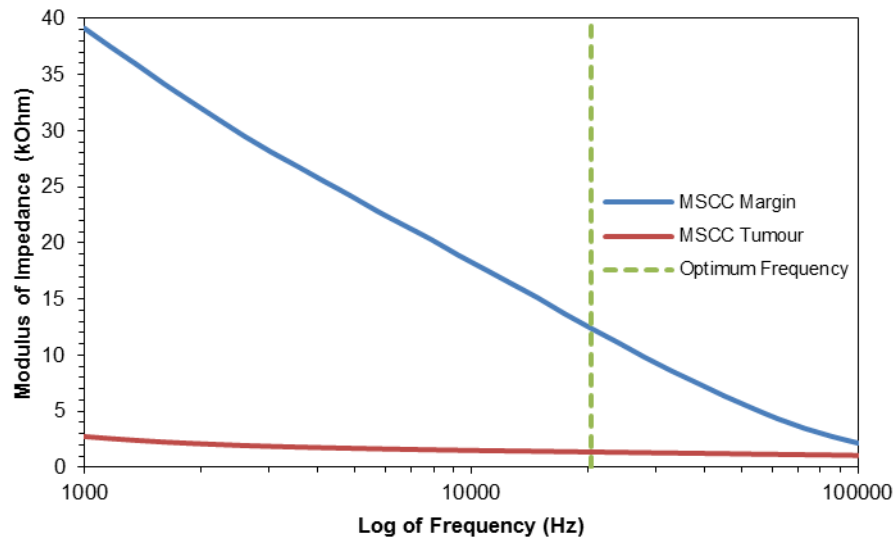


Figure 4.17: The Bode plot of the electrical impedance recordings taken from the metastatic squamous cell carcinoma (MSCC) specimen. N=1.

The Bode plots displayed showed that separation existed between the cancer and tissue margin recordings across all of the frequencies measured. This indicated that it was possible to differentiate between tissue types in patients who presented with MSCC tumours in the breast. It was not possible to perform a paired-samples T test as only one set of patient data was obtained for this cancer subtype. However, the mean values for the recordings obtained at the optimum frequency of 20,434 Hz showed a large separation (Figure 4.18).

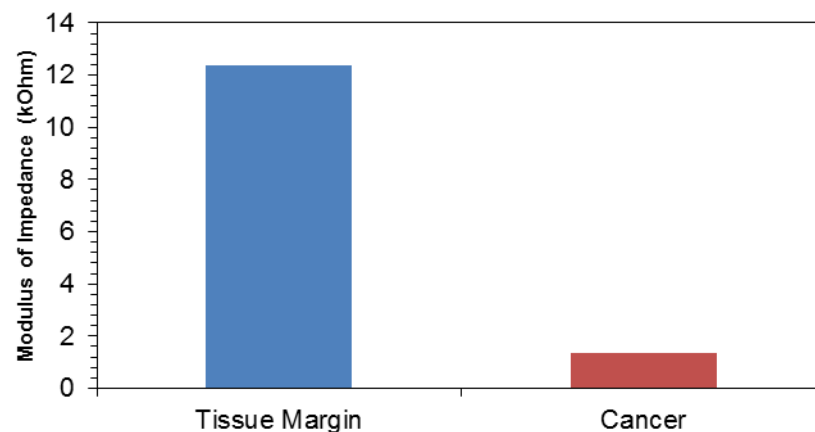


Figure 4.18: The mean values of the tissue margin and lesion recordings obtained at a frequency of 20 kHz from the tissue margins and cancer from the metastatic squamous cell carcinoma patient. N=1.

4.5.5.6.7 Fibroadenoma

A fibroadenoma is tumour formed of mixed fibrous and glandular tissue, typically occurring as a benign growth in the breast. Two patients who consented to the trial presented with a benign lesion within the breast. These were confirmed pathologically to be fibroadenomas. Although these samples were not technically cases of breast cancer they were included as part of the study to demonstrate the probes ability to differentiate between healthy and benign breast tissues specimens (Figure 4.19). The Bode plot displayed indicated that the probe was capable of differentiating between the tissue margins and the benign lesion of the patients who presented with a fibroadenoma across all 30 of the frequency points. A paired-samples T test was used to determine if the result obtained at the optimum frequency of 20,434 Hz showed a statistically significant difference between the tissue margin and the benign lesion (5,947 Ω ; $p = 0.029$) (Figure 4.20).

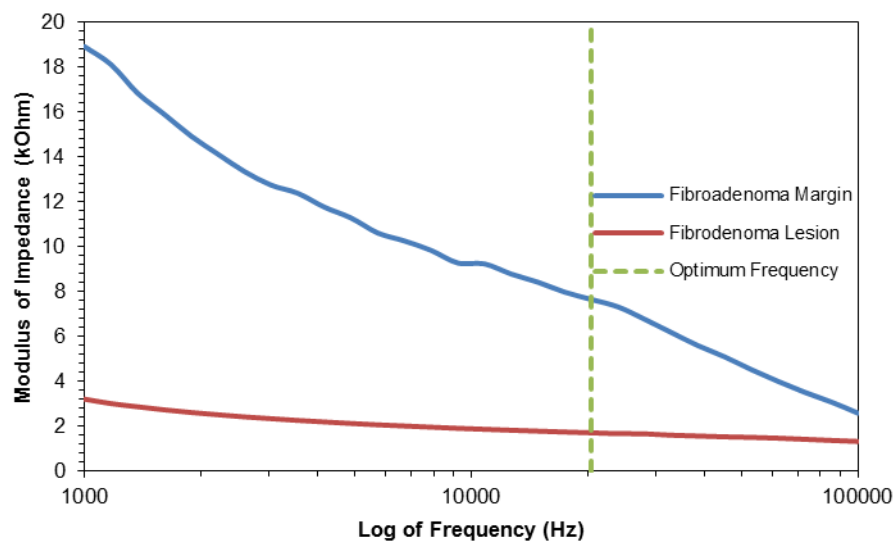


Figure 4.19: The Bode plot of the averaged electrical impedance results of the fibroadenoma patients consented to the clinical trial. N=2.

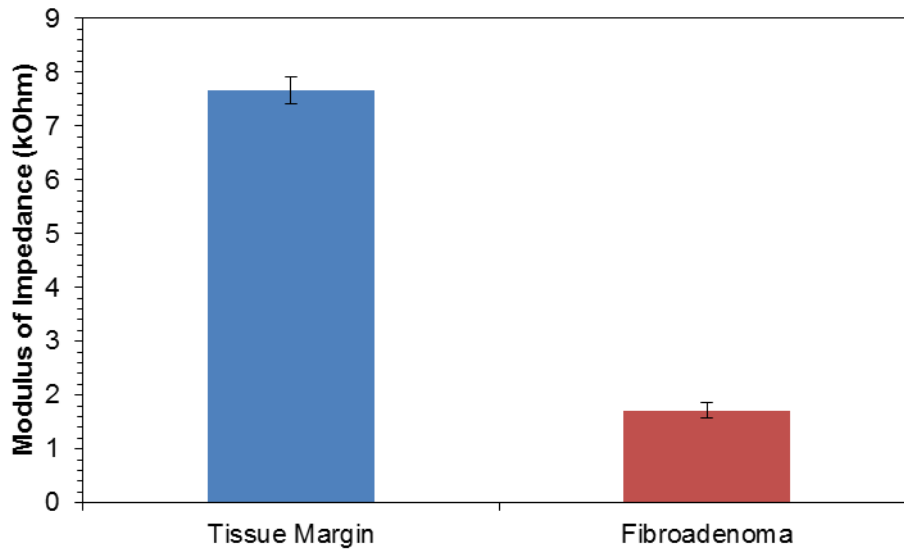


Figure 4.20: The mean \pm S.D. of the tissue margin and fibroadenoma recordings obtained at a frequency of 20 kHz from the tissue margins and benign lesions from the fibroadenoma patients. N=2; mean \pm S.D.; $p = 0.029$.

4.6 Discussion

It was determined from the statistical analysis performed in this chapter that the silicon prototype was capable of differentiating between healthy tissue margins and both benign and cancerous breast lesions. However, given the heterogeneous nature of breast cancer as a disease it has not yet been possible to differentiate between the many different subtypes that can be detected. The definitive sub-classification of breast cancer in to distinct groups is complicated by the very nature of the disease itself. The World Health Organisation published guidelines on the histological classification of breast tumours. There were eight tumour origins based on cell type with nearly 100 additional subtypes [5]:

- 1) Epithelial – 55 subtypes
- 2) Myoepithelial – 4 subtypes
- 3) Mesenchymal – 18 subtypes
- 4) Fibroepithelial – 6 subtypes
- 5) Tumours of the nipple – 3 subtypes
- 6) Malignant Lymphoma – 4 subtypes
- 7) Metastatic Tumours
- 8) Tumours of the male breast – 3 subtypes

In addition to the histology of the breast cancers it is also possible to classify each breast lesion based on molecular classification with six distinct categories: basal-like, ErbB2+, normal breast like, Claudin-low, luminal A and luminal B [6-8]. As part of the current study it was possible to analyse 6 histological subtypes of cancer with only one sample in most of the categories. Given the number of different breast cancer subtypes it would not be feasible to obtain representative sample cohorts for each of histological groupings without a very large multi-centre clinical trial conducted over many years. This is well beyond the scope of this current study as it would require significant resources, manpower and time.

The most important finding from the work presented in this chapter was the confirmation of the prototype silicon probes ability to differentiate between all of the cancer types combined and the associated healthy tissue margins. This demonstrates that the device is fit for purpose in the recording of *ex vivo* electrical impedance measurements from breast tissue samples. As the number of patients consented to the clinical trial continues to increase it should be possible to ascertain the true power of the probe in differentiating not only between healthy and cancerous lesions but also between cancerous and benign lesions which is one of the expected future uses of this device. Currently the sample sizes for the cancer sub-types are too low to draw appropriate conclusions about the probes true sensitivity and specificity in differentiating between breast cancer subtypes. It was possible to assess show a correlation between each of the 11 IDC Grade 3 study participants that indicated that there was a statistical similarity across all the patient samples recorded. This would suggest that it may be possible in the future to categorise cancer tumours based on electrical impedance but this study is too preliminary to be able to definitively conclude this. However, the real clinical benefit of this probe is in the differentiation of normal and abnormal tissues within the breast. The ability to distinguish between different sub-types of cancer may not ever be feasible using electrical impedance. The results outlined in this chapter showed that mean difference between the normal and abnormal tissues across each of the cancer sub-types was not sufficiently different from each other. This means that it would not be

possible to readily identify the individual cancer sub-type based solely on the electrical impedance. Any patient who is diagnosed as having breast cancer will undergo pathological investigation and molecular screening to determine the exact cancer type present within the breast as well as the cell surface receptors located on each cell. This diagnosis will then determine the treatment each individual patient receives. This cellular and molecular classification of cancer is far superior to anything that can be achieved by electrical impedance alone. Therefore, it is not necessary for the silicon probe device to be able to differentiate between cancer sub-types, only between cancer and non-cancer which was shown in this chapter to be possible.

The large variability observed between the electrical impedance readings obtained from the different patient samples may result from a number of different sources:

- 1) Probe contact and apposition
- 2) Cancer pathology
- 3) Extracellular fluids
- 4) Heterogeneous nature of breast cancer

The apposition of the recording electrodes to the exposed surface of the tissues of interest is extremely important to obtaining an accurate electrical impedance measurement. The current silicon prototype was not able to directly penetrate in to the tissues being recorded. Therefore, it was necessary to make an incision in to the tumour and tissue margins to access the recording sites. The variable firmness of the tumours and tissue margins meant that apposition of the electrodes to the tissue surface was often quite difficult but ultimately achievable. Cancerous lesions can develop as extremely heterogeneous masses with many different structures present within the tumour. In case of IDC lesions the histological presentation can include [5]:

- 1) Tumour cells that can be arranged in cords, clusters and trabeculae whilst some tumours are characterized by a predominantly solid or syncytial infiltrative pattern with little associated stroma

- 2) In a proportion of cases glandular differentiation may be apparent as tubular structures with central lumina in tumour cell groups
- 3) The cytoplasm is often abundant and eosinophilic
- 4) Nuclei may be regular, uniform or highly pleomorphic with prominent, often multiple, nucleoli, mitotic activity may be virtually absent or extensive
- 5) There may be highly cellular fibroblastic proliferation, a scanty connective tissue element or marked hyalisation
- 6) Focal necrosis may be present and is occasionally extensive
- 7) Up to 80 % will contain foci of associated DCIS
- 8) In a minority of cases a distinct lymphoplasmacytoid infiltrate can be identified

In the introduction of this thesis the term bio-impedance was described as the response of a living organism to an externally applied electric current, and is a measure of the opposition to the flow of that electric current through tissues [9, 10]. This opposition the current experiences when passing through these tissues is determined by a number of factors including the extracellular fluid, cell membrane, intracellular fluid and sub-cellular structures. The extremely variable nature of cancerous tumours has resulted in tissues which appear to effectively conduct an electrical current and thereby results in a low impedance modulus value being observed during experimental measurement in previously described literature [11-13]. This finding is in keeping with the results presented in this chapter.

Finally the effect of extracellular fluids at the site of incision in to the tissues could be a contributory factor to the variability of the observed impedance. These fluids could include blood from the excised tissue, intracellular fluid leaking from dead or dying cells and interstitial fluid which surrounds all cells. The varying degree to which any or all of these fluids were present at the time of the electrical impedance could potentially have had an influence on the measurements obtained. This is however a fundamental aspect of performing investigations on biological samples and the inter sample variation is impossible to overcome.

As part of the validation of the silicon probe device it was necessary to conduct impedance modulus recordings on freshly excised *ex vivo* breast tissue samples. It was not possible to control all of the potential variables that could have an effect on the recorded impedance values including patient age, cancer type and grade, time between removal and recording, amount of blood present at recording site, intracellular and extracellular fluid volumes as well as many other environmental and physiological variables. The design of the study protocol aimed to reduce the potential impact of these factors by performing the recordings under similar laboratory conditions each time and as soon after removal from the patient as feasibly possible (within 1 hour post removal). However, this validation study was only suitable for assessing the silicon probes ability to record *ex vivo* tissue. Performing recordings in the *in vitro* environment presents many different variables that need to be assessed but also eliminates some of the environmental factors associated with *ex vivo* measurements. This can include recording at body temperature, active blood flow, insertion through and into intact tissues, no applied pressure and probe placement without macroscopic identification as well as many other patient specific variables. The result presented in this chapter show that despite the many physiological and environmental variables that were present when recording the *ex vivo* tissue samples it was possible to differentiate statistically between 23 pairs of normal and abnormal tissue samples. This demonstrated that the silicon probe was able to detect the cellular difference between the different tissue types by measuring the impedance modulus.

4.7 Conclusions

One of the most significant obstacles encountered during the conduct of the clinical breast study was patient recruitment. A requirement of the medical scientists was to have tumour samples with a diameter of no less than 1.5 cm but preferably greater than 2 cm, the majority of the breast cancer patients undergoing surgery with Mr Martin O'Sullivan were identified through the BreastCheck screening service. As breast cancer screening aims to detect cancer at very early stages, tumour size can often be less than 15 mm [14]. As a result many of the patients presented with non-palpable tumours

which were only detected radiographically and were too small to be included in the study. This meant that the recruitment of patients was extremely slow with less than 1 patient per week being consented to the trial. It was also not possible to obtain electrical impedance recordings from the majority of wire-guided wide-local excision specimens. Five of the study participants that were lost to follow up underwent US wire-guided wide-local excision procedures. The laboratory protocol for histological processing of samples with inserted wire-guides prohibits the wire from being displaced prior to fixation and x-ray analysis. The point at which the wire-guide is inserted in to the lesion significantly inhibited the ability of the medical scientists to cut in to the lesion. This meant that it was often not possible to expose the interior aspect of the tumour. This additional exclusion criterion further limited the patient recruitment process and significantly reduced the total number of specimens from which recordings were obtained.

4.7.1 Future Work

The future work related to this experimental section involves the continued recruitment of suitable patients to provide a larger sample size for the analysis of the probes sensitivity and specificity. An increased variety of tissues being included for analysis could provide a valuable insight in to the ability of the probe to differentiate between normal, benign and cancerous tissues of breast origin. Of particular future clinical benefit would be differentiation and confirmation of benign breast lesions that could allow to patient to avoid undergoing surgery for removal of the tissues [15, 16]. This could potentially decrease the total number of patients requiring treatment for lesions that have been confirmed as benign. This could significantly reduce the cost to the healthcare system across the country and possibly worldwide. Another potential future application of the device could be during surgery for the accurate determination of cancer-free margins [17, 18]. There is no consensus on what constitutes a cancer-free margin worldwide and this can vary from no cancer cells touching the inked-margin to 1 cm of tissue between the two [18]. These assessments are only made a number of days post-surgery due to the histologic staining process involved. Therefore, an impedance tool capable of real-time determination of cancer-free surgical

margins could significantly decrease the re-excision rate for patients undergoing breast conservation surgery.

Future clinical trial studies will be required to determine the probes ability to screen and detect breast abnormalities including fibroadenoma, DCIS as well as invasive breast tumours. The overall sensitivity and specificity of the device will have to be assessed across each of the intended tissues of interest which may include other organs throughout the body such as the prostate which is the most common cancer in men worldwide [19]. The future development of these prototype devices will endeavour to produce a device that will act as an adjunct technology to the existing state of the art of digital x-ray mammography. These devices would provide essential diagnostic information which could inform a clinician's decision in the treatment of a patient.

A number of possible substrate materials will need to be trialled to assess the best one to use to increase the overall strength of the probe while maintaining the overall biocompatibility of the device. It would also eliminate the need to make an incision in to the area of interest in order to obtain the electrical impedance recordings. Most importantly the new instrument must be commercially viable and be user-friendly to ensure uptake and use by clinical and hospital staff. The predicted benefit of this device would be as an adjunct to x-ray mammography in the assessment of breast lesions, detected either clinically or by screening. It may potentially have a role to play in obtaining clear or negative margins during the breast cancer surgery. There is a significant potential benefit to using this probe in the determination of benign breast lesions. If a lesion could be confirmed as being non-cancerous it could potentially avoid the need for a CNB. This would significantly reduce the number of procedures being performed and would also reduce the number of benign lesions sent for histological analysis. It would also give the patient reassurance at the time of sampling that a cancerous lesion was not detected as well as having economic benefits to the health service.

A significant amount of research will be required in order to produce a new prototype of the silicon probe. The substrate material which will be chosen to

replace the silicon must be highly compatible with semiconductor fabrication processes, biocompatible and strong enough to withstand insertion into extremely dense cancerous tissues within the breast. An ideal solution to this problem would be to deposit the gold electrodes on to an existing CNB needle. This would allow for precise needle-tip localisation during sampling of breast lesions to ensure accurate tissue capture. It would also provide a substrate that is suitable for insertion in to cancerous tissues and is completely biocompatible with the human body. The major drawback to the use of these needles is the circular shape which is not compatible with current deposition processes. Therefore, further research will be required to produce a more robust prototype device that would allow for an expansion of the ongoing clinical study to investigate more of the probes capabilities.

4.8 References

1. Srinivasaraghavan, V., J. Strobl, D. Wang, J.R. Heflin, and M. Agah, *A comparative study of nano-scale coatings on gold electrodes for bioimpedance studies of breast cancer cells*. Biomedical microdevices, 2014. **16**(5): p. 689-696.
2. Posten, H.O., *Robustness of the two-sample t-test*, in *Robustness of statistical methods and nonparametric statistics*. 1984, Springer. p. 92-99.
3. Russo, J. and I.H. Russo, *Histological Evaluation of the Normal Breast*, in *Techniques and Methodological Approaches in Breast Cancer Research*. 2014, Springer. p. 45-73.
4. Edge, S.B., D.R. Byrd, C.C. Compton, A.G. Fritz, F.L. Greene, and A. Trotti, *AJCC cancer staging manual*. Vol. 649. 2010: Springer New York.
5. Tavassoli, F.A. and P. Devilee, *Pathology and genetics of tumours of the breast and female genital organs*. Vol. 4. 2003: Iarc.
6. Malhotra, G.K., X. Zhao, H. Band, and V. Band, *Histological, molecular and functional subtypes of breast cancers*. Cancer Biol Ther, 2010. **10**(10): p. 955-60.
7. Perou, C.M., T. Sorlie, M.B. Eisen, M. van de Rijn, S.S. Jeffrey, C.A. Rees, J.R. Pollack, D.T. Ross, H. Johnsen, L.A. Akslen, O. Fluge, A. Pergamenschikov, C. Williams, S.X. Zhu, P.E. Lonning, A.L. Borresen-Dale, P.O. Brown, and D. Botstein, *Molecular portraits of human breast tumours*. Nature, 2000. **406**(6797): p. 747-52.
8. Sorlie, T., C.M. Perou, R. Tibshirani, T. Aas, S. Geisler, H. Johnsen, T. Hastie, M.B. Eisen, M. van de Rijn, S.S. Jeffrey, T. Thorsen, H. Quist, J.C. Matese, P.O. Brown, D. Botstein, P.E. Lonning, and A.L. Borresen-Dale, *Gene expression patterns of breast carcinomas distinguish tumor subclasses with clinical implications*. Proc Natl Acad Sci U S A, 2001. **98**(19): p. 10869-74.
9. Coffman, F.D. and S. Cohen, *Impedance measurements in the biomedical sciences*. Stud Health Technol Inform, 2013. **185**: p. 185-205.
10. Ching, C.T., T.P. Sun, S.H. Huang, C.S. Hsiao, C.H. Chang, S.Y. Huang, Y.J. Chen, C.S. Cheng, H.L. Shieh, and C.Y. Chen, *A preliminary study of the use of bioimpedance in the screening of squamous tongue cancer*. Int J Nanomedicine, 2010. **5**: p. 213-20.
11. Morimoto, T., Y. Kinouchi, T. Iritani, S. Kimura, Y. Konishi, N. Mitsuyama, K. Komaki, and Y. Monden, *Measurement of the electrical bio-impedance of breast tumors*. Eur Surg Res, 1990. **22**(2): p. 86-92.
12. Morimoto, T., S. Kimura, Y. Konishi, K. Komaki, T. Uyama, Y. Monden, Y. Kinouchi, and T. Iritani, *A study of the electrical bio-impedance of tumors*. J Invest Surg, 1993. **6**(1): p. 25-32.
13. Mishra, V., H. Bouayad, A. Schned, A. Hartov, J. Heaney, and R.J. Halter, *A real-time electrical impedance sensing biopsy needle*. IEEE Trans Biomed Eng, 2012. **59**(12): p. 3327-36.
14. BreastCheck, *BreastCheck Programme Report 2013/14*. 2015. p. 13.
15. Jossinet, J., *Variability of impedivity in normal and pathological breast tissue*. Med Biol Eng Comput, 1996. **34**(5): p. 346-50.

16. Jossinet, J., *The impedivity of freshly excised human breast tissue*. *Physiol Meas*, 1998. **19**(1): p. 61-75.
17. Singletary, S.E., *Surgical margins in patients with early-stage breast cancer treated with breast conservation therapy*. *The American Journal of Surgery*, 2002. **184**(5): p. 383-393.
18. Morrow, M., *Breast conservation and negative margins: how much is enough?* *The Breast*, 2009. **18, Supplement 3**: p. S84-S86.
19. American Cancer Society, *Cancer Facts & Figures 2014*. 2014, American Cancer Society, Inc.: Atlanta.

Chapter 5

Conclusions

5. Summary and Future Work

5.1 Chapter 1 Summary

Over the last two decades there has been a significant amount of research conducted to investigate the use of electrical impedance to detect cancer in tissues throughout the body with particular focus on the breast. Prototype devices were previously described in the literature which used electrical impedance as both an imaging and invasive detection method. From the background literature it has been shown that skin surface EIT was not effective enough at detecting breast cancer especially in large breasts due to a poor depth of penetration. For this reason the technology did not provide a reasonable alternative to the gold standard of digital x-ray mammography. However, the use of electrical impedance as a detection method incorporated on to a minimally invasive needle/probe has the ability to prove extremely useful in a number of clinical settings. This includes benign lesion testing, biopsy needle localisation and cancer-free margin determination. By utilising a novel device in these areas there is a possibility to meet a clinical need which is as yet unmet, while also significantly reducing the financial burden on the healthcare system. By using a novel device to aid in the determination of benign breast lesions in settings such as the BreastCheck screening clinics in Ireland there could be a significant reduction in the number of patients undergoing core-needle biopsies and full histopathological analysis. This would reduce patient discomfort as well as reducing the workload on the hospital laboratory system. If successful, it also has the potential benefit of being able to re-assure patients immediately, which could significantly limit the anxiety associated with being called back for assessment following a screening mammogram.

5.2 Chapter 2 Summary

In this chapter the fabrication and characterisation of novel electrical impedance devices were investigated. Initially, stainless steel was used as the substrate material. This was ultimately unsuccessful and was replaced with silicon. This material is the most compatible with the fabrication processes currently used the Tyndall National Institute as well as the wider

semiconductor industry. It was possible to fabricate and package a prototype device that showed excellent surface properties when analysed with SEM, EDX, FIB and AFM. The probes also showed excellent electrochemical properties when tested extensively with CV and electrical impedance. The results obtained in this chapter showed that reproducible and reliable devices had been created that were capable of detecting electrical impedance signals. This formed the basis of the work conducted in chapter three.

5.2.1 Chapter 2 Future Work

The future work arising from the research in this chapter will involve the fabrication of the next generation of impedance sensors. This will require significant research in to the type of material used as the substrate for deposition as well as a method for patterning electrodes on to a curved surface. On completion of these investigations a new prototype that is more robust than the current silicon probe could be produced that would be suitable for testing in biological tissues.

5.3 Chapter 3 Summary

The research presented in Chapter 3 of this thesis involved the biocompatibility testing of the stainless steel and silicon devices and the testing of meat samples of bovine, ovine and porcine origin. The biocompatibility testing showed that the fabrication techniques and materials used in the development of the prototype devices did not adversely affect the growth of immortalised cell lines on their surfaces. This was determined using a number of techniques including nuclear staining, light, fluorescent and SEM and a resazurin cell viability assay. The importance of having a biocompatible device is particularly relevant in this project as the long term goal was to create a device which could be used to analyse tissues in human patients in a clinical setting. Approval for clinical testing of this type of device would never be granted without first demonstrating that the device would not cause an adverse reaction upon insertion in to a patient. In the second half of this chapter a series of experiments were conducted to demonstrate the ability of the prototype silicon probes to differentiate between fat and muscle tissues in *ex vivo* meat samples using the modulus of the impedance. The

results outlined showed that for all samples tested the probes were capable of differentiating between muscle and fat at three amplitudes of recording and across all frequencies tested. In addition to this, experiments were performed to determine what effect an applied external force and depth of recording may have on the electrical impedance signal observed. The results demonstrated that there was a negligible difference between the different variables measured.

5.3.1 Chapter 3 Future Work

The future work resulting from this chapter will mostly be focused on the testing of biological tissues. By assessing different healthy tissues it would be possible to generate a database of electrical impedance values. This could be used as a baseline for a future study of pathological animal tissues in both live and slaughtered animals. Any future prototypes developed as part of this work would need to be biocompatibility tested in the same manner as the probes described in this thesis.

5.4 Chapter 4 Summary

The work presented in this chapter details the research conducted as part of a first-in-human clinical trial investigating the ability of the silicon probe to differentiate between healthy and cancerous breast tissue in human patients. This trial was conducted from March 2015 to March 2016 in CUH in conjunction with the Departments of Surgery, Anaesthesia and Histopathology. A total of 33 patients were consented to the trial and recordings were obtained from 23 of these with 10 lost to follow up. The results showed that the probe was capable of differentiating the healthy tissue margins, benign and cancerous breast lesions. The tumours tested during the trial were divided according to the type and grade of the tumour present and each of these was confirmed histologically by a consultant histopathologist. This work was conducted as part of an ongoing clinical trial that will continue to collect and test patient samples obtained during breast surgery to provide a proof of concept of the probes ability to differentiate between human breast tissues. The results presented in this chapter show that the silicon probe prototype device was capable of differentiating between

healthy tissue margins, cancerous and benign lesions within the breast. The type or grade of tumour does affect the probes ability to determine differences between the tissues.

5.4.1 Chapter 4 Future Work

In the opening chapter of this thesis a key research questions was posed:

- 1) Can we use electrical impedance to differentiate between healthy and cancerous tissues of the breast?

Three additional research questions that will need to be investigated in the future are:

- 1) Can we provide real-time analysis of minimally invasive needle tip localisation during biopsies?
- 2) Can we improve margin determination during breast cancer surgery?
- 3) Can we provide a diagnostic tool for the determination of benign breast lesions?

It has been shown through the data presented in this thesis that it is possible to differentiate healthy, benign and cancerous tissues of the breast using electrical impedance. In order to answer the rest of these questions further research will be required that will build upon the foundation provided by the work presented in this thesis. The future work in this topic will be focused on the recruitment of a large patient cohort to enable the sensitivity and specificity of the electrical impedance device to be determined. It will also be necessary to recruit patients with as many different subtypes of cancer as possible to ensure that each one can be reliably differentiated from the surrounding healthy tissue.

5.5 Thesis Conclusion

The aim of this thesis was to develop a new method for differentiating between healthy and cancerous tissue types for the purpose of detecting breast cancer. The method by which this was achieved was to use semi-conductor fabrication techniques to produce a novel microelectrode impedance sensor. This was developed based on the work of previous

research groups who had demonstrated electrical impedance was effective at differentiating between tissue types within the human body. The data presented here showed that the techniques employed in the fabrication of a novel impedance sensor were suitable and resulted in a device that was suitable for use in a first-in-human clinical trial. As part of the study design, histological confirmation of probe placement was obtained which had not previously been assessed in any of the literature. This allowed the many different subtypes of cancer described in Chapter 4 to be identified and individually analysed. This was necessary because of the heterogeneous nature of breast cancer which means that it cannot be considered one single disease. This thesis has successfully provided a detailed description of the work undertaken in developing this novel method of tissue determination; has successfully achieved many of the research aims outlined in the opening chapter and has laid the foundation for research in to this area in the future.

Chapter 6

Appendices

6. Appendices

6.1 Patient Information Leaflet

Patient Information Leaflet

(Version: 1.4 Date: 23 Jun. 14)

Study title: Electrical Impedance Measurement of Healthy and Cancerous Breast Tissues *ex vivo*

Principal investigator's name:	Mr Martin O' Sullivan
Principal investigator's title:	Consultant Breast Surgeon
Telephone of principal investigator:	021 4920337
Co-investigator's name:	Dr Brian O'Donnell
Co-investigator's title:	Consultant Anaesthetist

You are being invited to take part in a research study carried out

at **Cork University Hospital by CUH and Tyndall National Institute.**

Before you decide whether or not you wish to take part, you should read the information provided below carefully and, if you wish, discuss it with your family, friends or GP (doctor). Take time to ask questions – do not feel rushed or under pressure to make a quick decision.

You should clearly understand the risks and benefits of taking part in this study so that you can make a decision that is right for you. This process is known as 'Informed Consent'.

You do not have to take part in this study and a decision not to take part will not affect your future medical care.

You can change your mind about taking part in the study any time you like. Even if the study has started, you can still opt out. You do not have to give us a reason. If you do opt out, it will not affect the quality of treatment you get in the future.

Why is this study being done?

This study is being conducted to determine if a new medical device (produced by researchers at the Tyndall National Institute, and doctors in

University College Cork and Cork University Hospital) is capable of identifying the difference between healthy and cancerous breast tissue. The device will be tested using tissue samples removed during surgery and that are undergoing normal processing by the Department of Pathology as part of the diagnostic process to confirm the presence or absence of a particular disease.

Who is organising and funding this study?

The study is being organised as a joint project between Cork University Hospital and the Tyndall National Institute as part of a PhD research project funded by Molecular Medicine Ireland. The device testing will be conducted by Niall Savage who is the PhD researcher involved with this project.

Why am I being asked to take part?

You are being asked to partake in this study because you are a patient of Mr Martin O'Sullivan and are undergoing surgery to remove an area of breast tissue as part of your treatment.

How will the study be carried out?

This study will be carried out in the Department of Pathology in CUH where the sample removed during surgery will be processed for diagnosis. Electrical recordings will be performed by Niall Savage in association with the biomedical science staff in the department during the initial sample processing.

What will happen to me if I agree to take part?

Should you agree to participate in this study you will be required to sign a consent form that allows your samples to be used as part of the trial investigation. Whether you wish to participate in the study or not there will be no change to your planned care. If you choose to participate in the study no additional tissue will need to be removed beyond what is required as part of your clinical treatment. The electrical recordings will not affect the quality of the sample being analysed by the Department of Pathology. Information regarding your diagnosed condition will be retained as part of the study for comparison to the electrical data findings. All information which might identify you individually will be removed and any medical information that is retained will not be disclosed.

What other treatments are available to me?

If you choose not to participate in this study your treatment will remain unaffected and your tissue samples will not be used in any aspect of this study.

What are the benefits?

The benefits of this research project will be in the potential development of a new medical device that will improve breast cancer patient care and diagnosis in the future. There will be no immediate benefit to you as a participant in this study.

What are the risks?

There are no foreseeable risks to you as a patient because the testing required by this study will be performed after the breast tissue has been removed and is sent to the pathology laboratory for processing. No extra tissue is required as the study will use samples from the tissue that is removed as part of your clinical care.

Will it cost me anything to take part?

There will be no additional costs applied to your treatment as a result of participating in this study.

Is the study confidential?

As part of the study it will be necessary for the researcher to compare the sample data with the diagnostic report produced by the Department of Pathology as presented to your consultant. Your individual patient number will be recorded along with any necessary information in regards to sample and disease diagnosis (e.g. age, sex, location of tumour, type and stage). All other biographical details will be recorded only on your medical records as part of normal hospital practice and will be accessible only by the medical staff of the hospital. All data generated during this study will be stored on secure servers maintained by the I.T Department of Tyndall National Institute. All tissue samples generated during surgery will be processed by the Department of Pathology according to standard operating procedures and will be archived accordingly. Data generated by this study may in future be published in scientific and/or medical journals but it will not be possible for you as a patient to be identified as a result as all relevant information will have been removed prior to publication.

Where can I get further information?

If you have any further questions about the study or if you want to opt out of the study, you can rest assured it won't affect the quality of treatment you get in the future.

If you need any further information now or at any time in the future, please contact:

Name: Niall Savage

Address: Tyndall National Institute, University College Cork, Cork, Ireland.

Phone No: 021 4205607

6.2 Patient Consent Form

PATIENT CONSENT FORM:

Clinical Research Ethics Committee of the Cork Teaching Hospitals

(Version 1.4; 09 Mar. 15)

CONSENT BY SUBJECT FOR PARTICIPATION IN RESEARCH PROTOCOL

Section A

Patient Name: _____ MRN: _____ DOB: ____/____/____

Title of Protocol: Protocol for Sampling Fresh Breast Cancer Tissue for Research Purposes

Doctor(s) Directing Research: Mr. Martin O'Sullivan

Phone: (C.I. phone no.) +353 21 4920337

You are being asked to participate in a research study. The doctors at University College Cork study the nature of disease and attempt to develop improved methods of diagnosis and treatment. In order to decide whether or not you want to be a part of this research study, you should understand enough about its risks and benefits to make an informed judgment. This process is known as informed consent. This consent form and the associated patient information leaflet give detailed information about the research study, which will be discussed with you. Once you understand the study, you will be asked to sign this form if you wish to participate.

Section B

I. NATURE AND DURATION OF PROCEDURE(S):

This research study will use cancerous and healthy breast tissue samples removed during surgery to allow testing of a prototype medical device which is designed to detect breast cancer using an electrical signal known as impedance. Each recording takes approximately 30 seconds and multiple recordings will be taken throughout a suspected lesion and in the surrounding healthy tissue.

II. POTENTIAL RISKS AND BENEFITS:

There is no foreseeable risk to you or your treatment as the procedure will only be conducted on tissue after its removal and in conjunction with the department of pathology to ensure the standard of care remains unaffected.

III. POSSIBLE ALTERNATIVES:

You may choose not to participate in this study as the process is voluntary.

Section C

AGREEMENT TO CONSENT

The research project and the treatment procedures associated with it have been fully explained to me. All experimental procedures have been identified and no guarantee has been given about the possible results. I have had the opportunity to ask questions concerning any and all aspects of the project and any procedures

involved. I am aware that participation is voluntary and that I may withdraw my consent at any time. I am aware that my decision not to participate or to withdraw will not restrict my access to health care services normally available to me. Confidentiality of records concerning my involvement in this project will be maintained in an appropriate manner. When required by law, the records of this research may be reviewed by government agencies and sponsors of the research.

I understand that the sponsors and investigators have such insurance as is required by law in the event of injury resulting from this research.

I, the undersigned, hereby consent to participate as a subject in the above described project conducted at the Cork Teaching Hospitals. I have received a copy of this consent form for my records. I understand that if I have any questions concerning this research, I can contact the doctor(s) listed above. If I have further queries concerning my rights in connection with the research, I can contact the Clinical Research Ethics Committee of the Cork Teaching Hospitals, Lancaster Hall, 6 Little Hanover Street, Cork.

After reading the entire consent form, if you have no further questions about giving consent, please sign where indicated.

Doctor

Signature of Patient

Parent or Guardian (If applicable)

Witness

6.3 Summary of C.V. for Chief Investigator

CV Summary Mr Martin O’Sullivan, Consultant Surgeon

Name: Martin James O’Sullivan
Date of birth: 19th July 1971
Nationality: Irish
Marital status: Married
Work address: Department of Surgery,
 Lead Surgeon,
 Cork University Hospital, BreastCheck,
 Wilton, Infirmary Road,
 Cork Cork
Contact address: See above
Telephone: +353 21 4920337 (work)
 +353 86 8130283 (mobile)
E-mail address: martin.osullivan1@hse.ie
Qualifications: M.B., B.Ch., B.A.O.
 F.R.C.S.I.
 M.A. (Healthcare Administration)

M.D.

Irish Medical Council Number: 19307

Curriculum vitae summary

Clinical experience

Consultant (Lead) Surgeon with BreastCheck South since 2007

Completed the Irish Higher Surgical Training Scheme in General Surgery including Fellowship in USA

Trained in Oncoplastic surgery in USA

Teaching

Extensive experience of undergraduate teaching throughout career

Experience as examiner and exam organiser of undergraduate examinations

Senior Lecturer, UCC

Instructor ALTS courses, 2004 onwards

Management

MA (honours) in Healthcare Administration

Academic record

Publications

>26 publications in peer-reviewed journals

Fifty-five published abstracts

Presentations

>100 communications to learned societies / meetings, both national and international, including three invited lectures

Distinctions

Honours in Surgery, Medicine & Paediatrics (three of the four subjects) in the final year medical examinations, 1995

Poster prize, **European Society of Surgery**, 4th annual meeting, Poland, December 2000

Inaugural **Charles Pannett medal, Society of Academic and Research Surgery** forum, London, January 2002

Poster prize, **12th Annual Medical Faculty Research Day**, Cork University Hospital, June 2004

6.4 Ethical Approval Application

Due to the size of the original application it was not possible to attach it as part of the thesis. It is available on request.

6.5 List of Oral and Poster Presentations

6.5.1 Conference Proceedings

1. “Development of a smart needle integrated with a micro-structured impedance sensor for the detection of breast cancer”, **N.T.P. Savage**, B.D. O'Donnell, M.J. O'Sullivan, E.J. Moore; World Congress on Medical Physics and Biomedical Engineering, June 7-12, 2015, Toronto, Canada. Volume 51, July 2015, Pages 1293-1296.

6.5.2 Oral Presentations

1. “Micro-structured Electrodes for the *in vitro* detection of Impedance in cancer cell lines”, **Niall T.P. Savage**; Brian D. O'Donnell; Martin J. O'Sullivan; Eric J. Moore; Molecular Medicine Ireland (MMI) Annual Scientific Meeting, 12th March 2014.

2. “Development of a smart needle integrated with a micro-structured impedance sensor for the detection of breast cancer”, **Niall T.P. Savage**; Brian D. O'Donnell; Martin J. O'Sullivan; Eric J. Moore; World Congress on Medical Physics and Biomedical Engineering, 7-12th June 2015.

3. “Development of a smart needle integrated with a micro-structured impedance sensor for the detection of breast cancer”, **Niall T.P. Savage**; Brian D. O'Donnell; Martin J. O'Sullivan; Eric J. Moore; Chemistry Postgraduate Research Day, 21st August 2015

4. “Development of a smart micro-structured impedance probe for the detection of breast cancer”, **Niall T.P. Savage**; Michelle Fitzgerald; Walter Messina; Brian D. O'Donnell; Martin J. O'Sullivan; Eric J. Moore; European Platform on Smart Systems (EPoSS) Conference 2015, 12-13th October 2015

6.5.3 Poster Presentations

1. “Development of a smart needle integrated with nanostructured impedance sensor for detection of breast cancer”, **Savage N.T.P**; O'Donnell B.D; O'Sullivan M; Moore E.J; Molecular Medicine Ireland (MMI) Annual Scientific Meeting, 14th March 2013.

2. "Impedance Detection of breast cancer and ductal carcinoma in situ", **Savage N.T.P**; O'Donnell B.D; O'Sullivan M; Moore E.J; Tyndall National Institute Internal Conference, 25th April 2013,
3. "Breast cancer and ductal carcinoma in situ identification using a dual-electrode system", **Savage N.T.P**; O'Donnell B.D; O'Sullivan M; Moore E.J; Royal Academy of Medicine in Ireland (RAMI) Conference, 20th June 2013.
4. "Breast cancer and ductal carcinoma in situ identification in cell culture models and *ex vivo* human tissue samples" **Savage N.T.P**; O'Donnell B.D; O'Sullivan M; Moore E.J; College of Medicine and Health (CoMH) Conference, 13th June 2013.
5. "Novel detection of breast cancer and ductal carcinoma in situ", **Savage N.T.P**; O'Donnell B.D; O'Sullivan M; Moore E.J; Conference on Analytical Science, Ireland (CASI) Conference, 1st and 2nd July 2013.
6. "Impedance detection of breast cancer and ductal carcinoma in situ", **Niall T.P. Savage**; Brian D. O'Donnell; Martin J. O'Sullivan; Eric J. Moore; Tyndall National Institute ICT For Health Conference, 16th September 2013.
7. "Micro-structured Impedance Electrodes for the Detection of Breast Cancer and Ductal Carcinoma in situ", **Niall T.P. Savage**; Brian D. O'Donnell; Martin J. O'Sullivan; Eric J. Moore; Micro-Nano-Bio Systems/European Platform on Smart Systems (MNBS/EpoSS) Conference, 23rd-25th September 2013. **Winner of Best Poster Award.**
8. "Micro-structured Impedance Electrodes for the Detection of Breast Cancer and Ductal Carcinoma in situ", **Niall T.P. Savage**; Brian D. O'Donnell; Martin J. O'Sullivan; Eric J. Moore; Smart Systems Integration (SSI) Conference, 26-27 March 2014.
9. "Development of a micro-structured electrode for the detection of breast cancer", **Niall Savage**; Brian O'Donnell; Martin O'Sullivan; Eric Moore; Department of Chemistry Postgraduate Research Day, UCC, 28th August 2014.

10. “Development of a smart needle integrated with a micro-structured impedance sensor for detection of breast cancer”, **Niall T.P. Savage**; Brian D. O'Donnell; Martin J. O'Sullivan; Eric J. Moore; Molecular Medicine Ireland (MMI) Annual Scientific Meeting, 24th March 2015.

11. “Gold Micro-Electrodes for the Detection of Breast Cancer in situ”, **Niall T.P. Savage**; Brian D. O'Donnell; Martin J. O'Sullivan; Eric J. Moore; Evolve Biomed Conference, 29-30th April 2015.

12. “Impedance Sensors for Biomedical and Bioassay Applications”, Lisa Helen, Walter Messina, **Niall Savage**, Michelle Fitzgerald, George Shorten, Bill Bennett, Martin O'Sullivan, Brian O'Donnell and Eric Moore; NanoMA 2015, 15-16th July 2015, Tsukuba, Japan.

13. “Impedance Sensors for biomedical & bioassay applications”, **Niall T.P. Savage**, Walter Messina, Michelle Fitzgerald, Lisa Helen, George Shorten, Michael W. Bennett, Martin J. O'Sullivan, Brian D. O'Donnell and Eric J. Moore; Micro-Nano-Bio Systems/European Platform on Smart Systems (MNBS/EPoSS) Conference, 12th-15th October 2015.

6.5.4 Demonstrations

1. “Impedance Sensors for Biomedical & Bioassay Applications”, **Niall Savage**; Michael Bennett; Martin O'Sullivan; Brian O'Donnell; Eric Moore; Tyndall National Institute Internal Conference, 7th-8th May 2014.

2. “Impedance Sensors for Biomedical & Bioassay Applications”, **Niall Savage**; Walter Messina; Michelle Fitzgerald; Lisa Helen; George Shorten; Michael Bennett; Martin O'Sullivan; Brian O'Donnell; Eric Moore; Tyndall National Institute-Teagasc MOU Signing Event, 3rd Oct 2014.

3. “Smart Probe”, **Niall Savage**; Tyndall Technology Days, 18-20th Nov 2014.

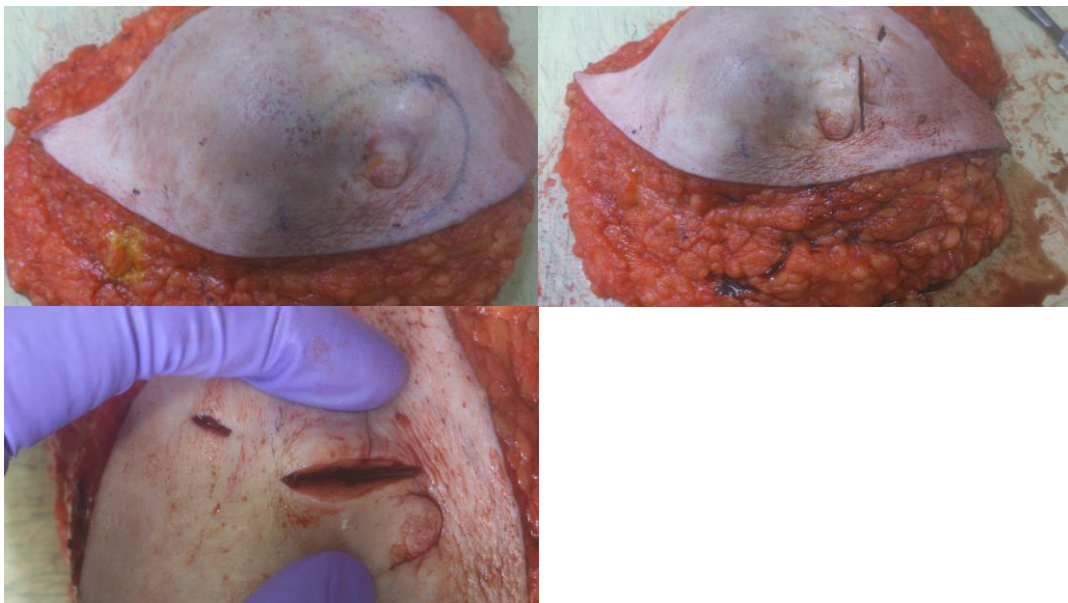
6.6 Clinical Trial Images

6.6.1 Macroscopic Images

Study Participant 05 - Wide-local Excision – 26mm Metastatic Squamous Cell Carcinoma



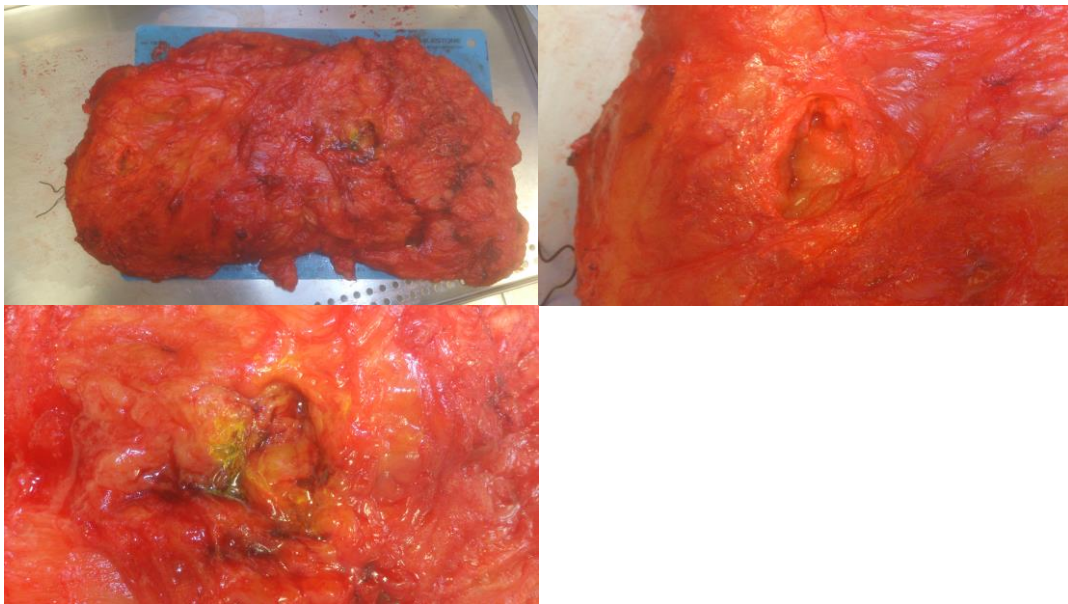
Study Participant 10 – Mastectomy – 95 mm Invasive Ductal Carcinoma Grade 3



Study Participant 11 – Wide-local Excision – 25 mm Invasive Ductal Carcinoma Grade 3



Study Participant 12 – Mastectomy – 18 mm Invasive Ductal Carcinoma
Grade 3



Study Participant 17 – Wide-local Excision – 21 mm Mixed Invasive Ductal
and Lobular Carcinoma Grade 2



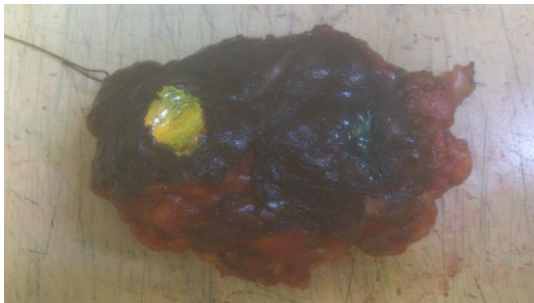
Study Participant 18 – Mastectomy – 27 mm Invasive Ductal Carcinoma
Grade 2



Study Participant 19 – Diagnostic Excision Biopsy – 25 mm Fibroadenoma



Study Participant 20 – Wide-local Excision – 34 mm Invasive Mucinous Carcinoma Grade 2



6.6.2 Microscopic Images

Study Participant 02

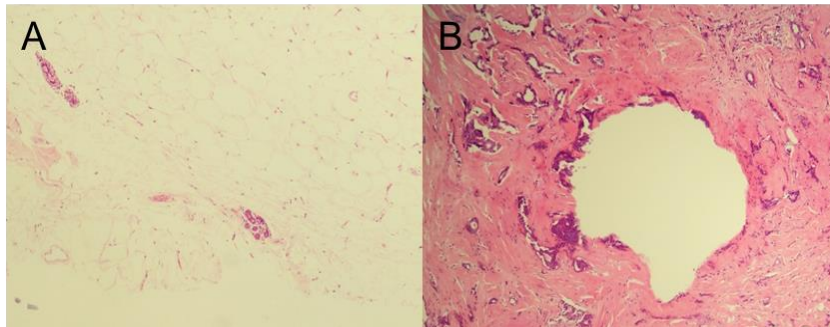
Gross Pathology:

Invasive Ductal Carcinoma Grade 2

Histologic Slide Analysis:

A) Normal Breast

B) Invasive Ductal Carcinoma Grade 2



Study Participant 03

Gross Pathology:

Invasive Lobular Carcinoma Grade 2

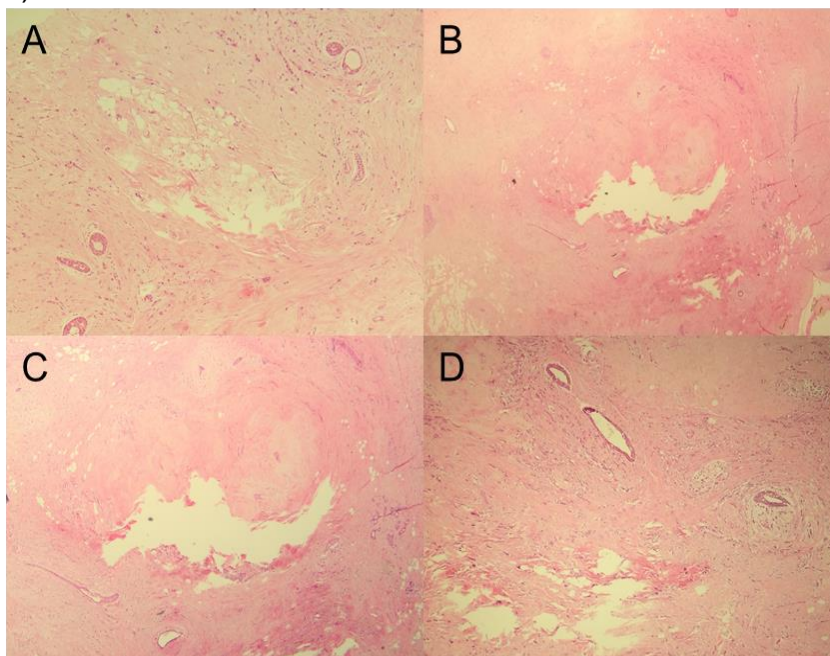
Histologic Slide Analysis:

A) Invasive Lobular Carcinoma Grade 2 Area 1

B) Invasive Lobular Carcinoma Grade 2 Area 2 (x4)

C) Invasive Lobular Carcinoma Grade 2 Area 2 (x10)

D) Invasive Lobular Carcinoma Grade 2 Area 3



Study Participant 05

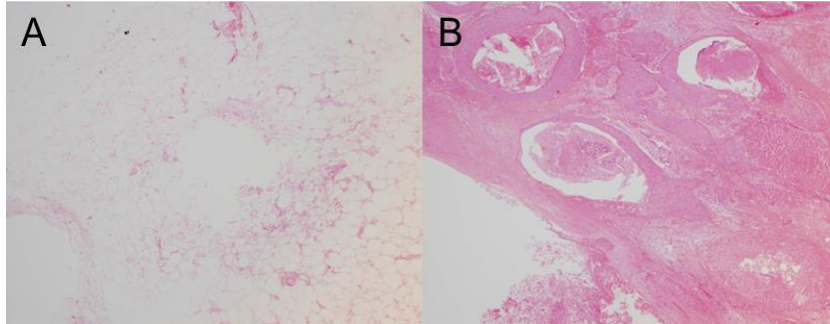
Gross Pathology:

Metastatic Squamous Cell Carcinoma

Histologic Slide Analysis:

A) Normal Breast

B) Metastatic Squamous Cell Carcinoma

**Study Participant 07**

Gross Pathology:

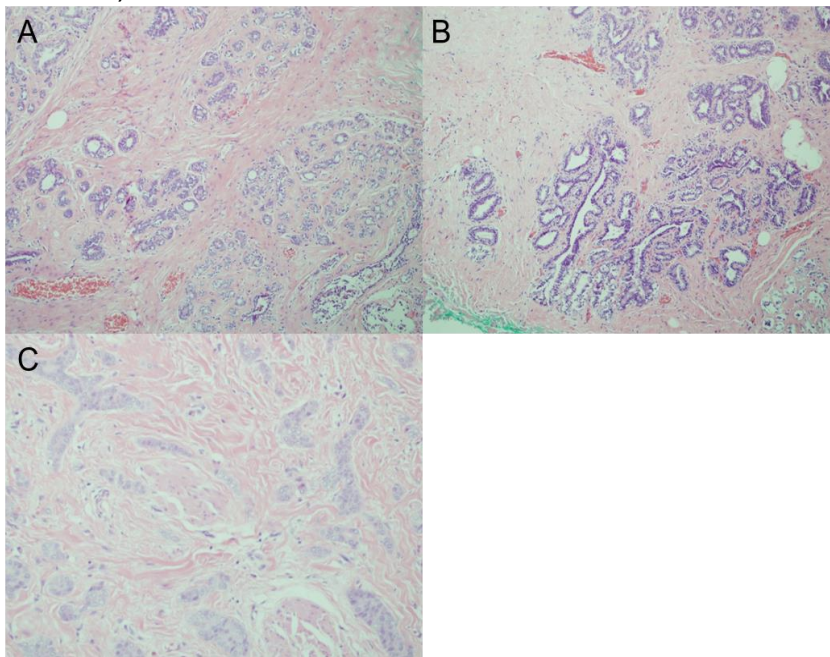
Invasive Ductal Carcinoma Grade 3

Histologic Slide Analysis:

A) Normal Breast 01

B) Normal Breast 02

C) Invasive Ductal Carcinoma Grade 3



Study Participant 08

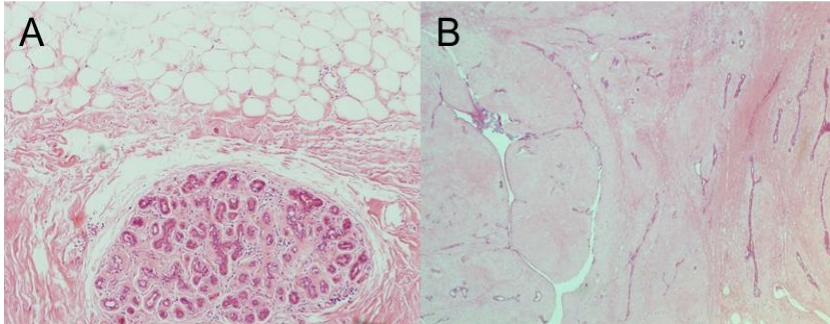
Gross Pathology:

Fibroadenoma

Histologic Slide Analysis:

A) Normal Breast

B) Fibroadenoma

**Study Participant 09**

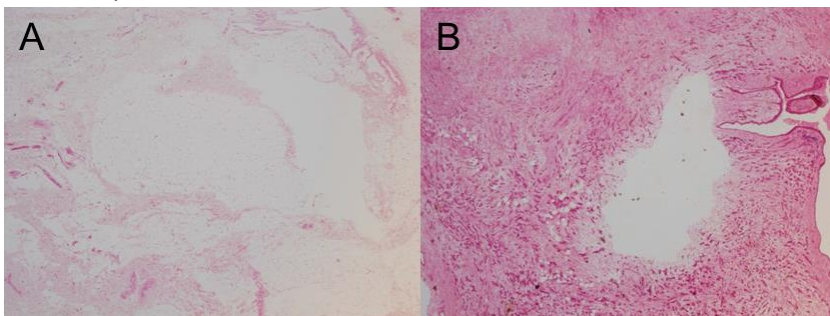
Gross Pathology:

Invasive Ductal Carcinoma Grade 2

Histologic Slide Analysis:

A) Normal Breast

B) Invasive Ductal Carcinoma Grade 2

**Study Participant 10**

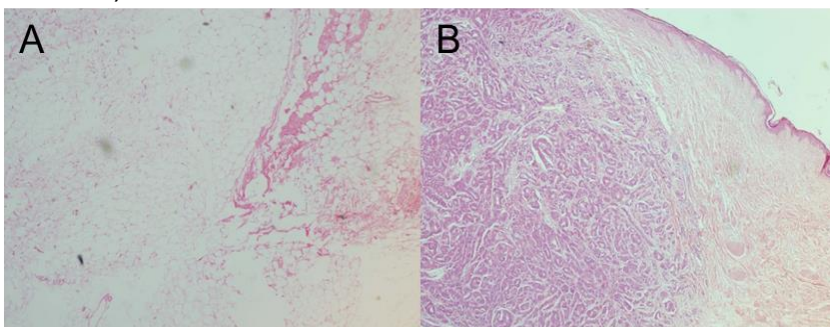
Gross Pathology:

Invasive Ductal Carcinoma Grade 3

Histologic Slide Analysis:

A) Normal Breast

B) Invasive Ductal Carcinoma Grade 3



Study Participant 11

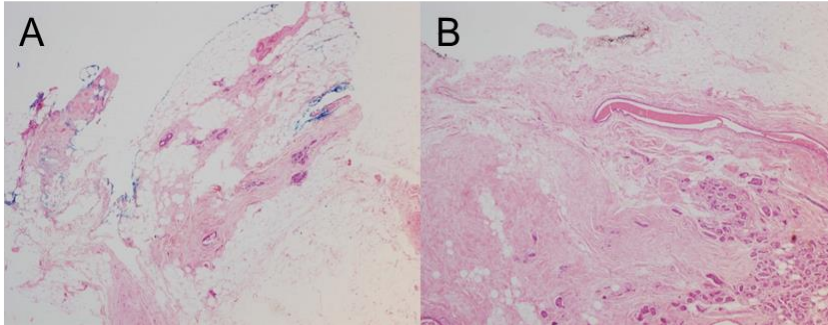
Gross Pathology:

Invasive Ductal Carcinoma Grade 3

Histologic Slide Analysis:

A) Normal Breast

B) Invasive Ductal Carcinoma Grade 3

**Study Participant 12**

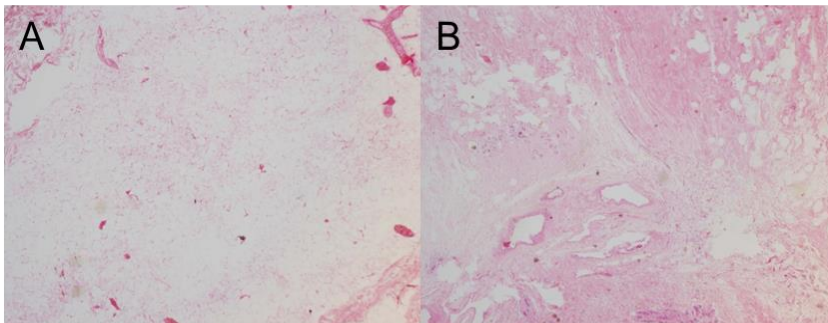
Gross Pathology:

Invasive Ductal Carcinoma Grade 3

Histologic Slide Analysis:

A) Normal Breast

B) Invasive Ductal Carcinoma Grade 3

**Study Participant 13**

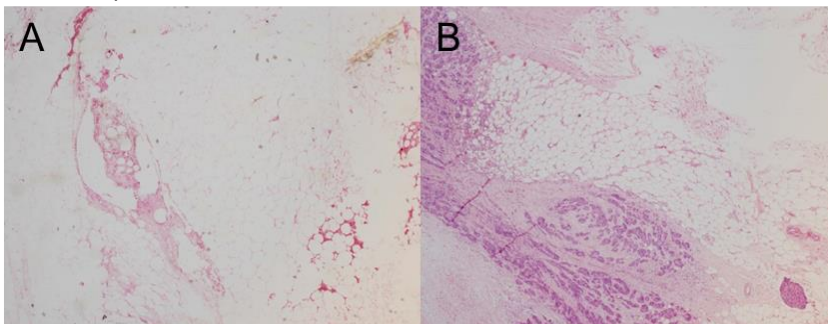
Gross Pathology:

Invasive Ductal Carcinoma Grade 3

Histologic Slide Analysis:

A) Normal Breast

B) Invasive Ductal Carcinoma Grade 3



Study Participant 14

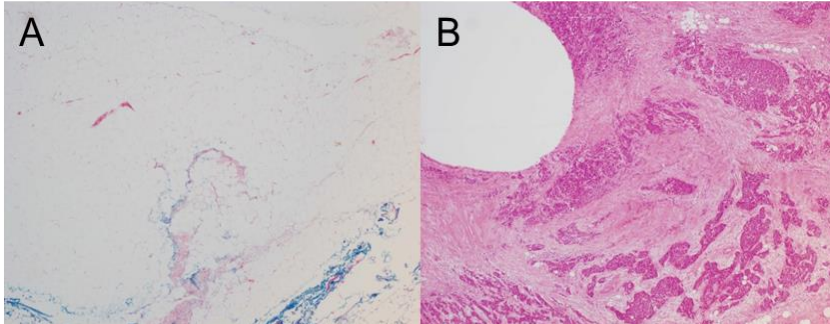
Gross Pathology:

Invasive Ductal Carcinoma Grade 3

Histologic Slide Analysis:

A) Normal Breast

B) Invasive Ductal Carcinoma Grade 3

**Study Participant 15**

Gross Pathology:

Invasive Ductal Carcinoma Grade 3

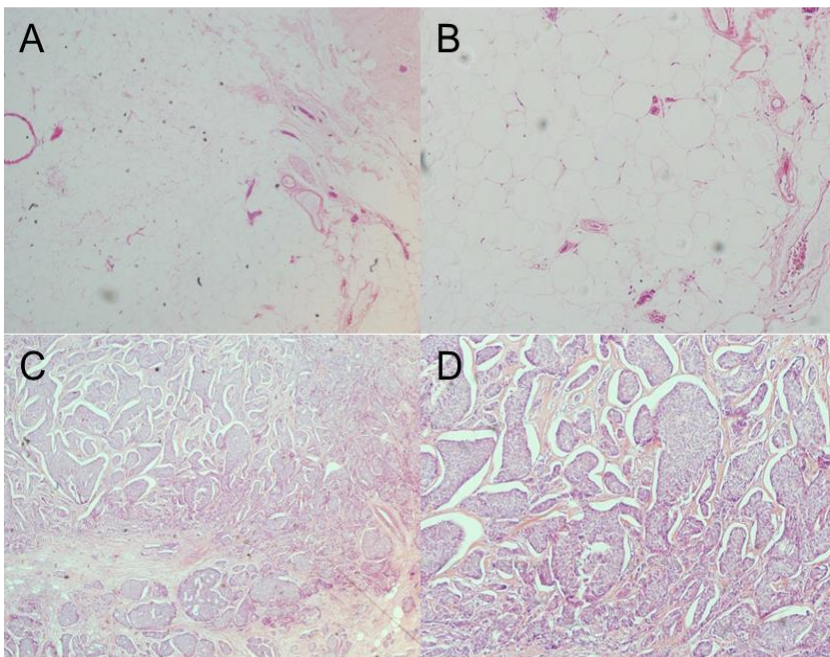
Histologic Slide Analysis:

A) Normal Breast (x4)

B) Normal Breast (x10)

C) Invasive Ductal Carcinoma Grade 3 (x4)

D) Invasive Ductal Carcinoma Grade 3 (x10)



Study Participant 17

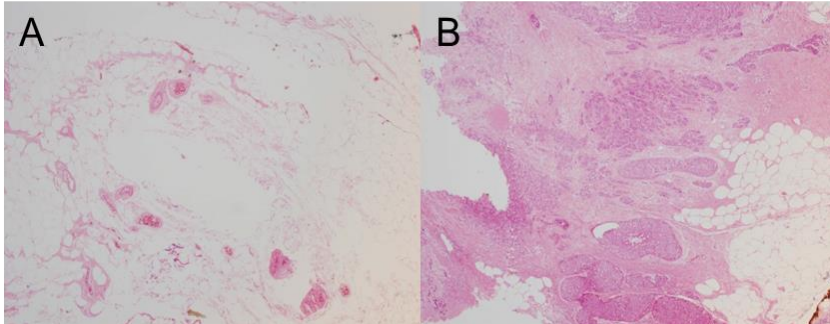
Gross Pathology:

Mixed Invasive Ductal and Lobular Carcinoma Grade 2

Histologic Slide Analysis:

A) Normal Breast

B) Mixed Invasive Ductal and Lobular Carcinoma Grade 2

**Study Participant 18**

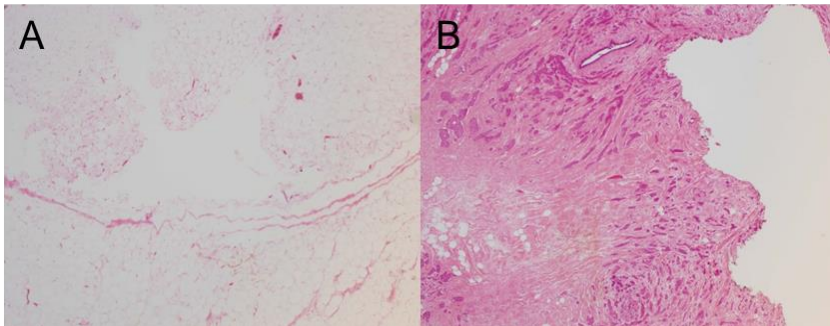
Gross Pathology:

Invasive Ductal Carcinoma Grade 2

Histologic Slide Analysis:

A) Normal Breast

B) Invasive Ductal Carcinoma Grade 2

**Study Participant 19**

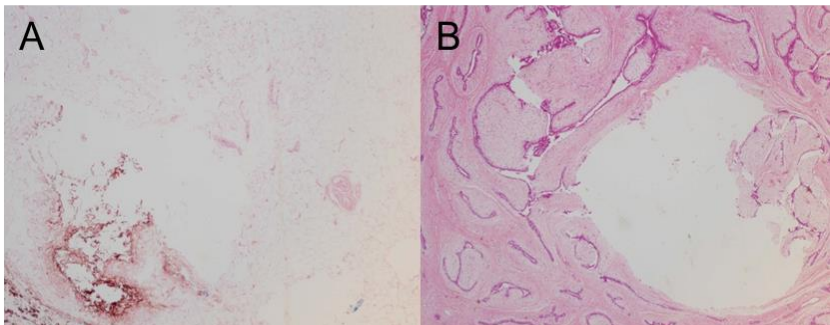
Gross Pathology:

Atypical Lobular Hyperplasia in Fibroadenoma

Histologic Slide Analysis:

A) Normal Breast

B) Atypical Lobular Hyperplasia in Fibroadenoma



Study Participant 20

Gross Pathology:

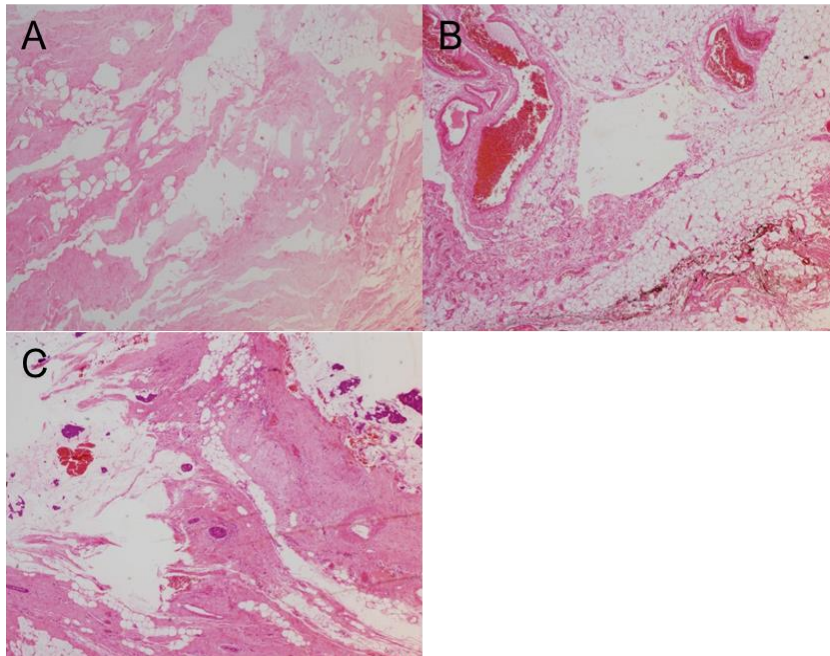
Invasive Mucinous Carcinoma Grade 2

Histologic Slide Analysis:

A) Normal Breast

B) Invasive Ductal Carcinoma Grade 2

C) Invasive Ductal Carcinoma Grade 2 Area 2

**Study Participant 26**

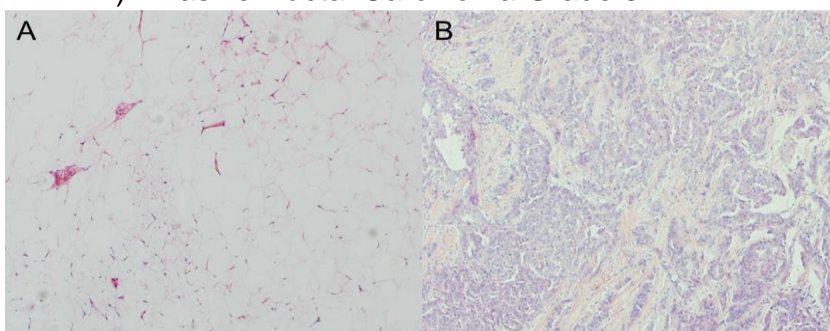
Gross Pathology:

Invasive Ductal Carcinoma Grade 3

Histologic Slide Analysis:

A) Normal Breast

B) Invasive Ductal Carcinoma Grade 3



Study Participant 27

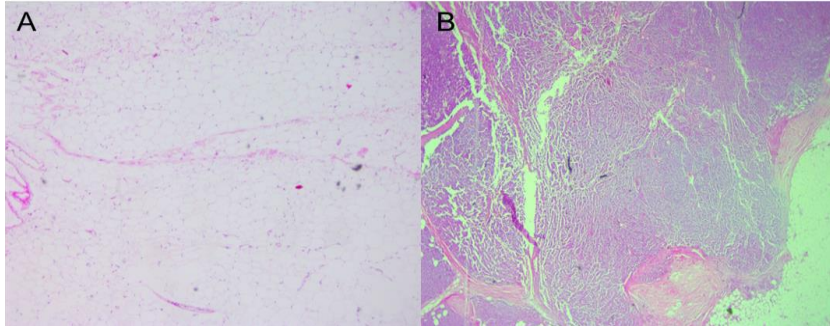
Gross Pathology:

Mixed Invasive Ductal and Lobular Carcinoma Grade 2

Histologic Slide Analysis:

A) Normal Breast

B) Mixed Invasive Ductal and Lobular Carcinoma Grade 2

**Study Participant 28**

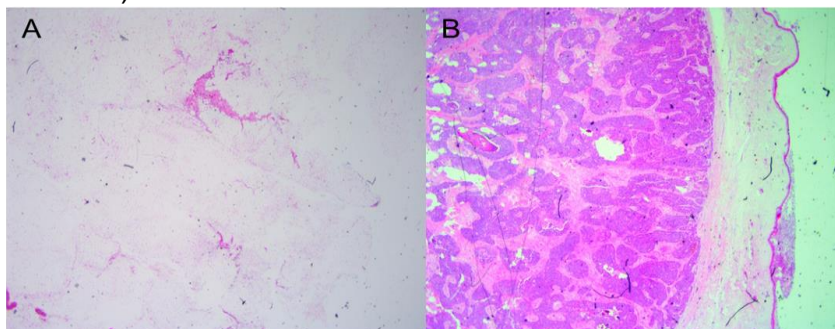
Gross Pathology:

Invasive Ductal Carcinoma Grade 3

Histologic Slide Analysis:

A) Normal Breast

B) Invasive Ductal Carcinoma Grade 3

**Study Participant 30**

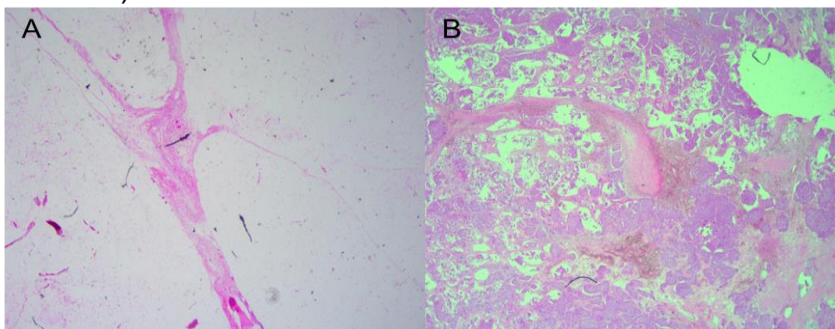
Gross Pathology:

Invasive Ductal Carcinoma Grade 3

Histologic Slide Analysis:

A) Normal Breast

B) Invasive Ductal Carcinoma Grade 3



Study Participant 31

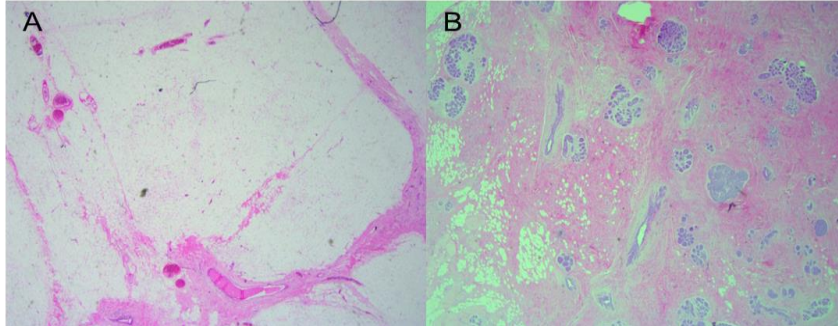
Gross Pathology:

Mixed Invasive Ductal and Lobular Carcinoma Grade 2

Histologic Slide Analysis:

A) Normal Breast

B) Mixed Invasive Ductal and Lobular Carcinoma Grade 2

**Study Participant 32**

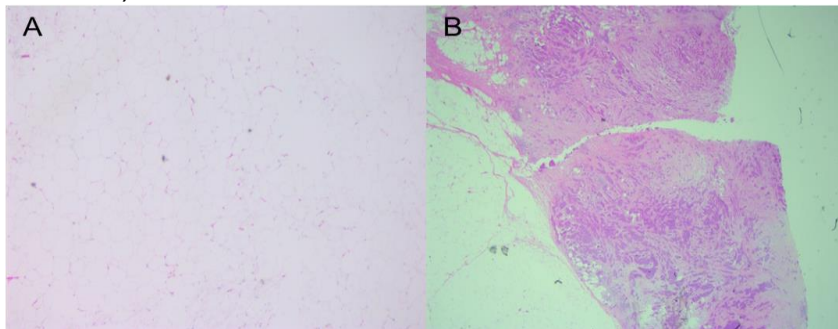
Gross Pathology:

Invasive Ductal Carcinoma Grade 3

Histologic Slide Analysis:

A) Normal Breast

B) Invasive Ductal Carcinoma Grade 3

**Study Participant 33**

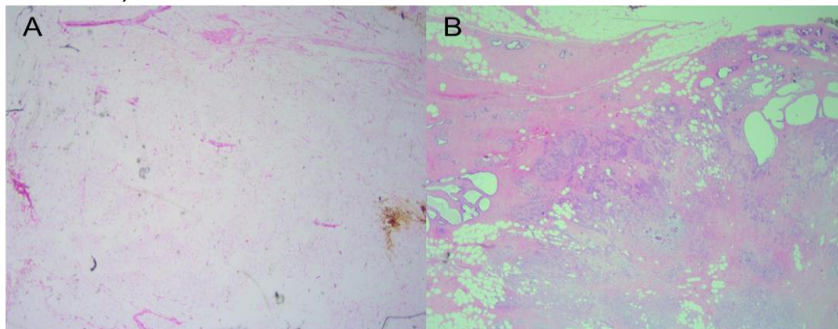
Gross Pathology:

Invasive Ductal Carcinoma Grade 2

Histologic Slide Analysis:

A) Normal Breast

B) Invasive Ductal Carcinoma Grade 2



6.7 Dimensions of Cell Culture Holders

Holder Section	Dimension	Size (mm)
Top of Holder	Width	30
	Depth	30
	Height	12
Media Well	Diameter	15
	Depth	10
Bottom Well Opening	Diameter	2
O-ring Recess	Diameter	5
	Depth	2
Bottom of Holder	Width	30
	Depth	30
	Height	12
Probe Recess	Width	3
	Depth	16
	Height	0.5
Screw Holes	Diameter	4

6.8 Paired-samples T test Outputs

6.8.1 Beef, Lamb and Pork

	Paired Differences					t	df	Sig. (2-tailed)
Tissue Type	Mean	S.D	S.E.M	95% C.I				
				Lower	Upper			
All Tissues	41653	18594	3578	34298	49009	11.640	26	0.000000000008
Beef	35607	16189	5396	23163	48051	6.598	8	0.000170
Lamb	58816	9933	3311	51180	66452	17,762	8	0.00000001
Pork	30537	15854	5284	18350	42724	5,778	8	0.000415

6.8.2 Clinical Trial Samples

	Paired Differences					t	df	Sig. (2-tailed)
Lesion Type	Mean	S.D	S.E.M	95% C.I				
				Lower	Upper			
All Samples	4340	4122	859	2557	6122	5.049	22	0.000047
All Cancer	4187	4290	936	2234	6139	4.470	20	0.000233
Primary Breast	3845	4098	916	1927	5763	4.196	19	0.000490
All IDC	3661	3748	967	1585	5737	3.783	14	0.002311
IDC G3	5111	4615	1391	2010	8212	3.673	10	0.004294
IDC G2	1329	651	325	293	2365	4.083	3	0.026547
Mixed IDC/ILC G2	2278	3985	2301	-7622	12179	.990	2	0.426417
Fibroadenoma	5947	383	271	2497	9397	21.906	1	0.029041